1995

The properties of Very High Energy gamma ray sources observed using the air Cherenkov technique

Gora Mohanty
Iowa State University

The properties of Very High Energy gamma ray sources observed using the air Cherenkov technique

by

Gora Mohanty

A Dissertation Submitted to the
Graduate Faculty in Partial Fulfillment of the
Requirements for the Degree of
DOCTOR OF PHILOSOPHY
Department: Physics and Astronomy
Major: Astrophysics

Approved:

Signature was redacted for privacy.

In Charge of Major Work

Signature was redacted for privacy.

For the Major Department

Signature was redacted for privacy.

For the Graduate College

Members of the Committee:

Signature was redacted for privacy.

Signature was redacted for privacy.

Signature was redacted for privacy.

Signature was redacted for privacy.

Iowa State University
Ames, Iowa
1995

TABLE OF CONTENTS

LIST OF TABLES

LIST OF FIGURES

ACKNOWLEDGEMENTS

I would like to acknowledge the invaluable help and advice of Dave Lewis and Dick Lamb at Iowa State. It is said that graduate students come to resemble their mentors—it would be my fortune if this were to even partly become true in my case. I would also like to thank Frank Krennrich, Mark Smucker, Ping Kwok, and Jeff Zweerink for the numerous ways that they have aided in this work.

I thank the various members of the Whipple Collaboration with whom I have come in touch. A big thank you to Glenn Sembroski and Mary Kertzman for allowing the use of their simulation program that is used in a large part of this dissertation. Detailed discussions with Michael Hillas were of inestimable help in tracking down the details of the simulations and often in uncovering my errors. Also, thanks to Dave Fegan, Trevor Weekes, Carl Akerlof, Adrian Rovero, Jim Buckley, Michael Schubnell, Steve Biller, Joachim Rose, Michael Cawley, Giuseppe Vacanti, Michael Punch and Josh Reynolds, all of whose effort has been made liberal use of here. To all the other people—too numerous to name here—that I met in the course of my visits to Arizona, I thank you for your ready friendship.

I am indebted to my parents and my family and relatives for their unfailing support, even halfway across the world. The friends I have made over the course of my graduate career were largely responsible for allowing me to survive through these last several years. In particular, I thank Dave Schwellenbach for fostering in me an appreciation of the things that really matter in life. Also, thanks to Kevin Kimberlin, Jonathan Lang, Stefan Kycia, Jennifer Thoelke, Meg Lysaght, Susan Kiehne, Alice and Linda Bailey, Jamie Lee, Vassilios Charmandaris, George Kopidakis, Sara Thiemann, Abram Morodi, Dustin Glist, Manuel Lozano, Patricia Pulvirenti, Dimitrios Kouzodis, Tony Parakka, and everybody else who have made my stay in Ames a wonderful experience. Also, a special thank you to Martha Camp, just because she

probably would not believe it. My gratitude to my cat, Bud for adopting me, and teaching me the secret of getting your own way in life—be furry and cute. Thanks to Goofball, Little, and Lucy for deigning to notice me.

Lastly, I thank the Divine for this wonderful and many-splendoured creation. From Him flows all knowledge and perfection—the shortcomings are all mine. I am as a child scrabbling at pebbles on the surface, while the vein of gold lies hidden beneath. I pray that this work might be accepted as an humble offering to further my mental and spiritual growth.

CHAPTER 1. INTRODUCTION

1.1 Gamma ray astrophysics

The origin of cosmic rays remains one of the outstanding unsolved problems in contemporary physics, even though it has been over 80 years since their discovery by Viktor Hess. Cosmic rays are ionized nuclei that have relativistic energies, and impinge on the Earth's atmosphere at a rate of $\sim 1000\mathrm{m}^{-2}\mathrm{s}^{-1}$. The highest energy cosmic rays are ultra-relativistic and a single particle might carry a macroscopic amount of energy. The origin of cosmic rays and the mechanism by which they are accelerated to such incredible energies is an intriguing puzzle that is still open to question. Over the years the study of the spectrum, chemical composition, and isotopic abundances of the cosmic rays have made it fairly clear that the bulk of the cosmic rays originate in the galaxy. Though not experimentally established, the currently attractive theory for the origin of these cosmic rays is Fermi acceleration in supernovae shock waves (see, for example, Axford [6]), which seems to offer a plausible explanation and agrees with the energetics expected from the rate of supernovae outbursts. The study of cosmic rays is an active area of research, and the most up to date references probably are to be found in the proceedings of the biennial International Cosmic Ray Conference, especially the invited, rapporteur, and highlight talks. There are several excellent texts, such as Longair [75], Gaisser [41], Hillas [56], Ginzburg [44], Hayakawa [52], Rossi [97], that serve as gentle introductions to the subject.

Gamma ray astronomy started as an outgrowth of cosmic ray physics, and the search for cosmic ray sources remains a common rationale for continued advancement of this field. Till about the two highest energy decades (10^{18} eV to 10^{20} ev), the arrival directions of cosmic rays at the Earth are rendered isotropic by the galactic magnetic

field. However, gamma rays, being uncharged, do not spiral along the magnetic field lines of the galaxy, and hence can be traced back to their source. Therefore, the hope was that by investigating the sources and plausible acceleration mechanisms for gamma rays, one can hope to glean clues about the origin of at least the galactic component of the cosmic rays. Gamma ray astronomy is already addressing crucial questions in cosmic ray physics, such as information about the variation of cosmic ray composition within the galaxy, and outside it. The search for TeV gamma ray emission from shell-type supernovae should, in the near future, restrict models for cosmic ray acceleration in supernovae shock fronts.

The spectrum of gamma rays stretches over more than fifteen decades, from the lowest energy of an electron rest mass ($\sim 5.11 \times 10^5$ eV) to the highest observed particle energies ($\sim 10^{20}$ eV), and covers a broad range of interaction physics and detection techniques. It is convenient to subdivide this huge span of energy into more sensible bands, as has been done by Weekes [116, Table 1]. His classification scheme, is shown in Table 1.1, which has been adapted from the text of the article. Later in

Table 1.1: Classification of gamma ray energy bands

Energy range (ev)	Nomenclature	Detection technique	Observation platform
$5.1 \times 10^5 - 1 \times 10^7$	Low/nuclear (LE)	NaI crystal	satellite
$1 \times 10^7 - 3 \times 10^7$	Medium (ME)	Compton telescope	satellite
$3 \times 10^7 - 1 \times 10^{10}$	High (HE)	spark chamber	satellite
$1 \times 10^{10} - 1 \times 10^{14}$	Very high (VHE)	air Cherenkov	mountain
$1 \times 10^{14} - 1 \times 10^{17}$	Ultra high (UHE)	air shower array	mountain
1×10^{17} upwards	Extremely high (EHE)	air shower array	sea level

this section, I shall describe the current status of the field, with an emphasis on the ME to VHE regime.

1.1.1 Current status

Recently, with the very successful operation of the satellite-based Compton Gamma Ray Observatory (CGRO), gamma ray astronomy is rapidly becoming a field of interest in its own right. Fig. 1.2 shows a picture of pointlike sources in the

sky, as seen in gamma rays at energies above 100 MeV. The Energetic Gamma Ray Experiment Telescope (EGRET) on board CGRO, has completed the first comprehensive all-sky survey at energies above 100 MeV. Fig. 1.2 shows a picture of (a) the entire sky, as seen in gamma rays above 100 MeV, including both diffuse emission and pointlike sources, and (b) pointlike sources in the sky that exhibit gamma ray emission above 100 MeV.

The highlights of the EGRET observations include 33 active galactic nuclei seen with a high significance (and 11 others with lesser significance), five pulsars with emission above 100 MeV, and several high-latitude unidentified sources often exhibiting significant time-variability, high energy gamma ray bursts upto an energy of about 25 GeV, high energy radiation from the Large Magellanic Cloud (LMC), and gamma ray emission from solar flares extending to energies of at least 2 GeV.

Observations made with the Burst And Transient Source Experiment (BATSE), which is also part of the CGRO satellite, have completely upset the previously accepted paradigm for gamma ray bursts. Fig 1.3 taken from [reference] shows the distribution on the sky for 921 bursts observed by BATSE. These show a remarkable degree of isotropy and have no correlation with the population of any known galactic objects. This, coupled with the fact that the energy distribution of the bursts does not exhibit the fall-off that would be expected if one were able to see to the edge of the distribution, seems to imply that these bursts originate at cosmological distances. This conclusion, if valid, leads to fantastic amounts of energies released over very short time scales, which is hard to reconcile with known physics.

The details of the CGRO observations can be found in a host of publications. See, for example, Gehrels et al. [43], Fichtel et al. [36], Fishman [37], Bertsch et al. [7], and Thompson et al. [110]. The sky maps reproduced here were obtained from the CGRO online electronic archives.

An adjunct to the EGRET observations has been the expansion of the catalogue of VHE source candidates for ground based observatories, especially of the air Cherenkov type that operate at energies just above those of EGRET. Indeed the Whipple Observatory has detected VHE gamma ray emission from the blazar, Markarian 421 (Mk421) in the EGRET list. Contemporaneous observations of Mk421 at several different wavelengths have been carried out, involving the Whipple 10-meter

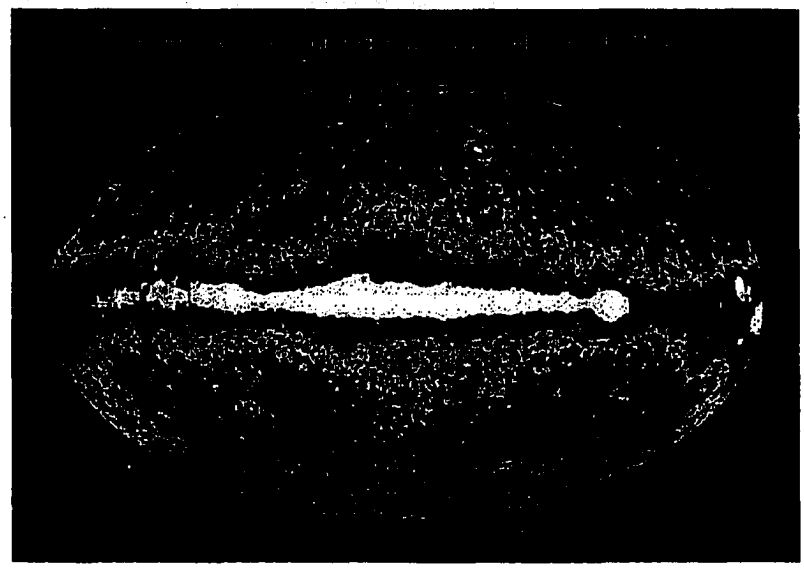

Figure 1.1: The sky in gamma rays above 100 MeV, as seen by EGRET (second phase) .

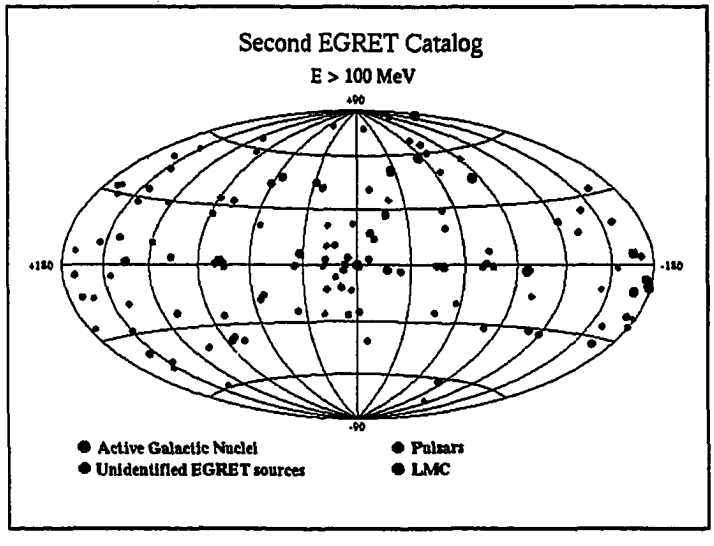

Figure 1.2: Pointlike sources detected by EGRET (second phase)

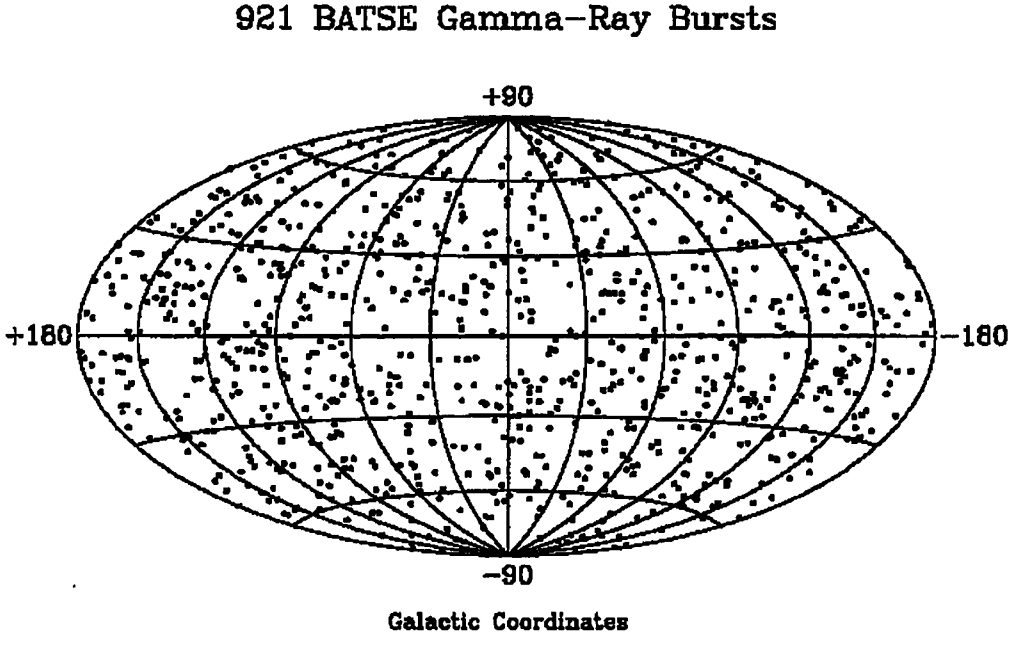

Figure 1.3: Distribution in the sky of 921 gamma ray bursts seen by BATSE.

telescope, CGRO, the X ray satellite ASCA, and a variety of other instruments (see Macomb et al. [77]). In the course of these, the Whipple Observatory detected a TeV flare where the flux above 250 GeV increased by nearly an order of magnitude from its quiescent levels (see Kerrick et al. [63]). This coincided to within a day of a flare at hard X ray energies, observed by ASCA (see Takahashi et al. [108]). Interestingly, there is little to no evidence for variability at other wavelengths, including the GeV energies of EGRET. This constrains the models for the emission mechanisms in gamma ray blazars, and long term monitoring of time variability can provide important clues as to whether the observed gamma ray emission is from hadronic jets or from electrons.

There has been a recent proliferation of air Cherenkov experiments throughout the world, and several more are in various stages of planning. Some of the more interesting experiments that utilize the air Cherenkov technique are, CANGAROO (Collaboration between Australia and Nippon for a Gamma-Ray Observatory in the Outback), AGSAT/THEMISTOCLE, and Potchefstroom. Other, higher energy detectors that record the cascade particles directly include HEGRA, CYGNUS, CASA-MIA, and the Tibet air shower array. Notable results include the detection of unpulsed VHE radiation from PSR 1706-44 in the Southern hemisphere by a joint Japanese-Australian collaboration (see Kifune et. al., [65]). Very recently, a detection has also been reported by the Whipple Observatory for the object Markarian 501 (Mk501) that has remarkably similar properties to Mk421, and is also at a low redshift (see Quinn et al. [91]). This object has not been detected by CGRO, which is an indication of the fact that the sensitivity of the Whipple imaging telescope exceeds that of EGRET, for a source with a hard spectrum.

The VHE energy regime is a largely unexplored window in the electromagnetic spectrum and seems to be in a unique position of being able to address several important astrophysical questions. These include:

1. *Blazar spectral breaks:* Determining the energies at which AGN spectra start falling off, and determining whether this cut off is intrinsic to the source or is caused by the scattering of the TeV gamma rays off the intergalactic infra-red radiation field (IIRF).

2. Measurement of the IIRF: To date, the VHE measurements of $\sim$ TeV flux from distant AGN's provide the most sensitive upper limit for the flux in a wavelength range of 10–12μm, including upper limits from direct experimental measurements (see, for example, Biller et al. [15] and other references in that paper). There have been other, more radical, propositions to use the information from the observed absorption spectrum from distant AGN's and the temporal profiles of observed bursts to measure everything from the intergalactic magnetic field to the Hubble parameter, but these will probably have to wait for later-generation detectors.

3. Pulsar spectral breaks: The pulsed flux of gamma rays from pulsars seems to disappear somewhere in the range of a few tens of GeV to about 200 GeV. Pushing the energy threshold of air Cherenkov telescopes to these levels is therefore a matter of great interest at present, and can conceivably be achieved by the next generation of Cherenkov telescopes.

4. Shell-type supernovae: As mentioned earlier in this section, the study of gamma ray emission in the VHE regime from shell-type supernovae constrains the models that predict the generation of low energy cosmic rays in such shock fronts. It is likely that in the very near future, air Cherenkov telescopes will be able to decide the question of whether these objects are the sources of low energy cosmic rays.

5. X-ray binaries: There have been several controversial reports of detection of X-ray binaries at energies ranging from $\sim$ TeV to $\sim$ PeV. Most results rely on looking for periodicities observed at lower energies. Detections have been claimed for Cygnus X-3, Hercules-X1, Centaurus X-3, Vela X-1, and the cataclysmic variable, Ae Aqr. One observation worth noting is a tantalizing report of the detection of an apparent pulsed flux from Hercules X-1, simultaneously by three independent groups. The observed period was slightly lower than the X ray period. While the question of whether X-ray binaries exhibit VHE (and higher energy) gamma ray emission is still decidedly a matter of who one talks to; as Cronin [27] notes, it is probably significant that the earlier reports have

not been substantiated by more recent ones from newer detectors with a higher sensitivity.

6. Serendipity: As the sky has still to be extensively studied in the VHE region of the electromagnetic spectrum, there is the possibility of chance discoveries of hitherto unsuspected sources that shine only at these energies. In this respect, VHE gamma ray astronomy at this point of time is often compared to the early days of X ray astronomy, before its rapid growth.

In all of these, there is a crucial step that needs to be taken from the simple detection of a source, to being able to describe its physical properties and emission mechanisms. To my mind, at least, that step is the sign of a maturing field that has evolved beyond the initial confusion and can properly be considered to be scientific in nature. A reliable method of estimating the spectra of gamma ray sources seen with an air Cherenkov telescope is therefore essential, and that is the subject of this thesis.

1.1.2 Guide to this thesis

This section should be properly subtitled, *"How to avoid reading most of this thesis."* The aim of this thesis is to describe a reliable method of the measurement of the spectra of VHE gamma ray sources, and specifically apply it to the Crab nebula. Chapter 2 discusses some historical aspects of the Crab supernova remnant, and observations of it. Chapter 3 describes the detector, and the technique used to detect high energy particles entering the Earth's atmosphere, and can be skipped by anyone familiar with the field. Chapter 4 is devoted to describing the procedure to be used for spectrum extraction, and is the main thrust of this work. Chapter 5 deals with checks on the simulations, and Chapter 6 presents the results of applying the procedure to various sets of VHE data on the Crab. Finally, Chapter 7 briefly discusses the results and outlines possible future strategies that might be adopted in this area.

CHAPTER 2. THE CRAB NEBULA

The Crab Nebula has been a perennial favourite of astronomical observers, from the ancient times of the original supernova explosion. So much so, that it is often remarked, only partly in jest, that modern astronomy can be classified into the study of the Crab and the study of everything else. This special treatment owes a lot to its status as a unique high energy astrophysical laboratory whose origin is well established, and which can be observed over a wide range of wavelengths.

2.1 Historical observations

The supernova explosion that resulted in the present day Crab Nebula probably occurred in July, 1054 and seems to have been recorded by independent Chinese and Japanese observers (see Clark [25] and Mitton [81]), though there is no contemporaneous record of it in European or Arabic tracts. Miller [80] has interpreted rock paintings of a crescent moon and a circle, found in Northern Arizona as representations of the Crab supernova explosion[1]. Since then, other similar paintings have been discovered at other places in the Southwest United States, the most famous of which is probably the samples from the Mimbres Indian pottery (see Robbins [94]). These conclusions for the North American records are still disputed however, as the details are often not completely correct, and the American Indians had little tradition of recording momentuous events, though they did practise astronomy. From the Chinese and Japanese accounts, the time of the explosion can be estimated as early morning (local time) on the 4th of July, 1054 A. D. The star reached a maximum apparent magnitude of about -5, bright enough to be visible in the day time. It

[1] At the time of the explosion, the moon as seen from the southwestern part of North America would have been a crescent close to the supernova position.

dwindled to the threshold of day time visibility—about -3.5 apparent magnitude—in approximately three weeks time, and remained visible to the naked eye for a period of about 21 months.

Seven-and-a-half centuries later, the nebulosity in the Crab region was discovered by Bevis, and it was later included as the first object in the famous Messier catalogue. Though there was great interest in the nebulae published in the catalogue, not much additional information was gathered on the Crab, till the observations made by the third Earl of Rosse in 1844. His initial drawings of the nebula probably led to the name of the Crab. The first photograph of the Crab was taken with a 20-inch reflecting telescope in 1892. The Crab appears as an amorphous distribution of hot gas, threaded through by a twisted maze of filamentary structures. The bright continuum emission from the Crab comes from the hot gas. Superimposed on top of this is the strong emission lines seeming to originate mostly from the filaments.

In 1948, an Australian group led by J. Bolton [16] discovered four radio sources, including one in the Taurus constellation that they labelled Taurus A. They also measured the position of this source next year, to an accuracy of about 7 arc-minutes, using a crude radio interferometer. This agreed with the optical position of the Crab, making it the first non-solar system radio source to be identified with an optical object. Alfvén and Herlofson suggested in 1950 that cosmic radio sources were due to synchrotron emission. The Russian astrophysicist, Shklovsky [104] is credited with first associating the continuum emission at visible wavelengths, from the Crab nebula with synchrotron radiation by electrons in a magnetic field. This meant that the observed light could be expected to be strongly polarized, and this was verified by observations made by Dombrovski, Vashakidze, and later Baade. Indeed the polarization is so strong that, at specific orientations of the polarizing filter, some of the bright parts almost entirely disappear. The Crab has remained of enduring observational interest at all wavelengths, and later in this section, I give details of some of the relevant observational data.

2.2 VHE gamma ray observations

A survey of VHE observations of the Crab nebula is made in each of the several excellent review articles in the field, e. g., Weekes [116, 118], Cronin et al. [27]. The Crab has been reliably detected by at least seven groups worldwide, and is the closest thing to a standard candle in the field of gamma ray astronomy, as all indications are that the flux is steady over a period of several years, and the fluxes inferred by the various groups are in fair agreement. Table 2.1, drawn from the above sources and from de Jager et al. [29], presents the most significant detections of the Crab Nebula. De Jager et al. [29] have produced a synchrotron-self Compton model for

Table 2.1: Observations of the unpulsed flux from the Crab Nebula.

Energy (TeV)	Integral Flux ($10^{-8}m^{-2}s^{-}$)	Experiment	Reference
0.2	170	Sandia	Akerlof et al. [3]
0.4	70	Whipple	Weekes et al. [119]
0.6	27	ASGAT	Goret et al. [45]
1.0	15	Whipple	Weekes et al. [119]
2.0	15	HEGRA	Krennrich et al. [66]
2.0	3.5	Themistocle	Djannati-Atai et al. [31]
7.0	0.75	CANGAROO	Tanimori et al. [109]
10	¡ 0.91	Tibet AS_γ	Amenomori et al. [5]
11	0.2	Themistocle	Djannati-Atai et al. [31]
24	¡ 0.14	AIROBICC	Aharonian [2]
30	¡ 0.18	Tibet AS_γ	Amenomori et al. [5]
39	¡ 0.066	HEGRA	Merck et al. [79]
70	¡ 0.045	CYGNUS	Alexandreas et al. [4]
115	¡ 0.032	CASA-MIA	Borione et al. [17]

the unpulsed flux from the Crab Nebula, that nicely fits the data points in the table above. This fit is shown in Fig. 2.1, reproduced from the De Jager et al. [29] paper. In this model, the $\sim$ TeV flux originates from the inverse Compton scattering of soft photons by a population of shock-accelerated, relativistic electrons that have energies to a few PeV. The parameter σ in the fit is the ratio of the energy density in the

The properties of Very High Energy gamma ray sources observed using the air Cherenkov technique

Gora Mohanty

Major Professor: Dr. D. A. Lewis, Iowa State University

This work describes the use of Monte Carlo simulations to develop a set of gamma ray selection criteria for images of Cherenkov light in air showers, taken using the Whipple Gamma Ray Collaboration's 10-meter atmospheric Cherenkov detector. These selection criteria are suitable for the extraction of the energy spectra of the observed sources, and have been applied to the Crab nebula. I describe the method for the spectrum extraction and discuss possible systematic biases in the derived spectra, arising from an energy dependence in the telescope triggering, image selection, and fluctuations in the observed amount of light.

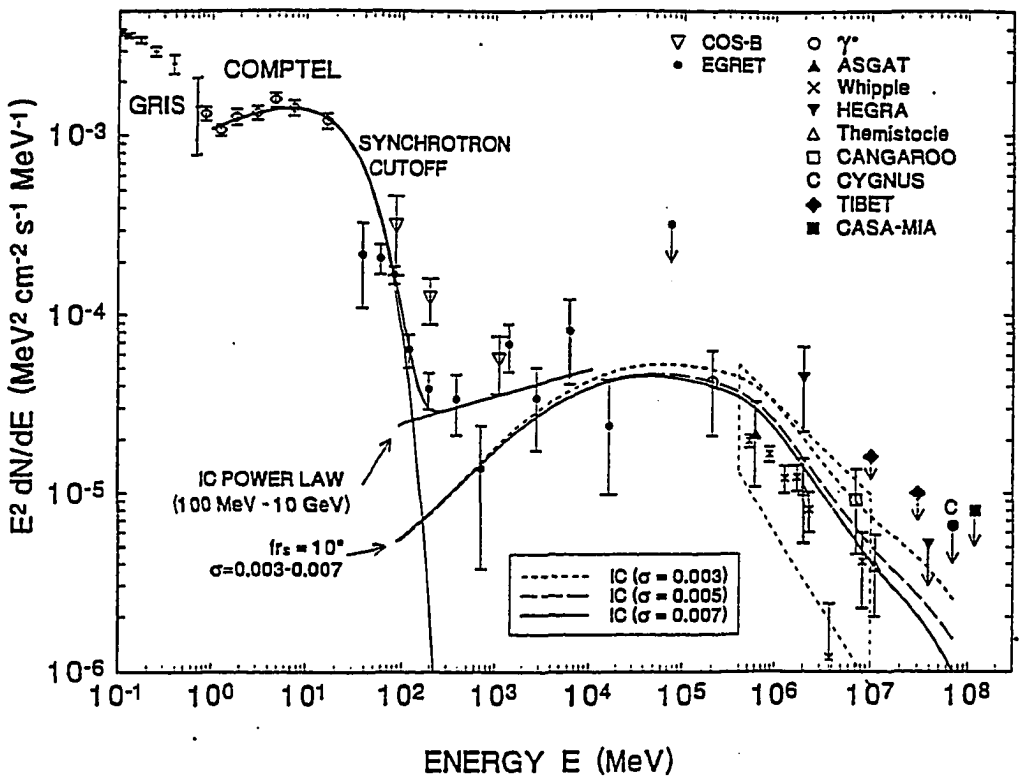

Figure 2.1: De Jager et al. fit to the unpulsed flux from the Crab nebula.

magnetic field to the electron energy density. The authors claim that the flux in the VHE range should be stable on a timescale of centuries, so that the Crab might indeed be the standard candle for gamma ray astronomy.

CHAPTER 3. THE IMAGING AIR CHERENKOV TECHNIQUE

3.1 Overview

This section discusses the process by which a high-energy particle entering the atmosphere initiates a cascade, the production of Cherenkov light in the cascade and the instrumentation that allows the detection of the Cherenkov light.

The atmospheric Cherenkov technique has been the most successful technique in the VHE band (0.1 Tev to 10 TeV), and is still currently the only practical choice. The fluxes of gamma rays in this energy regime are small enough to make satellite-borne detectors, with their small collection area, impractical. Also, shower maxima in the cascades at these energies occur high up in the atmosphere. The secondary particles in the cascade do not survive even to the highest observatory altitudes, and thus cannot be detected even by large arrays of particle detectors.

The air Cherenkov technique, in effect uses the whole atmosphere as a gigantic scintillation detector, with the high energy particles being stopped by the atmosphere and the actual observation being the Cherenkov light from the secondary particles. The principal problem in detecting gamma rays, using the air Cherenkov technique, has been the background of air showers created by high energy cosmic rays. These outnumber the gamma ray showers from a typical source by a factor of almost a thousand to one, and the Cherenkov light from these often closely resembles that from gamma ray showers. Thus an efficient technique is required to discriminate gamma ray showers from the background. This has been addressed very successfully by the imaging air Cherenkov technique discussed later in this chapter. For a general review of techniques, see, for example, reviews by Fry [39] and Weekes [116]. More recent reviews can be found in Cronin et al. [27] and Weekes [118].

3.2 Extensive air showers

A high energy cosmic ray or gamma ray entering the atmosphere with an energy greater than about 100 GeV, creates cascade showers containing several thousands of secondary particles. Early models for these were proposed independently by Bhabha and Heitler [8], and by Carlson and Oppenheimer [20]. Later developments have been made by a variety of people, e.g., Rossi and Greisen [96], Rossi [97], Greisen [46, 47], Snyder [107], Serber [103], Heisenberg [54], Bhabha and Chakrabarty [9, 10, 11]. General reviews of the theory and properties of these extensive air showers (EAS) may be found in Rossi and Greisen [96], Rossi [97], Greisen [46, 47], Hayakawa [52]; and more recently in Gaisser [41], Halzen [48]. Here I discuss the general properties of electromagnetic and hadronic showers.

3.2.1 Gamma ray showers

In a simple model for an electromagnetic shower, due to Heitler [53, pg. 232-240], the development takes place in steps of a radiation length. The primary gamma ray either pair-produces to give rise to an electron-positron pair or undergoes a Compton collision. In either case, secondary electrons are produced, that divide the energy of the primary gamma between them. These electrons, in turn lose energy by radiation (bremsstrahlung), producing more photons, with energy comparable to that in the electrons. The photons give rise to new electrons, which again produce more photons. A schematic picture of this is shown in Fig. 3.1. At each further step, the number of particles increases and their average energy gets smaller. This process continues till the average electron energy becomes low enough that ionization losses, from collision with air molecules, start dominating the radiation losses. Once that happens, the number of particles in the cascade starts decreasing rapidly, and the primary energy of the initial gamma ray is eventually dissipated into low energy electrons and ionization losses in the atmosphere. This model ignores other radiative processes with smaller cross-sections and completely glosses over the effect of small fluctuations in the early stages of a shower, that might have an important effect on the subsequent development. For example, if the first interaction of the primary gamma ray happens

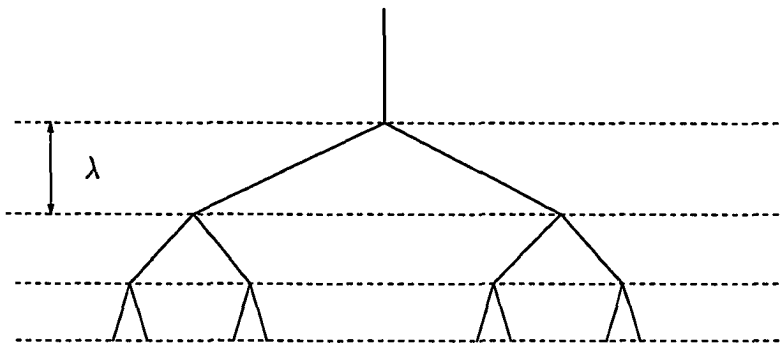

Figure 3.1: Simple cascade model. λ is the electron radiation length.

to be nuclear, producing hadrons[1], the rest of the shower resembles a hadronic, rather than an electromagnetic, shower.

It should be noted that, though the secondary particles tend to be strongly beamed in the forward direction due to the large momentum of the primary, they do get spread out laterally. This is mainly due to multiple Coulomb scattering of the secondary particles, with an occasional large deflection arising from a single scatter. Smaller contributions are made by the opening angles for pair production and electron bremsstrahlung. Multiple scattering has been treated by several different authors. (For a detailed explication and a general review see Scott [101].) The mean square angle of scattering, for an electron of rest mass m_e and energy E, in traversing an infinitesimal layer of thickness dt (measured in radiation lengths), is given by:

$$d\left\langle\theta^2\right\rangle = \left(\frac{E}{E_s}\right)^2 dt \tag{3.1}$$

where, E_s is a quantity with the dimension of energy, and is given by:

$$\begin{aligned} E_s &= m_e c^2 \sqrt{\left(\frac{4\pi}{\alpha}\right)} \\ &\cong 21 \text{ MeV} \end{aligned} \tag{3.2}$$

with c being the speed of light and $\alpha = 1/137$, the fine structure constant. For a

[1]This, of course, has a very small chance of happening. Gaisser [41, pg. 245] estimates the probability as about 0.003.

typical 100 MeV electron in a shower, the ionization losses are negligible and the energy remains approximately constant; so that Eq. (3.1) can be integrated to give:

$$\left\langle \theta^2 \right\rangle = \left(\frac{E}{E_s}\right)^2 t \tag{3.3}$$

Roughly speaking, the assumption of constant electron energy holds over one radiation length[2]. Hence, the root mean squared scattering angle for a typical electron, that survives on the average for a distance of one radiation length, is about 12° . Besides spreading the particles out laterally, a consequence of multiple scattering is that the track length of the relativistic charged particles is increased and they become longitudinally confined to a thin disk, often referred to picturesquely as a "swarm" of particles.

Normally, the cascade resulting from a primary gamma ray is almost entirely electromagnetic, though there is a muonic component that originates from photonuclear interactions and, to a much smaller extent, from direct muon pair-production. Similar cascades are also produced by cosmic ray electrons, though at a lower energy.

3.2.1.1 Cosmic ray showers An air shower inititated by a primary cosmic ray has the same basic cascade structure as outlined for an electromagnetic cascade (see 3.2.1), but there are some important differences. The cosmic ray initiated air shower can be considered to be made up of distinct hadronic, electromagnetic, and muonic components.

Consider the effect of the collision of a high energy cosmic ray proton with an atmospheric nucleus. The proton might survive (with reduced energy) and there might be a few secondary nucleons produced. The rest of the energy is given to other secondary particles, mostly charged pions. Due to the large momentum of the primary, all hadrons are beamed along the forward direction. If the charged pions have high enough energies, their lifetimes are relativistically time-dilated long enough that they interact rather than decaying. The secondary nucleons and charged pions continue to multiply in successive steps, until the average energy per particle drops

[2]A radiation length (see, for instance, [97, pg. 220]) is defined as the distance over which a particle loses $1/e$ of its initial energy, e being the base of the natural logarithm. For an electron in air, a radiation length is 37.1 g/cm^2.

below the threshold for pion production (about 1 GeV). This process, where the primary energy is distributed into pions, is referred to as pionization (see the classic paper by Pal and Peters [84]).

Neutral pions and eta particles typically decay immediately into gamma rays, each of which might initiate an electromagnetic subshower as described above. The muonic component arises from the decay of lower energy charged pions and kaons. Muons at these energies are highly penetrating as they lose energy only by decay or from ionization losses, both of which are negligible at moderately high energies.

The hadronic component is at the heart of a cosmic ray shower, feeding both the electromagnetic and muonic components. Fig. 3.2, based on similar diagrams from Longair [75, pg. 149], shows a picture of a shower initiated by, (a) a gamma ray, and, (b) a cosmic ray. Though highly stylized, it gives a flavour for the different processes taking place in these showers. From the cosmic ray shower diagram, it can be inferred that a little over a third of the energy at each hadronic interaction is channeled into the electromagnetic cascade. However, as the hadrons usually interact several times, most of the primary energy ultimately goes into the electromagnetic part. As the electromagnetic cascades develop rapidly, the most numerous particles in a cosmic ray shower are electrons and positrons, similar to the case of a gamma ray shower.

The lateral spread of the shower particles in a cosmic ray shower is greater than that for a gamma ray shower, a fact arising from the larger transverse momentum of the nuclear secondaries. The relevant quantity here is the ratio of a pion mass to an electron mass, $m_\pi/m_e \sim 300$. The larger lateral spread and the multi-cored natured of a cosmic ray shower is useful in distinguishing it from a gamma ray shower.

Nuclear primaries can be modelled simply as a collection of individual nucleons, with the primary energy partitioned between these. In this superposition model, a heavy nuclei shower is considered to be made up of A independent nucleonic showers, where A is the mass number for the primary. Hence, showers initiated by heavy nuclei are even more scattered than proton showers. This simple model is adequate for many purposes. A more accurate picture can be obtained by studying fragmentation histories of cosmic rays in nuclear emulsions.

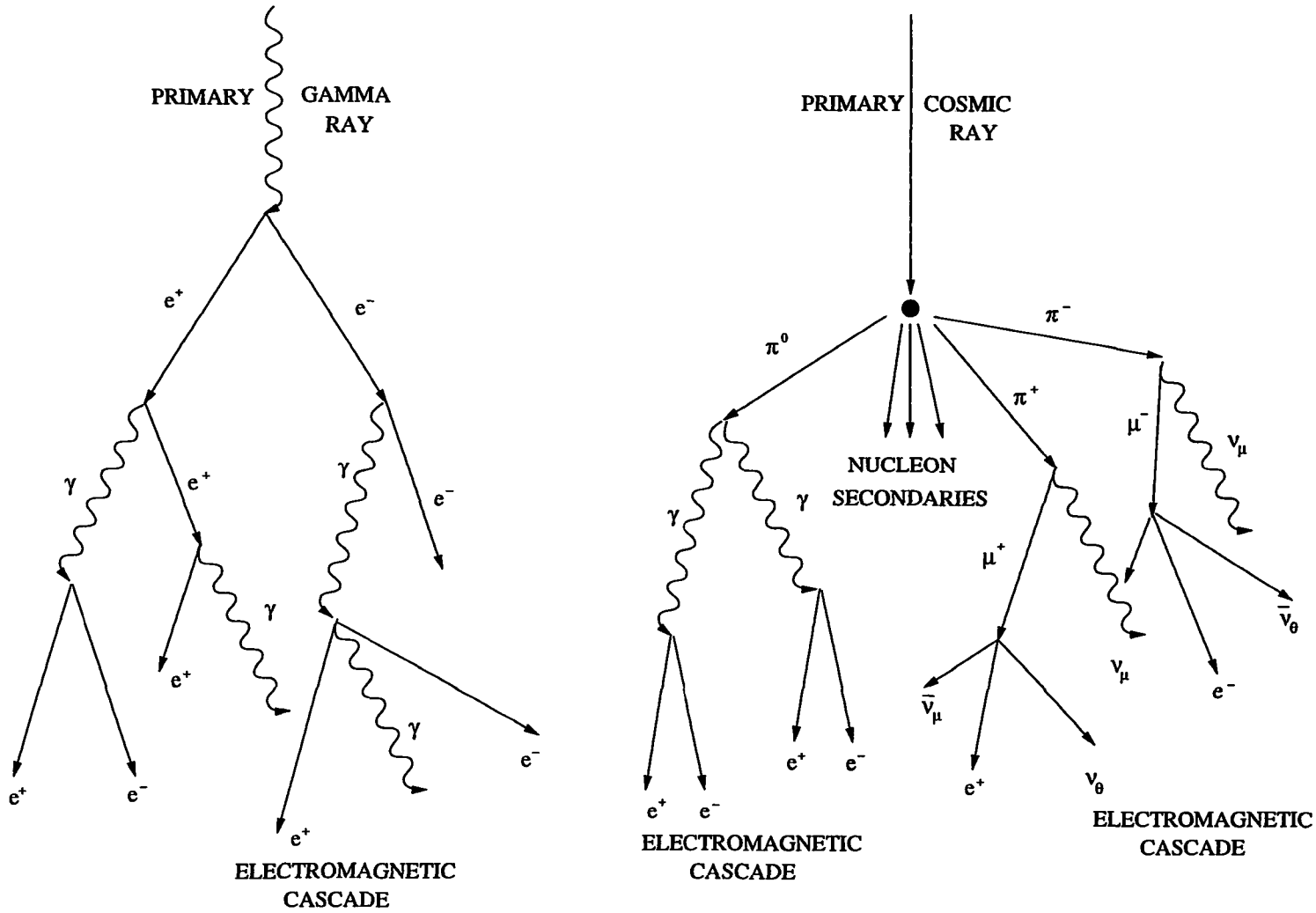

Figure 3.2: Schematic cascade picture. (a) Gamma ray shower. (b) Cosmic ray shower.

3.2.2 Cherenkov light in air showers

The Cherenkov effect arises from the coherent response of a dielectric media to a relativistic particle passing through it, at a speed exceeding the local phase velocity of light. The Cherenkov radiation from secondary particles in the atmospheric cascade created by a high energy primary will prove useful in detecting and characterizing these showers. This section discusses the origin of the effect and the properties of the radiation.

An interesting historical account of the discovery of the Cherenkov effect can be found in Jelley [60, pg. 1]. From this account, Cherenkov radiation was noticed as far back as 1910 by Mme. Curie, though it was not till 1937, that a correct theoretical explanation was given by Frank and Tamm. About at the same period of time, Cherenkov [24] conducted a series of elegant experiments in this area, which matched the theoretical predictions very well. According to Jelley, the first proposal to use a photomultiplier to detect Cherenkov light was made by Getting [42], and the first efficient detection was made by Jelley [59].

The Cherenkov radiation from a charged particle moving faster than the local phase velocity of light is analogous to the pressure shock wave created by supersonic flight. Detailed treatments of Cherenkov radiation can be found, for example, in Jelley [60, esp. Ch. 2 and 9], and Jackson [57, Sec. 13.5, pg. 638]. Rather than go through the details of the complex derivation I shall just quote their results here[3].

The refractive index of a medium, $n(\omega)$, can be related to its dielectric constant $\epsilon(\omega)$ by:

$$n^2(\omega) = \epsilon(\omega) \tag{3.4}$$

In the following calculations, we shall neglect absorption in the medium, so that $\epsilon(\omega)$ is real. For a particle of charge ze, travelling at a relativistic speed of $\beta = v/c$ in such a medium, Jackson gives the energy radiated as Cherenkov light per unit distance

[3]The Gaussian system of electromagnetic units is used throughout this work. See Jackson [57, Appendix, pg. 811] for a discussion of the various systems of units in use and how to convert between them.

along the particle track as (see [57, eq. 13.79, pg. 639], and [60, eq. 2.17, pg. 19]):

$$\frac{dE}{dx} = \frac{(ze)^2}{c^2} \int\limits_{\beta^2\epsilon(\omega)>1} \omega \left[1 - \frac{1}{\beta^2\,\epsilon(\omega)}\right] d\omega \tag{3.5}$$

Thus, the radiation is limited to a frequency band defined by $\beta^2\epsilon(\omega) > 1$. This is shown schematically in Fig. 3.3, borrowed from Jackson [57, Fig. 13.6, pg. 639]. The

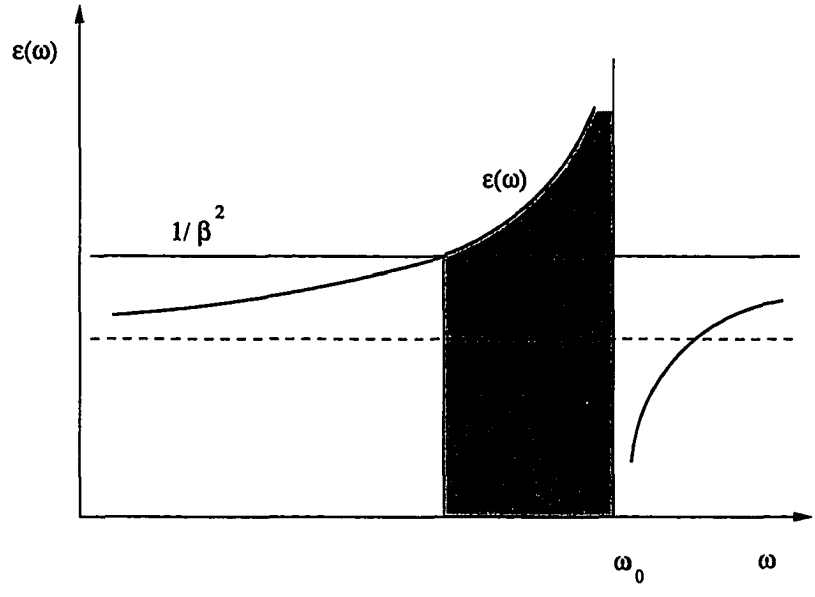

Figure 3.3: Schematic picture of Cherenkov band (shaded frequency region).

width of the Cherenkov band is large for $\beta \simeq 1$. However, the frequency band of interest is usually defined by other factors such as atmospheric transmittivity, mirror reflectivity, and photomultiplier quantum efficiency. Also, the Cherenkov radiation is emitted at a characteristic angle that can be derived by a Huygen wavelet construction (see, for example, Jelley [60, Fig. 1.2 and Eq. 1.1, pg. 5]). Alternatively, the radiation can be considered to be an electromagnetic wave travelling in the direction $\mathbf{E} \times \mathbf{B}$, and the angle can be found by approximating the distant fields by their asymptotic forms (see Jackson [57, sec. 13.5, pg. 638]). The Cherenkov angle, θ_c, is given by:

$$\cos\theta_c = \frac{1}{\beta\, n(\omega)} \tag{3.6}$$

Typically, the Cherenkov angle in air is of the order of several milli-radians.

The energy radiated, per unit path length, as Cherenkov light can be estimated in a simple model valid for a low density medium. In this model (see Jackson [57, sec. 7.5, pg. 284]), the refractive index is approximately given by:

$$n(\omega) = 1 + \left(\frac{\omega_p^2}{\omega_0^2 - \omega^2}\right) \tag{3.7}$$

where, ω_p is the plasma frequency, and ω_0 is the resonant frequency. Substituting Eq. (3.7) and Eq. (3.4), in Eq. (3.5), with $\beta \sim 1$, and evaluating the integral approximately in its region of validity, the energy radiated, per unit path length, as Cherenkov light is given by (compare with Jelley [60, Eq. 2.19, pg. 21]):

$$\frac{dE}{dx} = \frac{(ze)^2}{2c^2}\omega_p^2 \ln\left(\frac{\omega_0^2 + \omega_p^2}{\omega_p^2}\right) \tag{3.8}$$

For a typical medium, $\omega_p = 1 \times 10^{15}$ Hz, $\omega_0 = 6 \times 10^{15}$ Hz, so that dE/dx for an electron is of the order of 15 keV/cm. This is only ~ 0.1 % of the energy loss due to ionization, i.e., only a tiny fraction of the primary energy goes into Cherenkov radiation in the atmosphere.

The energy radiated as Cherenkov light can be usefully recast in terms of the number of photons emitted in traversing a path length of x. Assuming x is small enough that the change in energy of the particle over that distance is negligible, Eq. (3.5) gives the number of Cherenkov photons, N radiated over that length, in a wavelength band defined by λ_{min} and λ_{max}, as:

$$N = 2\pi\alpha x \left(\frac{1}{\lambda_{min}} - \frac{1}{\lambda_{max}}\right)\left(1 - \frac{1}{\beta^2 n^2}\right) \tag{3.9}$$

where, $\alpha = e^2/\hbar c$, is the fine structure constant. Or, from the definition of the Cherenkov angle, θ_c in Eq. (3.6), the number of photons, is given by:

$$N = 2\pi\alpha x \left(\frac{1}{\lambda_{min}} - \frac{1}{\lambda_{max}}\right)\sin^2\theta_c \tag{3.10}$$

which is the well-known Jelley formula (compare with Jelley [60, Eq. 2.22, pg. 22]).

To summarize, Cherenkov light in the atmospheric cascades initiated by high energy particles, originates mainly from the secondary electrons that are themselves

moving at relativistic speeds. The light is emitted at a small angle relative to the particle track. However, the particles themselves may be scattered out to large angles from the shower axis, by multiple scattering. Thus it is possible to detect Cherenkov light in atmospheric cascades even at large angles. The Cherenkov angle and the light intensity increase with both β and the refractive index, n. As a relativistic particle gets deeper in the atmosphere it sees a higher refractive index. However, the particle is also losing energy, so that β is decreasing. It is possible to estimate the threshold energy for Cherenkov light emission and the maximum Cherenkov angle (see, for example, Jelley [60, sec. 9.3, pg. 218]). The refractive index of the atmosphere is very nearly unity, so that it is convenient to write it as, $n = 1 + \eta$, where η is small. At the threshold for Cherenkov light emission, $\beta(1 + \eta) = 1$. Thus, for $\eta \ll 1$, the threshold energy, E_{min}, (including the particle rest mass energy, m_0c^2) is given by:

$$\begin{aligned} E_{min} &= \gamma_{min}\, m_0c^2 \\ &\simeq \frac{m_0c^2}{\sqrt{2\eta}} \end{aligned} \tag{3.11}$$

where, $\gamma = (1 - \beta^2)^{-1/2}$, is the relativistic gamma factor. Similarly, using the fact that $\theta_c \ll 1$, and $\eta \ll 1$, both sides of Eq. (3.6) can be expanded in a power-series, to give:

$$1 - \frac{\theta_c^2}{2} = 1 - \eta \tag{3.12}$$

which provides an estimate for the maximum value of the Cherenkov angle as:

$$(\theta_c)_{max} \simeq \sqrt{2\eta} \tag{3.13}$$

At an altitude of 8 km[4], the maximum Cherenkov angle is 0.9° and the energy threshold for an electron is 33 MeV.

3.2.3 Differences in gamma ray and cosmic showers

A discussion of the difference between gamma ray and cosmic ray showers can be found, for example, in Hillas [55]. Here, I limit myself to describing a few of the most significant differences.

[4]This is the average position of shower maximum for a shower initiated by a 1 TeV gamma ray

From the discussions in the previous sections, cosmic ray showers differ from gamma ray showers in having a hadronic and muonic component in addition to the electromagnetic component. It is difficult to detect the hadronic component owing to its small lateral extent compared to the spread in the shower particles. The muons are highly penetrating, and are the most obvious difference between the showers. However, they are produced high up in the atmosphere, and thus, their number distribution at observatory level is broader, making them difficult to detect without a large-area detector. Also, they make up a relatively small fraction of the particles in a hadronic shower, so that they are not very well suited for the efficient rejection of hadronic showers.

Cosmic ray showers penetrate deeper into the atmosphere, on the average, than gamma showers. As the cosmic ray showers get closer to the detector, it is to be expected that more of the ultraviolet light from these showers will survive atmospheric attenuation. Thus the proportion of ultraviolet light in the image might be used as a discriminant (see [23] for an example of this). Other possibilities discussed by Hillas include timing of the Cherenkov photons with a resolution of the order of a nanosecond (local Cherenkov light from prompt muons in the cosmic ray showers arrives before the light from the cascade particles), and measurement of the polarization of the Cherenkov photons.

Undoubtedly, the most successful technique in distinguishing between gamma ray showers and hadronic showers at gamma primary energies of about a TeV, has been the imaging of the Cherenkov light. A low resolution image of the shower can be made using an array of photomultiplier tubes to detect the Cherenkov light. A schematic picture of such an atmospheric Cherenkov telescope [5], with a small field of view, is shown in Fig. 3.4. The Cherenkov light is emitted along a small cone about the shower axis. Typically, the shower core is at a large distance from the detector, so that the intersection of the narrow field of view with the Cherenkov cone yields an elliptical image in the focal plane of the detector. Because of the smaller transverse momentum in an electromagnetic cascade, the light from gamma ray showers tends to be more concentrated than that from proton showers. This

[5] An example of such a detector is the 10-meter detector of the Whipple Observatory, discussed in the next section.

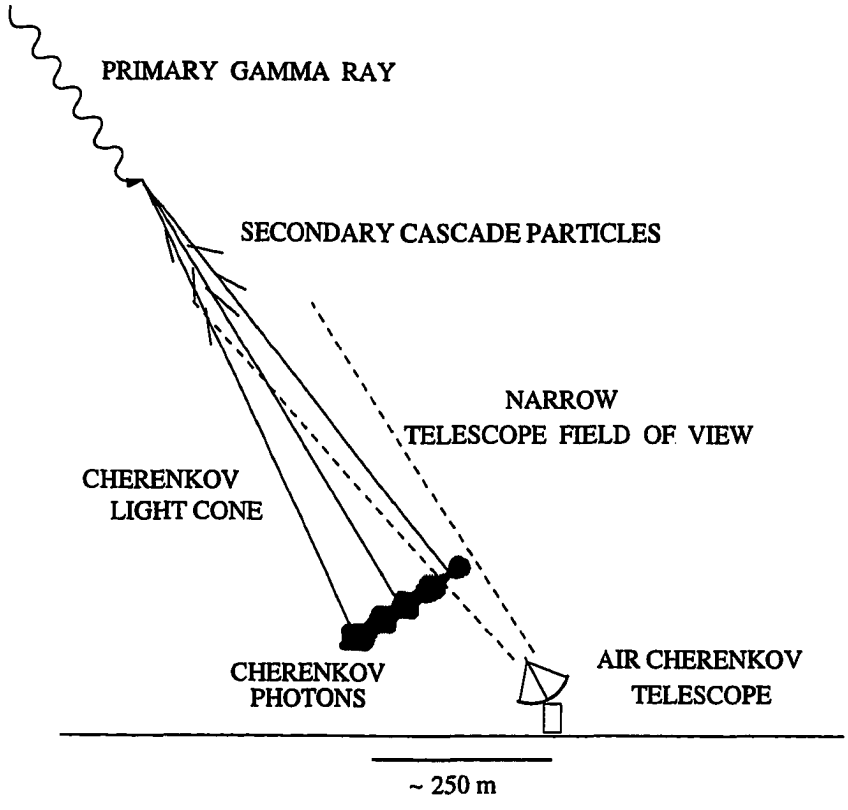

Figure 3.4: Schematic representation of the operation of an air Cherenkov telescope.

translates to narrower images for the gamma ray showers (for examples of simulated images, see 3.3.7). Also, the gamma rays originate from a point source at which the telescope is directed, while the cosmic ray showers do not have a preferred arrival direction. Hence, the axes of gamma ray images tend to point towards the centre of the field of view (the source position), though this is somewhat distorted by noise in the images. Even with the present crude imaging techniques, it is possible to reject over 99.9 % of the background showers, while still retaining over a third of the gamma-ray-like showers, and there are indications that the difference between gamma ray and cosmic ray images actually increases with energy.

Fig. 3.5 shows simulated showers initiated by, (a) a 0.35 TeV shower and, (b) a 1

Tev proton. The particle tracks[6] in the cascade are shown for all particles above the Cherenkov threshold. Fig. 3.6 shows the Cherenkov photons from the same showers (without night-sky noise) in the focal plane of a detector with the approximate characteristics of the Whipple 10-meter are shown. The model detector is located 75 m from the shower core. The plot illustrates the general idea that gamma ray showers are more concentrated, and the corresponding images are narrower, as compared to cosmic ray showers.

3.2.4 Design considerations for an air Cherenkov telescope

Consider the magnitude of the problem of using the imaging air Cherenkov technique to identify VHE gamma rays from a point source (a discussion of this can be found in Weekes [116, sec. 2.2, pg. 13]). Firstly, the site for a Cherenkov telescope should be at high altitude in order to get closer to the position of shower maximum for the cascades. Also, it must have a dry climate, as observations of Cherenkov light from air showers is possible only under clear, moonless conditions. Even at the best of locations, the duty cycle for observation is only a little over 10 %.

Next, the Cherenkov light from the atmospheric cascades must be picked out from the background of the night-sky light. Fluctuations in the night-sky brightness normally overshadow the Cherenkov light flashes—that is why these flashes are not visible to the naked eye. In order to register the Cherenkov light flash, the integration time of the detector must be tuned to the duration of the light flash. This is of the order of a few nanoseconds, and thus both a detector with a fast response, and high-speed electronics are required. While high quality mirrors are not required[7], a large reflector that collects as much light as possible, is desirable.

The field of view of the detector is defined by the angular extent of the shower light. It should be noted that the centroid of the image moves outwards in the detector field of view with an increase in the impact radius. Thus, a larger angular field of view improves the collection area of the telescope, but at the price of accepting

[6]For clarity, the lateral scale is expanded, each track is indicated by only a few points.

[7]The smallest scale structure in the Cherenkov light image is expected to be of the order of 0.1° , which is crude by the standards of optical telescopes.

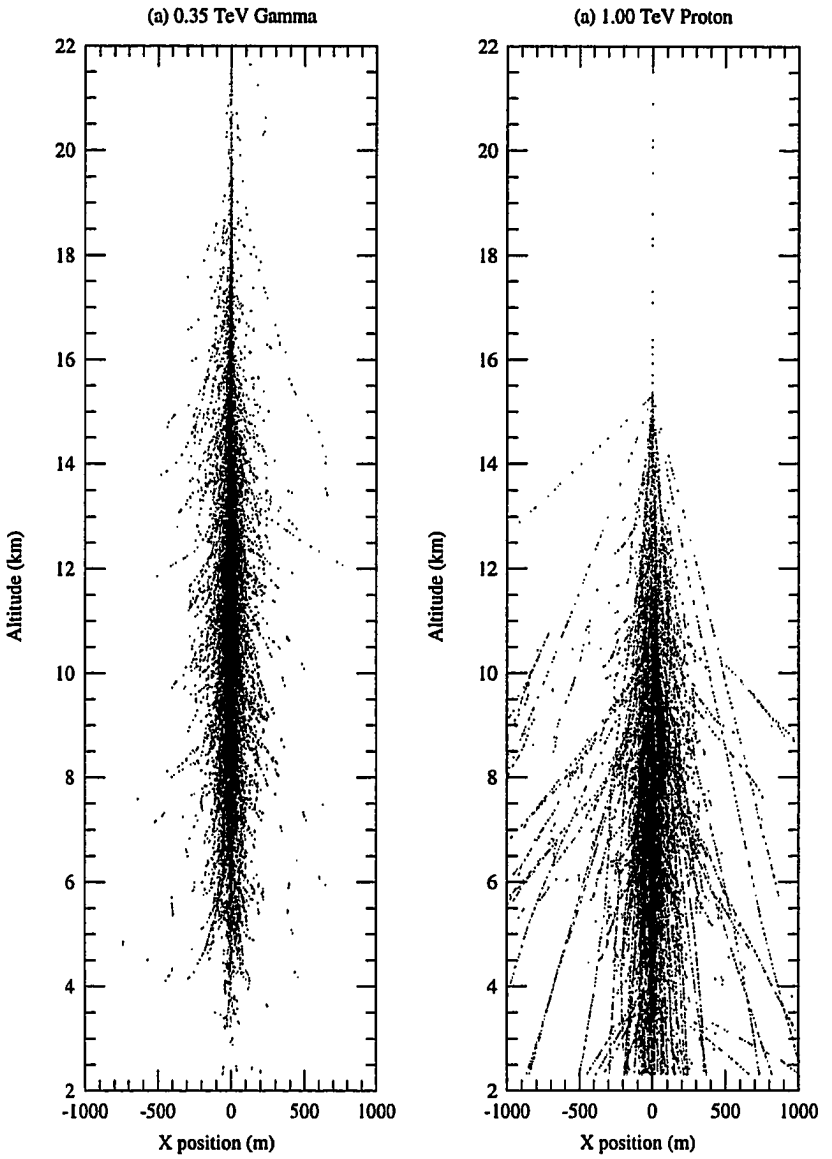

Figure 3.5: Particle cascade in the atmosphere

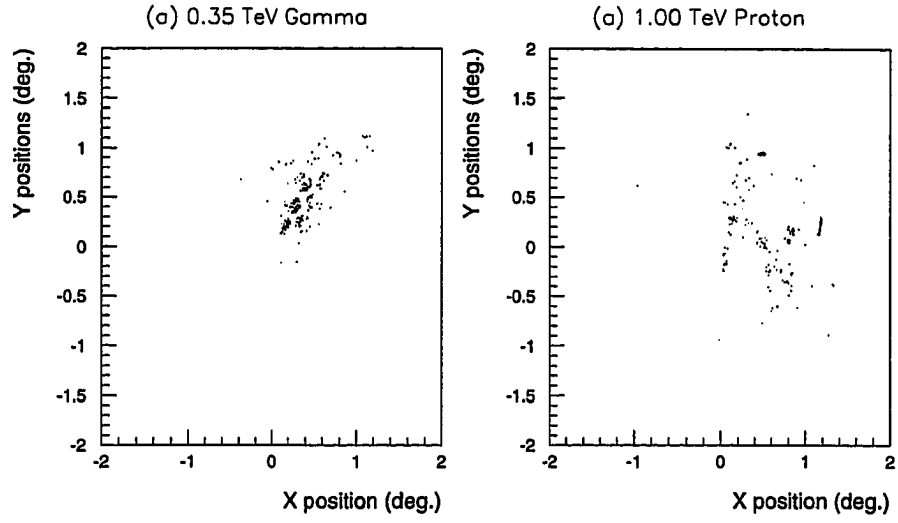

Figure 3.6: Cherenkov light pool in the focal plane

more night-sky light. The detector should have good angular resolution if imaging is to be used as an efficient means of rejecting the huge background of Cherenkov light from cosmic ray showers. Finally, it should be kept in mind that the spectrum of the Cherenkov light is biased to the ultraviolet end of the spectrum[8], so that the detector must have significant response at these low wavelengths.

A further dimension is added to the problem if one wishes to measure the energy spectrum of the observed gamma ray sources. As only a tiny fraction of the primary energy is actually emitted as Cherenkov light, reconstructing an input spectrum from the observed images is a difficult proposition. Also, typically an air Cherenkov detector has a small field of view so that only part of the light is seen.

The reason that it is feasible to get even a rough estimate of the primary energy, is that the amount of Cherenkov light seen in a shower is closely related to the total numbers and track lengths of the secondary charged particles. This in turn depends

[8]Refer to Eq. (3.10), which shows that the Cherenkov emission spectrum scales as $1/\lambda^2$. Though this is somewhat distorted by atmospheric absorption, the observed Cherenkov light is still predominantly in the near ultraviolet.

directly on the primary energy, so that the amount of Cherenkov light observed is an indirect measure of the primary energy. Other factors that help are the strong forward beaming of the secondary particles due to the large initial momentum of the primary, and the small temporal extent of the cascade which allows reduction of the night-sky background, by tuning the detector integration time to the duration of the flash.

The energy resolution is still poor, however, as fluctuations in the cascade process, particularly in the early stages, greatly alter the number of relativistic particles at shower maximum. This is somewhat mitigated by the depth of the atmosphere, which is about 20 electron radiation lengths deep at the Whipple Observatory altitude, and hence tends to smooth out fluctuations in the cascade process. Thus, not only does the atmosphere act as the scintillation detector for this technique, it also serves as the calorimeter!

3.3 The Whipple 10-meter detector

The Whipple Gamma-Ray Collaboration is made up of members from five U. S. institutions and three overseas universities. The U. S. institutions are, the Smithsonian Astrophysical Laboratory, Iowa State University, University of Michigan, and Purdue University. The overseas universities are University College, Dublin; St. Patrick's College, Maynooth; and University of Leeds. It came into existence in the early eighties, when gamma ray astronomy was at a very early stage of development; with inconsistent results from different detectors, and signals that were often at wide variance with expectations. The Whipple Collaboration has been one of the pioneers in this field. A testimonial to this can be seen in the recent worldwide interest in imaging air Cherenkov detectors that are designed on the Whipple model.

The Whipple Observatory is located at Mt. Hopkins in Southern Arizona, approximately fifty miles from Tucson. The main instruments located at this site are the 10-meter and the 11-meter (which is actually only about 8.5 m in diameter) telescopes. This work analyzes only data taken with the 10-meter, so that I shall restrict myself to describing only that instrument. The 11-meter is similar in many ways to the 10-meter, the basic difference being that it has a parabolic shape and incorpo-

rates time-to-digital converters (TDCs) in the electronics, so that the arrival times of the Cherenkov photons in different channels can be timed with resolution of the order of a few nanoseconds (see Schubnell [100]). Fig. 3.7 shows pictures of the two telescopes. The following description of the telescope hardware draws considerably from Lang [69].

The 10-meter detector has gone through several incarnations since its construction in 1968. Very early observations with it are described in Weekes et. al. [115]. The imaging era with the 10-meter began in 1982 with the installation of a prototype 19-pixel camera designed at Dublin (see Fegan et. al. [35] and Clear et. al. [26]). This was upgraded to a 37-pixel camera in late 1983, with the custom built electronics being replaced by CAMAC units in 1986 (see Reynolds [93]). In May 1988, the 37-pixel camera was replaced by the so-called high resolution camera (HRC), with 109 elements and a smaller pixel size in the inner portion. In the spring of 1992, the 11-meter was successfully deployed and work was started on a link between the two telescopes that would allow stereoscopic imaging of a source (see Schubnell et. al. [100]). Very recently, the data acquisition system has been completely revamped (see Rose et. al. [95]), with an upgrade in both hardware and software. It is now possible to operate each telescope independently or in a joint stereo-viewing mode. Here, I shall discuss only data taken in between 1988 and 1992, with the 109-pixel high resolution camera. Minor instrument modifications, such as repositioning of the tubes in the camera, will be made note of where appropriate.

3.3.1 Optics

The 10-meter reflector consists of a 248 spherical facets mounted in a hexagonal pattern on a spherical steel framework with a radius of curvature of 7.3 m. The overall spherical bowl has an opening diameter of about 10 m. The plate scale, i.e., the linear displacement in the focal plane per unit angular displacement relative to the optic axis, is thus 12.8 cm/degree and the reflector is a f/0.7 system. Each individual mirror has a radius of curvature of 14.6 m, and is aligned to a common focus at the centre of curvature of the framework, i.e., at a distance of 7.3 m from

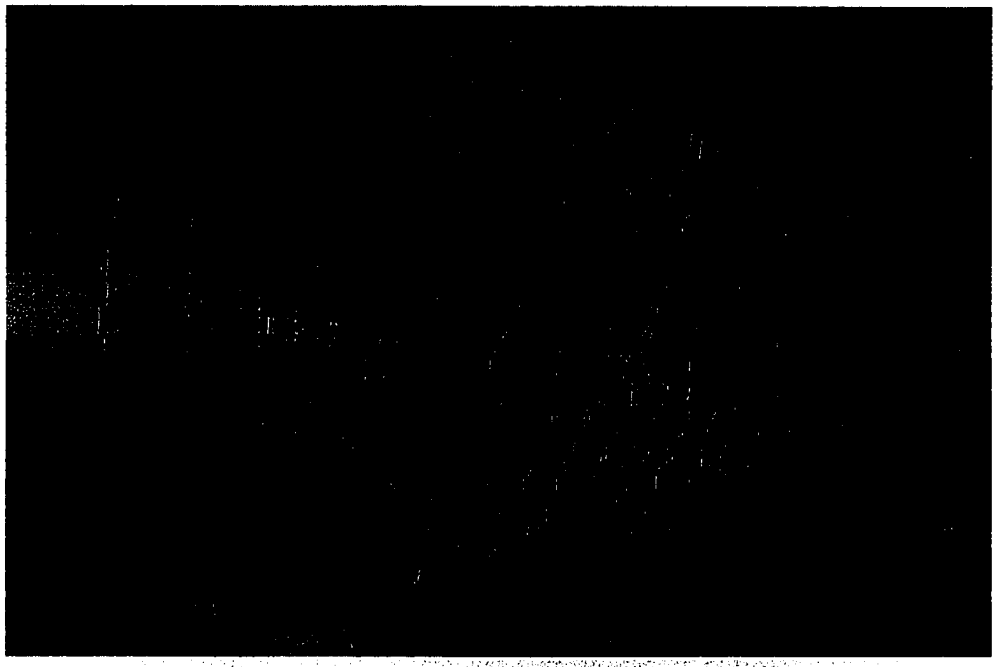

The 10-meter telescope

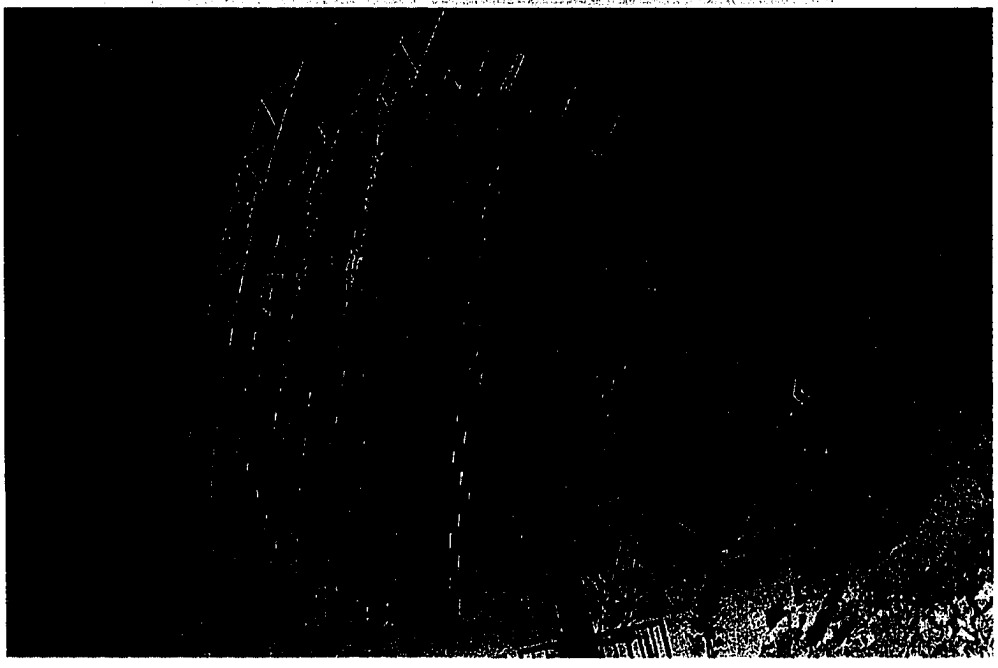

The 11-meter telescope

Figure 3.7: The Whipple gamma ray telescopes on Mt. Hopkins, Arizona

the reflector. The mirrors are front-aluminized with a silicon dioxide overcoating[9].

The unusual design of the reflector is based on the solar concentrator proposed by Davies et. al. [28], later adapted for astronomical purposes by Hanbury-Brown [50, 51]. The details of the optics of such a telescope have been investigated at length by Lewis [70, 72]. Lewis notes the advantages of such a design as being:

1. all facets are identical and interchangeable, making fabrication, replacement and alignment easier.

2. the structure is rigid and compact, a point worth considering as the telescope moves through a wide range of elevations, and is exposed to windy conditions.

3. spherical aberration is eliminated for rays along the optic axis without the need for a parabolic structure. Also, though this was not a design criterion for Davies et. al., Lewis has demonstrated that off-axis aberrations are also reduced.

A disadvantage of the Davies design is that, owing to the overall spherical shape, the light rays reflected from the outer mirrors can arrive at the focal plane six nanoseconds before the rays from the central mirrors. This is sufficient to make the reflector unsuitable for investigating differences in the temporal profile of gamma ray and cosmic ray showers. Also, an integration time longer than the intrinsic spread of the Cherenkov light pulse is needed, thereby introducing additional night-sky noise that degrades the image.

For on-axis rays, the dominant form of aberration is the astigmatism of the individual facets. This arises from the fact that rays which do not strike a facet mirror exactly at its centre, form two line foci—a sagittal focus and a tangential one—with a disk of minimum confusion taken to be halfway between them. For the outer mirrors, the plane of the disk of minimum confusion is also significantly different from the overall image focal plane (plane of the PMT array), so that its size on the image plane is increased by the projection. Lewis calculates the size of this

[9]These are the 1988 mirrors that used the Liberty mirror coating, spec. 150. The present mirrors, *circa 1993,* are coated in-house with anodized aluminium, using a procedure developed by the Fly's Eye group. The new coating has an enhanced ultraviolet response, and is more durable.

disk of least confusion to be 4.4 cm (0.34°) for the outermost ring of mirrors, and negligibly small for the inner rings.

For off-axis light rays, there is a "global" form of aberration that arises from the overall shape of the reflector. The reader is referred to the Lewis paper [72, sec. 3] for a detailed description of this aberration, which causes the light from a point source to be spread into a double (cometary) ring on the focal plane. The size of the cometary circle increases rapidly as the source is moved more and more off-axis and the global aberration soon dominates the image shape. Other classical aberrations, like spherical aberration, coma etc. are of the same order as alignment errors in mounting the mirrors and can be lumped together as contributing an additional random error, distributed as a Gaussian with a width of 1.3 cm (0.1°).

Lewis [72, Fig. 2] has demonstrated that the measured point spread function of the 10-meter reflector, for both on-axis, and off-axis sources can be fit by a raytracing program that includes both individual and global aberrations and a Monte Carlo estimate of the other errors modelled as a Gaussian distributed random variable, as described above. The calculated curve is normalized to match the intensity of the highest data point, but there are no other free parameters. For the on-axis source, the measured values of the full width at half-maximum (FWHM), and the root mean squared (RMS) width are 0.12° and 0.05° , respectively. For the 1.25° off-axis source, the FWHM is comparable at 0.14° , but the RMS width of 0.13° is significantly larger.

Also, of interest is the light concentration efficiency of the telescope. Again Lewis [72, Fig. 5] shows the fraction of light included inside a disk with diameter given by the abscissa of the plot. Three cases are shown, where the point source is, (a) on the optic axis, (b) displaced 0.5° from the optic axis, and (c) displaced 1.5° from the axis. He demonstrates that a parabolic mirror gives slightly better light concentration capabilities for an on-axis source, and slightly worse capabilities for an off-axis source.

To summarize, the point spread function is small enough ($\sim$ 1.3 cm) to warrant the use of small photomultiplier tubes[10]. The reflector design eliminates spherical aberration, and reduces off-axis aberrations as compared to a parabolic mirror. A

[10]As described in the next section, the inner tubes have an active area of diameter 2.9 cm (0.22°).

consequence of the global aberrations to be noted is that for off-axis rays, common in the Cherenkov light from atmospheric cascades, it tends to make *all* images point towards the centre. As the "pointing" of the images is characteristic for gamma ray showers from a point source at the centre of the field of view, this hampers somewhat the discrimination of the gamma showers from the background.

3.3.2 The photomultiplier tube array

The actual detector of Cherenkov light flashes is located in the focal plane of the reflector, and consists of a hexagonal close packed array of 109 photomultiplier tubes (PMTs). The use of photomultiplier tubes date back to experimental research done in the early thirties, and they are still unparalleled in their sensitivity at detecting electromagnetic radiation.

Fig. 3.8 is a schematic picture of the arrangement of the PMT array, showing the PMT numbering scheme. The drawing is to scale, with the diameter of the tube representing the sensitive area of the tube rather than its physical size. Each of the 91 inner tubes has a sensitive photocathode diameter of 2.9 cm , which corresponds to a field of view of 0.22° . This is well matched to the reflector aberrations, discussed in the previous section on optics. These PMTs are Hamamtsu R1398, UV glass tubes, which were chosen for their fast response, enhanced ultraviolet quantum efficiency[11] and, large sensitive area relative to the tube size. The outermost ring of the camera consists of 18 large PMTs, each with a photocathode diameter of 4.3 cm (0.34°). The larger size of the tubes in this ring corresponds to the larger off-axis aberrations. These tubes are of type RCA 6342/IV and have been reused from the old 37-pixel camera. Commercial bases are used for the PMTs and the tubes themselves have electrostatic and magnetic shields. The signal from each tube is carried through $\sim$ 50 m of RG58 coaxial cable to the data acquisition electronics located in the control room.

In addition to the numbering, the PMTs are also commonly classified by the

[11]From the discussion in sec. 3.2.3, the collection of more UV light might appear to be a disadvantage as it would favour the detection of cosmic ray showers that have a larger fraction of UV light. However, for an imaging detector, the gain in image characterization by collecting more light outweighs this disadvantage.

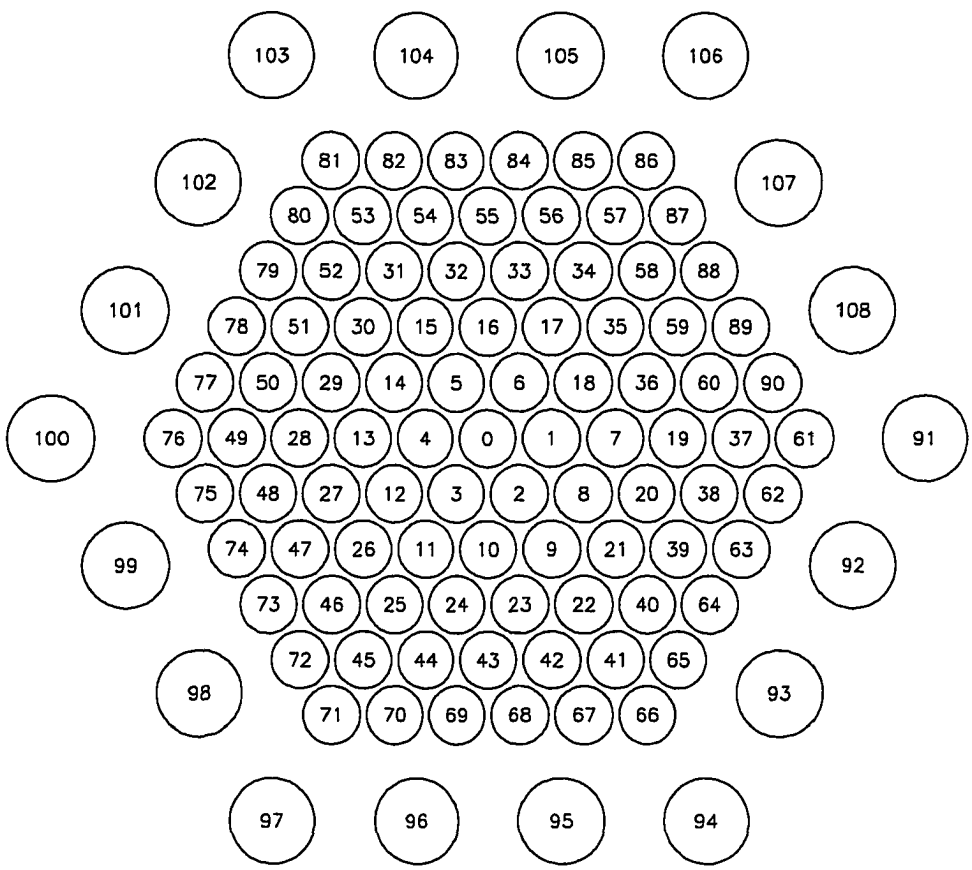

Figure 3.8: Positions of the PMTs in the focal plane.

concentric ring that they are located in. The innermost tube is called zone 0, and the rest of the rings are labelled zones 1 through 6, with zone 6 being the outermost ring of 18 large PMTs. The current from each tube is constantly monitored by a display pattern of light-emitting diodes (LEDs), arranged in the same manner as the PMTs. If the current in a PMT exceeds a preset threshold (usually, about 40 μamps), the corresponding LED changes colour from green to red. This alerts the operator, who can turn off the high voltage to that PMT, thereby removing it from the imaging array. This monitoring system also allows for an approximate check on pointing—when the telescope is pointed at the guide star for a source, the star should illuminate the innermost PMT, and the corresponding LED should flash red. Further, it alerts the observer to bright stars in the field of view of the detector and gives a crude idea of sky brightness conditions. In more recent versions of the camera, this system is supplemented with a more sophisticated monitoring module that is integrated with the data acquisition system, and allows recording of PMT currents as well as of singles rates in each individual channel. The camera field of view is also monitored with a video camera mounted beneath the focus box. The video camera has been replaced subsequently by a small charged coupled detector (CCD) imaging system that keeps track of the four brightest stars in the field of view at any given time, and thus can be used to cross-check pointing accuracy.

The relative gains of the PMTs are regularly recorded for each night of observation. This is done by illuminating the entire camera with the spatially uniform and intense light from a pulsed "Optitron" nitrogen arc lamp mounted at the centre of the reflector, facing the camera. Roughly once in each dark observation period, the high voltages supplied to the PMTs is also adjusted to get uniform relative gains across the camera face.

3.3.3 Data acquisition electronics

The data acquisition system is responsible for recording the data with the desired degree of accuracy. It has to first determine whether a triggering event has occurred, and if so, it has to record all relevant instrument parameters for that type of event. The event arrival times must be recorded to an accuracy and precision that allows for the Fourier analysis of sources that are suspected to be periodic. The system is

built around commercial CAMAC modules, with several custom made devices. A number of electronic logic standards including ECL, fast NIM and TTL are used in the system. The CAMAC system is interfaced to a Digital Equipment Corporation LSI 11/73 computer which stores the data on hard disk, after performing several online quality checks. The data is copied to magnetic tape nightly, for archival and distribution to the other institutions in the collaboration. I emphasize again that this discussion pertains to the system for the 10-meter detector that was in use prior to 1995.

Fig. 3.9 is a simplified block diagram showing the essential parts of the data acquisition system, that is reproduced from Lang [69, Fig. 4.4, pg. 82]. The PMT signals from the camera are fed into the control room via RG58 coaxial cables. The signals are then amplified by a bank of LeCroy 612A amplifiers, which consists of 10 units, each unit having 12 channels. Besides the 109 PMT channels, the extra 11 channels have been used in the past for a variety of independent triggering mechanisms (see, for example Lang [69, sec. 4.5, pg. 84]). Each channel has two AC-coupled outputs and a DC-coupled output. The DC-coupled output is used to run the LED display that monitors the PMT currents. One of the AC-coupled outputs goes to a LeCroy 4413 CAMAC discriminator which is used to define the trigger logic that determines whether a Cherenkov light trigger has occurred. The other AC-coupled output is fed through a 60 ns delay cable to a LeCroy 2249A analog-to-digital converter (ADC), which integrates the PMT pulse. The delay cable ensures that the system has sufficient time to recognize the presence of a trigger and still record the the 109 pixel values.

Several triggering modes have been used for the detector in the past. For this work, I shall consider only the specific Cherenkov event trigger mode that is defined by at least two of the inner PMTs exceeding a preset discriminator threshold. For the 1988-89 observing season, the preset threshold approximately corresponds to 50 counts registered by the ADC converter. (Sec. 3.4 describes how this and other numbers might be determined from the data.) The number of tubes, N, required out of the inner 91 in order for the Cherenkov trigger condition to met can be adjusted in the hardware. The analog outputs of the 91 "channel discriminators" for the inner 91 tubes are daisy-chained together to form a pulse proportional to the number of

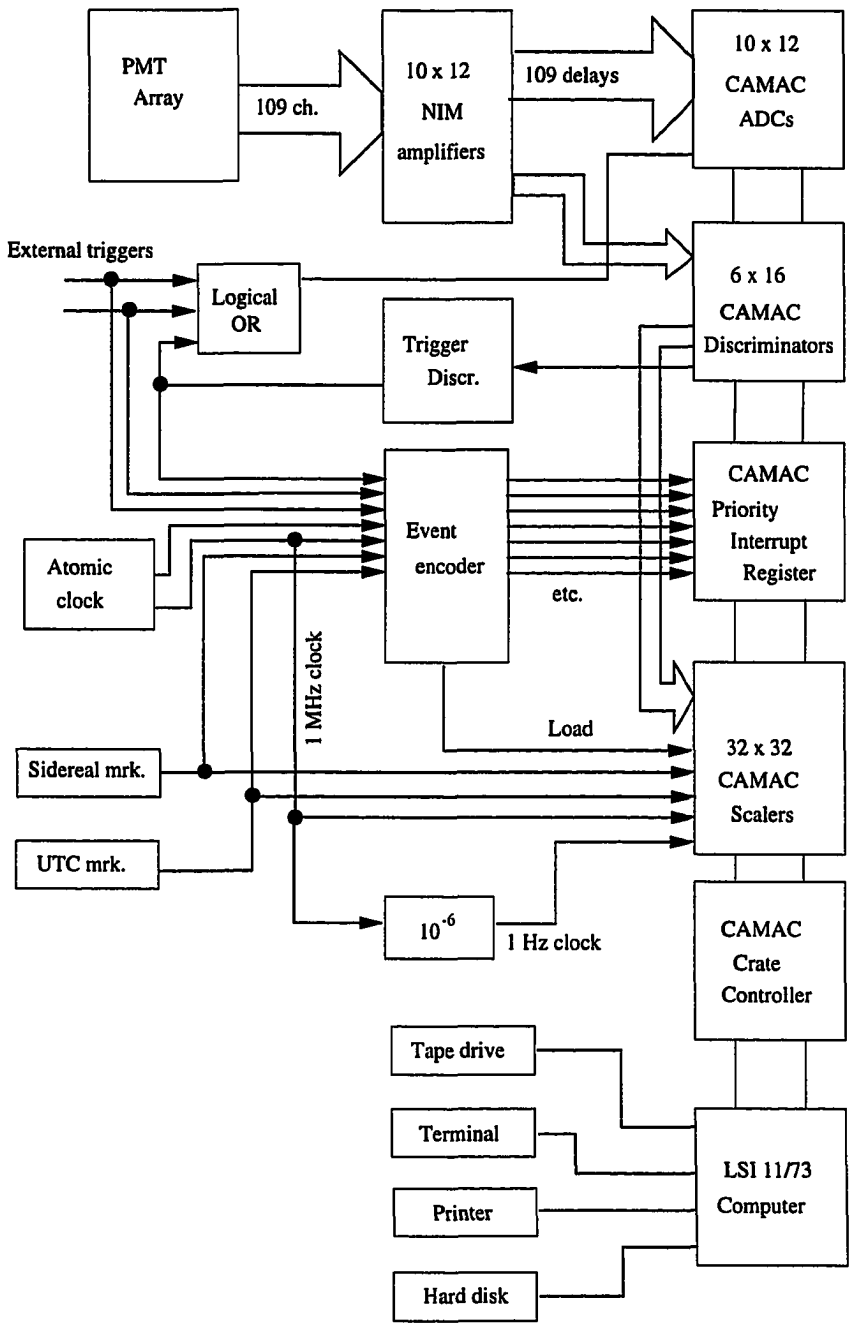

Figure 3.9: Block diagram of 1988-89 data acquisition system

discriminators which have fired, i.e., the pulse height is proportional to the total number of channels in which the signal has exceeded the preset threshold. This pulse is then sent to the "overall trigger discriminator" that determines whether the number of channels that have fired is sufficient to meet the Cherenkov trigger condition. The output from the overall trigger discriminator is then used to open the ADC gates and record the signal in each channel. Besides Cherenkov triggers, a variety of other triggers have also been used. These include triggering modes that are used to record other events of interest and artificial triggers for routine instrument monitoring events. These trigger sources include:

1. an artificial trigger for the "sky pedestals" that record the ADC channels with the high voltages for the PMTs switched on, and the telescope pointed at the sky. This serves as a measure of the fluctuations in the night-sky brightness.

2. an artificial trigger for the "normal pedestals" that record the ADC values with the PMT high voltages off, and thus measure electronic noise and pedestal jitter in each channel.

3. a trigger for the nitrogen arc lamp that is turned on once a night, prior to observation, and is used to calibrate the relative tube gains.

4. a trigger for timing pulses, which inject timing markers into the data stream approximately once a minute.

5. a trigger from a 12-element particle detector array located around the 10-meter reflector position.

6. at times, a dedicated muon telescope has been mounted along the axis of the 10-meter, and a trigger for this has been included.

7. for the 1989-90 observing season, an independent triggering system derived from single PMTs viewing 1.5 meter diameter mirrors that are mounted on the side arms of the 10-meter reflector.

The origin of a system trigger is determined by a custom built event encoder that assigns a code to each type of event. The event encoder output is then fed to a priority

interrupt register that generates an interrupt for the data-acquisition computer. The computer then reads the event codes, the time and, for a Cherenkov trigger, also the 109 ADC values for each channel.

The ADCs have a gate width of 25 ns. This is of long duration compared to the 3-5 ns time of the Cherenkov light flash and is needed to encompass the $\sim$ 6 ns spread introduced by the spherical reflector, the variations in PMT transit times, and the pulse widening introduced by the 50 m runs of cables from the focus box to the control room.

The absolute event timings are obtained by introducing timing events into the data stream, approximately once every minute. These include times from three independent clocks. A Sulzer sidereal clock is used for the sidereal time (ST), a WWVB-based clock for the universal time (UT) accurate to 0.5 ms, and a portable atomic (rubidium) clock to cross-check the UT time. The UT markers from the rubidium clock are offset by 30 s from the WWVB-based clock. Also, it is calibrated regularly by physically taking it to the Fort Huacacha Army Base, which maintains absolute UT time to an accuracy of 1 μs. The use of three clocks reduces systematic timing errors. Besides the absolute time recorded every minute, each event is also assigned a relative time. This is derived by counting clock ticks from a 1 MHz clock and a 1 Hz clock, with latching scalers of type LeCroy 4434. The 1 MHz clock comes from a portable atomic clock, and is divided by 10^6 to give a synchronous 1 Hz clock. The scalers have 24-bit resolution so that the 1 MHz scaler overflows every 16.777216 s. These overflows are kept track of by the 1 Hz scalers. The scalers are run continuously, and can be read through the CAMAC crate controller into the data-acquisition computer. Recently, the timing system has been updated to include a global positioning system (GPS) clock good to an absolute time of $\sim$ 1 μs, and an oscillator and TDCs that interpolate relative times to an accuracy of several ns.

The telescope tracking system runs on an Apple II microcomputer running a FORTH environment. The microcomputer uses an internal UT clock to continuously compute the current position of the source being tracked, and accordingly adjusts the azimuth and elevation of the reflector. The UT tracking clock is regularly cross-checked against the WWVB-based clock to guard against tracking errors. The 8-bit digital shaft encoders are used to calculate telescope position with a resolution

of 0.04° . Tracking errors are usually within 0.1° , cumulative over azimuth and elevation, unless, of course, the source is in transit and has an apparent motion too rapid for the telescope to keep up with.

3.3.4 System performance

The usual Cherenkov trigger for the 10-meter telescope is defined as at least two of the inner 91 PMTS exceeding a preset threshold within the duration of a coincidence window of 10 ns width. The preset discriminator threshold level is fixed just above the point of intersection of the night-sky noise spectrum with the Cherenkov light spectrum from background cosmic ray showers. A typical spectral curve is shown in Fig. 3.10, with the selected trigger threshold as indicated. This setting reduces false triggers from night-sky brightness fluctuations. The main source of false triggers in the 10-meter detector is from charged particles, mostly muons, in cosmic ray cascades that pass through the PMT array, producing Cherenkov light in the glass of the PMT window. The flux of local muons is dependent on the zenith angle and peaks at a zenith angle of about 30° (see, for example, Gaisser [41, sec. 6.3.5, pg. 81]. Thus, the number of false triggers arising from these can be expected to increase with zenith angle. The rate of such triggers can be measured by operating the 10-meter with an opaque lid on the camera. Lang [69] quotes the number of such triggers as 15 per minute at a zenith angle of 0° , increasing to 35 per minute at a zenith angle of 60° . These false triggers are easily rejected by software cuts as the signals appear in just two of the PMTs. The rate of false coincidences, R, due to random fluctuations, from a n-fold trigger obtained from a system of m PMTs, can be obtained from the following formula, modified from Janossy [58]:

$$\begin{aligned} R &= \binom{m}{n} k^n \, (\Delta T)^{n-1} \text{ Hz} \\ &= \frac{m!}{(m-n)!\, n!} k^n \, (\Delta T)^{n-1} \text{ Hz} \end{aligned} \tag{3.14}$$

where, k is the singles rate in each PMT, and ΔT is the width of the coincidence window. For the 10-meter system, with $m = 91$, $n = 2$, $k = 1$ Hz, and $\Delta T = 10$ ns, there is a false coincidence once every 6.8 hours, on the average, which is a completely negligible rate.

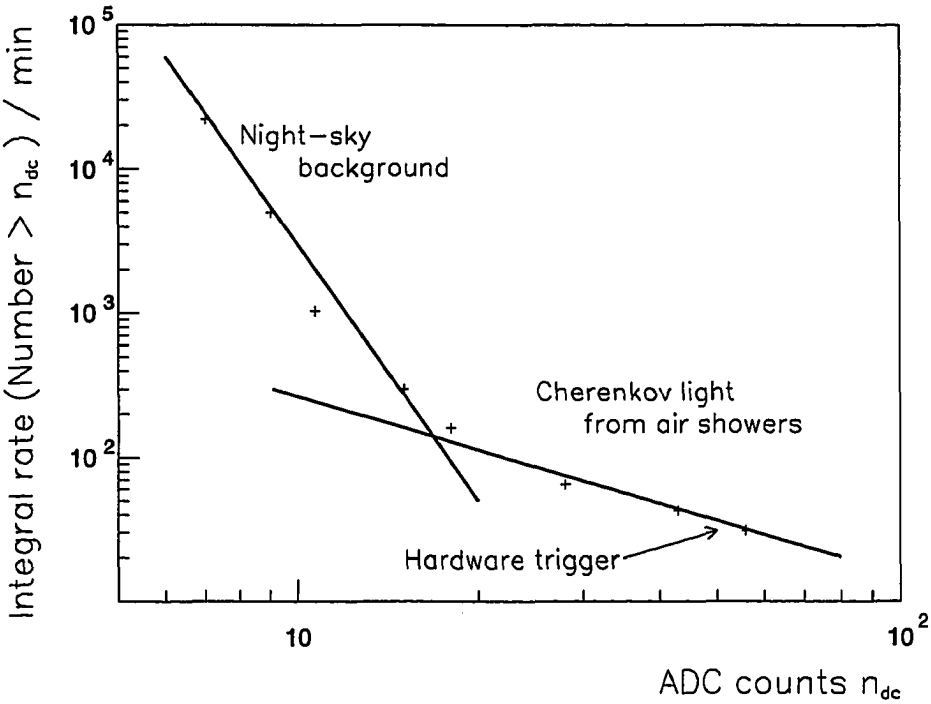

Figure 3.10: Bias curve for telescope hardware trigger

The gate width of the ADCs is set at 25 ns. However, the dead time of the system is dominated by other factors—it takes 2 ms to read out the ADCs and 20 ms for the computer to write an event to the core memory buffer. The 10-meter is typically operated at event rates of 4-8 Hz, so that the dead time can be neglected[12].

For a discussion of the detector noise parameters, see Kwok [67, esp. Appdx. A3, pg. 156], Cawley [21, 22], and Lewis [71]. This is also further discussed in the context of the 1988-89 Crab database in Sec. 3.4.2.2. The noise in the system originates from three different sources:

[12]The new data acquisition system has much smaller dead times and can be operated at event rates of upto 50 Hz!

1. *Night-sky noise:* This arises from fluctuations in the night-sky brightness. This can be measured from the standard deviations in the sky-pedestals, where the telescope is artificially triggered while pointed at the sky. This is measured to be about 3.0 digital counts for the 2.9 cm inner tubes, and slightly smaller for the outer tubes, which in general have lower high voltages applied in order to make the camera response uniform across its face.

2. *Signal noise:* This is caused by the fluctuations of the signal inside the PMT.

3. *Electronic noise:* This is due to pedestal jitter and other sources of noise in the channel. It can be measured from the pedestal variances with the high voltages to the PMTs turned off. This is found to be about 1.1 digital counts and is small in comparison to the other factors.

3.3.5 Observing modes

The 10-meter telescope is operated mainly in two different modes, each suited to a different type of observation. These are described below:

1. *ON/OFF mode:* In this mode, the detector tracks the "ON" (source) region for a given length of time, usually for 28 sidereal minutes. Then, in an intervening 2 minutes, the reflector is slewed back to a background region that corresponds to the same part of the sky, in both elevation and azimuth, that was covered by the source. This "OFF" region is tracked for the same amount of time. This is suited for the analysis of time-invariant excess (often referred to in the field as DC excess) from a steady source. In this mode, the duty cycle, however, is less than 50 %. In this work, all the data relating to spectrum estimation for a source is taken in this mode.

   Sometimes, more time is spent in the ON region than in the OFF region. In this case, the significance of the DC excess must be calculated carefully (see Li et.al. [74] for a discussion of how to estimate the significance correctly). In rare cases of monitoring a well-established source, all the time is spent in tracking the source, with zero OFF source time. Here, the background is estimated by extrapolating from those parts of the ON source distributions that are believed

to originate from background showers, e.g., the region of the "alpha plot" at values of alpha greater than about 15° (see the discussion on current status in Weekes [118]). Similar methods are also followed by different outside groups, for example, Tanimori et al. [109], Kifune et al. [65]

2. *Tracking mode:* The source is tracked continuously for periods of one to two hours at a time. In this mode, it is difficult to estimate the background in order to calculate a DC excess. This is suitable for studying a source suspected of episodic and/or periodic emission of VHE gamma rays. For episodic bursts of sufficient strength, the detection can be noted in an increase of count rates over a short time scale as compared to the count rate averaged over a long time period in which the source is mostly inactive. For periodic sources, a signal is detected by a periodicity search based on event arrival times.

3.3.6 Processing of the telescope data

The data from the Whipple Observatory is distributed to all of the member institutions, via the Internet. Each institution analyzes the data using independent analysis programs[13].

At Iowa State University (ISU), the data analysis is done on the departmental workstations that are part of the campus-wide Project Vincent computer system. The data is archived on magnetic tape and longer duration magneto-optical disks. The analysis routines are mostly written in C, by Mark Smucker, David Lewis and myself. As it is a completely independent system from that of the Smithsonian Institution's local group at Tucson, Arizona it serves as an independent check of the data reduction and analysis. There are small differences in the two analysis packages, e.g., we have chosen to eliminate in software, tubes that have abnormal-looking gains or gain variances. A careful cross-check was done between the two packages, with these differences temporarily removed, and they were in perfect agreement.

[13]This might change in the near future as the collaboration moves to higher data rates, and a unified data reduction and analysis package

3.3.6.1 The data stream The data, as downloaded from Tucson, is in compressed binary format, with the filename indicating the source and the run number. At ISU, it is converted to ASCII at the first step, and all subsequent processing is done with ASCII files. This has the advantage that one does not have to worry about differences in binary representations while transferring from one computer system to another. Also, the data can be manipulated at each stage by standard UNIX programs and shell scripts.

Fig. 3.11 shows a flowchart summarizing the data processing steps at ISU. Each intermediate ASCII file consists of records, one per line, that are labelled by the first field. These are described in greater detail below:

1. *Conversion to ASCII:* The raw binary data files are denoted by a .dat suffix for the filename, e.g., cr0702.dat, which would be run number 702 on the Crab (code CR). These binary files are processed to yield ASCII files, with names where the .dat suffix is replaced by a .gnt suffix. Each record in a .gnt file has one line per 10-meter event. The first field is a label for the event type, e.g., 10MGAINS for a nitrogen gains record. The rest of the fields are, in order, the run number, calendar date, event code, two independent clock readings that give the universal time for the event, and the number of PMTs in the camera at that time. The remainder of the record is the list of relevant readings from the PMT array, e.g., for each Cherenkov trigger event there are 120 values of the ADC counts registered in each channel. The .gnt file includes the header comments, a pedestal record (including pedestal means and variances), a gains record (with gains and gain variances), UT and sidereal minute markers, and injected sky pedestals (where these have been included in the telescope data stream). Thus, it is complete in itself and can be processed independent of any other files.

2. *Noise reduction:* The .gnt files are then passed through a noise reduction filter to give "cleaned" .cln files. The noise reduction program has switches for the type of input being processed (10-meter data/11-meter data/Monte Carlo simulations), and the type of cleaning desired (simple thresholding vs. the Akerlof morphological cleaning procedure). Details of the cleaning algorithm are

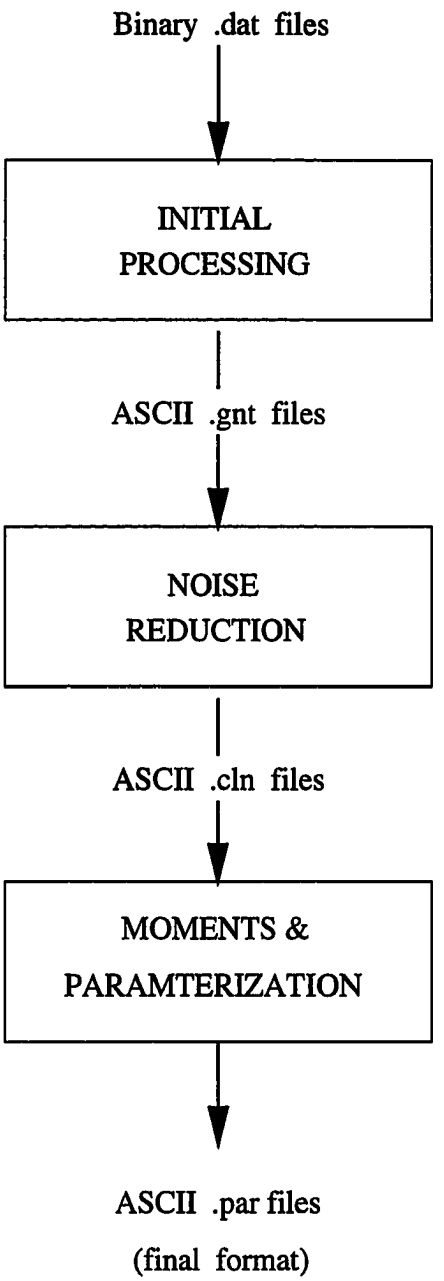

Figure 3.11: Flowchart for the data processing at ISU

described in sec. 3.3.6.3.

3. Image parameterization: The last step in the process is the parameterization of the cleaned images. This calculates moments for the image based on the tube positions and counts in each channel. These are calculated to the third moment, though we usually make use of only the first and second moments, plus the zeroth moment (total number of ADC counts in the cleaned image). The final output for each event is a record containing the list of the relevant Hillas parameters (and for the Monte Carlo simulations, an energy and a impact radius). See 3.3.6.4 for more details about the moments calculation and parameterization. Appendix B describes the Hillas parameters. The filenames have the .cln suffix replaced by .par.

The data is archived in both compressed binary and .gnt format. To save disk space, the files are often processed in a shell script that pipes the output through the various steps without actually saving the intermediate files. The final .par files are usually small enough to be stored on the computer's hard disk. The processing is fast enough that, if needed, each archived file can be easily reprocessed.

3.3.6.2 Flat-fielding of the camera The high voltages applied to the PMTs are adjusted at the beginning of each dark observation period in order to ensure that the gains[14] are roughly equal for all PMTs. "Flat fielding" makes the camera response uniform across its face by removing the effects of small differences in the absolute gains between the various PMTs. This is done by looking at the events recorded each night with the nitrogen arc lamp.

The flashes from the nitrogen arc lamp are passed through a diffuser before they reach the PMT array, so that the illumination is uniform across the camera face. Biller [13] has done preliminary investigations of this and finds a good degree of uniformity in the light from the nitrogen arc lamp, at the camera face. These are

[14]It should be noted that what I refer to as "gains" here, and elsewhere in this work are actually the inverse gains for the PMT, i.e., in order to flat field the camera the PMT counts must be multiplied by this number, rather than being divided by it. This slightly complicates the calculation of the variances for the gain, but this nomenclature is in line with prior usage in the collaboration.

of sufficient intensity to trigger the telescope (indeed, additional dead time must be introduce into the electronics to avoid overflowing data acquisition buffers that would cause a system crash), and have a duration of 2 ns to 10 ns. About 500 such events are recorded in order to have adequate statistics. After pedestal subtraction, the mean signal in each tube compared to the average mean over all tubes, is a measure of its relative gain. This relative gain factor is then used to renormalize the ADC counts for that PMT channel, thereby removing the effects of the small differences in gain. An alternative method of calculating relative gains, that gives comparable results, is to examine the pulse height spectra for all the tubes.

3.3.6.3 Noise reduction techniques The images of Cherenkov light obtained with the 10-meter are corrupted by the noise from various components, as described in sec. 3.3.4. This noise contamination degrades the image and causes a distortion in the calculated Hillas parameters. Thus, a good noise reduction technique is essential to recover the actual image characteristics.

Early noise reduction techniques involved a simple threshold, usually about 10 digital counts. Any tube with a value less than this threshold was removed from the image. A slightly better approach is to use a bilevel threshold that reflects the lateral distribution of the light in gamma ray showers. However, this still does not take into account the differences in the amount of noise present in different PMTs. Also, the use of an absolute threshold for all tubes implies that changes in the reflectivity of the mirror and in tube characteristics with aging is not compensated for. These problems are addressed by the so-called Akerlof morphological cleaning procedure (see [89, 88]). This processes each event in two passes through the data, after pedestal subtraction. The first pass identifies "image tubes," which have a signal greater than a preset "picture threshold." The second pass adds "boundary tubes" to the image. These are adjacent to an image tube and have a signal greater than a lower "boundary threshold." The values of the picture and boundary thresholds are optimized to supercuts and the 1988-89 Crab database, and are set at, respectively, 4.25 and 2.25 times the pedestal standard deviation for the tube.

3.3.6.4 Moments and image characterization The final step after gain renormalization, pedestal subtraction and noise cleaning is to calculate the moments, and from these, the relevant Hillas parameters for the image. The moments are based on the ADC counts in each selected channel and the tube coordinates in the detector focal plane. Only first and second order moments are required for the Hillas parameters used in supercuts, and extended supercuts. Other image parameters such as "asymmetry" also use the third order moments.

The zeroth order moment is simply the total of the ADC counts for all PMTs included in the image. In qualitative terms, the first order moment describes the image position in the focal plane, while the second order moment has information about the extent of the image. The third order moment can be looked upon as describing variations in the overall shape of the image in the focal plane. The definitions of the Hillas parameters and a geometrical interpretation can be found in Appendix B.

3.3.7 Examples of images from the data

Fig. 3.12, and Fig. 3.13 show examples of the data processing for the telescope, at various stages: (a) the raw data, which consists of the ADC counts registered in each tube for a triggering event, (b) the counts after pedestal subtraction and gain renormalization, (c) the counts after application of the Akerlof cleaning algorithm, and (d) the geometrical interpretation of the parameterized image (in this final step, the image has been shown rotated to the positive x-axis, as after parameterization the actual position of the image on the camera face, is no longer known). Fig. 3.12 is an example of an image that would be accepted as a gamma ray shower, while Fig. 3.13 is clearly a background shower and would be rejected.

3.4 Estimation of detector properties

Any method of extracting a spectrum must address the difficult question of the calibration of the detector. There is no VHE gamma ray source that is well established enough to act as a "standard candle," independent of simulations. Because of the overwhelming background of cosmic ray showers, it is not currently feasible to experimentally determine characteristics of gamma ray showers. Hence, the problem

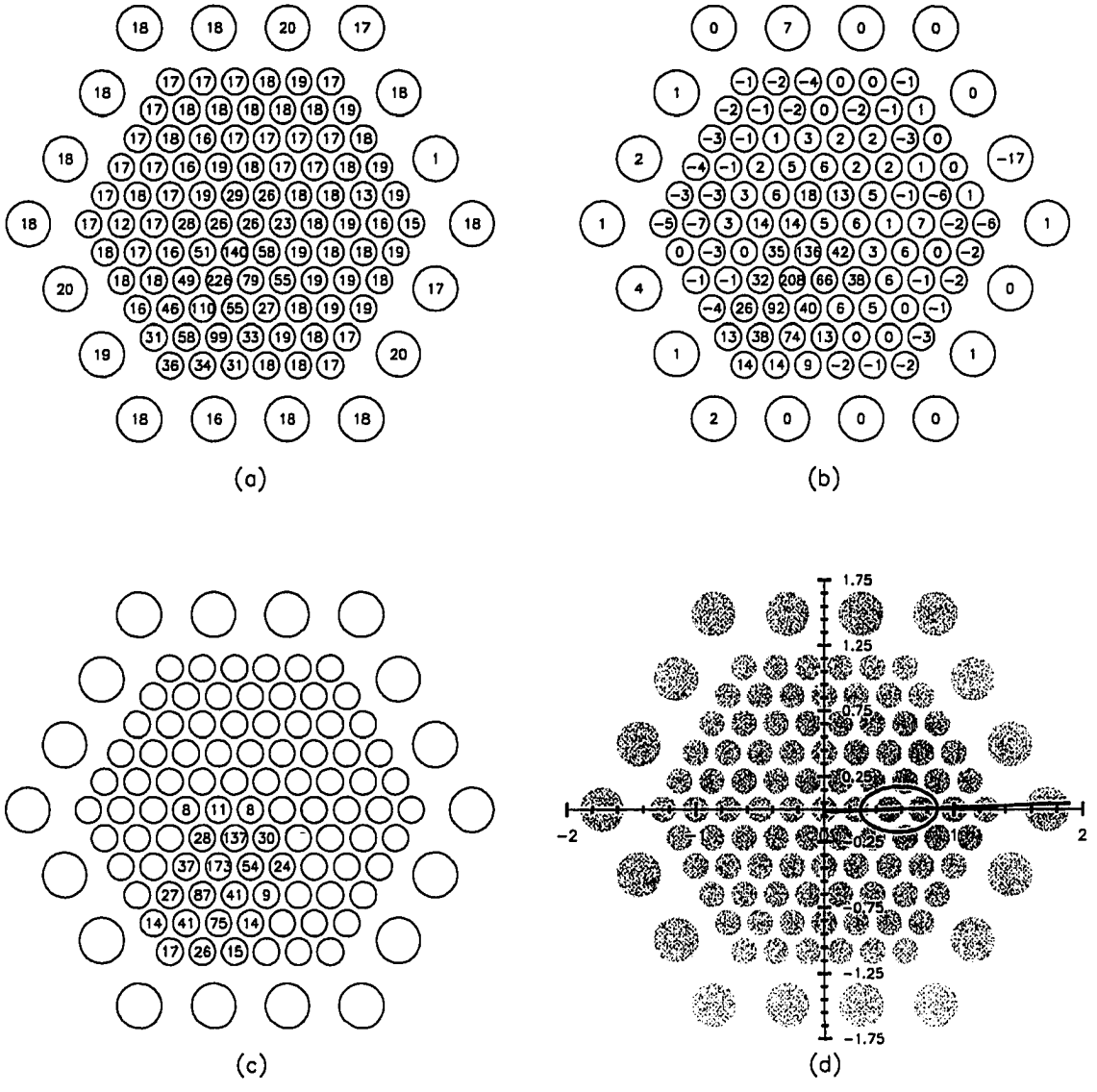

Figure 3.12: Images at various stages of the data processing for a gamma ray like image.

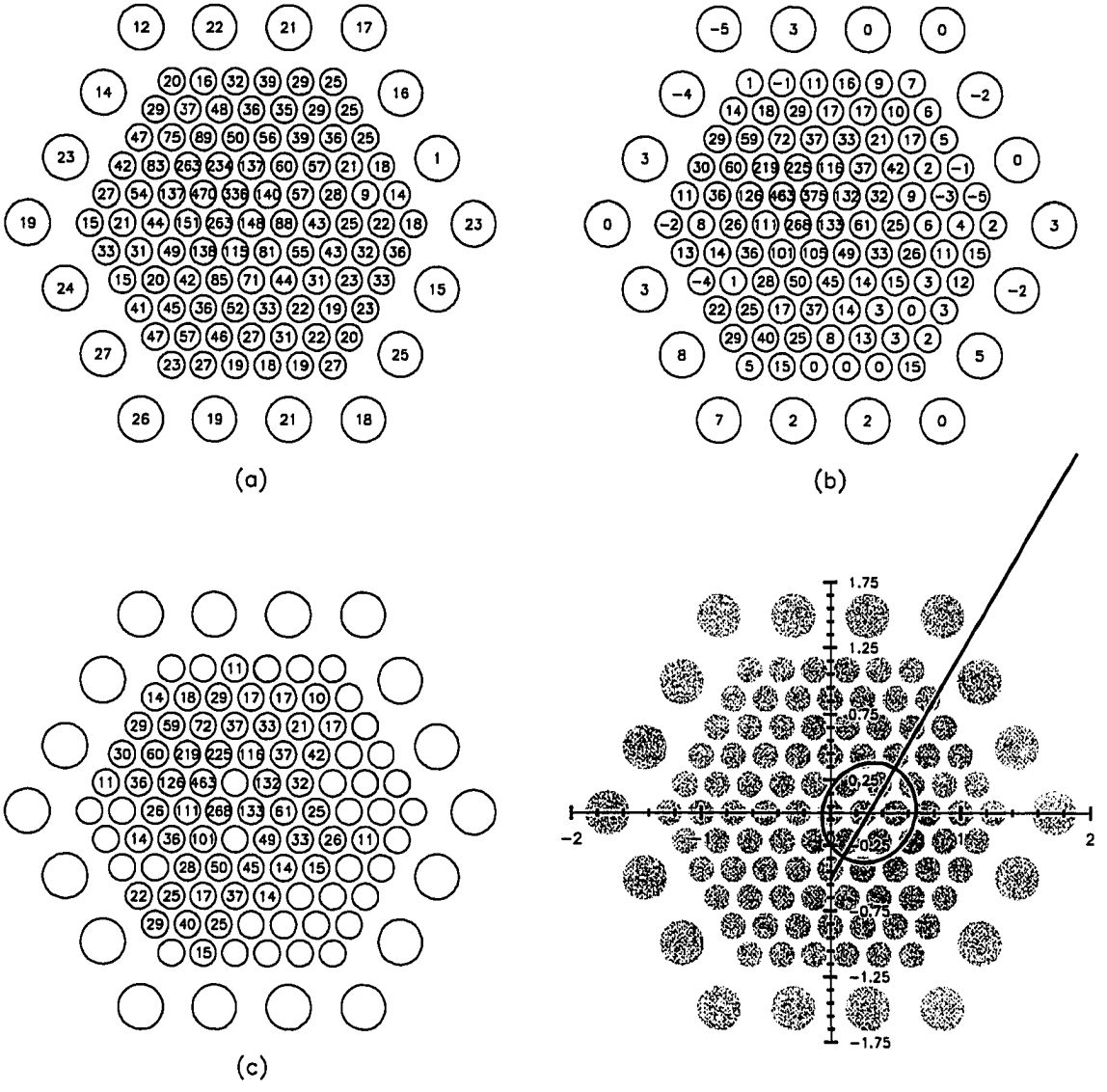

Figure 3.13: Images at various stages of the data processing for a background cosmic ray image.

of detector calibration is usually handled by Monte Carlo simulations of both gamma ray and cosmic ray showers. This means that the detector parameters that are used in the Monte Carlo simulations must be obtained from the data or explicitly measured. Parameters such as night-sky noise, hardware trigger threshold can be directly inferred from the data. Other parameters, such as mirror reflectivity, photoelectron to digital count conversion factor cannot be calculated from the data, and were often not routinely measured. For these, we have taken the approach of starting out with relatively well known values for the 1988-89 Crab database, and using the background cosmic ray rates to scale to other observational epochs. Other approaches to the detector calibration, using muon rings in the data, have been discussed by Jiang et. al. [61]. Biller [14] has compared various calibration methods applied to January 1995 data and derived results that agree within the error bars. I shall compare some of our scaled numbers with his results, and show them to be in agreement.

I shall start by giving the values of the detector parameters used for the 1988-89 database, including how they are derived. Then I shall show an example of the parameter scaling to other epochs. Final values used for each observing season are given in the data analysis chapter (see 6.1). There are other input parameters to the simulations that model, for example the pressure-density scaling in the atmosphere and the atmospheric absorption for Cherenkov light. These are usually derived from standard texts and are described in the section on simulations (see sec. 4.2).

3.4.1 1988-89 parameters

3.4.1.1 Discriminator trigger thresholds The hardware trigger threshold is determined by the setting of the trigger discriminator. This is a voltage threshold that must be exceeded by at least two of the inner 91 tubes, and roughly corresponds to a reading of 50 ADC counts. However, because of variations in the shape of the PMT pulse, and its timing relative to the ADC gate, there is some amount of jitter in this value. An example of this is shown in Fig. 3.14, which shows the distribution of ADC counts in the two tubes registering the highest number of counts, for all triggering events in the Crab 1988-89 database. Fig. 3.14(a) shows the full range of the ADC counts for the two highest tubes, while Fig. 3.14(b) is restricted to the low end to show the position of the mean hardware threshold. Gain renormalization and

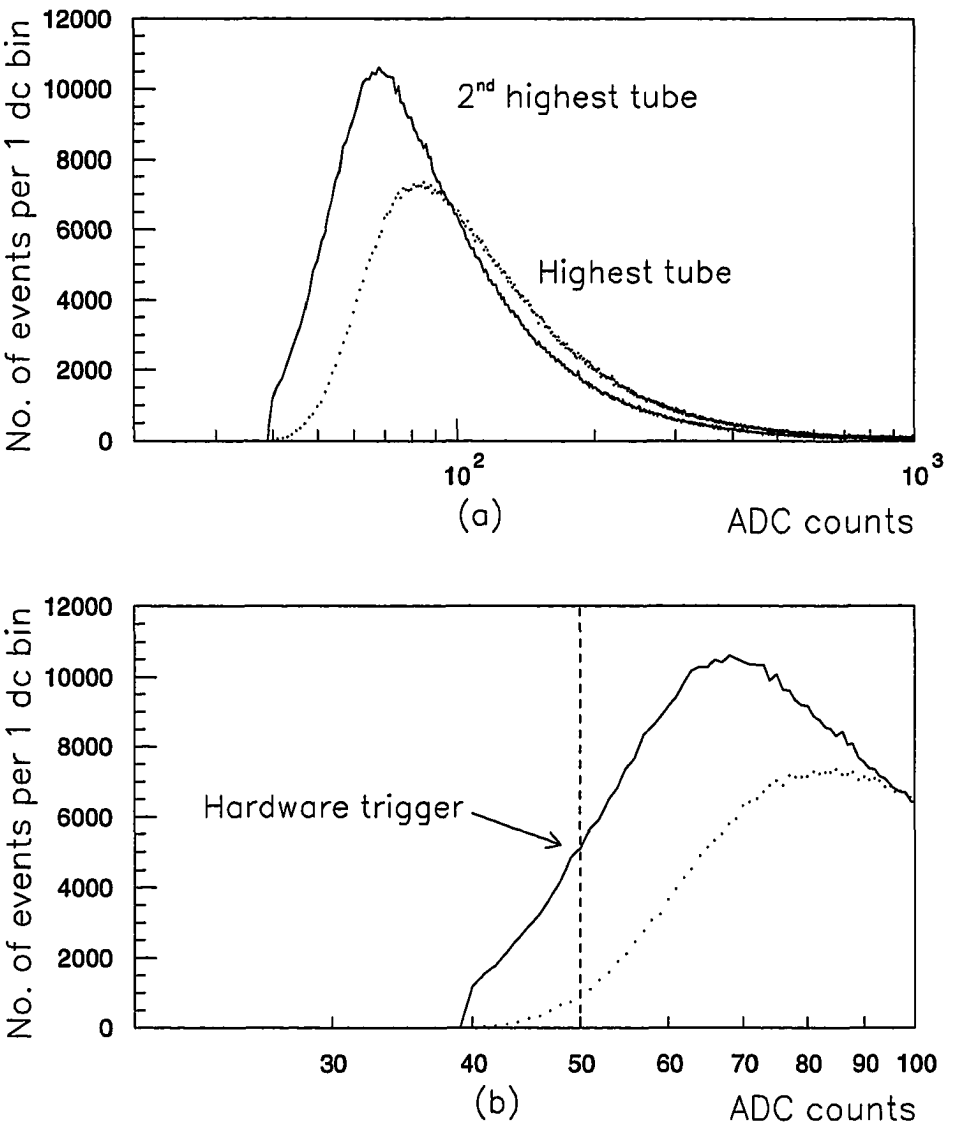

Figure 3.14: Derivation of the hardware trigger threshold from the counts in the two highest tubes

pedestal subtraction have been carried out, but no image cleaning has been done so that this represents the raw event rate from the telescope. As the trigger condition involves two out of the inner 91 tubes, the distribution for the second highest tubes carries information about the hardware trigger threshold[15]. If the hardware trigger threshold were absolutely fixed in terms of the ADC counts, this distribution would be zero till the trigger level, and would then rise up vertically. The jitter in the hardware trigger causes this step function to be smeared out about the mean value for the trigger level.

The half-maximum point on the rising part of the distribution for the second highest tube is usually chosen to be the value of the trigger threshold (this is marked on Fig. 3.14(b)). The hardware trigger threshold might be adjusted for each season, in order to maintain the same event rates in spite of decreasing mirror reflectivity. However, this can be directly measured from the data and this is done for each data set. In this work I have used a more sophisticated treatment that tries to model the actual behaviour of the trigger discriminator, which exhibits a soft turn-on rather than a hard edge. This was done at the urging of Michael Hillas, and draws on the work done by Biller [12], though I have used a slightly different approach. Other work along this line has been done by Sembroski [102].

We start by considering the distribution of ADC counts in the second highest tube, that determines the trigger for the telescope. This distribution, $F(x)$ can be expected to follow a power-law spectrum which is the convolution of the raw (unobserved) power-law spectrum, $P(x)$, of pulse heights arising due to Cherenkov triggers from light in the shower, with the discriminator trigger function, $D(x)$. Experimentally, we observe that this convolution can be approximated by a simple product, viz.,

$$F(x) = P(x)\, D(x) \tag{3.15}$$

For large enough pulse heights, the probability of the discriminator trigger turn-on

[15]There is some small probability that the two highest tubes in the event record might *not* correspond to the ones involved in the actual trigger. That is neglected here.

approaches unity, so that we have:

$$F(x) \longrightarrow P(x), \text{ as } x \text{ becomes large} \tag{3.16}$$

i.e., for large x, the observed pulse height spectrum approaches the raw pulse height spectrum. Thus, we can find the raw pulse height spectrum, $P(x)$, by fitting the observed spectrum, $F(x)$, beyond large values of x. This is done later, in sec. 3.4.3 (see, in particular Eq. (3.32), and Fig. 3.21). As the detector is typically biased well away from the night-sky noise (see sec. 3.3.4 and Fig. 3.10), almost all the observed triggers are due to Cherenkov light, and the raw spectrum is independent of the pulse height, x. Hence, from the knowledge of $P(x)$ at large x, we can find the discriminator trigger function, as:

$$D(x) = F(x)/P(x) \tag{3.17}$$

This procedure is shown in Fig. 3.15. First, we obtain the raw pulse height spectrum, by fitting the observed spectrum at large x. Then, the discriminator trigger function is found by fitting $F(x)/P(x)$ for all values of x. The points with the error bars show $F(x)/P(x)$ obtained from the trigger rates in the data, and the solid line shows the fit. The fitted discriminator trigger function for 1988-89 is parameterized as:

$$D(x) = \begin{cases} 0, & \text{if } x < 22.5; \\ \frac{2}{\pi} \arctan\left[1.0 \times 10^{-6} (x - 22.5)^{3.85}\right], & \text{otherwise.} \end{cases} \tag{3.18}$$

3.4.2 Mirror reflectivity and PMT quantum efficiency

Approximately two-thirds of the mirrors were coated just prior to the 1988-89 observation season. This was done by a commercial organization—the Liberty Mirror Company. The coating matched their specification no. 1050, which has high ultra-violet reflectivity. For the mirror reflectivity in the simulations we use a wavelength dependent curve that is 85 % of the manufacturer's specified reflectivity curve. This reduction takes into account the fact that not all the mirrors were recoated, and

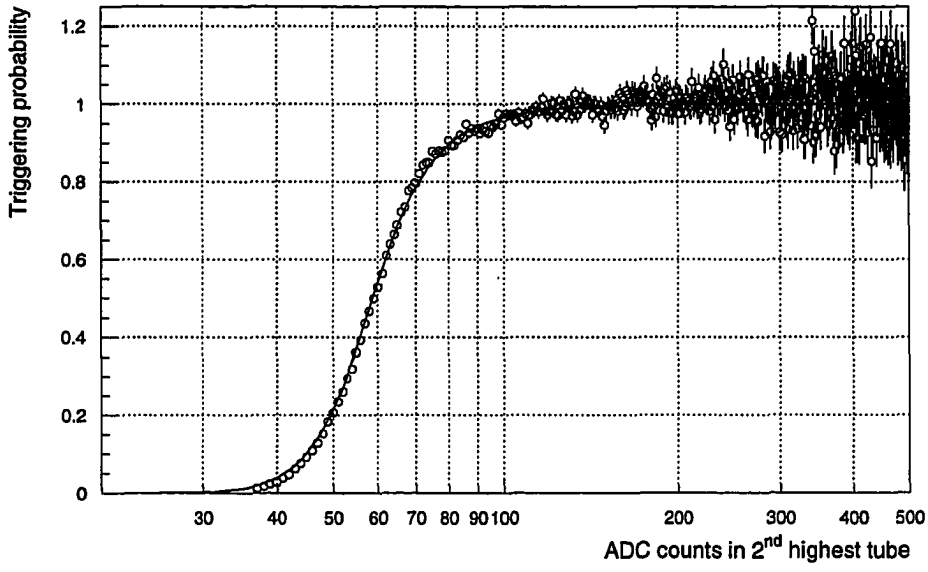

Figure 3.15: Modelling the discriminator trigger function.

that the reflectivity of the coating degrades fairly rapidly with exposure to ambient weather. The PMT quantum efficiency is also taken from the manufacturer's response curve for a Hamamatsu R1398 UV glass tube.

Fig. 3.16(a) compares the reflectivity curve used by us, with a recent measurement made on an unweathered sample of the 1988-89 coating on the mirrors. Though the curves appear to differ, it should be kept in mind that the mirrors degrade rapidly on exposure to weather, and we are seeking an average reflectivity over a period of several months. Further, the differences at large wavelengths are minimized by the falling Cherenkov light spectrum. We chose to use the manufacturer's specification in preference to this measurement as we felt that it better represented the average reflectivity of all the weathered mirrors in the reflector. Fig. 3.16(b) shows the PMT quantum efficiency derived from the manufacturer's specification curve. Fig. 3.17 shows the overall reflectivity, defined as the mirror reflectivity multiplied by the PMT quantum efficiency. Both the measured reflectivity and our assumed curve are shown. The mirror reflectivity is thus fairly well known for the 1988-89 database.

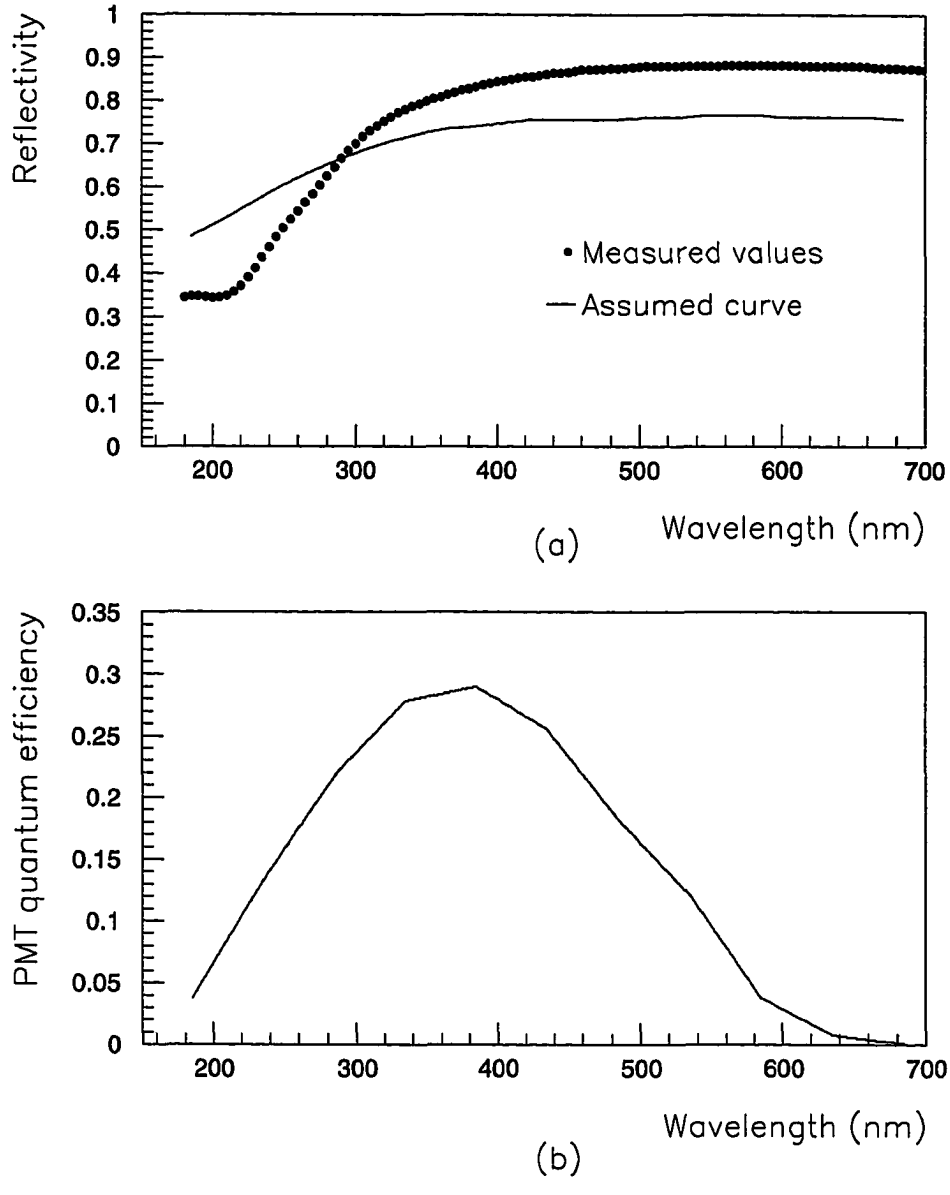

Figure 3.16: (a) Mirror reflectivity curves. (b) Manufacturer's specification for the PMT quantum efficiency.

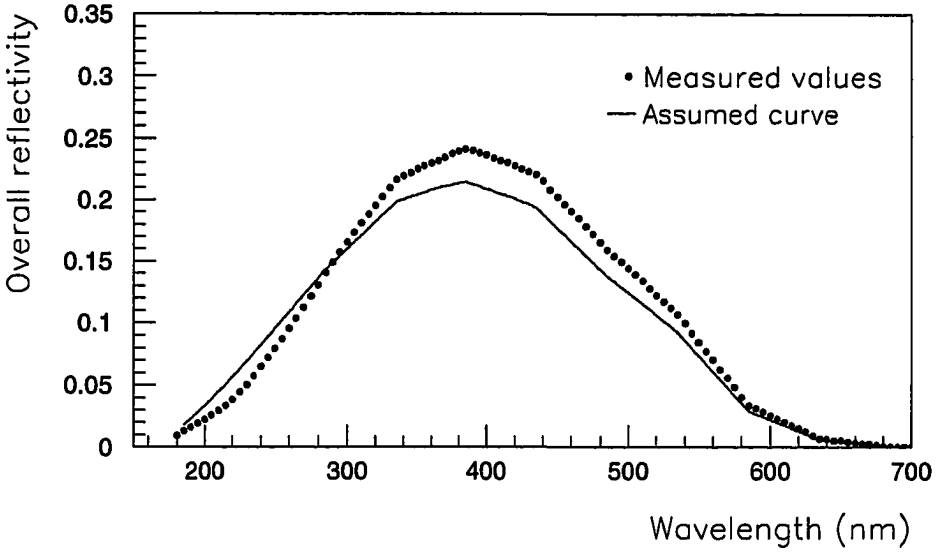

Figure 3.17: PMT quantum efficiency convoluted with mirror reflectivity

For subsequent years, the mirrors degraded from exposure to the weather, and the reflectivity was not routinely monitored. Therefore I show later (see sec. 3.4.3), how the mirror reflectivity might be extrapolated to later seasons, using the background cosmic ray rates.

3.4.2.1 Conversion to ADC counts The signals from the PMTs are fed to the control room through $\sim$ 50 m of coaxial cable and then amplified by a factor of 10. Cable loss can be measured by using the centroid of the energy spectrum of a radioactive source attached to a PMT. This is first measured with the PMT being hooked up to the electronics via the long cable. Then the cable is removed, and the centroid is re-measured. The ratio of the two measurements gives the fractional loss in the cable. Kwok [67, Appdx. A3.3] estimates this as 0.73. Following Kwok, the

photoelectron to ADC count conversion factor, g, is then given by:

$$\begin{aligned} g &= (\text{current gain of PMT}) \times \left(1.6 \times 10^{-19}\,\text{C}\right) \times 10 \times 0.73 \\ &\quad \times (1024\,\text{d. c.}\,/256\,\text{pC}) \end{aligned} \tag{3.19}$$

Kwok estimates $g = 0.85$ d. c./p. e., which is the value that we have used in our simulations for the 1988-89 database. Again, this conversion factor was not routinely measured for subsequent years, and I show how later (see sec. 3.4.3), how it might be estimated.

As noted above, there are other possible approaches to estimating this conversion factor. Biller [14] summarizes the different methods, and I have demonstrated that our extrapolated numbers agree with his results. (This is described in Mohanty [82, sec. 2.4].)

3.4.2.2 Noise values There are three main sources of noise in the system:

1. *Night-sky noise:* This arises from fluctuations in the night-sky brightness. As the discriminators and ADCs are ar-coupled to the tubes, we are are interested only in the variance of the night sky noise, and not its mean. These can be measured from the variances in the sky pedestals, and are usually slightly smaller for the outer tubes which have smaller applied voltages.

2. *Signal noise:* It is well known that the noise in a PMT departs from Poissonian statistics (see, for example, the discussion in the RCA handbook [92, Appdx. G]). This is usually ascribed to two factors. Firstly, the cascade of events through the dynode chain is influenced by fluctuations in the first few dynodes, so that the overall results are non-Poissonian even though the secondary emission from each individual dynode might follow Poisson statistics. The second factor is that the physical non-uniformity of the dynodes might lead to non-Poissonian fluctuations. The secondary electrons emitted from dynode have a so-called Polya or compound Poisson distribution. This looks like a Poisson distribution in the limit of low fluctuations and an exponential distribution at the other limit. The variance of this compound distribution is thus theoretically restricted to lie between the almost-Poisson variance at the low end, and the exponential variance at the high end.

3. *Electronic noise:* This is caused by jitter in the applied pedestals and other sources of noise in the channel. It can be measured from the pedestal standard deviations with the high voltage to the PMTs turned off, and is also incorporated into the standard deviations seen in the sky pedestals. From three pedestal files taken near the start of the 1988-89 observing season, the electronic noise is estimated to have a standard deviation of 1.1 dc. As it adds in quadrature to the night sky noise, this contribution is relatively small.

Kwok [67, Appdx. 3] has examined the night-sky noise, and the signal noise. The development in this section broadly follows along the same lines, though I have improved on his methods in places.

Though the variance of the night sky noise is measured directly from the sky pedestal files, it is instructive to attempt to estimate the expected night noise in the PMTs. In principle, this can be done by folding in a known spectrum for the ambient night sky light with the mirror reflectivity and the PMT quantum efficiency. The night sky spectrum at visible wavelengths (300 nm to 700 nm) is fairly well known (see, for example, Allen [1]), and has even been measured over the years at Kitt Peak (see Massey et al. [78], Broadfoot et al. [18]). The brightness in the near ultraviolet is not as reliably known. As I am only after an approximate number here, I have chosen to extrapolate from the visible spectrum.

Fig. 3.18 shows the expected contribution to the number of photoelectrons from the night sky background. Fig. 3.18(a) is a plot of the night sky intensity, taken directly from Allen [1, sec. 62.]. I have done the simplest extrapolation of assuming a constant intensity below 320 nm[16] The intensity can be converted into the expected number of photoelectrons per PMT per event, by multiplying it with (i) the reflector area (85 m^2), (ii) the solid angle subtended by the photo-cathode area of each PMT (9.3×10^{-6} sr for the 1 inch tubes, 2.7×10^{-5} sr for the 2 inch tubes), (iii) a 25 ns integration time for the PMT pulse, (iv) a factor of λ/hc to convert from energy to number of night sky photons (λ is the wavelength at mid-bin), and (v) the overall reflectivity (mirrors + PMTs) at mid-bin. This is shown in Fig. 3.18(b) for both the

[16]Reasonable changes in this extrapolation have only a small effect on the final answer, as the overall reflectivity in this region is pretty low.

1 inch and 2 inch tubes. Integrating over a Cherenkov wavelength band of 185 nm to 685 nm gives the expected mean number of night sky photoelectrons per PMT per event, to be 3.9 for the 1 inch tubes, and 7.7 for the 2 inch tubes. These are comparable to Kwok's numbers which were probably derived with different night sky intensities in the ultraviolet. He gets 4.2 pe for the 1 inch tubes and 8.3 pe for the 2 inch tubes.

As the tubes are ar-coupled to the data acquisition system, we record only the standard deviations for the night sky noise, and not the mean values. If the noise were Poisson distributed, we would expect to see standard deviations of:

$$\begin{aligned} \text{S. D. of 1 inch tubes} &= 1.97\,\text{pe} \\ \text{S. D. of 2 inch tubes} &= 2.77\,\text{pe} \end{aligned} \tag{3.20}$$

These standard deviations would be scaled by the pe-to-dc conversion factor (0.85 dc/pe for the 1 inch tubes, and 0.45 dc/pe for the 2 inch tubes), so that the expected standard deviations of the night sky noise in ADC counts, under the assumption of a Poisson distribution would be:

$$\begin{aligned} \text{S. D. of 1 inch tubes} &= 1.67\,\text{dc} \\ \text{S. D. of 2 inch tubes} &= 1.25\,\text{dc} \end{aligned} \tag{3.21}$$

We know from the 1988-89 data that the observed standard deviations in the sky pedestals are:

$$\begin{aligned} \text{S. D. of 1 inch tubes} &= 3.14\,\text{dc} \\ \text{S. D. of 2 inch tubes} &= 2.74\,\text{dc} \end{aligned} \tag{3.22}$$

This includes an electronic noise with a standard deviation of 1.1 dc. Assuming these two contributions to add in quadrature, the observed standard deviations solely due to the night sky noise are:

$$\begin{aligned} \text{S. D. of 1 inch tubes} &= \sqrt{3.14^2 - 1.1^2}\,\text{dc} = 2.94\,\text{dc} \\ \text{S. D. of 2 inch tubes} &= \sqrt{2.74^2 - 1.1^2}\,\text{dc} = 2.51\,\text{dc} \end{aligned} \tag{3.23}$$

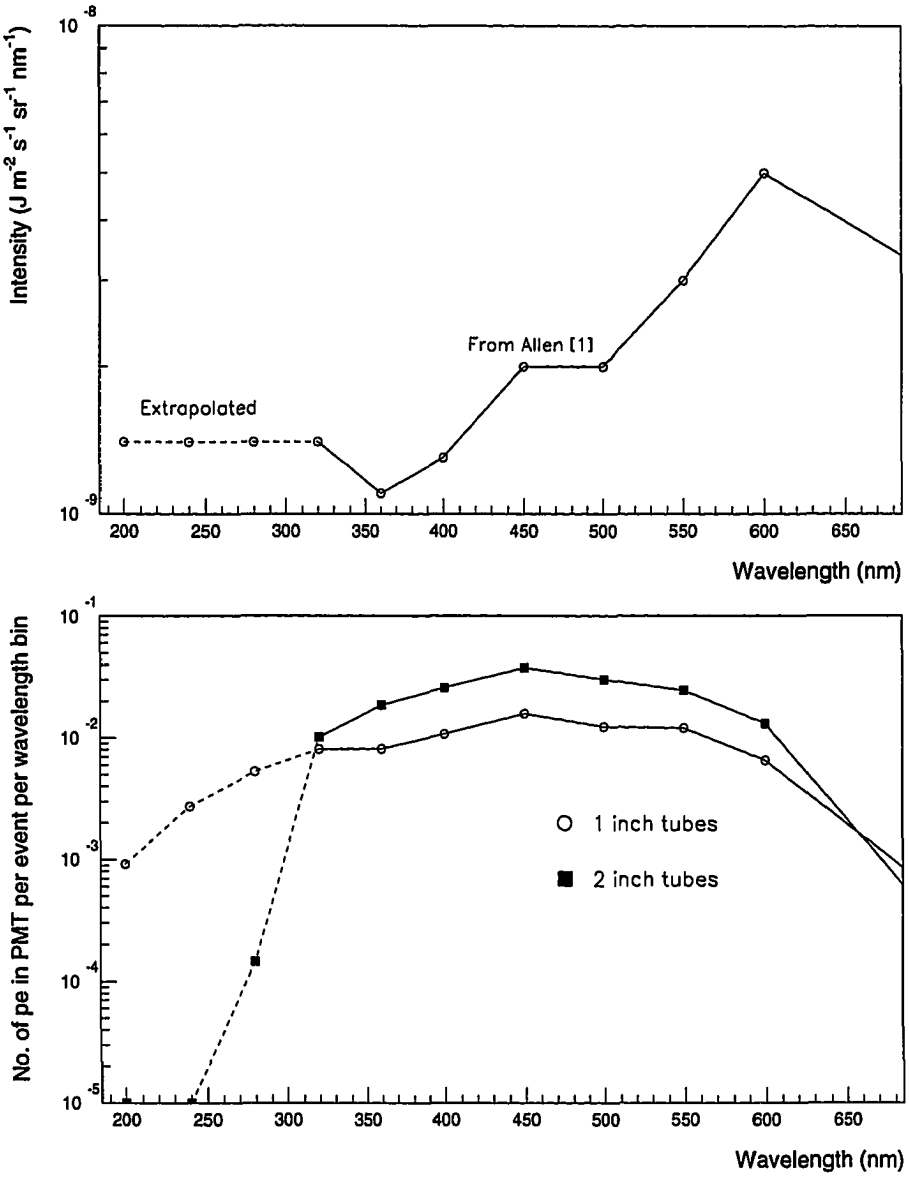

Figure 3.18: Contribution of night sky brightness to PMT counts.

Hence, the non-Poissonian behaviour of the PMTs for the night sky noise can be quantified as below:

$$\frac{(\text{S. D. of 1 inch tubes})_{obs.}}{(\text{S. D. of 1 inch tubes})_{Poisson}} = \frac{2.94}{1.67} = 1.76$$

$$\frac{(\text{S. D. of 2 inch tubes})_{obs.}}{(\text{S. D. of 2 inch tubes})_{Poisson}} = \frac{2.74}{1.25} = 2.19 \qquad (3.24)$$

This is in fair agreement with Kwok's numbers, though it should be noted that he gets slightly different values for the calculated night sky noise and does not include the effect of the electronic noise. By looking at the ratio of the measured and expected noise, Kwok concludes that the night-sky noise exceeds the theoretical upper limit of the exponential variance for both the 1 inch tubes and the 2 inch tubes.

Kwok also estimates the signal noise from the nitrogen files, using a method developed by Dave Lewis. If the camera is uniformly illuminated by the nitrogen flash lamp, the signal in any given PMT should be proportional to the intensity of the light at the camera face, and the variation in the signal should be a measure of the noise. As there is no independent measure of the light intensity, the average of the counts in all tubes for a given event (after removal of the pedestals) is taken to represent the light intensity at the camera face for that event. Thus for event j, the average light intensity is:

$$\langle n_{ij} \rangle = \frac{1}{109} \sum_{i=1}^{109} n_{ij} \qquad (3.25)$$

where, n_{ij} is the ADC counts in tube i for event j. An example of the distribution of counts in PMT # 10 for a nitrogen file (n20670) is shown in Fig. 3.19 below. Then, from all the events in a nitrogen file, we can construct a chisquare statistic for tube i, as follows:

$$\chi_i^2 = \frac{1}{N-1} \sum_{j=1}^{N} \frac{(n_{ij} - g_i \langle n_{ij} \rangle)^2}{\sigma_{sig}^2 + \sigma_{sky}^2 + \sigma_{elec}^2} \qquad (3.26)$$

where, N is the total number of events in the nitrogen file, and σ_{sig}^2, σ_{sky}^2, and σ_{elec}^2, are, respectively, the variances (in ADC counts) of the signal noise, the night sky noise, and the electronic noise. The last two can be measured directly from the data, as described earlier. The variance in the signal noise, for PMT i in event j, can be

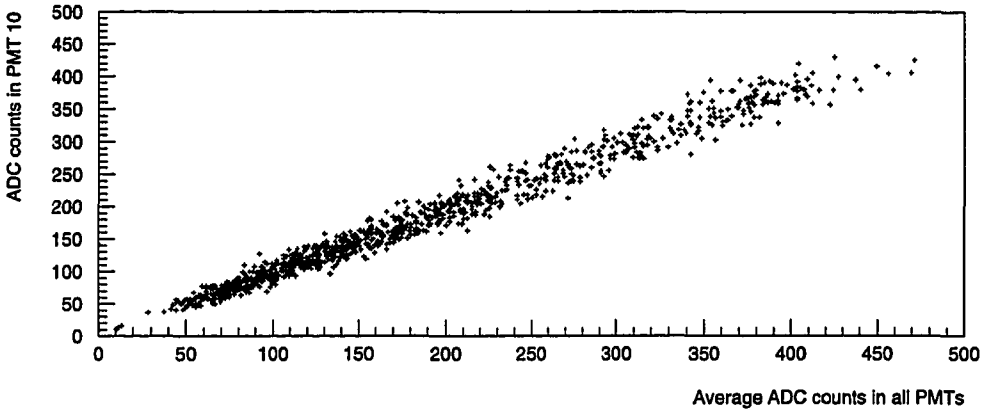

Figure 3.19: Response of tube # 10 to the nitrogen flash lamp. Pedestals have been removed from both axes.

approximated as $\sigma^2_{sig} \sim \alpha\, n_{ij}$, so that the above equation can be written as:

$$\chi^2_i = \frac{1}{N-1} \sum_{j=1}^{N} \frac{(n_{ij} - g_i \langle n_{ij} \rangle)^2}{\alpha\, n_{ij} + \sigma^2_{sky} + \sigma^2_{elec}} \tag{3.27}$$

Now, α can be adjusted to make $\chi^2 \sim 1$, and that value of α can be taken to represent the best-fit value for the variance in the signal noise. I have used nine nitrogen files from the start of the 1988-89 season and get mean values of χ^2 for the 1 inch and 2 inch tubes to be:

$$\begin{aligned} \langle \chi^2 \rangle &\sim 1 \qquad \text{for 1 inch tubes if } \alpha = 1.35 \\ \langle \chi^2 \rangle &\sim 1 \qquad \text{for 2 inch tubes if } \alpha = 0.90 \end{aligned} \tag{3.28}$$

Although this is in exact agreement with Kwok's values, this method has significant problems. Occasionally the counts in a particular PMT fall well below the average for

that event. Such tubes need to be eliminated from the image, as otherwise they would have an unacceptably large contribution to the calculated χ^2. Thus, the following procedure is used to massage the data. First, for each nitrogen file considered, all tubes that have (i) a relative gain greater than 3 or less than 0.3, or (ii) a relative gain deviation greater than 1.0 or less than 0.04, are rejected. Then, for each event, the pedestals are subtracted from the counts, and an average over all tubes is calculated. Next, all tubes in that event that have counts greater than twice the average, or less than half the average are rejected. The average is recomputed over the accepted tubes, and χ^2 calculated, as given by Eq. 3.27. Finally, for a given tube all events that contribute more than 5.0 to χ^2 are rejected. This is a bit tricky, as by doing this, one picks the maximum value that a given event can contribute to χ^2, and the estimated value of α does seem to depend on the chosen cut-off.

A better method to estimate the signal noise is to use a Monte Carlo technique to reproduce the observed variances. I treat the 1 inch tubes and the 2 inch tubes differently throughout. For each event in a nitrogen file from the data, I separately average the 1 inch tubes and the 2 inch tubes. This average represents the mean amount of light seen by each tube. The tubes are then binned by the difference between the actual counts in the tube and the expected mean, thus building up a distribution of the variances seen in the tube counts, from the data. Then, for each tube I generate a Gaussian distributed random number with mean equal to the average from the data, and with a variance equal to the sum of the expected variances of the different noise contributions, viz., $\alpha\, n_{ij} + \sigma^2_{sky} + \sigma^2_{elec}$. I bin these simulated tube counts in the same way as for the data, and then adjust α till I match the distribution from the data.

This is shown in Fig. 3.20. The points with the error bars are the distributions from the data, while the solid lines represent the simulated distributions that best fit the data. The simulated distributions seem to be slightly shifted from the data, possibly due to imperfect pedestal subtraction and gain renormalization. Fig. 3.20(a) is for the 1 inch tubes, and Fig. 3.20(b) is for the 2 inch tubes, so that we conclude that,

$$\alpha = 1.5 \qquad \text{for 1 inch tubes}$$

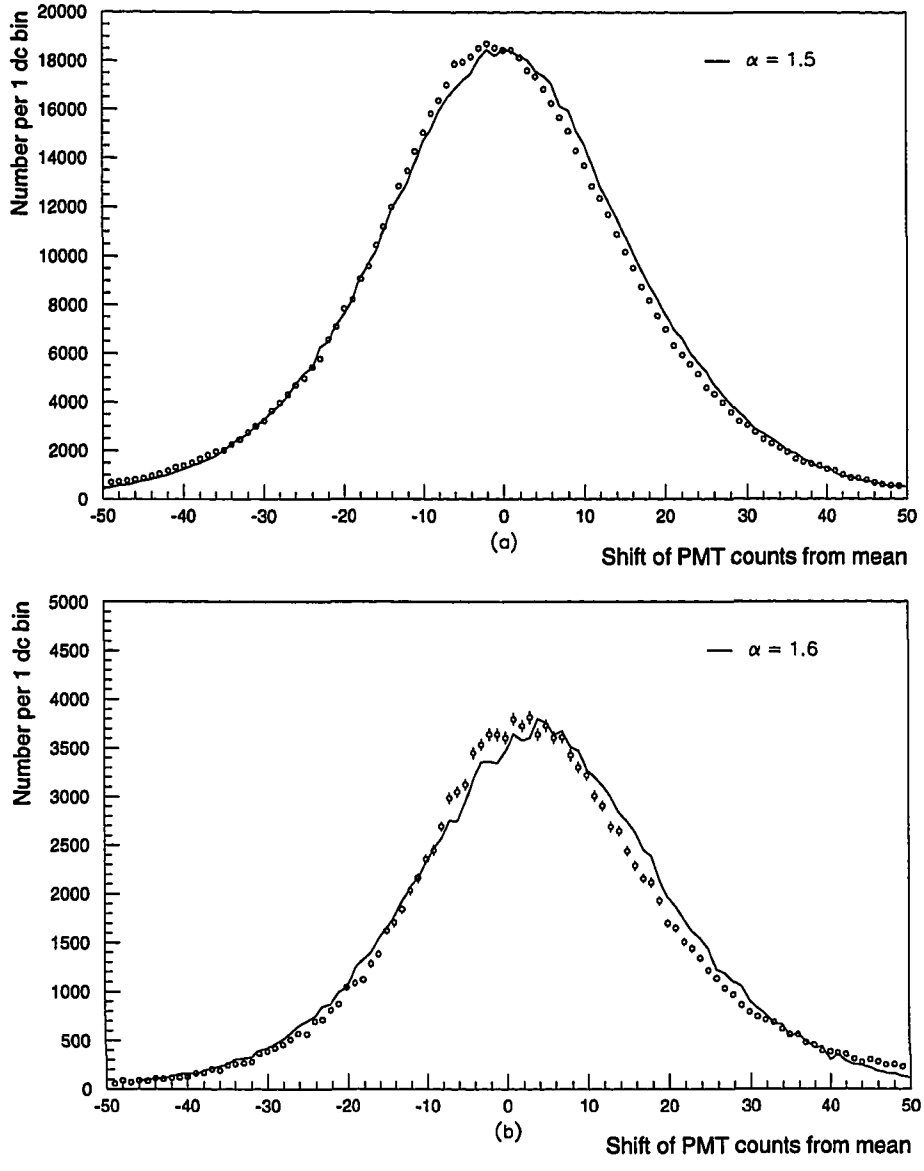

Figure 3.20: Signal noise in the PMTs. (a) 1 inch tubes, and (b) 2 inch tubes.

$$\alpha = 1.6 \qquad \text{for 2 inch tubes} \tag{3.29}$$

I estimate the errors in the derived value of α to be about 15 %, as a 15 % change in α is clearly seen to give a worse fit. Thus, this result is significantly different from Kwok's results for the case of the 2 inch tubes. We shall apply these values for the non-Poissonian nature of the signal noise to the data from all the observing seasons.

3.4.3 Scaling to other epochs

This section describes a method we have developed to extrapolate quantities like mirror reflectivity from one observational epoch where it might be known, to another epoch where it is unknown. The method uses the integral rates of background cosmic ray showers to scale these quantities. Also, it allows us to separate the mirror reflectivity from the photoelectron to ADC count conversion factor.

I start by defining some nomenclature. Let the wavelength dependent mirror reflectivity be $m(\lambda)$, the wavelength dependent PMT quantum efficiency be $q(\lambda)$, and let g be the photoelectron to ADC count conversion factor which has the PMT current gain, cable losses and amplifier gain lumped together (see sec. 3.4.2.1). Define an overall reflectivity, r that includes both mirror reflectivity and PMT quantum efficiency, and is integrated over wavelength, thus:

$$r = \int m(\lambda)\, q(\lambda)\, d\lambda \tag{3.30}$$

Then, the "throughput" of the telescope, that measures its efficiency at converting Cherenkov photons in the showers to ADC counts, is just gr.

We shall consider the background cosmic ray shower rates sufficiently above the hardware trigger threshold, so that these are unaffected by the jitter in the hardware threshold. From independent measurements of the cosmic ray spectrum (see, for instance, [106]), we know that the differential flux of cosmic rays is a power law with an index of -2.65, viz.,

$$\frac{dF(E)}{dE} \propto E^{-2.65} \tag{3.31}$$

where, E, is the (for us, unknown) primary energy of the cosmic ray. From the 10-meter data, we see that the observed differential rates of the background cosmic ray

showers, in terms of the counts in the second highest tube[17], n, is well described by a single power law with a best fit spectral index of -2.33, viz. :

$$\frac{dF(n)}{dn} \propto n^{-2.33} \tag{3.32}$$

An example of the fit is shown in Fig. 3.21, which shows both the binned differential data points with statistical error bars, and the fitted spectrum.

By comparing Eq. (3.31) with Eq. (3.32), we can conclude that the relationship between the counts in the second highest tube, n, and the primary cosmic ray energy, E, must itself be a power law of the form:

$$n \propto E^{\beta} \tag{3.33}$$

Also, for a given primary cosmic ray energy, we expect that a change in the throughput of the telescope should cause an exactly proportional change in the counts in the second highest tube, n. Thus, n must also scale as the throughput, gr, and the index, β, must be independent of the throughput. This is indeed observed in the data, where the observed differential background rate always has a slope of -2.33, so that the background rates for different observing seasons is a set of parallel lines. The observed counts in the second highest tube can therefore be expressed as:

$$n \propto g\,r\,E^{\beta} \tag{3.34}$$

Consider Fig. 3.22, which shows schematically, the effect of a change in the throughput of the telescope on the background rates. The curve labelled 1 is considered to be the initial integral spectrum for the background, and the curve labelled 2 shows the integral background spectrum resulting from a reduction in the throughput. From Eq. (3.34), a change in the telescope throughput, that moves the rates from point A on curve 1 to point B on curve 2, is equivalent to a change in the threshold energy on curve 1, that slides the rates from point A to point C. Let F_1, F_2, be the rates at points A and B, respectively. Let n_1, n_2, be the counts in the

[17]The counts in the second highest tube are an approximate measure of the primary energy. It is preferable to use this measure rather than the total ADC counts, as it is expected to have a smaller variance for background cosmic ray showers.

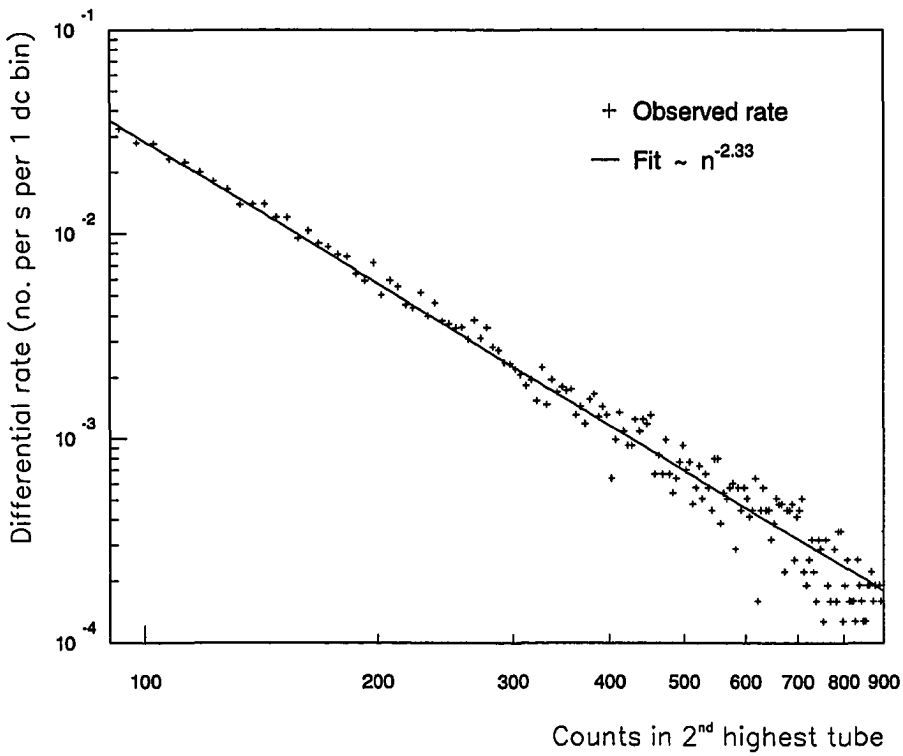

Figure 3.21: Background rates and fitted spectrum.

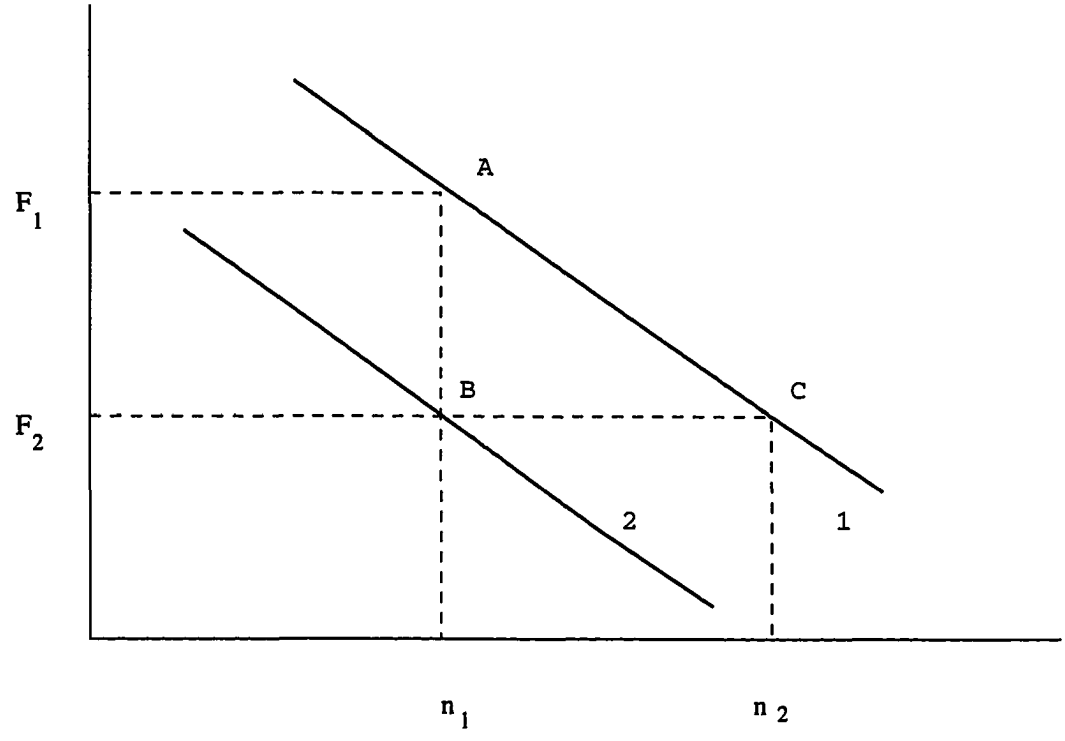

Figure 3.22: Change in background spectrum due to a reduction in the telescope throughput.

second highest tube,at points B and C, respectively. Then, we have from Eq. (3.34):

$$\frac{n_2}{n_1} = \frac{g_1 r_1}{g_2 r_2} \tag{3.35}$$

Also, as the integral background rates are power laws with the same index of -1.33, though with different flux constants, we can express them as:

$$F_1 = \alpha_1 n_1^{-1.33} \tag{3.36}$$

$$F_2 = \alpha_2 n_1^{-1.33}$$

$$= \alpha_1 n_2^{-1.33} \tag{3.37}$$

where, α_1, α_2, are numeric flux constants. The above two equations for the rates can be combined to give:

$$\frac{F_2}{F_1} = \left(\frac{n_2}{n_1}\right)^{-1.33} \tag{3.38}$$

Substituting for n_2/n_1 from Eq. (3.35) in Eq. (3.38), we have:

$$\begin{aligned} \frac{F_2}{F_1} &= \left(\frac{g_1 r_1}{g_2 r_2}\right)^{-1.33} \\ &= \left(\frac{g_2 r_2}{g_1 r_1}\right)^{1.33} \end{aligned} \tag{3.39}$$

which can be inverted to give a relationship between the telescope throughputs for curves 1 and 2, in terms of the observed integral background rates, F_1, and F_2. This is given by:

$$\begin{aligned} \frac{g_2 r_2}{g_1 r_1} &= \left(\frac{F_2}{F_1}\right)^{1/1.33} \\ &= \left(\frac{F_2}{F_1}\right)^{0.75} \end{aligned} \tag{3.40}$$

Eq. (3.40) gives the ratio of the throughputs of the telescopes for two different observing seasons. Next, we consider how to separate this into the overall reflectivity (mirrors + PMT efficiencies) and the photoelectron to ADC count conversion factor. In order to do this, we will also need the night-sky noise for the two seasons, as measured from the standard deviations, σ, in the sky pedestals. The variances in the sky pedestals can be attributed mainly to Poisson fluctuations in the night-sky brightness. Thus, we expect the sky pedestal standard deviation (in photoelectrons) to scale with the overall reflectivity as $\sqrt{r}$. This would be further amplified by a factor of g in passing through the cables and amplifiers, so that the sky pedestal standard deviations measured in ADC counts are given by:

$$\sigma \propto g\sqrt{r} \tag{3.41}$$

Thus, the standard deviations for the two observational epochs are related by:

$$\frac{\sigma_1}{\sigma_2} = \frac{g_1\sqrt{r_1}}{g_2\sqrt{r_2}} \tag{3.42}$$

Eq. (3.40) and Eq. (3.42) can now be combined to give the overall reflectivity, r, and the photoelectron to ADC count conversion factor, g, independent of each other. I show an example of this procedure in sec. 3.4.3.2, below.

This procedure assumes that the wavelength dependent characteristics of the telescope are not significantly changed from one season to the next, so that the reflectivity is well described by an overall value, integrated over wavelengths. Also, as we are going to apply the extrapolated values from the background cosmic ray showers to the gamma ray simulations, we are making the implicit assumption that the spectral content of the Cherenkov light from both kinds of showers do not differ significantly at mountain altitude.

3.4.3.1 Aside: background calibration As an aside, we can use the discussion in the previous section to develop a calibration for the background cosmic ray showers, that gives the total ADC counts, n, in terms of the primary cosmic ray energy, E.

The differential rate of the background showers must be the same, irrespective of whether we consider the rates in terms of n, or in terms of E. Thus, we have:

$$\frac{dF(n)}{dn}\,dn = \frac{dF(E)}{dE}\,dE \tag{3.43}$$

By substituting from Eq. (3.31) in Eq. (3.43), we have:

$$\frac{dF(n)}{dn}\,dn \propto E^{-2.65}\,dE \tag{3.44}$$

By using Eq. (3.33) to substitute for E, and dE, in Eq. (3.44) above, we get:

$$\frac{dF(n)}{dn}\,dn \propto (n)^{(-1.65-\beta)/\beta}\,dn \tag{3.45}$$

This can now be directly compared to the observed differential background rates in terms of the total ADC counts, n, which is given in Eq. (3.32). Matching the spectral index gives us the following relation for β:

$$\frac{-1.65-\beta}{\beta} = -2.33 \tag{3.46}$$

which gives, $\beta = 1.24$, so that Eq. (3.34) expressing the total ADC counts in terms of the primary energy for the background cosmic ray showers can be written as:

$$n \propto g\,r\,E^{1.24} \tag{3.47}$$

3.4.3.2 Example: scaling from 1988-89 to 1990 Here, I show an example of applying the procedure described above to scale from the 1988-89 observing season to the 1990 observing season. We shall assume that the mirror reflectivity and the photoelectron to ADC counts conversion factor are known for 1988-89 (as given in sec. 3.4.1), and we wish to estimate the unknown values for 1990. Fig. 3.23 shows the differential background rates for the two seasons, along with the fitted spectrum. First we find the ratios of the telescope throughputs for the two seasons,

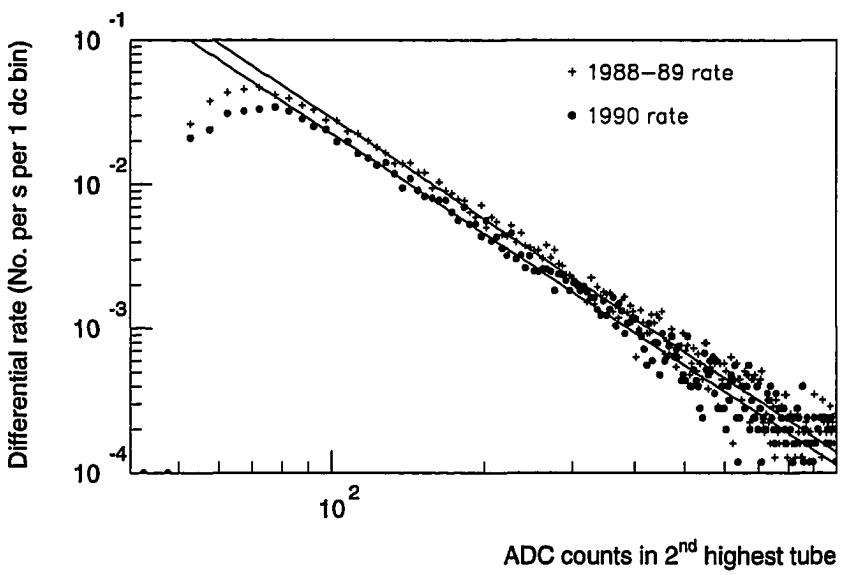

Figure 3.23: The differential event rates for 1988-89 and 1990, showing the effect of a change in reflectivity.

using Eq. (3.40). To avoid systematic errors arising from differences in detector elevation angles, and cloud coverage for the two seasons, we shall use "zenith files" taken in A-quality weather to do the scaling. These are data files taken with the telescope pointed at the zenith, so that the elevation angle is always 90° . I have taken seven zenith files from the 1988-89 data with a total observation time of 6282.3 s, and six

zenith files from 1990 with a total observation time of 5028.5 s. I compare the integral rates above six different thresholds, ranging from 90 ADC counts to 300 ADC counts, to check that the ratio is independent of the chosen threshold. Also, note that the minimum threshold for this comparison is well above the detector threshold of about 50 ADC counts. The comparison is shown in Table 3.1 below. From the values in

Table 3.1: Comparison of background rates between 1988-89 and 1990.

Threshold	1988 rate	1990 rate	F_{90}/F_{88}	$g_{90}r_{90}/g_{88}r_{88}$
90	2.44	1.94	0.80	0.84
100	2.14	1.69	0.79	0.84
200	0.81	0.66	0.81	0.86
300	0.42	0.36	0.86	0.89
400	0.25	0.21	0.84	0.88
500	0.16	0.14	0.88	0.90

the table, we take the ratio of the telescope throughputs to be given by:

$$\frac{g_{90}\, r_{90}}{g_{88}\, r_{88}} = 0.87 \tag{3.48}$$

The night-sky noise standard deviations as measured from the sky pedestals for the 1988-89 season is 3.14 ADC counts for the 2.9 cm inner tubes, and 2.74 ADC counts for the 4.3 cm outer tubes. For the 1990 season, the measured standard deviations are 3.61 ADC counts for the 2.9 cm inner tubes, and 3.33 ADC counts for the 4.3 cm outer tubes. Hence, from Eq. (3.42), we have:

$$\frac{g_{90}\sqrt{r_{90}}}{g_{88}\sqrt{r_{88}}} = \frac{\sigma_{90}}{\sigma_{88}} \tag{3.49}$$

Thus, from the standard deviations for the 2.9 cm inner tubes, we have:

$$\frac{g_{90}\sqrt{r_{90}}}{g_{88}\sqrt{r_{88}}} = 1.15 \tag{3.50}$$

and, from the standard deviations for the 4.3 cm outer tubes,

$$\frac{g_{90}\sqrt{r_{90}}}{g_{88}\sqrt{r_{88}}} = 1.22 \tag{3.51}$$

These are fairly consistent with each other, so that we use the value:

$$\frac{g_{90}\sqrt{r_{90}}}{g_{88}\sqrt{r_{88}}} = 1.2 \tag{3.52}$$

Solving Eq. (3.48) and Eq. (3.52), we have:

$$\frac{g_{90}}{g_{88}} = 1.66 \tag{3.53}$$

$$\frac{r_{90}}{r_{88}} = 0.53 \tag{3.54}$$

Thus, we conclude that in 1990 the telescope throughput was 53 % of that in 1988-89. Also, using the value of $g_{88} = 0.85$ d.c./p.e. derived by Kwok, (see sec. 3.4.2.1), the photoelectron to ADC count conversion for 1990 is estimated as 1.41 d.c./p.e.

CHAPTER 4. EXTENDED SUPERCUTS

4.1 Motivation for building the ISU set of simulations

The standard analysis technique for the Whipple data has been the supercuts method, which uses a passband independent of the shower energy (total light), in the parameters width, length, alpha and distance. Also, it is optimized to the 1988-89 Crab database and preferentially selects smaller, low-energy showers. Thus, while it has been very successful in identifying gamma ray sources it is unsuitable for energy spectrum determination as it discards most of the high-energy showers.

The primary motivation for starting the ISU simulation program was to devise a set of gamma ray image selection cuts that were built upon standard supercuts, but allowed for a scaling of the cuts with the shower energy. The intent was to reduce the bias introduced in the energy spectrum by the image selection process. Also, as these cuts were derived from simulations, they had the desirable feature of starting with an *a priori* understanding of the physics of the cascade process, as compared to standard supercuts that were derived from the 1988-89 Crab database.

The ISU set of simulations were also entirely independent from the simulations of Michael Hillas, that had so far been used by the Whipple Collaboration, and thus provided a cross-check.

Significant portions of the computer simulation code have been written at ISU. This has provided us familiarity with the code and a better understanding of the assumptions that go into it, which is a safeguard against bugs in the code. Finally, the available computing resources at ISU meant that we could build up adequate Monte Carlo statistics in a reasonable amount of time. In later sections of this chapter I comment on the degree to which these aims were achieved.

4.2 Simulation programs

This section describes the details of programs used at ISU in the simulation of the detection of Cherenkov light in an air shower created by a high-energy particle entering the atmosphere. The process is divided into three logically distinct steps, (i) the particle cascade, (ii) Cherenkov light generated by ultra-relativistic particles in the cascade, and (iii) the detection of the Cherenkov light by the Whipple 10-meter detector. Each of these steps is handled by a separate program, described below. In the parts of the code written at ISU, our aim has been to generate clear and correct rather than fast-running code.

4.2.1 Simulation of the particle cascade

The first program, that simulates the particle cascade is written in Fortran by Kertzman et. al. [64] and is part of their KASCADE system. The authors credit Gaisser, Stanev, Wrotniak and others with originating and modifying many of the algorithms used in this program. We have replaced the ionization subroutine with a more realistic one and have made other minor modifications.

The same program handles both VHE gamma ray and cosmic ray (presently, only protons) air showers. The shower model is three-dimensional and each particle in the shower is individually followed. This is done by slicing the particle track in the atmosphere into segments characterized by their length along the particle track. For each segment, the ionization energy loss is computed and the particle energy at the segment midpoint is used to figure the change in direction due to multiple scattering and bending in the geomagnetic field. The magnetic field is treated as a dipole field with strength and dip angle appropriate for the observatory location[1]. The model for the Earth's atmosphere is a fit to the "U. S. Standard Atmosphere, 1976" [114, 111] that sub-divides the atmosphere into three regions, and for each region assumes a different exponential relation between the density and the altitude.

A particle is followed till it interacts, decays, goes below the observatory altitude or loses sufficient energy to fall below the threshold for Cherenkov light emission (see,

[1]Mt. Hopkins, in our simulations

Eq. (3.11)). The program handles various particle types that have different interaction processes. Gamma rays can Compton scatter or pair produce. Electrons and positrons undergo bremsstrahlung. Charged pions and kaons can interact or decay, while the neutral ones are assumed to immediately decay. Protons and neutrons can interact while neutrinos and anti-neutrinos are discarded.

Various initial quantities can be specified in an input file. These include the primary particle type, its energy and initial direction cosines, the depth of the injection point and that of the observatory, the maximum segment thickness and switches for the processing of different types of particles. Also, it is possible to specify that the primary particle energy be chosen from a spectrum in a given energy range and to have its arrival direction distributed randomly in azimuth. The output from the program is a segment-by-segment list of various appropriate quantities, e.g., particle type, energy, initial and final directions, etc. In our simulations, the primary particle is injected at a depth of 5 g/cm^2 and the observatory is located at a depth of 763 g/cm^2 (corresponding to 2307 m, the altitude of the Whipple Observatory). The maximum length of a segment of a particle track is set at 0.01 electron radiation lengths (7.4 g/cm^2). The threshold for Cherenkov light emission, below which particles are no longer tracked is taken to be 25 MeV. The magnitude of the magnetic field is 0.5 G and the dip angle is 30°, appropriate for the position of Mt. Hopkins.

4.2.2 Cherenkov light simulation

The second program is written in C and models the emission of Cherenkov light by charged particles above the Cherenkov energy threshold. For each output segment from the cascade program, Cherenkov light is generated if the particle energy at the midpoint is above the Cherenkov threshold. The number of Cherenkov photons to be generated is calculated as a Poisson deviate with mean given by the Jelley formula (see Eq. (3.10)). Each photon is emitted at the Cherenkov angle appropriate for the refractive index of the atmosphere at that altitude. The point of emission along the particle track in the segment is chosen randomly, as is the azimuthal angle with respect to the particle track. The photon is also assigned a random wavelength in the chosen Cherenkov wavelength band.

The pressure-density scaling for the model atmosphere used here is identical

to the one in the cascade program. The atmospheric transmission probability for a Cherenkov photon of a given wavelength is calculated using a set of optical extinction coefficients derived by Sembroski [64] using information taken from Valley [113]. An up to date reference for extinction coefficients can be found in Jursa [62]. The effect of atmospheric absorption is taken into account only approximately, in that it is assumed to reduce the intensity of the observed Cherenkov light but not affect the angular spread; a simulated Cherenkov photon can be absorbed in the model atmosphere, but its propagation direction is not altered by the atmosphere. Also, the speed of propagation of the Cherenkov photons in the atmosphere depends on the refractive index, which varies with altitude. This is not taken into account in our simulations, so that the arrival times of the photons at the observatory level are inaccurate. This loss of accuracy is not an issue for us, as we do not use the photon arrival times, but might be important, e.g., for a detector that precisely times the arrival of the signal in order to measure wave front curvature.

A large fraction of the computational time is spent in tracking each individual Cherenkov photon to the observatory level. In order to save time, it is possible to apply various detector dependent absorption factors at the outset. Thus, a wavelength dependent mirror reflectivity and PMT quantum efficiency can be applied along with the atmospheric absorption, to estimate the fraction of the generated Cherenkov photons in a given wavelength band that are likely to survive. Then the program needs to track only that fraction of the photons. This reduces the number of Cherenkov photons to be tracked by a factor of eight to ten. An alternative approach is to track only a constant fraction of the Cherenkov photons, independent of wavelength. As long as this fraction is greater than the combined effects of atmospheric absorption and detector efficiency at any wavelength, no error is introduced. This approach has the advantage that it allows the application of different detector efficiencies, say for a different type of PMT, to the same set of simulations. We have used both approaches without noticing a significant difference in the final results.

There is also provision in the program to displace the shower core from the detector position. This can be used to place the shower cores for a succession of simulated showers at a fixed distance from the detector, or to scatter them uniformly over a specified area centred about the detector. Care is taken to ensure that this is

done properly for both vertical and non-vertical incidence of the primary particle.

As this program reads a segment-by-segment record of the simulated cascade process, it is also possible to build a profile of the cascade in terms of quantities like the numbers of the various types of particles and their lateral and angular distributions as a function of depth and energy, the track length integral for charged particles, the lateral and angular distribution of Cherenkov light and so on. These quantities are of interest in themselves and can also be used to cross-check the results of the Monte Carlo simulations against average numbers obtained from numerical integration or from analytic calculations applicable in the appropriate energy regimes.

In our simulations, we have assumed a Cherenkov wavelength band of 185 nm to 685 nm, encompassing the range of wavelengths where there is significant atmospheric transmission and detector response. By reference to the formulae in Eq. (3.6) and Eq. (3.10), we see that the Cherenkov angle and the number of photons produced are both dependent on the refractive index of the atmosphere, which varies with wavelength. However, there is only a weak dependence on the wavelength, and to a good approximation, these can be calculated at a single, representative wavelength. We have chosen a wavelength of 400 nm, which is approximately the wavelength where the detector response is peaked. A detector radius of 5.2 m, slightly wider than the Whipple 10-meter telescope, is used in deciding which photons are to be kept. When using the second strategy of tracking a constant, wavelength-independent fraction of the generated Cherenkov photons, we retain 35 % of the photons. The final output is a list of photons for each simulated shower. The shower record that separates one shower from the next provides information about the position of the shower core with respect to the detector, the initial direction cosines of the primary particle etc. Each photon record contains all relevant information about that Cherenkov photon, such as its position, arrival direction, wavelength, altitude of emission and type of particle that generated that photon. All Cherenkov photons hitting the detector are retained in the output file, irrespective of their arrival directions.

4.2.3 Model of the 10m detector

The third program models the detection of Cherenkov light by the 10-meter detector of the Whipple Observatory (see 3.3). It takes each simulated Cherenkov

photon and ray-traces it through the mirrors to the PMT array. Each mirror is treated as a spherical surface for the purposes of ray-tracing. This neglects the faceted nature of the reflector, but is a fairly good approximation as the individual hexagonal facets overlap each other slightly, so that the gaps between them are negligible. Both global mirror aberrations and individual facet aberrations are taken into account. (See 3.3.1 for a discussion of the optical properties of the reflector.) Mirror reflectivity, and PMT quantum efficiency are also applied at this stage. The assumed mirror reflectivity is tuned to the observation epoch being considered, while the quantum efficiency is taken from the manufacturer's curve for a Hamamatsu 1398 UV glass tube.

Simulated night-sky noise, arising from fluctuations in the sky brightness is added, as is signal noise arising from the non-Poissonian counting statistics in the PMT's. Tube gains are assumed to be unity, which closely approximates the relative tube gains from the data. Pedestals are ignored, as in the simulations this would just involve adding and subtracting a constant to the tube counts. The effect of the pedestal variances is lumped together with the night-sky noise. A conversion factor is also applied to scale photoelectrons to ADC counts, thus compensating for the combined effects of cable losses and amplifier gains. Finally, a trigger condition is applied, which is usually of the form of a fixed threshold (in digital counts) that must be exceeded by at least two of the inner 91 tubes. The exact numbers used for quantities like the noise variances, photo-electron to digital count conversion factor, trigger threshold, etc. are derived from the data (see 3.4).

The natural coordinate system for the cascade program and the Cherenkov light generating program is one with the z-axis along the zenith direction and the x and y axes defined by the direction of the geomagnetic field. However, for the detector program, the intuitively appealing coordinate system is one with the z-axis along the optic axis and the x and y axes defined by the positions of the PMT's in the focal plane. Hence, the detector program needs to translate between these two coordinate systems. To visualize the problem, imagine a primary particle that is incident at an angle to the zenith and consider the difference in the image formed by a reflector pointed vertically upwards and an image formed by a reflector pointing along the incidence direction of the primary particle.

The program also allows for the arrival directions of the simulated particles to be

randomized over the field of view of the PMT array. This would be appropriate, for example for simulating background cosmic-ray showers that do not have a preferred arrival direction. It is sufficient to do this randomization at this final stage rather than in the entire cascade process as the detector field of view is small (approximately 4° by 4°).

The final output for each simulated shower is a list of counts registered in each channel, in a format similar to the processed data files, so that both Monte Carlo files and data files can be fed through the same image cleaning and parameterization programs.

4.3 Various kinds of simulations

At the operating energies of the Whipple 10-meter detector, the gamma ray flux from a source like the Crab nebula is swamped by the isotropic background of cosmic rays. Typically, the ratio of the fluxes of gamma rays to cosmic rays is one to several hundred. Thus, in order to understand the detector background, one must also simulate air showers initiated by cosmic rays.

The simulation of cosmic ray air showers presents several difficulties. Firstly, it entails modelling of nuclear interaction processes, which in some cases, are not fully understood. This means that the simulation of hadronic showers is more problematic than that of gamma ray showers which are almost entirely electromagnetic in this energy range.

Another difficulty is computational in nature. Consider the composition of cosmic rays above about one TeV (the nominal threshold of the Whipple 10-meter telescope for proton initiated showers). From calculations using the spectra of various cosmic ray components [106]; above a threshold of about 1 TeV cosmic ray particles are approximately 45 % protons, 25 % helium-type nuclei, 15 % oxygen-type nuclei and 15 % iron-type nuclei. Thus, in order to study the background it is not sufficient to simulate only protons—one must also simulate heavy nuclei. In the approximation of simple superposition, each high energy nucleus is treated as a collection of nucleons with the total energy, on the average, equally divided between all constituent nucleons. Thus, the simulation of one shower initiated by an iron nucleus of a given

energy is equivalent to fifty-six simulations of proton initiated showers! This is a significant increase in the computational time needed, even if we take into account the fact that the energy per nucleon is correspondingly reduced. Gaisser and others [40, 32] have suggested that a more accurate picture of air showers initiated by heavy nuclear primaries is provided by using nuclear fragmentation cross-sections rather than simple superposition. As a primary heavy nucleus incident on the atmosphere typically breaks up into a smaller number of fragments than the number of nucleons, this somewhat mitigates the computational difficulties. On the other hand, the knowledge of the fragmentation probabilities is far from complete.

Also, one has to distribute the arrival directions of simulated cosmic ray showers over all possible orientations in the field of view of the detector in order to model the isotropic nature of the cosmic ray flux. As the Cherenkov light in these showers is less concentrated than for gamma ray showers, this means that often the simulated showers do not trigger the detector. Hence in order to get a significant number of triggering simulated showers one has to start out with a larger sample, again increasing the computational time requirements.

One of the current areas of active effort in ground based gamma ray astronomy is the push to lower energies. As already noted, above about 200 GeV, the background for an imaging atmospheric Cherenkov detector like the Whipple 10-meter is mainly the Cherenkov light from electrons and positrons in hadronic showers. Below that however, the dominant background is the Cherenkov light from relativistic muons in hadronic showers, that survive long enough to come close to the detector. Hence, in order to understand the low energy behaviour of the detector one must also ensure that the muon production in the simulations is working correctly, or else simulate the effect of Cherenkov light from muons using experimental muon spectra. This example also serves to illustrate the present incomplete understanding of the cascade processes, as there is a discrepancy between the theoretical and observed muon numbers in hadronic showers (see, for example, Gaisser [41, esp. chap. 16]). This might be explained in terms of a increase with energy in the cross-section for the production of pions in the collision between an air nucleus and an incident high-energy hadron, and in the increase with energy of the inelasticity [2] into pions for a nuclear target.

[2]Here, the inelasticity is defined as the fraction of the total energy *not* carried

Both of these enhance pion production and consequently, muon production in the cascade. It is also possible that the primary composition of cosmic rays at higher energies is richer in heavy nuclei, which would also lead to increased numbers of low energy muons in hadronic cascades.

More surprisingly, there are some indications [99, 30] of muon-enhanced signals from point sources, i.e., from air showers initiated by uncharged particles, most likely gamma rays. This is much more problematic to explain as, even an order of magnitude increase with energy in the muon photoproduction cross section might not be enough to explain this enhancement (again see, Gaisser [41, chap. 16, pg. 247]).

4.4 Databases used in this work

This section describes the different types of databases used in this work. These cover the different kinds of particle simulations discussed in the previous section—presently, we have simulated only protons and gamma rays.

When simulating the response of an atmospheric Cherenkov detector, it is possible to adopt two broad strategies. In the first and more usual approach, the detector is placed at the origin and the shower cores are scattered uniformly in area around it, out to a specified maximum radius. Also, the energy of the primary particle is drawn from a power-law spectrum. The advantage is that this approach corresponds closely to the working of an actual telescope and it is straightforward to relate the simulation derived parameters to those from the actual data. The drawback is that, since a large fraction of the area is at the outer perimeter, most of the simulated showers are at large impact radii and the sampling of nearby showers might be incomplete. Also, the power-law spectrum usually has a steeply-falling index so that most of the simulated showers are of low energy and the high energy end is not properly investigated.

We have chosen a different approach which gives a better sampling of the entire range of impact radii and energies, though at the cost of additional computational time and added complexity in estimating parameters to compare to the data. Several discrete energies are chosen in the range of interest; and at each energy, a fixed number

---

away by the leading nucleon. Thus, for an inelasticity of 0.7, the leading nucleon gets 30 % of the total energy.

of showers are simulated at each of several discrete impact radii. To save time, fewer showers are simulated at the highest energies.

Initially, only showers with the primary particle vertically incident were simulated. This was done mostly for convenience, it is easier to set up the detector coordinates and simpler to calculate quantities like effective detector area. However, in the data, the primary particle is incident non-vertically (for example, the average elevation of the Crab nebula in the 1988-89 database is about 70°). Therefore, we have also built a set of non-vertical shower simulations to investigate the zenith angle effect.

There are four databases used in this work, three are of gamma ray showers and one is of proton showers:

1. *Gamma ray showers at fixed energies, impact radii:* These form the main set of simulations from which we derive the extended supercuts and other quantities of interest. The simulations are done at several fixed primary energies, ranging from 0.05 TeV to 20 TeV. At each energy step, showers are simulated at each of several different impact radii, ranging from 0 m to 300 m in steps of 25 m. The number of showers at each impact radius ranges from is shown in Table 4.1. Later, when using the results of these simulations, we include appropriate weighting factors for the impact radius and for the primary energy. All showers in this set are initiated by vertically incident gamma rays.

2. *Gamma ray showers, distributed uniformly in area and with a built-in spectrum:* This a set of about 20,000 simulated gamma ray showers that are distributed uniformly in area out to a maximum radius of 250 m. The primary energy is drawn from a power-law spectrum with a differential index of -2.4, from 0.10 TeV upwards. It is also possible to get a different spectral index by thinning the showers either at the high energy or low energy end. This set of showers is used mainly as a check to see that the weightings in the main database have been done correctly, and that we can reliably extract the built-in spectrum using the main database. This is discussed later 5.1. In this set also, the primary gamma ray is always vertically incident.

3. *Non-vertical gamma showers:* This is a set of about 50,000 simulated gamma ray

Table 4.1: Number of simulated showers at each primary energy and impact radius

	Impact radius (m)												
Energy (TeV)	0	25	50	75	100	125	150	175	200	225	250	275	300
0.05	500	500	500	500	500	500	500	500	506	500	500	500	500
0.10	500	500	500	500	506	500	500	500	500	500	500	500	500
0.15	500	500	655	500	500	500	500	500	500	500	500	500	500
0.20	500	500	500	500	500	500	490	500	500	500	500	500	500
0.25	600	566	500	500	500	500	530	500	595	493	500	500	509
0.30	500	500	500	500	500	500	500	500	502	500	500	575	900
0.35	150	150	150	150	150	150	150	150	150	150	150	150	150
0.40	150	150	150	150	150	150	192	150	157	150	150	150	150
0.45	150	150	150	150	150	147	150	150	150	150	150	150	150
0.50	150	150	150	150	150	150	239	150	150	150	150	150	150
0.60	75	75	75	75	75	75	125	75	75	75	75	75	75
0.70	75	75	75	75	75	75	75	75	75	75	75	75	75
0.80	75	75	75	75	75	75	125	75	75	75	75	75	75
0.90	75	75	75	75	75	75	75	75	75	75	75	75	75
1.00	75	75	75	75	75	75	75	75	75	75	75	75	75
1.20	40	40	40	40	40	40	40	40	40	40	40	40	40
1.40	40	40	40	40	40	40	40	40	40	40	40	40	40
1.60	40	40	40	40	40	40	40	40	40	40	40	40	40
1.80	40	40	40	40	40	40	40	40	40	40	45	40	40
2.00	40	40	40	40	40	40	40	40	40	41	40	38	40
2.50	45	45	45	45	45	45	45	45	45	45	45	45	25
3.00	45	45	45	45	45	45	45	46	45	45	45	45	45
3.50	63	45	65	45	45	45	45	45	45	45	45	45	45
4.00	45	45	46	45	50	63	45	45	47	45	45	45	45
5.00	48	48	48	48	48	48	48	48	48	48	48	48	48
6.00	48	48	48	68	48	48	48	48	48	48	48	48	48
7.00	3	3	3	48	39	3	34	48	48	47	48	48	48
8.00	3	3	3	48	48	32	48	48	29	48	46	48	45
10.00	4	4	4	49	49	19	49	49	26	49	49	49	24
12.00	5	5	5	26	15	10	39	17	5	25	25	16	9
15.00	5	5	5	25	25	11	25	17	5	25	25	12	10
20.00	4	5	5	25	25	19	25	25	9	25	23	15	14

showers that is used to investigate zenith angle effects. The showers here are also distributed uniformly in area out a radius of 250 m and have a built-in power-law spectrum with a differential index of -2.4. The primary particle is incident at a zenith angle of 20° which corresponds to the average elevation of the Crab nebula data. The arrival direction of the primary particle is randomized in azimuth. Strictly speaking, the arrival directions of the simulated showers should also be confined to the azimuthal position of the source. This might make a difference, for example if the geomagnetic field had a significant effect on the development of the cascade and consequently, on the shape of the Cherenkov light images. However, we do not see any significant variations in image shape with azimuth, and hence we have used all these simulated showers irrespective of arrival direction. At a later date, we might supplement these with non-vertical showers at still lower elevations.

4. *Cosmic ray showers:* At present, the only background cosmic ray showers that we can simulate are those initiated by protons. Though only about half of the cosmic ray showers above our operating threshold are from protons, it is expected that the proton showers form a significant fraction of those that actually trigger the telescope. We have a set of about 15,000 of these proton showers, distributed uniformly in area out to a radius of 225 m, and having a built-in power law spectrum with a differential index of -2.65, from an energy of 0.3 TeV upwards. These are used to compare with the cosmic ray images taken from the data. Ultimately, with a full set of helium and heavy nuclei simulations we aim to use these to measure the spectrum of cosmic rays as observed by our telescope. Also, a thorough understanding of the background will enable us to use a maximum likelihood method to extract the spectrum of gamma ray sources.

4.5 Extended supercuts

This section describes, in detail, the development of the so-called extended supercuts (the name derives from the fact that it is based upon the standard supercuts technique, but improves upon it at high energies). We shall assume that we start

with a set of simulations at discrete energies and impact parameters, as in the main database. Also, it is assumed that the detector-dependent quantities are already correctly applied using numbers derived from the data. Later, I shall consider the effect of systematic uncertainties arising from the imperfect knowledge of some of these quantities 6.2.1.4.

4.5.1 Energy dependence of the Hillas parameters

The Hillas parameters characterize the images formed in the focal plane of the camera by Cherenkov light in extensive air showers. (See Appdx. B, for a description and a geometrical interpretation of the Hillas parameters. It has been understood for quite some time that the Hillas parameters should have a dependence on the energy of the shower. In terms of directly observed quantities, this translates to a dependence on the total amount of light seen in the shower. Physically, it is easy to understand this dependence from the fact that as the energy of the primary particle increases, it is more likely to penetrate deep into the atmosphere before it interacts. This means that shower maximum for the particle cascade occurs at a lower altitude—closer to the detector. Thus, the detector sees more light, and the parameters like width, and length that measure the extent of the shower tend to be larger. Another consequence is that the light from penetrating showers is seen by a larger number of tubes and at an intensity well above the noise threshold so that the shower axis is better defined and the image points better to the source location, i.e., alpha is smaller. Thus, it is to be expected that as the energy of the primary particle increases, the shape parameters get larger while the orientation parameter, alpha decreases.

Recall that the Monte Carlo database has simulations done at discrete energy steps and discrete impact radii. Also, the number of simulations done at each energy step were chosen somewhat arbitrarily, and do not reflect an energy spectrum. Thus, to find the energy dependence of the Hillas parameters, we must put in appropriate weighting factors to reflect the fact that the showers are not distributed uniformly over the area, and the fact that the primary energies are not drawn from a spectrum. Also, rather than finding the energy dependence, we find the dependence on the total number of counts registered in all selected ADC channels, henceforth denoted by n_{dc}. (I shall also refer to this quantity as the "total ADC counts," and it has been referred

to as "size" by other authors.)

Let us consider, in detail, the process of finding the energy dependence of some Hillas parameter—call it x. We take all the Monte Carlo showers that trigger the detector, and bin them by the total ADC counts, n_{dc}. For a given n_{dc} bin, we wish to calculate an appropriately weighted mean for the parameter x; such that the distribution of x, given n_{dc}, is identical to the distribution that would be obtained from showers scattered uniformly over the area and with primary energies drawn from a specified power-law spectrum. Each n_{dc} bin contains showers with different primary energies, E_i, and different impact radii, r_j. Hence, the contribution to the parameter mean from each shower must be weighted by the following factors:

1. the probability of obtaining the energy E_i from the specified power-law spectrum. For a differential power law of the form $dn/dE = \alpha E^{-\gamma}$, this probability is proportional to $E_i^{-\gamma}\,\Delta E_i$.

2. the probability of obtaining the impact radius, r_j. This is proportional to ΔA_j, where ΔA_j is the area of the annulus centred at r_j.

3. The probability of a shower with energy E_i and impact radius, r_j, triggering the detector, and ending up in that n_{dc} bin. This is given by:

$$\frac{\text{No. of triggering showers at } E_i, r_j}{\text{No. of showers simulated at } E_i, r_j} \times \frac{\text{No. of showers in that } n_{dc} \text{ bin at } E_i, r_j}{\text{No. of triggering showers at } E_i, r_j}$$

$$= \frac{\text{No. of showers in that } n_{dc} \text{ bin at } E_i, r_j}{\text{No. of showers simulated at } E_i, r_j} \tag{4.1}$$

Consider the k^{th} bin in n_{dc}. Let the total number of simulated showers with energy E_i and impact radius, r_j, be M_{ij}. Of these M_{ij} showers, let the number that end up in this bin be denoted by m_{ijk}. Then, the weighting assigned to a shower in this bin, with energy E_i and impact radius, r_j, is given by:

$$w_k\,(E_i, r_j) = E_i^{-\gamma}\,\Delta E_i\;\Delta A_j\;\frac{m_{ijk}}{M_{ij}} \tag{4.2}$$

Consider the parameter x. Let x_{kl} denote the value of the parameter for event l, in bin k. Then, the mean value of the parameter, in bin k, is given by:

$$\langle x \rangle_k = \frac{\sum\limits_l (x_{kl}\, w_{kl})}{\sum\limits_l (w_{kl})} \tag{4.3}$$

where, w_{kl} is given by Eq. (4.2). (I have added a subscript l, to indicate that it is the weight appropriate for event l, in bin k.) The summation is over all events in bin k. The sample variance, and the variance in the mean, in the k^{th} bin, are given, respectively, by:

$$s_k^2 = \frac{\sum_l w_{kl} \left(x_{kl} - \langle x \rangle_k\right)^2}{\sum_l (w_{kl})} \tag{4.4}$$

$$\sigma_k^2 = \frac{s_k^2}{n_{eff}} \tag{4.5}$$

where, n_{eff} is the effective number of events, given by:

$$n_{eff} = \frac{\left[\sum_l (w_{kl})\right]^2}{\sum_l (w_{kl})^2} \tag{4.6}$$

This method of calculation of the weighted mean and variance is taken from Lyons [76, pg. 13].

4.5.2 Functional fits to the parameters

In the previous section, we found the parameter means, and the errors in these for each of the n_{dc} bins. Given these, we proceed to find functional forms to fit the distributions. Fig. 4.1 shows the parameter distributions and the fits to these for each of the Hillas parameters, width, length, alpha, and azwidth, for the observing season 1988-89. Distance is almost independent of n_{dc}. The other parameters are all fit nicely by the same functional form:

$$\text{fit} = (\text{const.}) + (\text{const.}) \times \ln(n_{dc}) \tag{4.7}$$

Also, in line with our expectations, width, length, and azwidth all increase with n_{dc}, while alpha decreases, i.e., showers with more light are larger and point better. To give a feeling for the numbers involved, here are the parameter fits for 1988-89:

$$\begin{aligned} (\text{width}) &= -0.048 + 0.025 \ln(n_{dc}) \\ (\text{length}) &= 0.132 + 0.018 \ln(n_{dc}) \end{aligned}$$

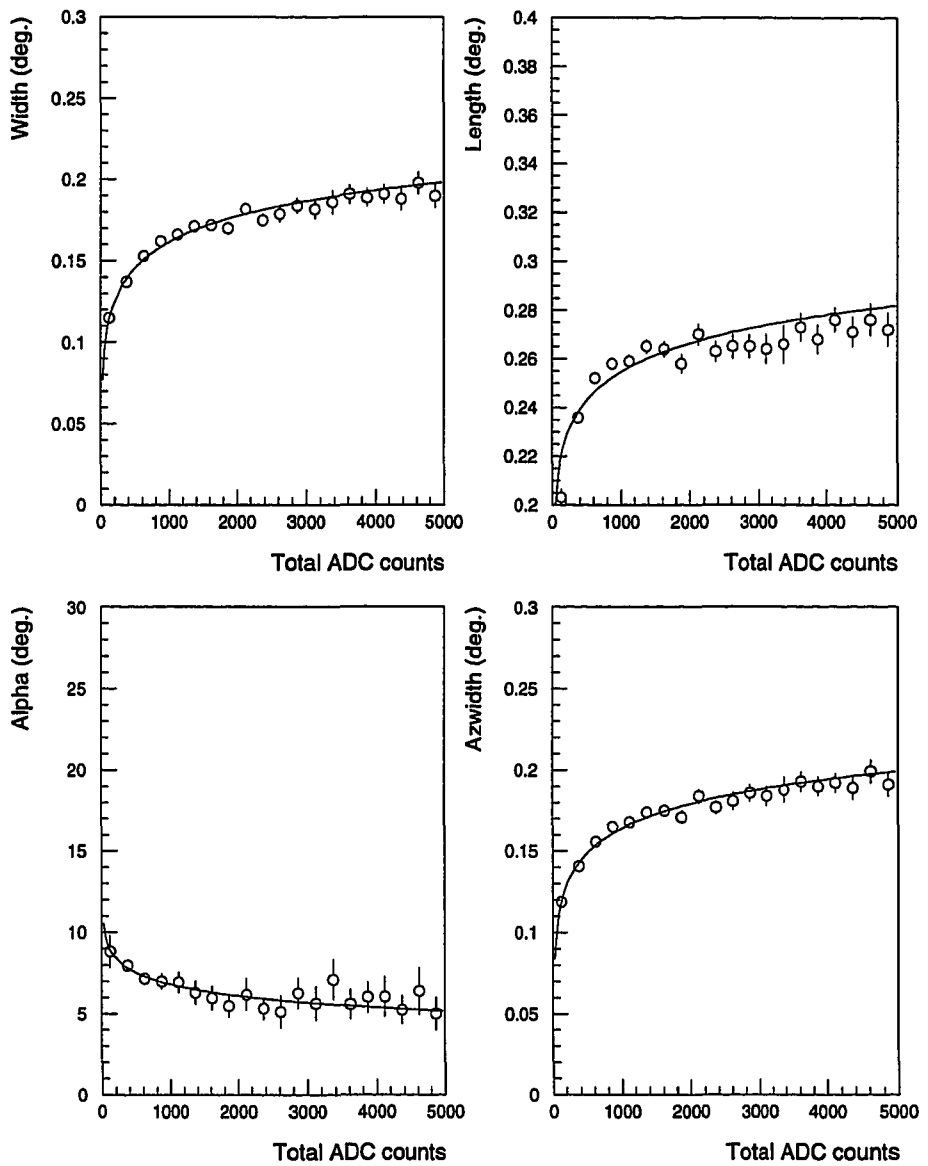

Figure 4.1: Energy dependence of the Hillas parameters.

$$\begin{aligned} (\text{alpha}) &= 12.65 - 1.05 \ln (n_{dc}) \\ (\text{distance}) &= 0.814 \\ (\text{azwidth}) &= -0.048 + 0.025 \ln (n_{dc}) \end{aligned} \tag{4.8}$$

Further, it should be noted that these fits do depend weakly on the assumed spectral index in the simulations [see sec. 4.5.1, esp. Eq. (4.2)]. The above fits hold for a power-law spectrum with a differential index of -2.5

Fig. 4.2 shows an example of how the parameter fits depend on the spectral index. The fits to width and alpha are shown for three different values of the index, ranging from -2.0 to 3.0. It is interesting to note that, in the case of width, at a given value of n_{dc}, the parameter mean increases with an increase in the magnitude of the spectral index, i.e., for a given amount of light, the width increases as the energy spectrum becomes steeper. Length and azwidth also exhibit similar behaviour, although they have not been shown here. The physical origin of this behaviour is that, for a given n_{dc} bin, the relative proportion of low energy showers grows with a steeper spectrum. For a low energy shower to have the same amount of light as a higher energy shower it must be closer to the detector, and the cascade must be further developed. Thus, the shape parameters, that measure the extent of the cascade, are larger for the low energy shower, and therefore, the mean width is larger for a steeper spectrum. Also, the centroid for the low energy showers is closer to the centre of the field of view, so that the axis is less well defined and alpha is, in general, larger.

Another point worth noting is that the general shape of the distributions do not change markedly with the spectral index, they are still well fit by the same functional form. As we shall see later, we define a passband for a given parameter that has the same shape as its functional fit. Thus the efficiency of the cut in the parameter, as defined by the passband, is fairly insensitive to the spectral index of the gamma ray source being studied.

Finally, it is remarkable that each parameter has a clear $\ln (n_{dc})$ functional dependence. It is tempting to speculate that this dependence is inherent in the cascade process itself, rather than being a detector artifact. While this has yet to be rigorously investigated, such a dependence might arise from the fact that the size of the observed Cherenkov light image depends on the degree of development of the shower

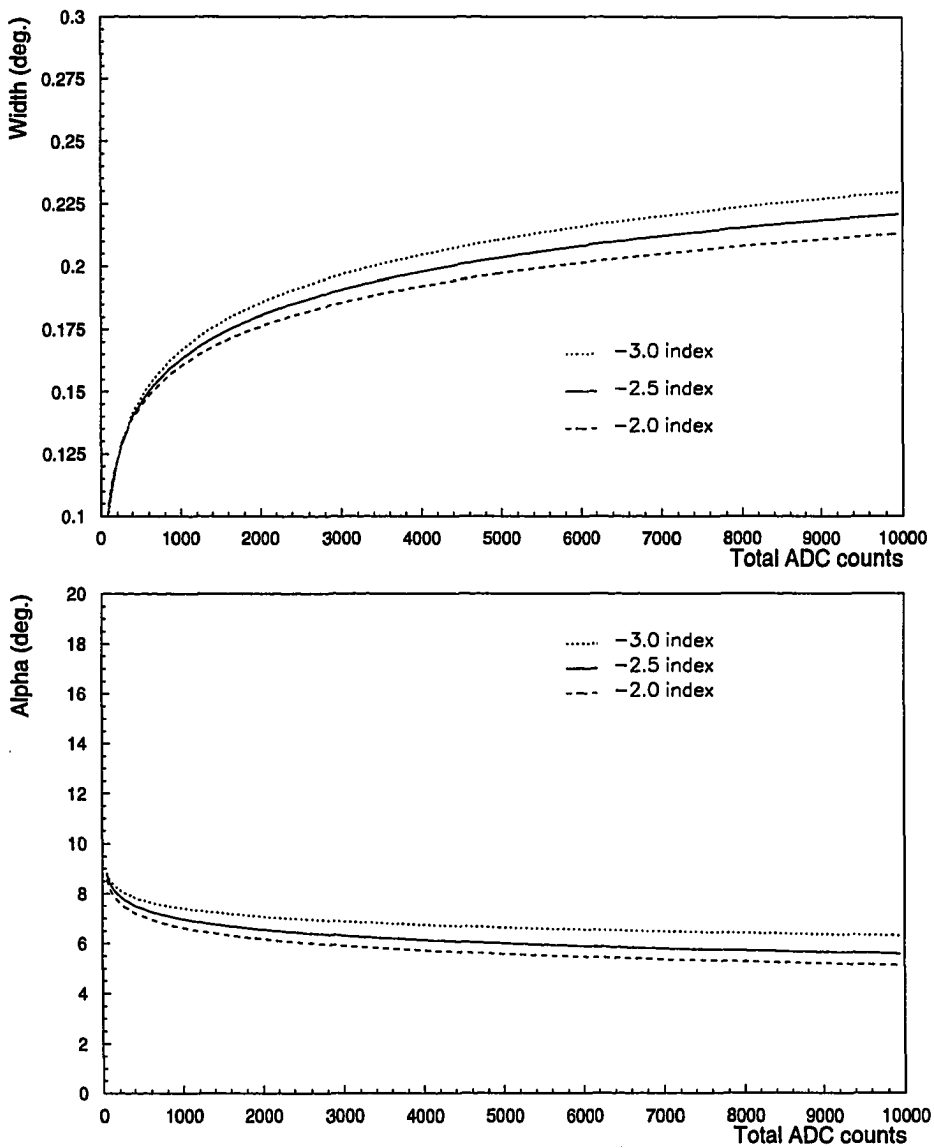

Figure 4.2: Variation of fit with spectral index.

which, in turn, depends on the depth in the atmosphere to which the primary particle penetrates. This depth of the first interaction scales as the logarithm of the energy of the primary particle. As discussed earlier (see Sec. [?]), the observed total ADC counts is a measure of the primary energy, so that the parameters that measure the extent of the shower can be expected to exhibit a logarithmic dependence on the total ADC counts.

4.5.3 Optimization of the cuts

The chief motivation in developing extended supercuts was to have a set of cuts that have an efficiency comparable to supercuts, without being biased towards preferentially selecting low energy showers. We use the same parameters as in supercuts; namely, width, length, alpha and distance. However, instead of having the passband independent of the total light, we shall allow it to scale as per the functional fits in the previous section. Thus, we look for a passband that has the same shape as the fit curve, i.e., at each value of n_{dc}, the upper and lower bounds of the band are just the fit curve shifted vertically.

In order to optimize the cuts, we need to define a quality factor that defines how good a particular set of cuts are in picking out a gamma ray signal from the background. A commonly used quantity is the so-called Q-factor, defined as the ratio of the efficiency of the cuts in selecting gamma ray showers to their efficiency in selecting background showers. With the efficiency, ε, defined simply as the fraction of showers passing the cut, this becomes,

$$\begin{aligned} Q &= \frac{\varepsilon_\gamma}{\sqrt{\varepsilon_b}} \\ &= \frac{\text{Fraction of gamma ray showers passing cuts}}{\sqrt{\text{Fraction of background showers passing cut}}} \end{aligned} \tag{4.9}$$

For the simulated gamma ray showers, the fraction passing, is weighted appropriately by the area and the energy spectrum. For the background, we use showers from the

OFF region of the data for the observing epoch that we are considering[3,4]. It is also possible, to consider the efficiency as a function of the total ADC counts, n_{dc}. In that case, the efficiency is defined to be the fraction of the showers in a particular n_{dc} bin that pass the cuts. To distinguish the two, whenever I refer to the n_{dc}-dependent efficiency I shall explicitly write it as $\varepsilon(n_{dc})$, with the corresponding Q-factor written as $Q(n_{dc})$.

The following procedure is used to optimize the position of the upper and lower bounds, with one parameter being optimized at a time:

1. To start with, the lower bound is held fixed at some assumed value, and the upper bound is allowed to vary. For each step in the upper bound, we calculate the efficiencies, ε_γ, ε_b, and the Q-factor. Thus, we build a plot of Q as a function of the position of the upper bound, relative to the fit curve. The peak of this curve defines the optimal position for the upper bound.

2. Next, the upper bound is held fixed at the optimal value and the lower bound is allowed to vary. As for the upper bound, ε_γ, ε_b, and Q are calculated, and the position of the lower bound chosen so that Q is maximized. This gives the optimal lower bound.

3. Finally, we iterate through the procedure, using the newly optimized value for the lower bound, rather than the initially assumed value. However, we have almost always found that the procedure converges in one iteration.

This procedure for optimizing the cut is illustrated graphically in Fig. 4.3 which shows an example of the steps in the procedure for the parameter, width. Fig. 4.3(a) shows the efficiencies and Q-factor as a function of the shift of the upper bound from the fit curve, with the lower bound held fixed at the initial assumed value. The position corresponding to the peak of the Q-factor curve is taken as the optimal

[3]The use of background from the data compensates for systematic changes over time, e.g., in camera configuration. It is not absolutely essential to use the OFF-source region. Other background data from the same period will suffice.

[4]It is also possible to use simulated background showers. We do not have an adequate set of these, at present.

position for the upper bound. This is marked by the solid vertical line in Fig. 4.3(a). Fig. 4.3(b) shows the same quantities for the lower bound, with the upper bound held fixed at the optimized value found in the first step. Fig. 4.3(c) shows the second iteration on the upper bound, with the lower bound now fixed at the optimized value from the second step. Note that the position of the optimal upper bound does not change, though Q increases slightly. In searching for a bound the step sizes used are, 0.002° for the width, length and azwidth, 0.02° for distance and 0.2° for alpha. The optimal positions of the upper and lower bounds, as found above, define the optimal set of extended supercuts. In order to maximize the retention of gamma rays, these bounds are relaxed so as to pass a minimum fraction of the simulated gamma ray showers[5] This relaxed set of cuts will be referred to as "loose extended supercuts." The positions of the bound for this set are indicated by the dashed vertical lines in Fig. 4.3.

Fig. 4.4 considers the n_{dc}-dependence of the efficiencies, for the parameter, width. Fig. 4.4(a) shows a two-dimensional histogram representation of $Q(n_{dc})$, as a function of both n_{dc} and the shift in the upper bound. Fig. 4.4(a) is a gray-scale color map, where the darker regions correspond to a higher value for $Q(n_{dc})$. (For easier visualization, the histogram is restricted to a smaller range in the upper bound.) Fig. 4.4(b) shows $Q(n_{dc})$ as a function of the shift in the upper bound, for three different n_{dc} bins, i.e., three slices through the two-dimensional histogram. Note that the optimal position of either bound is fairly independent of n_{dc}. Also, the maximum value of $Q(n_{dc})$ increases with n_{dc}, i.e., the cuts improve with energy! This leads to the interesting conclusion that the gamma-hadron separation in the Hillas parameters is actually greater at higher energies. Each parameter is separately optimized, as simultaneous optimization of several parameters is considerably more complicated, and a preliminary investigation seemed to indicate no significant improvement with simultaneous optimization.

Again, to give an idea of the size of the passbands in the various parameters, here is the set of loose extended supercuts, optimized for the 1988-89 Crab nebula

[5]This fraction is usually about 90 %.

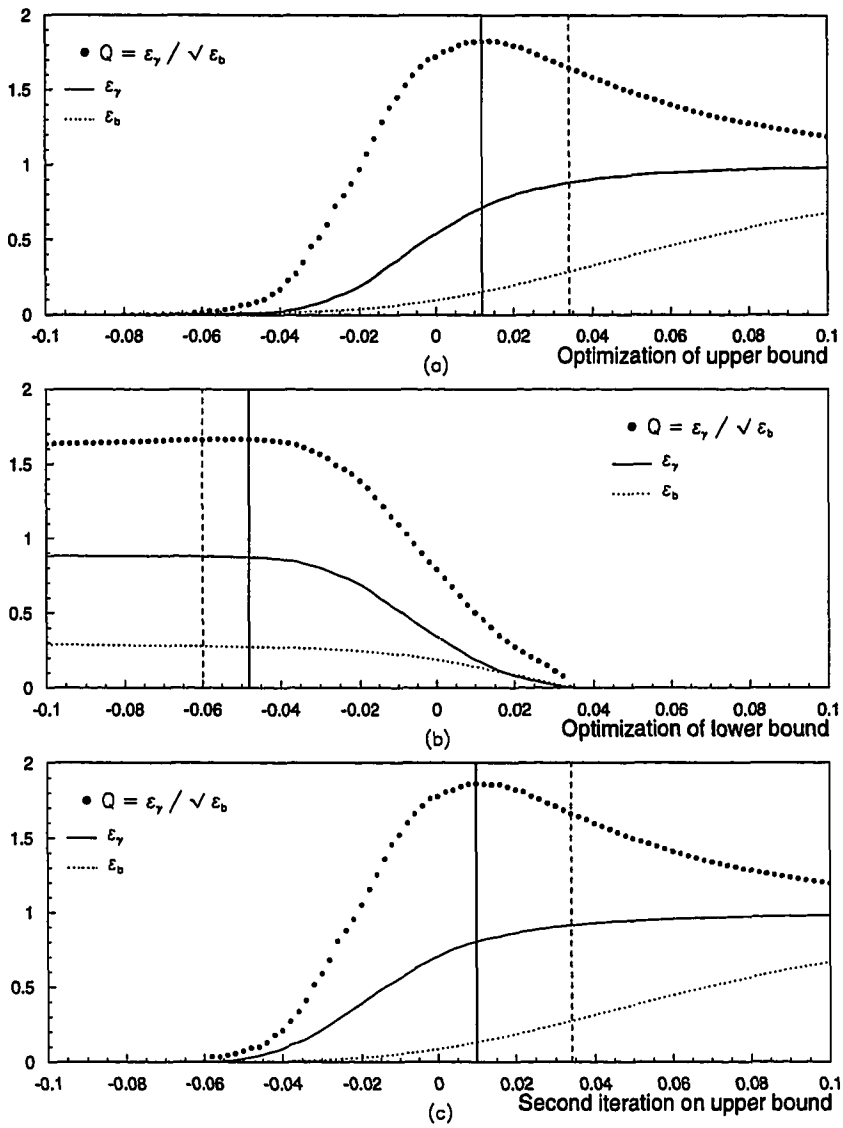

Figure 4.3: Steps in the optimization of the cuts on width. The positions of the bounds in each case are indicated by the vertical lines, the solid line being the optimal position and the dashed line the position of the loose bound.

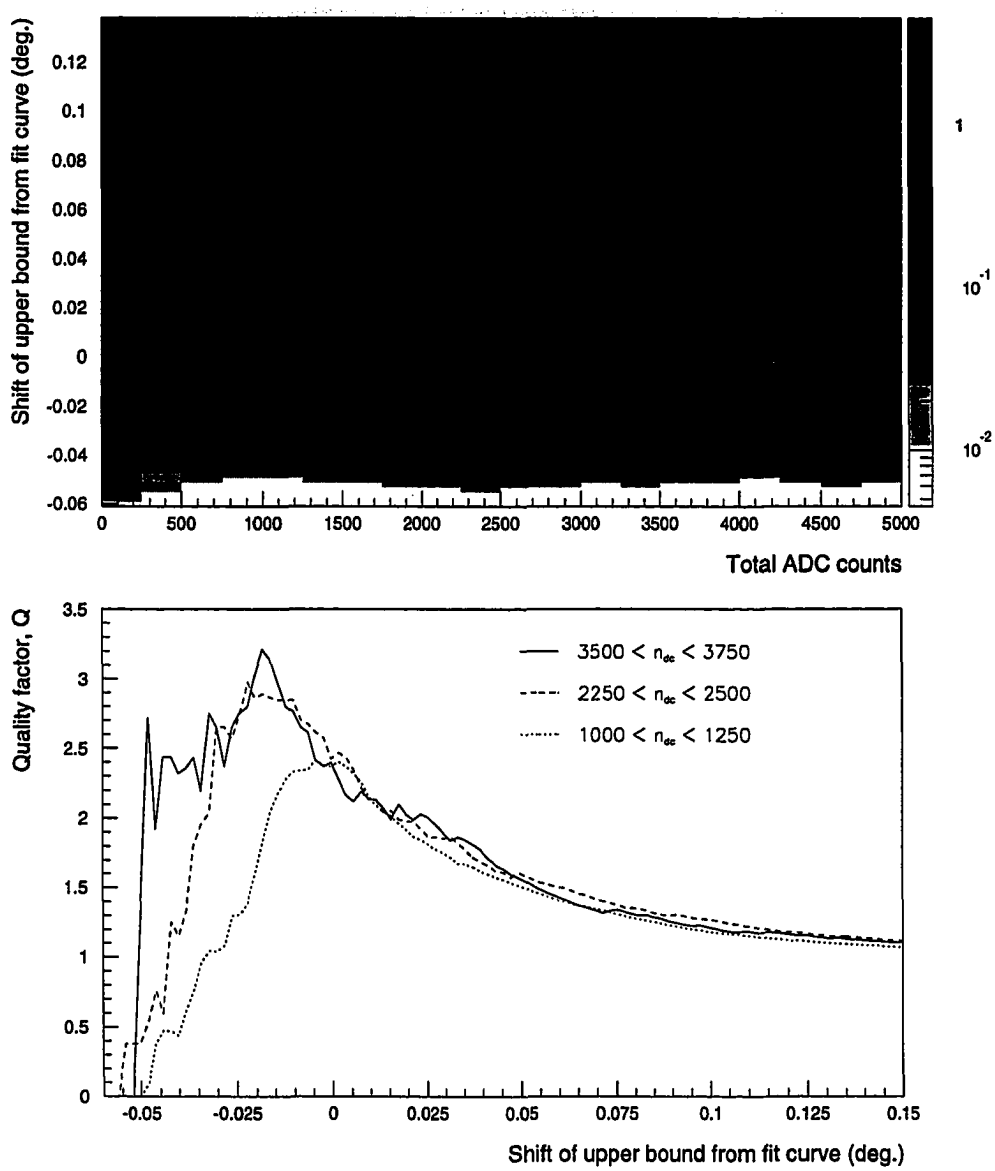

Figure 4.4: Dependence of the efficiency of the cut in width, on the total ADC counts.

database:

$$\begin{aligned}
[-0.011 + 0.025\ln(n_{dc})] - 0.060 < (\text{width}) &< [-0.011 + 0.025\ln(n_{dc})] + 0.034 \\
[0.124 + 0.019\ln(n_{dc})] - 0.090 < (\text{length}) &< [0.124 + 0.019\ln(n_{dc})] + 0.044 \\
(\text{alpha}) &< [11.09 - 0.60\ln(n_{dc})] + 8.4 \\
0.50 < (\text{distance}) &< 1.2
\end{aligned} \tag{4.10}$$

The expressions in the parentheses above are the functional fits to the parameters, as given in Eq. (4.8). They have been written in this form to emphasize the values of the upper and lower bounds. Fig. 4.5 compares these passbands for width, length, alpha, and azwidth with those for standard supercuts. Standard supercuts was derived directly from the 1988-89 Crab data, and it can be seen that there is good agreement between the two sets of cuts at low energies, where most of the showers are. However, the passbands are quite different at higher energies.

Below is the "extended azwidth" cut, that is *not* a part of extended supercuts. It might be used, for example, in selecting gamma ray showers for pulsar timing purposes, where the emphasis is on retaining as many of the gammas as possible.

$$[-0.003 + 0.024\ln(n_{dc})] - 0.064 < (\text{azwidth}) < [-0.003 + 0.024\ln(n_{dc})] + 0.038 \tag{4.11}$$

4.6 Effective area of detector

At the highest energies, an atmospheric Cherenkov detector can see showers more than 200 m away. The so-called detector area is the effective collection area it has for gamma ray showers. As some selection criteria must be applied to pick out gamma ray showers from the background, the detector area will depend on the set of cuts chosen. In particular, the detector area will be larger if the cuts are more efficient.

Again, we shall use the main database at discrete energies and impact radii. First, consider the question of finding the trigger area, i.e., the effective area for gamma ray showers triggering the detector in its normal operating mode, with no

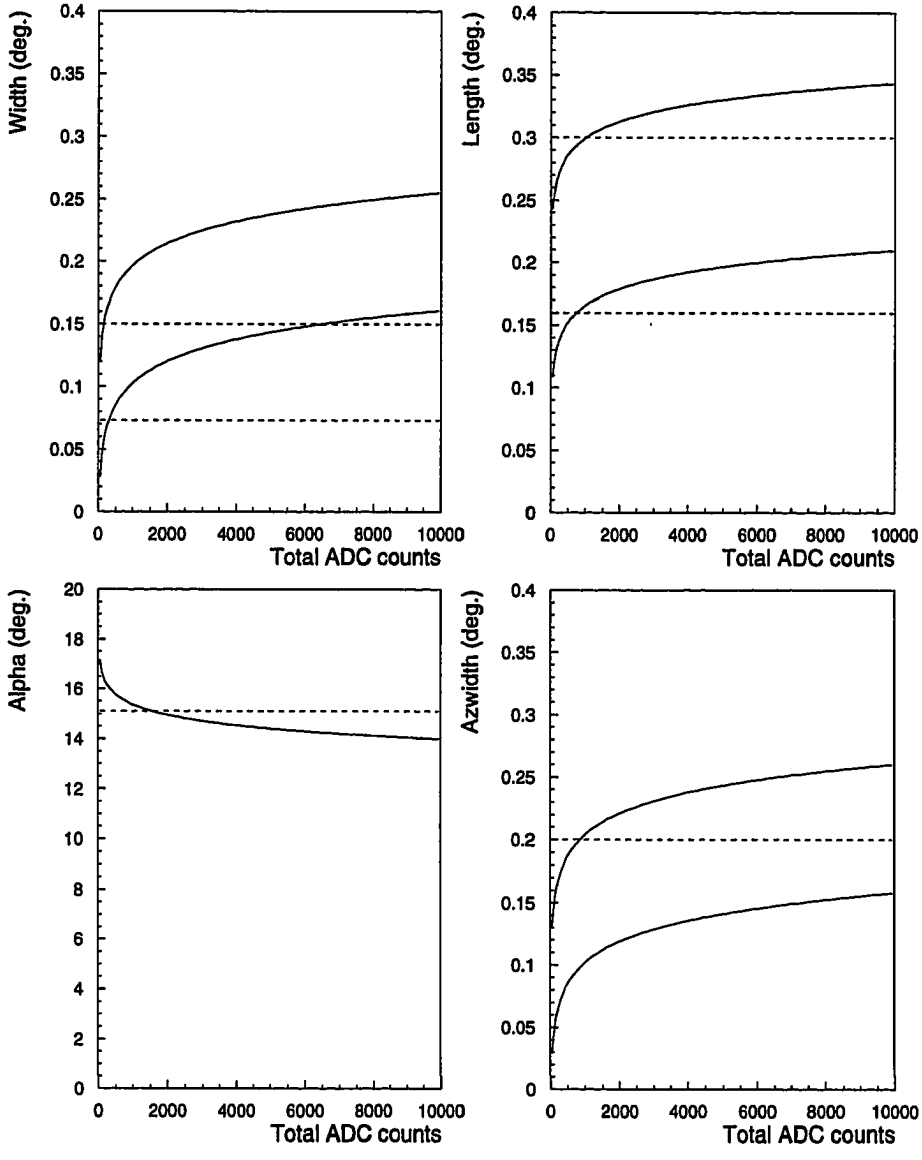

Figure 4.5: Comparison of loose extended supercuts (solid lines) with standard supercuts (dashed lines).

other selection applied. For a given energy and impact radius, we can consider each simulated shower to be drawn from a binomial distribution. Thus, the number of independent trials is equal to the total number of simulated showers at that energy and impact radius, and the number triggering gives the number of successes. Let the number of simulated showers at energy E_i and impact radius r_j, be denoted by M_{ij} and let the number triggering the model detector be m_{ij}. In particular, we shall be interested in the quantity $f_{ij} = m_{ij}/M_{ij}$, the relative number of successes in M_{ij} trials. For this quantity, the mean and variance are given by:

$$\mathcal{E}(f_{ij}) = \frac{1}{M_{ij}}\mathcal{E}(m_{ij}) = \frac{m_{ij}}{M_{ij}} \tag{4.12}$$

$$Var(f_{ij}) = \frac{1}{M_{ij}^2}Var(m_{ij}) = \frac{1}{M_{ij}}\frac{m_{ij}}{M_{ij}}\left(1 - \frac{m_{ij}}{M_{ij}}\right) \tag{4.13}$$

where, $\mathcal{E}[f_{ij}]$ denotes the expectation value of f_{ij}, and I have used the well-known formula for the variance of a binomial value (see, for example, Frodesen [38, pg. 67]). It is easy, to calculate the detector area and its variance, given f_{ij}, the relative number of successes. Viz.,

$$\begin{aligned} A(E_i) &= \int_0^\infty \frac{m_{ij}}{M_{ij}} 2\pi r\, dr \\ &= \sum_j \frac{m_{ij}}{M_{ij}} \Delta A_j \end{aligned} \tag{4.14}$$

$$\begin{aligned} Var[A(E_i)] &= \sum_j (\Delta A_j)^2\, Var\left(\frac{m_{ij}}{M_{ij}}\right) \\ &= \sum_j (\Delta A_j)^2\, \frac{m_{ij}}{M_{ij}}\left(1 - \frac{m_{ij}}{M_{ij}}\right) \end{aligned} \tag{4.15}$$

As earlier, ΔA_j is the area of the annulus centred at r_j. When using the detector area for the spectrum estimation, it is preferable to parameterize the area to smooth out fluctuations in the simulations.

The parameterized fit to the area, using trigger plus extended supercuts is shown in Fig. 4.6(a). Fig. 4.6(b) shows the parameterized fits to the effective area, for three cases: trigger only, trigger plus standard supercuts, and trigger plus extended supercuts. Also, the reflectivity, etc., are as appropriate for the 1988-89 observing

epoch. It is evident from the figure that, for retaining gamma ray showers, extended supercuts is comparable to standard supercuts at low energies and performs much better at high energies. for the 1988-89 database, the parameterized form for the collection area, using extended supercuts, is given by:

$$A(E) = 1.46 \times 10^4 \arctan\left(17.5 \times E^{3.83}\right) \ln(8.19 \times E) \exp(-E/27.4) \qquad (4.16)$$

Fig. 4.7 shows the simulated detector response using only the trigger criterion, for gamma ray showers drawn from a power-law spectrum with a differential index of -2.65, i.e., the same index as the background cosmic rays. This is obtained from the previous "trigger area" curve by folding in a power-law spectrum with a -2.65 spectral index. We define the threshold energy of the detector as the energy corresponding to the peak of this response curve. From the figure, the threshold energy of the detector for the 1988-89 epoch is estimated to be about 450 GeV. It should be mentioned that other, less conservative, definitions of the energy threshold are also used in the field of VHE gamma ray astronomy—such as the 50 % point or the 95 % point on the initial, rising part of the response curve.

4.7 Estimation of the primary energy

This section discusses the estimation of the energy of the primary particle from the observed image parameters. An increase in the primary energy leads to an increase in the number of particles in the cascade and thus increases the shower size. This also gives rise to a larger image and an increase in the amount of light seen. Thus, the energy reconstruction must use the total digital counts n_{dc} as a starting point. Another factor to consider is the impact radius of the shower core. For showers of a given energy, if the impact radius is smaller, the shower is closer to the detector and more light is seen. Though we cannot measure the impact radius directly with an atmospheric Cherenkov detector, it can be related to the parameter, distance. "Distance" measures the displacement of the shower centroid from the centre of the field of view, and thus has a rough correspondence with the impact radius.

Initially, we used only n_{dc} to reconstruct the primary energy. Later, we have also included distance in the energy estimate. This form of the energy estimate, $\tilde{E} =$

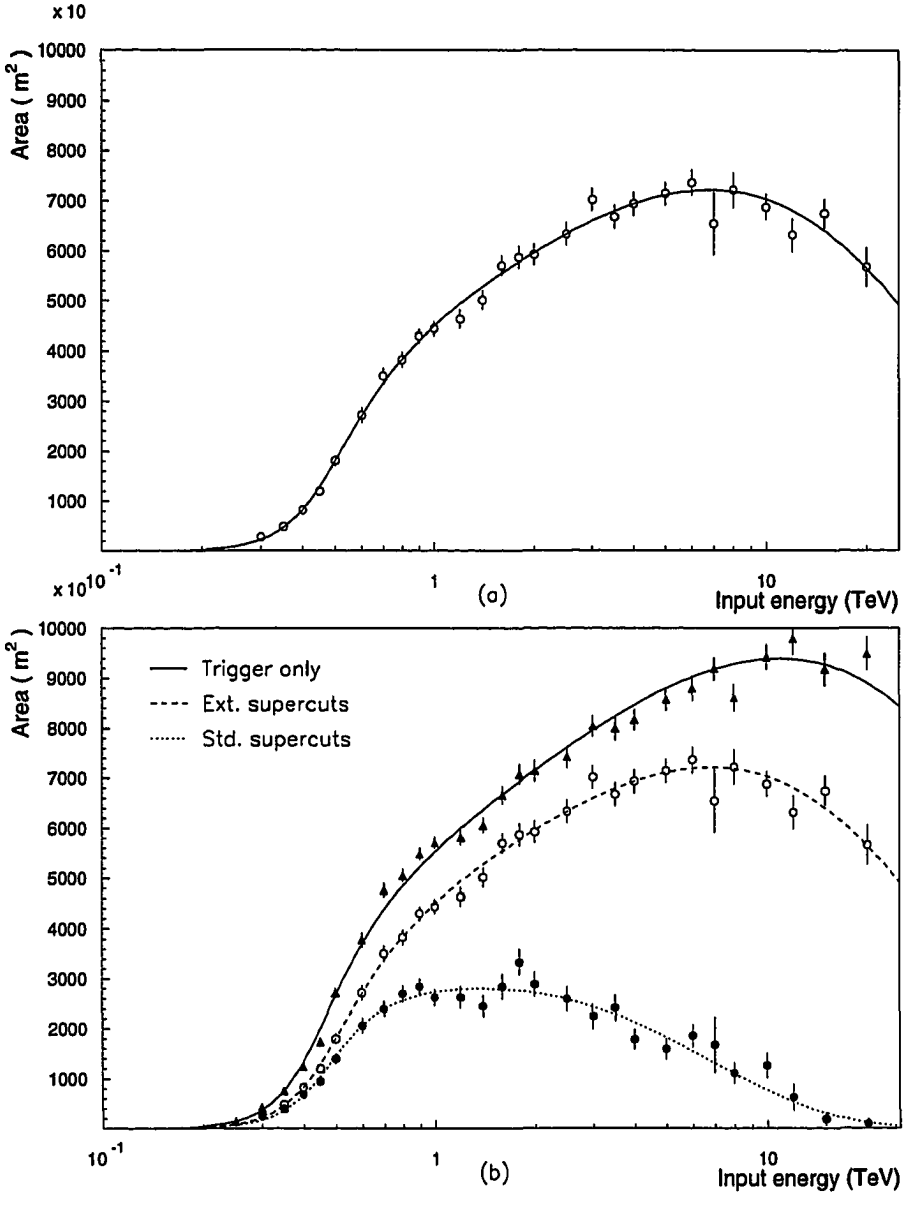

Figure 4.6: (a) Parameterized collection area for extended supercuts. (b) Comparison of the area for different selection criteria

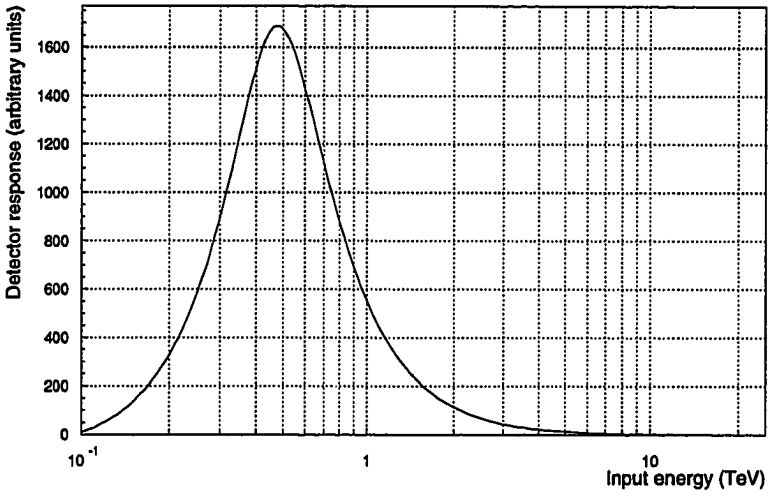

Figure 4.7: Threshold area for the detector

$\tilde{E}(n_{dc}, dis)$, has been suggested by Plyasheshnikov [86]. In this section, we present the energy estimate, both with and without distance included as a parameter, and show that the inclusion of distance does lead to a smaller scatter in the estimated energy. I shall refer to the known Monte Carlo input energy as E, and the reconstructed energy as $\tilde{E}$. When it is not clear from the context, I shall distinguish between the energy estimate with and without distance by explicitly including a functional dependence where needed, viz. , $\tilde{E}(n_{dc}, dis)$.

4.7.1 Estimate independent of distance

Here, I try to find a functional form for the energy estimate, using only the total ADC counts, n_{dc}. At each energy step, E_i, we calculate the average of the total ADC counts, n_{dc}, for all showers at this energy that have triggered the telescope *and* passed the extended supercuts selection. This averaging, of course, includes the appropriate weighting for the impact radius and for the probability of a shower of that energy triggering the detector and passing extended supercuts. Let M_{ij} denote the number of showers simulated at an energy E_i, and an impact radius r_j, and m_{ij} denote the

number that trigger the detector and pass extended supercuts. The weight assigned to a shower at energy E_i and impact radius r_j, would be:

$$w_i\,(r_j) = \Delta A_j \frac{m_{ij}}{M_{ij}} \tag{4.17}$$

Label the events at energy, E_i, by the index k, so that $(n_{dc})_{ik}$ denotes the total ADC counts for the event k at that energy. Then, similar to the calculations of the parameter means in 4.5.1, the average of the total digital counts is given by:

$$\langle n_{dc} \rangle_i = \frac{\sum\limits_k [\,(n_{dc})_{ik}\ w_{ik}\,]}{\sum\limits_k (w_{ik})} \tag{4.18}$$

where, w_{ik} is given by Eq. (4.17). (I have again added a subscript k, to indicate that it is the weight appropriate for event k.) The summation is over all events at energy E_i that trigger the detector and pass extended supercuts. The sample variance, and the variance in the mean, at energy E_i, are given, respectively, by:

$$s_i^2 = \frac{\sum\limits_k w_{ik}\,[(n_{dc})_{ik} - \langle n_{dc} \rangle_i\,]^2}{\sum\limits_k (w_{ik})} \tag{4.19}$$

$$\sigma_i^2 = \frac{s_i^2}{n_{eff}} \tag{4.20}$$

where, n_{eff} is the effective number of events, given by:

$$n_{eff} = \frac{\left[\sum\limits_k (w_{ik})\right]^2}{\sum\limits_k (w_{ik})^2} \tag{4.21}$$

By finding the average of the total ADC counts at each energy step, we get an idea of the average variation of n_{dc} with the energy. Fitting this function, using the means and variances calculated as above, gives us n_{dc} as a function of the input energy E. For the energy estimation function we use the inverse of this relationship. As an example, for the 1988-89 epoch, the relationship between n_{dc} and E is found to be:

$$n_{dc} = 3.46 \times 10^3 \arctan\left[0.0944\ (E + 0.683)^{1.48}\right] \tag{4.22}$$

which, when inverted, gives the desired energy estimation function,

$$\tilde{E}\,(n_{dc}) = -0.683 + 4.95\,\left[\tan\left(2.89 \times 10^{-4}\,n_{dc}\right)\right]^{0.677} \tag{4.23}$$

As an inverse trigonometrical function is being used for the original fit of n_{dc}, the solution for the estimated energy is not unique, and care must be taken to select the correct branch of the function. This complicated form for the energy estimation function is necessary in order to get a good fit to the simulations. This fit is shown in Fig. 4.8(a) for all simulated energies. Fig. 4.8(b) shows a comparison between the estimated energy obtained from Eq. (4.23) above, and the actual Monte Carlo input energies. The ideal curve, $E = \tilde{E}$, is also shown on the same plot as a solid line. Thus, we see that Eq. (4.22) gives a good fit, and the mean estimated energy is shown to be free of bias, at least to the highest energies[6].

4.7.2 Distance-dependent energy estimate

A shower of a given energy will, in general, produce more light if it is at a smaller impact radius, i.e., closer to the detector. Though we do not observe the impact radius directly, it can be related to the observed parameter, distance, which is a measure of the angular displacement of the Cherenkov light in the shower. The reason that there is a good degree of correlation between the impact radius and the distance is that most of the observed light is emitted by relativistic particles close to shower maximum. For a typical shower, this corresponds to a region that is only about a hundred metres thick, so that the Cherenkov photons are emitted at a fairly constant angle. Thus, the spatial extent of the observed Cherenkov light is closely related to the Cherenkov angle near shower maximum.

Fig. 4.9 shows the simulated lateral distribution of Cherenkov light, i.e., the density of Cherenkov photons as a function of distance from the shower core, for showers at three different energies, (i) 0.4 TeV, (ii) 1 TeV, and (iii) 5 TeV. The lateral distribution has a characteristic "volcano-like" shape, with the Cherenkov photon density being almost uniform within the rim, and falling off rapidly outside

[6]As the telescope threshold energy is estimated to be about 450 GeV, and the spectrum of all typical sources falls rapidly with energy, we are not too concerned about errors made in estimating energies above several TeV.

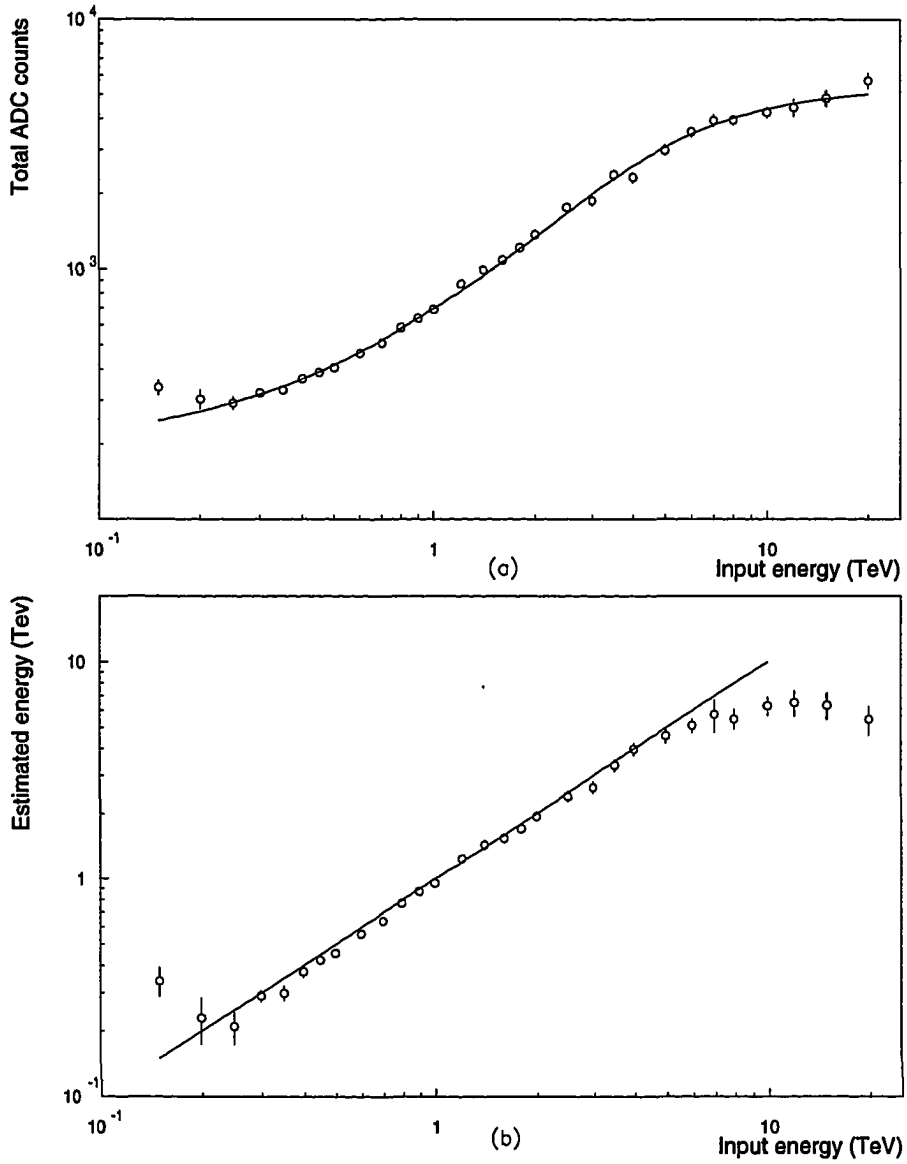

Figure 4.8: (a) n_{dc} fit used for the energy estimate. (b) The performance of the energy estimation function.

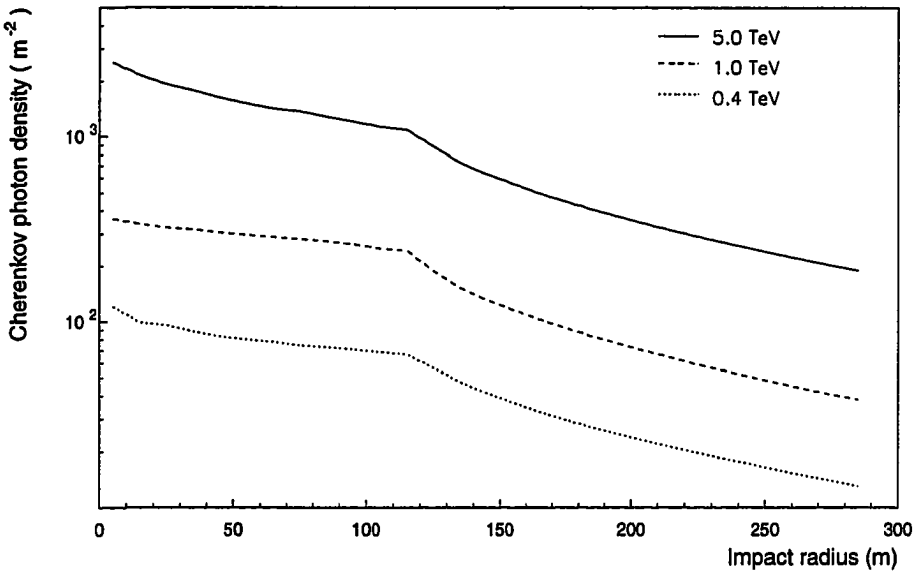

Figure 4.9: Lateral distributions of the Cherenkov light from simulated showers at different energies.

it. The rim of the volcano is at a distance of about 125 m, almost independent of the primary energy. From the discussion in sec. 4.6, the collection area of the detector extends out to a radius of about 50m, well within the volcano rim, at an energy of 0.4 TeV. At 1 TeV, the detector sees out to about 100m, whereas it is about 150 m at 5 TeV. Thus, as the primary energy increases, showers are detected out beyond the rim, where the light density decreases sharply with impact radius rather than being fairly independent of radius. This would mean that at larger energies, the observed light from the shower would also depend on the impact radius—besides the usual energy dependence. In terms of direct observables, this translates to a distance dependence of the total ADC counts, in addition to the normal energy dependence. Another point worth considering is that, by restricting the accepted range in the distance parameter, one might hope to sharpen the energy resolution. The obvious trade-off in doing this is that the detector area is decreased at high energies, as most of the showers there are at large distance values and would not be accepted. Finally,

it should be noted that at the highest energies, a typical shower might be truncated by the edge of the field of view. This is illustrated in Fig. 4.10 which shows the ADC counts registered by each tube in the image for (a) a 1 TeV shower, and, (b) a 20 TeV shower. For the 1 TeV shower, the image is clearly contained almost entirely within the camera, with no light in the outer ring of tubes. However, the 20 TeV shower image is clearly truncated by the edge of the camera. This truncation, if typical of the showers at that energy, could lead to their mis-identification as lower energy showers, and it then might be necessary to reject these showers by restricting the distance cut.

From the preceding discussion, it seems advantageous to put in a distance dependence, at least for the high energy showers. Also, it might be necessary to restrict the distance cut in order to reject incompletely sampled showers at the edge of the camera, and in order to improve the energy resolution. In this section, I describe the procedure use to add a distance dependence to the energy estimate. The question of restricting the distance cut is addressed in the data analysis chapter.

We follow broadly the same procedure as in the case where the energy estimate was based solely on the total ADC counts, n_{dc}. Thus we seek a fit for n_{dc}, based on the Monte Carlo input energy, E, and the Hillas parameter, distance. This should have the form:

$$n_{dc} = f(E)\, g(dis) \tag{4.24}$$

This separable form of the energy dependence and the distance dependence allows one to use the inverse of the equation to find the estimated energy. Viz.,

$$\tilde{E} = f^{-1}\left[\frac{n_{dc}}{g(dis)}\right] \tag{4.25}$$

Here are the steps used to find a distance-dependent energy estimate.

1. We start with the same fit of n_{dc} as a function of E, as in the distance independent case. This is as given by Eq.(4.22). Thus, we have:

$$n_{dc} = f^{(1)}(E) \tag{4.26}$$

2. Next we investigate the distance dependence of the quantity $n_{dc}/f^{(1)}(E)$, at each of the discrete simulated energy steps. This is shown in Fig. 4.11 for

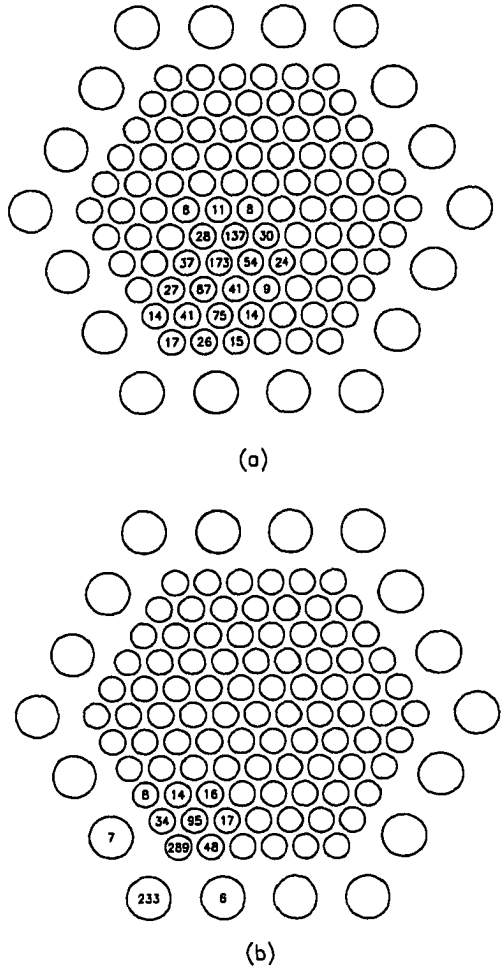

Figure 4.10: Simulated images for (a) a 1 TeV shower, and, (b) a 20 TeV shower, showing the truncation of the latter image by the edge of the camera

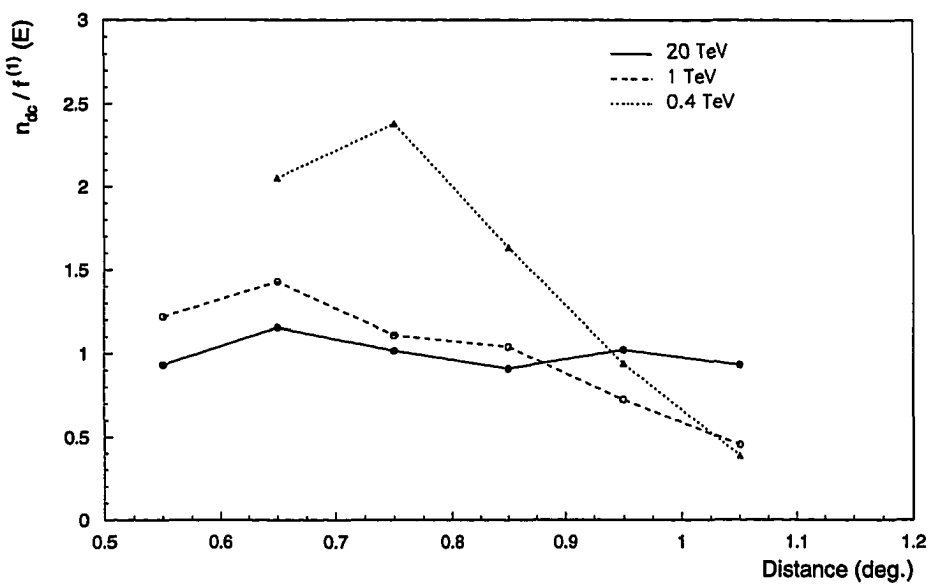

Figure 4.11: Distance dependence of the energy estimate.

three representative energies, 0.4 TeV, 1 TeV, and 5 TeV. As expected, there is a distance dependence only for higher energies. Thus, we obtain a fit to the distance dependence at higher energies, of the form:

$$n_{dc} = g\,(dis) \tag{4.27}$$

3. In the final step, we do a second iteration on the energy dependence, by fitting $n_{dc}/g\,(dis)$ to E, to get:

$$\frac{n_{dc}}{g\,(dis)} = f^{(2)}\,(E) \tag{4.28}$$

This procedure can be repeated over further iterations, but it usually converges at this point. Thus, the final form of the n_{dc} dependence on energy and distance is given by:

$$n_{dc} = f^{(2)}\,(E)\; g\,(dis) \tag{4.29}$$

which can be inverted to give the energy estimation function.

For the 1988-89 observing season, the final form of the fit for the total ADC counts, n_{dc} is given by:

$$n_{dc} = 8.61 \times 10^3 \arctan\left[0.0657\ (E + 0.459)^{1.35}\right] \times \exp\left[-\frac{(d-0.72)^2}{0.12}\right] \tag{4.30}$$

By inverting this we get the following form for the energy estimation function:

$$\tilde{E} = -0.747 + 6.43\ \left[\tan\left\{1.58 \times 10^{-4}\, n_{dc} \exp\left[\frac{(d-0.72)^2}{0.13}\right]\right\}\right]^{0.655} \tag{4.31}$$

Again, care should be taken to choose the appropriate branch of the trigonometrical function.

4.7.3 Mixed energy estimate

In the previous sections, we started out with a simple energy estimate, based only on the total ADC counts. Then, we discussed the need for including a distance dependence. The form of the fit for n_{dc} in terms of the energy, E, and the distance, dis, was given by:

$$n_{dc} = f(E)\ g(dis) \tag{4.32}$$

This separable form of the fit was necessary so that it can be inverted to obtain the energy estimation function. However, as we saw in the last section, the total ADC counts has a distance dependence only for high energy showers, so that the energy dependence and the distance dependence are not really separable.

To get around this difficulty, we can use what I refer to as a "mixed" energy estimate, which first uses an energy estimate based only on the total ADC counts. If the estimated energy comes to be greater than some minimum energy, $\tilde{E}_{switch}$, then a distance dependence is used, as per the discussion in the previous section. The minimum energy, $\tilde{E}_{switch}$ is chosen by examining the simulations to find the energy at which the total ADC counts start exhibiting a distance dependence (see Fig. 4.11).

For the 1988-89 season, the minimum energy $\tilde{E}_{switch}$ is found to be 0.9 TeV, and final form of the energy estimate is then given by:

$$\tilde{E} = \begin{cases} -0.683 + 4.95\ \left[\tan\left(2.89 \times 10^{-4}\, n_{dc}\right)\right]^{0.677}, & \text{if } \tilde{E} \leq 0.90; \\ -0.747 + 6.43\ \left[\tan\left\{1.58 \times 10^{-4}\, n_{dc} \exp\left[\frac{(d-0.72)^2}{0.13}\right]\right\}\right]^{0.655}, & \text{otherwise.} \end{cases} \tag{4.33}$$

Fig. 4.12 compares the estimated energy obtained from the mixed energy estimate in Eq. (4.33) above, to the Monte Carlo input energy. The solid line is the ideal energy estimate, $\tilde{E} = E$. The fit works well, and the mean estimated energy is free of bias over a wide range of energies. By comparison to Fig. 4.8(b), it can be seen that the roll-off evident at high energies in the distance-independent case has been avoided.

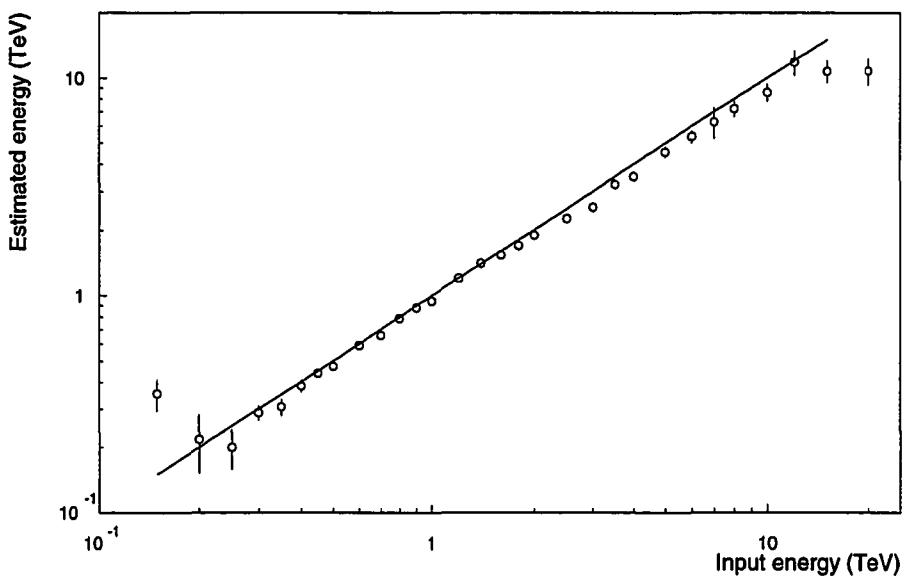

Figure 4.12: Performance of the mixed energy estimate

4.7.4 Resolution of the energy estimation function

The amount of Cherenkov light in an air shower initiated by a high energy gamma ray is related to the number of particles at shower maximum in the cascade. This in turn depends strongly, on the depth of the first interaction for the primary particle. Therefore, the fluctuations in the observed amount of light derive from variations inherent in the cascade process itself, i.e., an atmospheric Cherenkov detector has intrinsically poor energy resolution. This means that, there must be some provision to compensate for the energy resolution, irrespective of the actual gamma ray selection

criteria used.

For a given energy estimation function, we proceed to find the energy resolution function by considering the distribution of estimated energies for showers with a fixed input energy. (For early investigations along this line, see Plyasheshnikov [86].) The energy resolution function, $\psi\left(E,\tilde{E}\right)$ is defined as a probability density, so that $\psi\left(E,\tilde{E}\right)\,d\tilde{E}$ represents the probability that a shower with primary energy E has a reconstructed energy in the infinitesimal interval $\left(\tilde{E},\tilde{E}+d\tilde{E}\right)$. Also,

$$\int\limits_{\Delta\tilde{E}} \psi\left(E,\tilde{E}\right)\,d\tilde{E}, \tag{4.34}$$

represents the probability that a shower with a reconstructed energy in the finite range $\left(\tilde{E},\tilde{E}+\Delta\tilde{E}\right)$, has a primary energy, E. The energy resolution function must have the following properties:

1. It must be normalized, viz. ,

$$\int\limits_{0}^{\infty} \psi\left(E,\tilde{E}\right)\,d\tilde{E}=1 \tag{4.35}$$

2. It must be bias-free, i. e. , for gamma ray showers with a fixed primary energy, E, the mean of the reconstructed energy, $\left\langle\tilde{E}\right\rangle$, given by:

$$\left\langle\tilde{E}\right\rangle=\int\limits_{0}^{\infty} \psi\left(E,\tilde{E}'\right)\,\tilde{E}'\,d\tilde{E}, \tag{4.36}$$

must coincide with the input energy, E.

Additionally, it is desirable that the energy resolution function be narrow in order to increase the accuracy of the spectrum determination.

As we are going to be dealing with discrete energies, we find a histogram version of the resolution function, using the following steps, for each Monte Carlo input energy, E_i:

1. We take all simulated gamma ray showers at energy E_i, that have triggered the model detector and passed extended supercuts. We find the reconstructed energy for each shower, by using an appropriate energy estimation function, and bin them by the reconstructed energy.

2. For the input energy, E_i, consider the k^{th} bin in the reconstructed energy. This bin contains showers with the same input energy, but with different impact radii, r_j. Therefore, we need to weight the showers by the impact radius. Let m_{ijk} be the number of showers in the k^{th} bin with energy, E_i and impact radius, r_j, and let M_{ij} be the total number of simulated showers at E_i, r_j. Hence, we are interested in the fraction of these showers that show up in the k^{th} bin. This is given by $f_{ijk} = m_{ijk}/M_{ij}$. Considering this to represent the relative number of successes in M_{ij} trials for the binomially distributed variable, m_{ijk}, we can calculate the variance in this quantity as:

$$Var\left(f_{ij}\right) = \frac{1}{M_{ij}^2} Var\left(m_{ijk}\right) = \frac{1}{M_{ij}} \frac{m_{ijk}}{M_{ij}} \left(1 - \frac{m_{ijk}}{M_{ij}}\right) \tag{4.37}$$

Therefore, the weight, w_k associated with the k^{th} estimated energy bin, and the variance, σ_k^2, in this weight is given by:

$$w_k\left(r_j\right) = \sum_j \Delta A_j \frac{m_{ijk}}{M_{ij}} \tag{4.38}$$

$$\sigma_k^2 = \sum_j \left(\Delta A_j\right)^2 \frac{1}{M_{ij}} \frac{m_{ijk}}{M_{ij}} \left(1 - \frac{m_{ijk}}{M_{ij}}\right) \tag{4.39}$$

where, as earlier, ΔA_j is the area of the annulus centred at r_j.

3. Thus, we can consider the bins in $\tilde{E}$ to define a histogram, with the height of the k^{th} bin being proportional to the weight, w_k. The resolution function must also be renormalized to unity, by dividing each w_k by the sum of the weights in all estimated energy bins.

The mean of the histogram is given by:

$$\left\langle \tilde{E} \right\rangle_i = \frac{\sum_k \left(\tilde{E}_k w_k\right)}{\sum_k \left(w_k\right)} \tag{4.40}$$

where, $\tilde{E}_k$ represents the estimated energy for bin k. In order for the energy estimate to be bias-free, the mean, $\left\langle \tilde{E} \right\rangle_i$ must coincide with the input energy, E_i. The sample variance in the estimated energy is given by:

$$s_i^2 = \frac{\sum_k w_k \left(\tilde{E}_k - \left\langle \tilde{E} \right\rangle_i\right)^2}{\sum_k \left(w_k\right)} \tag{4.41}$$

Note that, here we are interested in the sample variance, rather than the variance in the mean, as we are going to address the question of how well can we reconstruct the energy of a particular shower.

4. We look upon the histograms above, as Monte Carlo approximations to the "real" energy resolution function, with the sample variances from the histograms approximating the actual variance. In order to avoid being limited by fluctuations in the Monte Carlo results, we choose to fit the energy resolution histograms with a Breit-Wigner form[7]. This allows us to make the energy resolution functions bias-free by forcing the mean estimated energy to agree with the Monte Carlo input energy.

   The normalized Breit-Wigner, or Cauchy, distribution is given by:

$$f\left(\tilde{E}\right) = \frac{\Gamma}{2\arctan\left(\tilde{E}_L/\Gamma\right)} \frac{1}{\left(\tilde{E}-\tilde{E}_0\right)^2+\Gamma^2} \tag{4.42}$$

   The usual caveats for using a Cauchy distribution as a probability density function, apply here (see, for example Frodesen [38, pg. 123-126]). Specifically, the distribution must be truncated at some point, in order for the moments to exist. Here, I have chosen to truncate the distribution at $\left(-\tilde{E}_L, \tilde{E}_L\right)$, where the limiting estimated energy, $\tilde{E}_L$ is chosen so that the range excludes the estimated energies of only a few per cent of the simulated showers at any input energy step. The mean of the distribution is at $\tilde{E}_0$, and it has a characteristic width of Γ.

5. By fitting the energy resolution histograms with a Breit-Wigner distribution, we obtain the characteristic widths of the distribution at each Monte Carlo input energy step. This is shown in Fig. 4.13 for the 1988-89 data, using both the distance-independent energy estimate and the mixed energy estimate. As there is some scatter in the Breit-Wigner widths, we fit the widths as a function of the input energy, and use the fit value at each energy step. Thus, the final

[7] A Gaussian form would work almost as well within the statistics of the simulations. However, there does seem to be a higher tail in the histograms than would be expected from a Gaussian distribution.

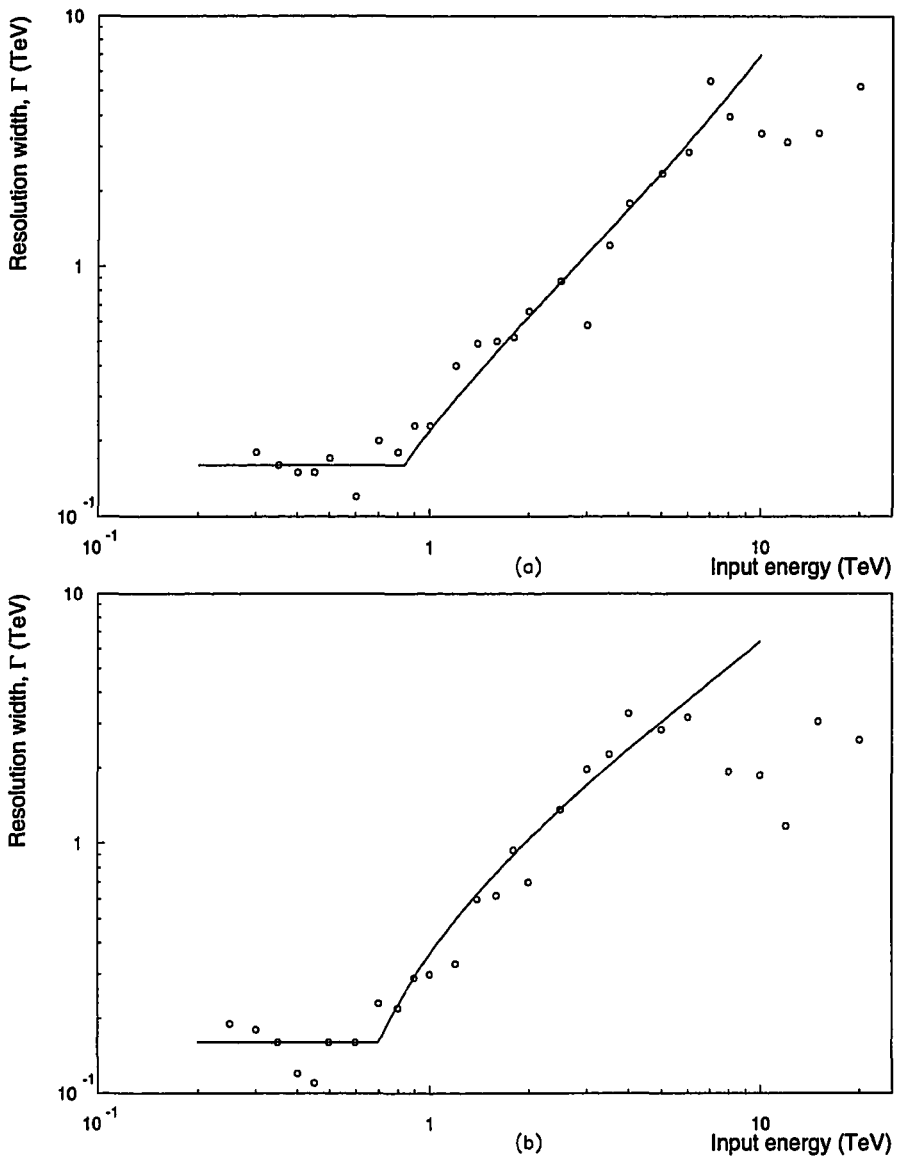

Figure 4.13: Fits to the Breit-Wigner widths

energy resolution function to be applied to the data, has a Breit-Wigner form, with mean equal to the input energy, and having a characteristic width obtained from the fit to the Monte Carlo derived widths. Also, it should be noted that the widths are smaller for the mixed energy estimate.

Fig. 4.14 shows examples of the resolution functions, $\psi\left(E,\tilde{E}\right)$, for the mixed energy estimate applied to the 1988-89 data. The points with the error bars represent the histogrammed resolution functions, derived from the simulations as described above. The solid line represents the Breit-Wigner fit to the histogram versions. Due to fluctuations in the simulated showers, the mean energy for the resolution functions is slightly different from the actual energy. If not corrected, this would introduce a bias when applying the resolution functions to the data. Thus, we constrain the energy resolution functions actually used for analyzing the data to have an unbiased mean, and a width derived from the fit in Fig. 4.13. These are shown by the dashed line in each case.

It can be seen from the figure that the fit to the Monte Carlo histograms works fairly well, though there are large error bars associated with the Monte Carlo points. Also, the fitted energy resolution function is reasonably close to the one that is actually used. The fit to the Breit-Wigner widths is given by:

$$\Gamma = \begin{cases} 0.16, & \text{if } E < 0.70; \\ -0.31 + 0.67E, & \text{otherwise.} \end{cases} \tag{4.43}$$

for the distance-independent case, and by

$$\Gamma = \begin{cases} 0.16, & \text{if } E < 0.83; \\ -0.10 + 0.28E + 0.04E^2, & \text{otherwise.} \end{cases} \tag{4.44}$$

for the distance dependent case. Finally, it should be emphasized that the extracted spectrum is fairly independent of the actual form chosen for the energy resolution functions, but does depend on its variance.

4.8 Method of spectrum extraction

This section puts together all the various pieces that have been discussed in this chapter, outlining a method that uses a least-squares fit to estimate the spectrum

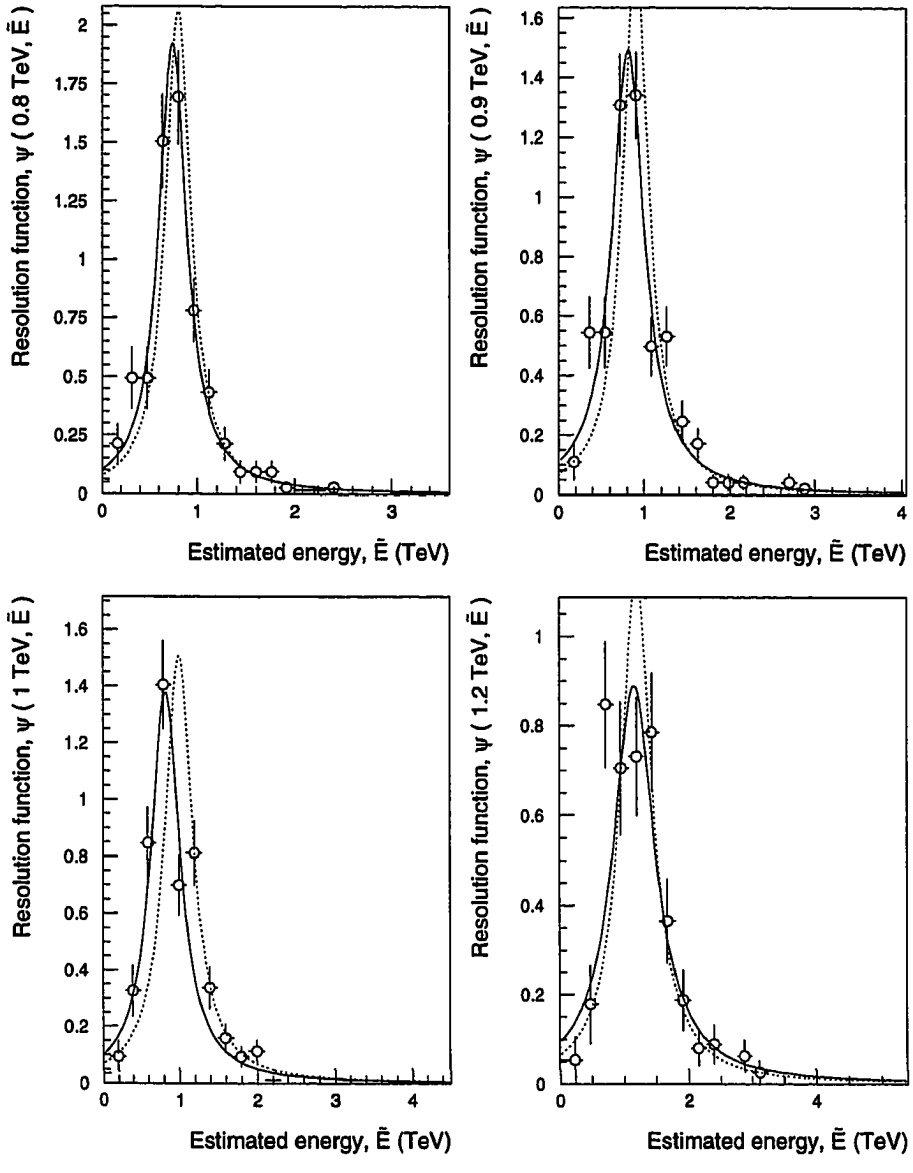

Figure 4.14: Examples of energy resolution functions at several different input energies.

parameters of the source. We assume that the source spectrum is defined by a differential power-law of the form:

$$\frac{dN(E)}{dE} = \alpha E^{-\gamma} \tag{4.45}$$

where $N(E)$ is the number of gammas, per unit area and, per unit time, with energy E (measured in TeV). We shall call α the flux constant, and γ, the spectral index. Although, I have used extended supercuts for the gamma ray selection, no part of this section is specific to it. A similar approach has been described by Lewis [73]. Other approaches, suitable for an atmospheric Cherenkov detector like the Whipple 10-meter, are discussed elsewhere [85, 112].

4.8.1 Observables from the data

In the typical operating mode of the telescope (see 3.3.5), a certain number of events are collected from the direction of the "source" over a period of time, and another set of events is collected from a "background region" for an equal amount of time. After applying extended supercuts to select gamma-ray-like showers, an energy is assigned to each selected event under the assumption that it was initiated by a gamma ray. The selected gamma rays are then binned by this estimated energy, yielding histograms $N_{on}\left(\tilde{E}_k\right)$ and $N_{off}\left(\tilde{E}_k\right)$, for the on-source and off-source region, respectively. The estimated number of gamma ray events in each bin is then given by:

$$N_g\left(\tilde{E}_k\right) = N_{on}\left(\tilde{E}_k\right) - N_{off}\left(\tilde{E}_k\right) \tag{4.46}$$

Let T be the duration of the on-source observation.

4.8.2 Estimations from the simulations

Next, we use the Monte Carlo simulations to form an estimate to the expected number of gamma rays in the data, given a particular spectrum. I shall first write an expression for this estimate and then justify it.

The Monte Carlo estimate for the expected number of gamma rays is given by:

$$\widetilde{N}_g\left(\tilde{E}_k\right) = T \int_0^\infty dE\, \alpha E^{-\gamma} A(E) \int_{\Delta\tilde{E}_k} d\tilde{E}'\, \psi\left(E, \tilde{E}'\right) \tag{4.47}$$

There are three main components in the above expression:

1. *Energy spectrum:* This determines the probability of obtaining a shower with a real energy of E, given that particular spectrum. Here, the factor for this is $\alpha E^{-\gamma}\, dE$.

2. *Collection area:* For a shower with a real energy, E, the detector area, $A(E)$, represents the probability that a shower of that energy triggers the detector and passes the gamma ray selection criteria.

3. *Energy resolution:* This represents the probability that a shower with a real energy, E, ends up in that particular estimated energy bin, having width $\Delta\tilde{E}_k$ at $\tilde{E}_k$. It should be appropriate to the energy estimation function used in estimating the energy of the events in the data. Here, this probability is represented by the second integral.

It is instructive to take a closer look at the meaning of the second integral. From the discussion in sec. 4.7.4, $\int_{\Delta\tilde{E}} \psi\left(E,\tilde{E}\right)\, d\tilde{E}$, represents the probability that a shower with an estimated energy in the finite range $\left(\tilde{E},\tilde{E}+\Delta\tilde{E}\right)$, has a real energy, E. This is shown graphically in Fig. 4.15, which shows three energy resolution functions of the Breit-Wigner form. These have different means, and overlap a certain estimated energy band, shown by the vertical lines. The area under the function, inside the vertical lines, represents of the integral over the energy resolution function. Note that the value of the integral is small when the mean of the energy resolution is widely different from the energy bin being considered, i.e., for a given estimated energy bin, the probability of a shower ending up in that bin is small if the primary energy is very different.

The above discussion is closely related to the situation in estimating the expected number of gamma rays in the data. For example, Fig. 4.15(a) would be the case where the real energy, E, was well below the estimated energy bin; Fig. 4.15(b) would apply to when the real energy was close to the estimated energy, and Fig. 4.15(c) would hold when the real energy was well above the estimated energy. Thus, the integral over the resolution function, for the estimated energy bin being considered, weights

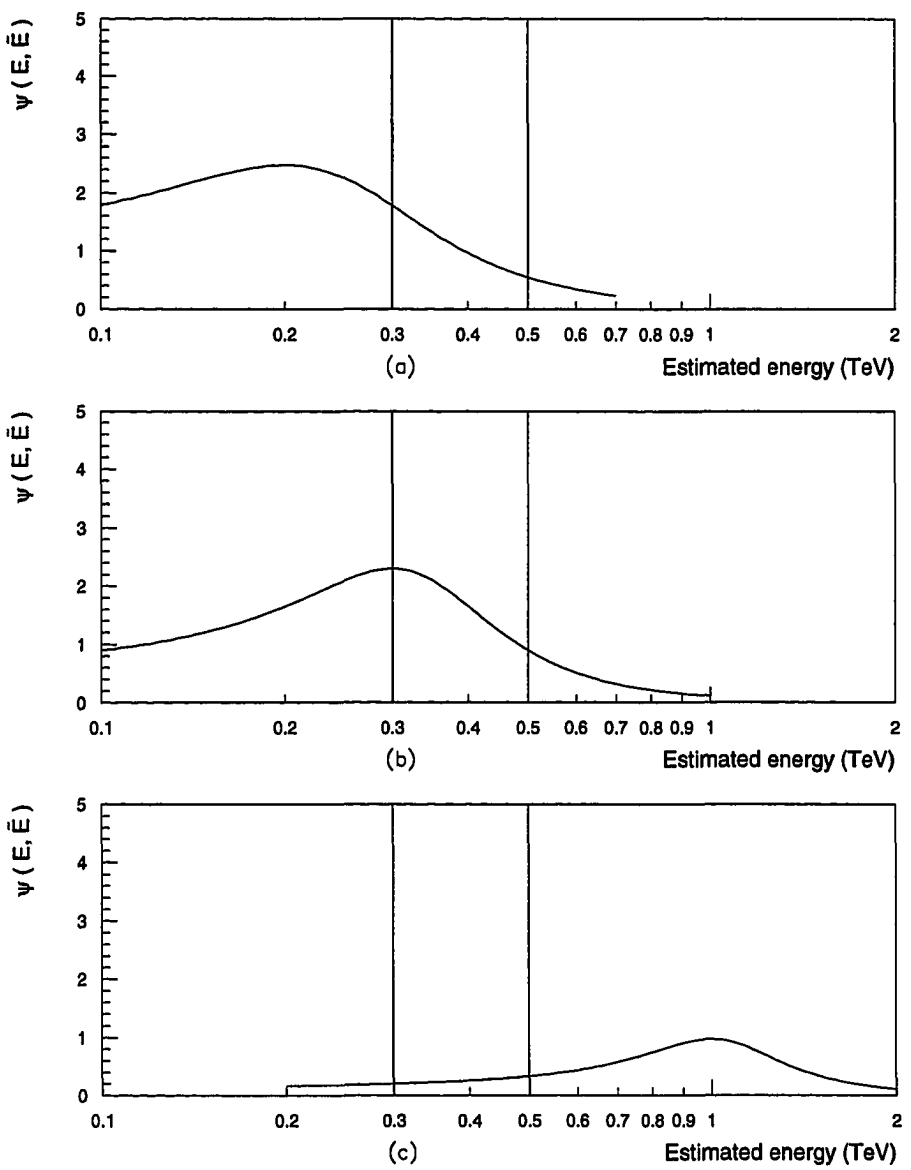

Figure 4.15: The significance of the energy resolution functions. (a) $E \ll \tilde{E}$, (b) $E \sim \tilde{E}$, and (c) $E \gg \tilde{E}$

showers that are close to the bin higher than showers that are further away. The width of the resolution function defines "close" and "far" for this weighting.

Fig. 4.15 also indicates the choice of an appropriate size for the estimated energy bins in the data. If the bins are too large (compared to the width of the resolution function), the effect of the telescope energy resolution is lost in the error due to coarse binning. If the bins are too small, the values of the integral will also be small for most energies, so that there are very few events in each bin, and statistical errors become large. A suitable bin size is the width of the energy resolution function at the centre of the bin.

4.8.3 Least-squares fitting

For each estimated energy bin in the data, we have the observed number of gamma rays, as given by Eq, (4.46). We also have a Monte Carlo estimate to this number from Eq. (4.47). Hence, we can find a statistic, given by:

$$\chi^2 = \sum_k \frac{\left[N_g\left(\tilde{E}_k\right) - \widetilde{N}_g\left(\tilde{E}_k\right)\right]^2}{N_{on}\left(\tilde{E}_k\right) + N_{off}\left(\tilde{E}_k\right)} \tag{4.48}$$

This statistic should be distributed as chisquare, with degrees of freedom equal to the number of estimated energy bins, minus two. The above equation, and the chisquared distribution from the data, can also be used to estimate the statistical errors in the flux constant, α, and the spectral index, γ. This technique is applied to the data in 6.1.

It should be recalled that we start out with an assumed spectral index in the Monte Carlo simulations, which is used to appropriately weight the contributions from each discrete energy. Thus, the Monte Carlo estimate for the number of gamma rays in the data, and consequently, the above fit, depend on this assumed index. Therefore, we must iterate over the entire procedure, using the fitted spectral index as the starting point for the next iteration, till we reach convergence. However, as the weights change only slowly with the spectral index, we have found the procedure to converge in a single iteration.

CHAPTER 5. CHECKS ON SIMULATIONS

Due to the extremely low fluxes of VHE gamma rays, and due to the presence of the enormous background of cosmic ray showers, it is not currently feasible to directly measure parameters of gamma ray showers from experiment, and hence the use of simulations is a must. A Monte Carlo simulation method seems to be the most direct way of dealing with the fluctuation inherent in the cascade process. In previous sections I have noted several difficulties in obtaining a sufficient set of simulations for both gamma ray and cosmic ray showers. With this in mind, and because the derived results are very heavily reliant on the simulations, it is prudent to carefully examine each step and to have a cross-check wherever possible.

In this section, I shall try to establish the reliability of the ISU simulations. I shall start with several self-consistency checks for the simulations, and for the method of spectrum extraction. This will include examples of the extraction of a built in spectrum from a semi-independent set of simulations. I also describe the results of detailed comparisons with the simulations carried out at the University of Leeds by Hillas and West [120]. Next, I shall make comparisons with parameters from the data, mostly with the parameters of background cosmic ray showers. This is not as complete as would be desirable, because we do not yet have a complete set of simulations of cosmic ray showers, and are restricted to using only simulated proton showers for the comparison. Finally, I shall compare average numbers of various shower quantities to analytical solutions obtained under different approximations.

5.1 Vertically incident gamma ray showers

Here, I consider the two gamma ray databases that have the primary gamma ray incident along the zenith. These are, (a) the main database of gamma ray showers,

at discrete energies and impact radii, and (b) the smaller database of gamma ray showers distributed uniformly in area and with a built in power law spectrum. Due to the relatively small number of triggering showers in the subsidiary database, I have reused the simulated showers twice, with different locations for the shower cores in each case.

I shall first describe some simple checks, e.g., checking the distribution of shower cores to ensure that they are uniformly distributed in area. Next, I shall compare Hillas parameter fits, detector area curves, and energy estimates obtained from the main database with those from the subsidiary database. This serves as a check that the various weightings have been properly carried out. Finally, I shall use quantities from the main database and follow our prescribed method of spectrum extraction to measure the built in spectrum for the smaller database. This is not an entirely independent test, as we have used the same simulation programs to generate both databases. However, it is an important demonstration of the validity of the method.

5.1.1 Self-consistency checks

The Monte Carlo simulations are stored on magnetic tape as shower-by-shower lists of photons striking the model 10-meter detector. The first tests carried out are simple automated scripts that check to see that all records have the requisite number of fields, and none of the files are truncated.

The next check is to ensure that the positions of the shower cores has been correctly chosen in the simulations. For the main database, at each energy, the simulations are done at discrete radii. At each radial step, the shower cores should be distributed uniformly in azimuth. Fig. 5.1 shows all simulated showers in the main database at impact radii of 50 m, 100 m and 300 m. Each shower is represented by a single dot, with the individual points merged into a continuous line. It is apparent that the distribution in azimuth is indeed uniform. For the subsidiary database, the showers are scattered uniformly in area out to a radius of 250 m. Fig. 5.2(a) is a scatter plot of the x and y positions of the shower cores (the detector is located at the origin), which seems to be uniform in area. Fig. 5.2(b) shows the number of showers per 10 m radial bin. This grows proportionally with the radius, r, as would be expected of a distribution uniform over the area. The small database had a nominal

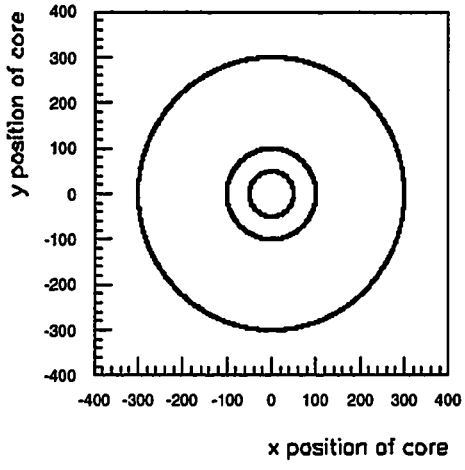

Figure 5.1: Azimuthal distribution of showers in main database.

differential spectral index of -2.5 built into it. Fig. 5.3 shows the distribution of the number of simulated showers, binned by energy, along with a power law spectrum fitted to the known input energies. This fitted power law is:

$$\frac{dN(E)}{dE} = 928 \left(\frac{E}{1TeV}\right)^{-2.58} \text{ showers/TeV} \tag{5.1}$$

As the showers are distributed uniformly in area, out to a radius of 250 m, the simulated differential spectrum can therefore be written as:

$$\frac{dN(E)}{dE} = 4.73 \times 10^{(}-3) \left(\frac{E}{1TeV}\right)^{-2.58} \text{ showers/TeV} \tag{5.2}$$

5.1.2 Hillas parameter distributions

The next comparison to be made is in the distributions of the Hillas parameters. As extended supercuts considers the parameter distributions to be a function of the total ADC counts, n_{dc}, we shall only consider this form of the distributions. Also,

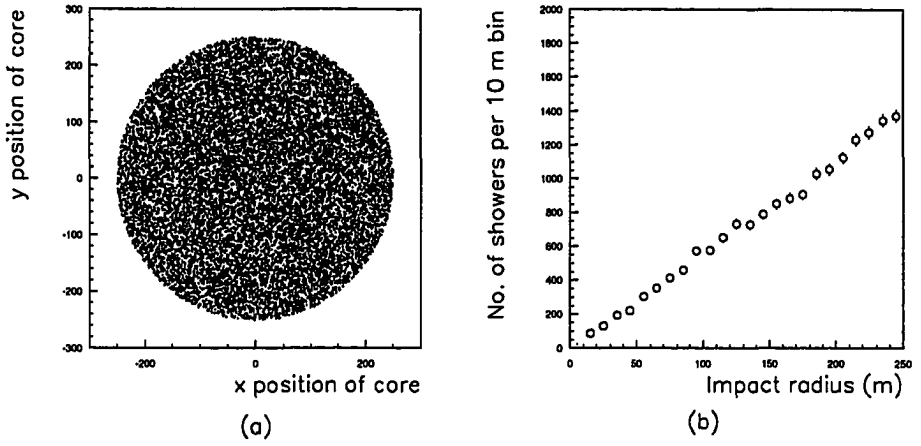

Figure 5.2: Spatial distribution of showers in subsidiary database.

the detector parameters applied to both databases are those appropriate for 1988-89 (see sec. 3.4.1 for the actual values used).

The main database is used to calculate the parameter means and the variances in these, for each n_{dc} bin, as described in sec. 4.5.1. These are then fit by functions that scale as $\ln(n_{dc})$, as shown in sec. 4.5.2. Fig. 5.4 compares these fits along with the errors at each n_{dc} bin (shown as the lines with errorbars), with a scatter plot of the distributions from the subsidiary database. The distributions for the parameters, width, length, alpha, azwidth and distance are shown. There seems to be reasonable agreement within the statistics in the simulations.

5.1.3 Effective detector area

Fig. 5.5 shows the effective detector area, as calculated from each of the two databases in the case of (a) trigger only, and (b) trigger plus extended supercuts.

For the main database, the area is calculated as described in sec. 4.6, and the

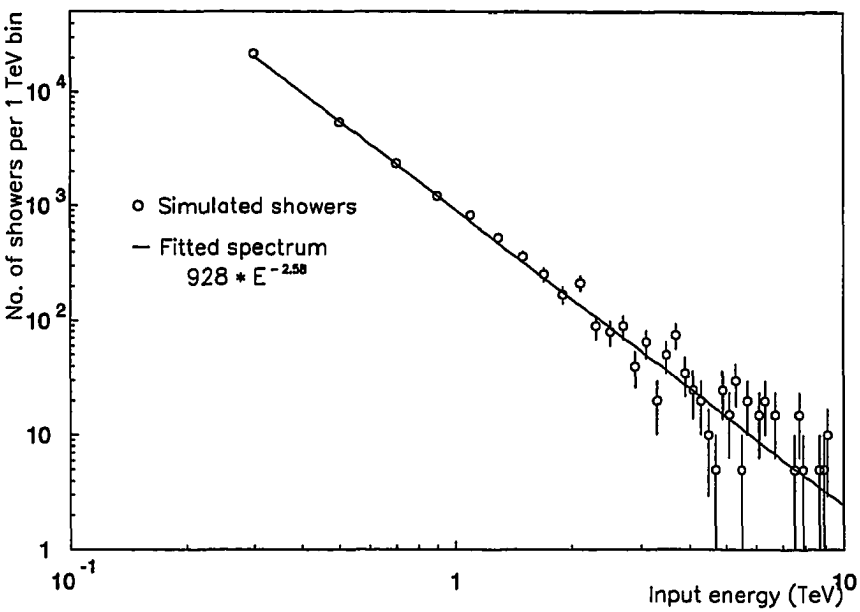

Figure 5.3: Fitted spectrum for the simulated showers in the subsidiary database.

parameterized area is shown by the solid line. For the subsidiary database, we first calculate the fraction of simulated gamma rays triggering in radial bins, and then proceed as for the main database. The area from the subsidiary database is indicated by the points with errorbars. Note that the subsidiary database has simulated showers only out to a radius of 250m so that both the mean area, and the variance in the mean are underestimated for high energies. There is good agreement between the two databases.

5.1.4 Energy estimate and resolution

The main database has simulations done at discrete energy steps, while in the subsidiary database, the primary energy is drawn from a power law spectrum with a differential index of -2.58. The first approach makes it easier to obtain an energy estimate and the resolution in the energy estimate. However, the second approach is closer to the actual operation of the detector, and it must be demonstrated that the

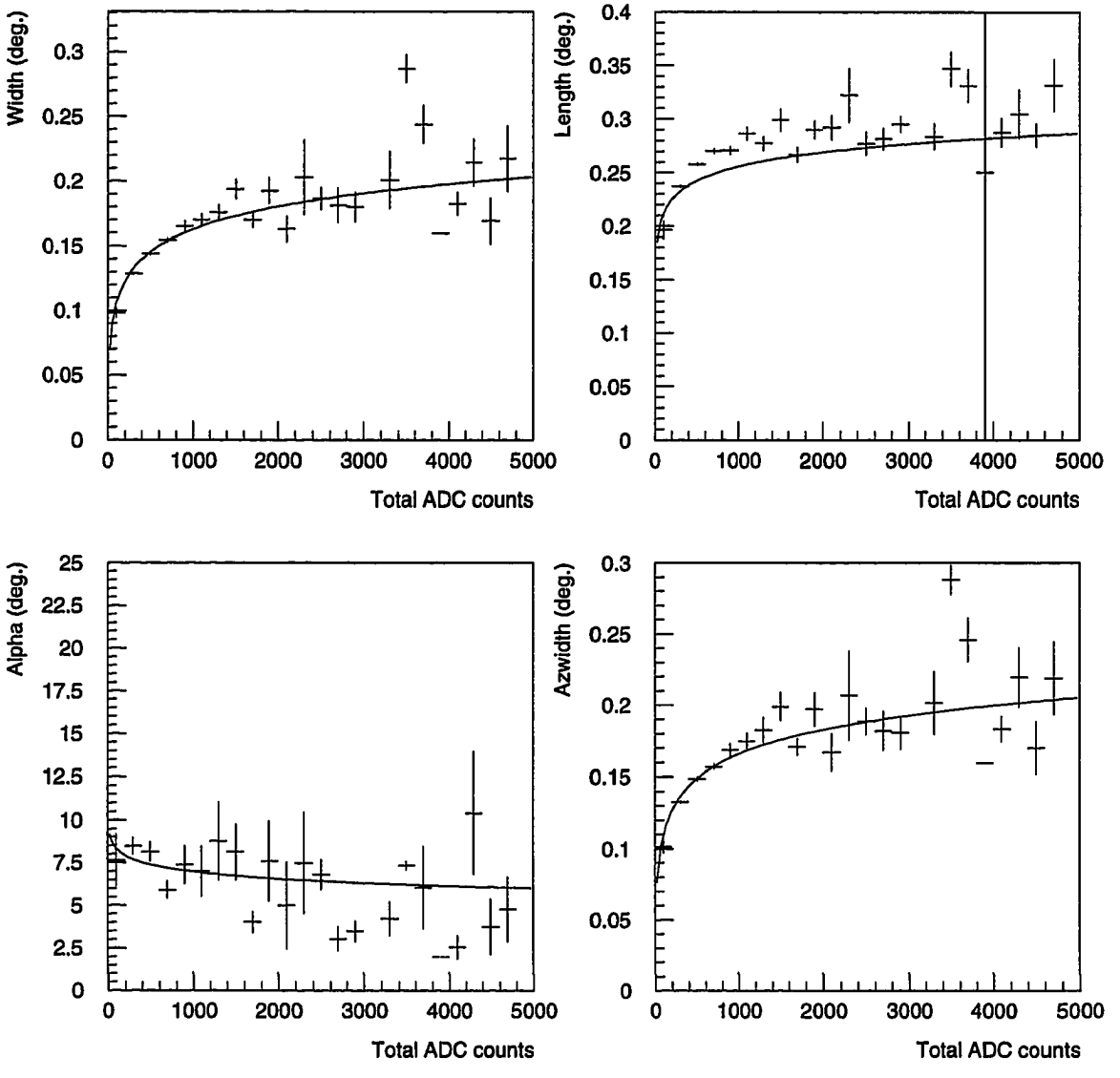

Figure 5.4: Comparison of Hillas parameters between main and small databases.

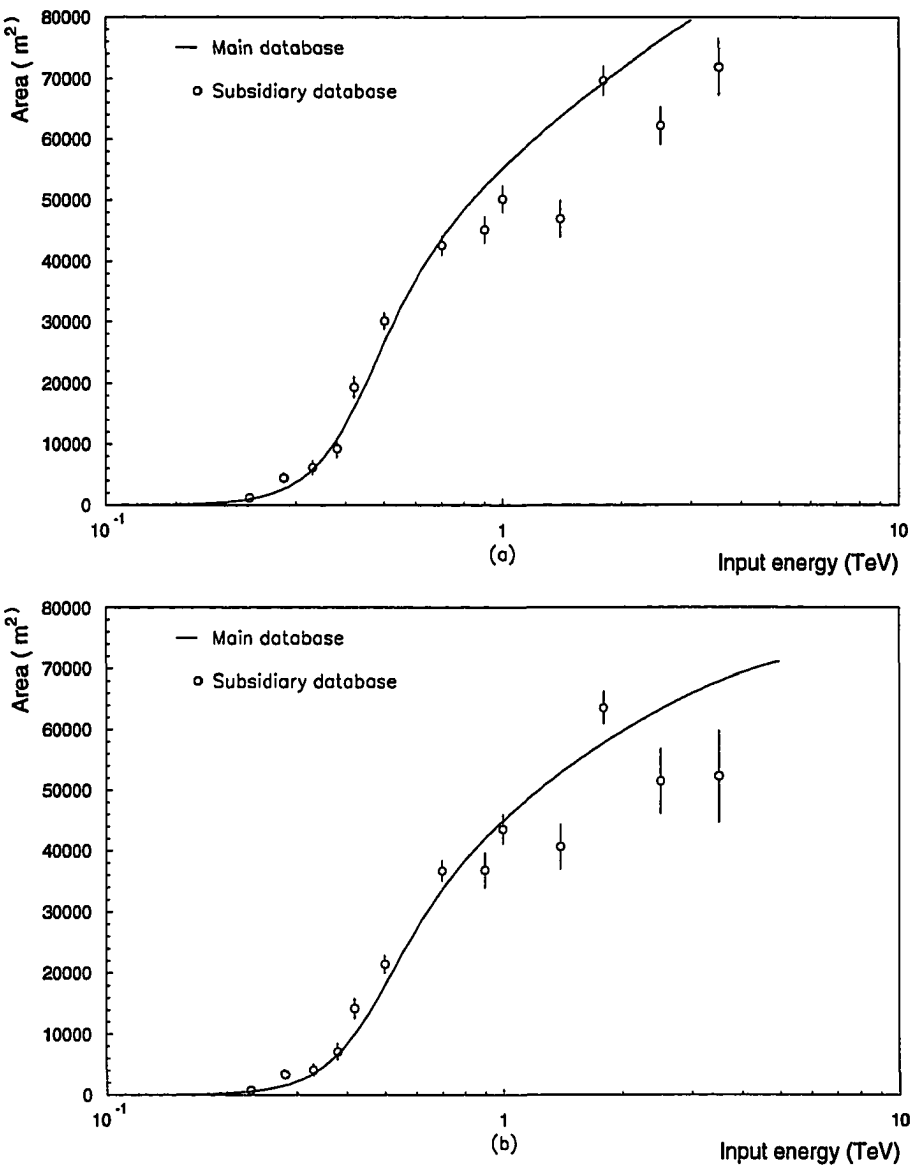

Figure 5.5: Comparison of collection areas from the two databases. (a) Only trigger applied, and (b) trigger plus extended supercuts

energy estimate from the main database is indeed reliable.

Fig. 5.6 compares the energy reconstructed, as per the estimate from the main database (see sec. 4.7.3), to the known input energies in the simulations for the subsidiary database. This is shown as a scatter plot. Fig. 5.6(a) uses the distance-independent estimate, while Fig. 5.6(b) uses the mixed energy estimate. In both cases, the ideal curve that would result for a perfect energy estimate function is shown by the solid, diagonal line. The dashed error box shows the expected sample standard deviations in the energy estimate. It can be seen that both estimates reconstruct the mean energy fairly well and the distance-dependent energy estimate has less of a spread in the reconstructed energy.

5.1.5 Background showers

Here, I compare our simulation of proton-initiated showers with the background cosmic ray showers from the data. This set of simulations is far from complete, as only about half the cosmic ray showers above our operating threshold are protons. Also, I do not feel that we have adequate Monte Carlo statistics for even the proton showers. However, I hope to demonstrate that we get reasonable agreement with this limited set of proton simulations.

5.1.5.1 Input spectrum The set of simulations that this report is based on consists of 14, 824 proton initiated showers. The primary particle is incident along the zenith. The arrival directions of the primary particles are randomized over a cone of half-angle 3° (solid angle on sky 0.0086 sr), centred at the zenith[1]. The shower cores are distributed uniformly in area, over a circle of radius 225 m (area 1.59×10^5 m^2), with the detector at the centre. The primary energies are drawn from a power-law spectrum, with an input differential spectral index of -2.65, and range from 0.3 TeV to 10 TeV.

To get an idea of the trigger rate and the parameter distributions, each shower has been re-used 30 times, with different random arrival directions in the 3° cone

[1]The solid angle is probably too small. This particular choice follows by adding a 2° field of view to a Cherenkov cone of $\sim 1°$, which of course ignores the multiple scattering angle and the transverse momentum from nuclear interactions.

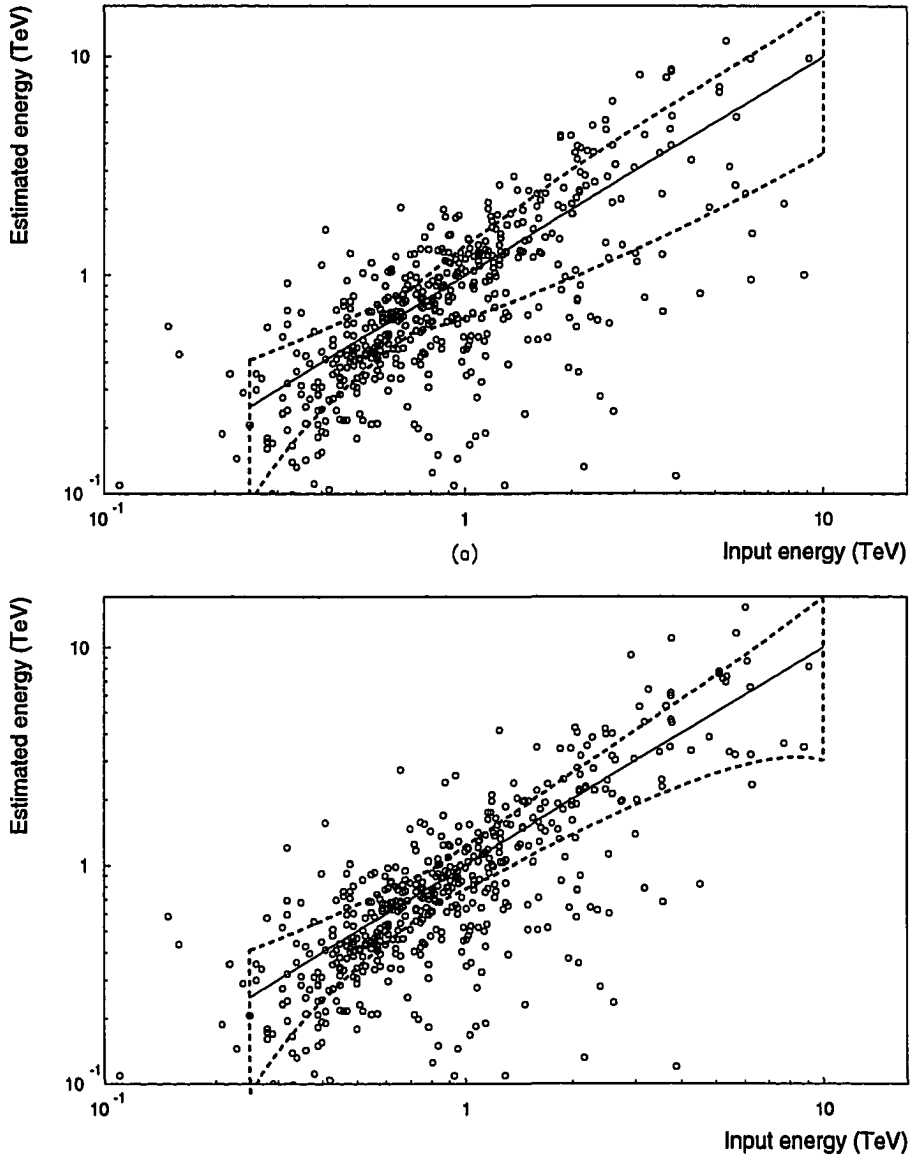

Figure 5.6: The energy estimate from the main database applied to the small database. (a) Distance independent estimate, and(b) Mixed energy estimate

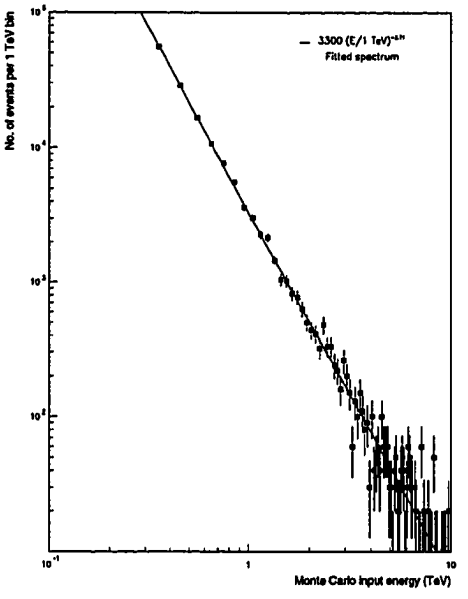

Figure 5.7: Fit to the energy spectrum of the simulations.

and different noise values in the image. For our usual input parameters for the noise, mirror reflectivity, photoelectron to ADC counts conversion factor etc. I get about 570 independent triggers out of a total of about 2100 triggering showers. In a quick look through the results, the images of the same shower looked quite different, both in the total ADC counts and in the Hillas parameter values, so that it is probably fair to re-use them these many times.

Fig. 5.7 shows the spectrum fitted to the input energies to the Monte Carlo simulations. The fitted spectrum, with 1σ statistical errors, is:

$$\left(\frac{dN}{dE}\right)_{MC} = (3.3 \pm 0.75) \times 10^3 \left(\frac{E}{1\,\mathrm{TeV}}\right)^{-2.71\pm0.015} \quad \frac{\#}{\mathrm{TeV}} \tag{5.3}$$

Dividing by the area and solid angle covered by the simulations, the fitted Monte Carlo differential spectrum is:

$$\left(\frac{dN}{dE}\right)_{MC} = (2.4 \pm 0.55) \left(\frac{E}{1\,\mathrm{TeV}}\right)^{-2.71\pm0.015} \quad \frac{\#}{\mathrm{m^2\ sr\ TeV}} \tag{5.4}$$

Dividing by the area and solid angle covered by the simulations, the fitted Monte Carlo differential spectrum is:

$$\left(\frac{dN}{dE}\right)_{MC} = (2.4 \pm 0.55)\left(\frac{E}{1\,\mathrm{TeV}}\right)^{-2.71\pm0.015} \quad \frac{\#}{\mathrm{m^2\ sr\ TeV}} \tag{5.5}$$

The actual differential spectrum for the flux of all cosmic ray particles (in what I call "proton equivalents," i.e., the flux described in terms of the number of nucleons) in this energy regime, can be parameterized as given below. This is derived as described in Appdx. C.

$$\left(\frac{dN}{dE}\right)_{CR} = 0.144\left(\frac{E}{1\,\mathrm{TeV/nucleon}}\right)^{-2.71} \quad \frac{\#}{\mathrm{m^2\ s\ sr\ (TeV/nucleon)}} \tag{5.6}$$

Note the difference in the units between Eq. 5.5 and Eq. 5.6—there is no notion of a time of observation in the simulations. Hence, if we are going to compare the Monte Carlo rates to the rates per second in the data, the simulation numbers must be divided by the factor $2.4/0.144 = 16.67$. Also, as each simulated shower is re-used 30 times, the overall renormalization factor for the Monte Carlos is $30 \times 16.67 = 500$.

5.1.5.2 Differential trigger rates This section compares the differential trigger rates of background showers from a zenith file (ZN0805, calendar date 881114), with the Monte Carlo simulations. The events in the zenith file have undergone pedestal subtraction, gain renormalization and morphological cleaning, but no additional software trigger has been applied. Three different photoelectron to ADC count conversion factors have been used in the simulations, (i) 1.15 d. c./p. e., (ii) 0.85 d. c./p. e., and (iii) 0.67 d. c./p. e. The second value is Kwok's measured value that we have used in our simulations for the 1988-89 database. The other two values approximately reflect a 25 % change on either side of this accepted value.

As the hardware trigger involves two tubes out of the inner 91, the event rates are simply the rates in the second highest tube for each event, ignoring the small probability that the second highest tube in the recorded image might not correspond to the actual triggering tube.

The differential event rate is shown in Fig. 5.8 for the zenith file data and for the three Monte Carlo cases. Also shown are two representative error bars for the

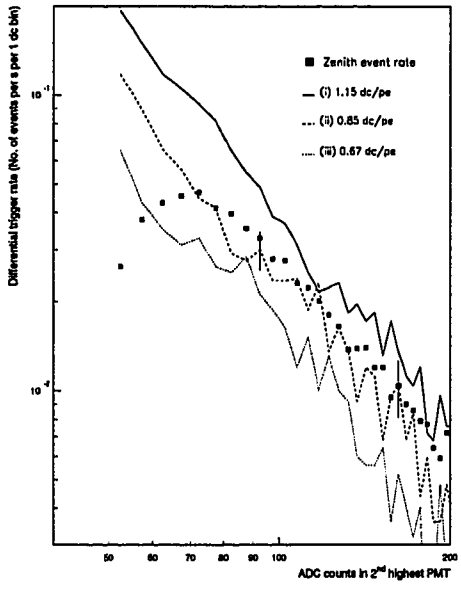

Figure 5.8: Comparison of differential event rates between the simulations and real data.

statistics in the simulations, at the low energy and at the high energy end. The statistical errors in the data are about half of these error bars shown and have been omitted for clarity. It would appear that the curve for a pe-to-dc conversion factor of 0.85 dc/pe (case (ii)) agrees with the data, within the error bars, which is reassuring as that is the value used in our simulations. However, this apparent agreement is somewhat misleading as the abscissa is restricted to a fairly small number of ADC counts and the simulations do not match the data very well at the high energy end even in this restricted range. Hence this should be taken as an indication that the simulations are not obviously incorrect, rather than as a reliable estimate of the photoelectron to ADC count conversion factor.

5.1.5.3 Hillas parameter distributions Fig. 5.9 shows a comparison of the Hillas parameter distributions, between the zenith file data and the Monte Carlo simulations with a photoelectron to ADC counts conversion factor of 0.85 d. c./p. e.

The Hillas parameters shown are the total ADC counts, width, length, alpha, distance and azwidth. In order to make the histograms comparable in size, each of them has been scaled by the total number of events.

For the total ADC counts, histograms with a bin size of 250 ADC counts are shown. For the other parameters, there are two kinds of distributions shown side-by-side. The first one is a simple histogram for the parameter distribution. The second one is a plot of the distribution of the parameter as a function of the total ADC counts (these are the sort of distributions used for extended supercuts). In the second case, the simulations are indicated by the points with error bars, while the data is represented by the dotted line. The statistical errors in the data are much smaller than for the simulations, and have been ignored.

It is evident from the figure that the simulations have problems in reproducing the distributions from the data. We seem to have too many showers at the low end of the total ADC counts distribution, and not enough at the high end. This is probably a reflection of the fact that there are a lot more high energy showers in the data, and that we do not have simulations of heavy nuclei. However, given all the assumptions made in this work, and given the insufficient statistics, the degree of agreement is not unreasonable.

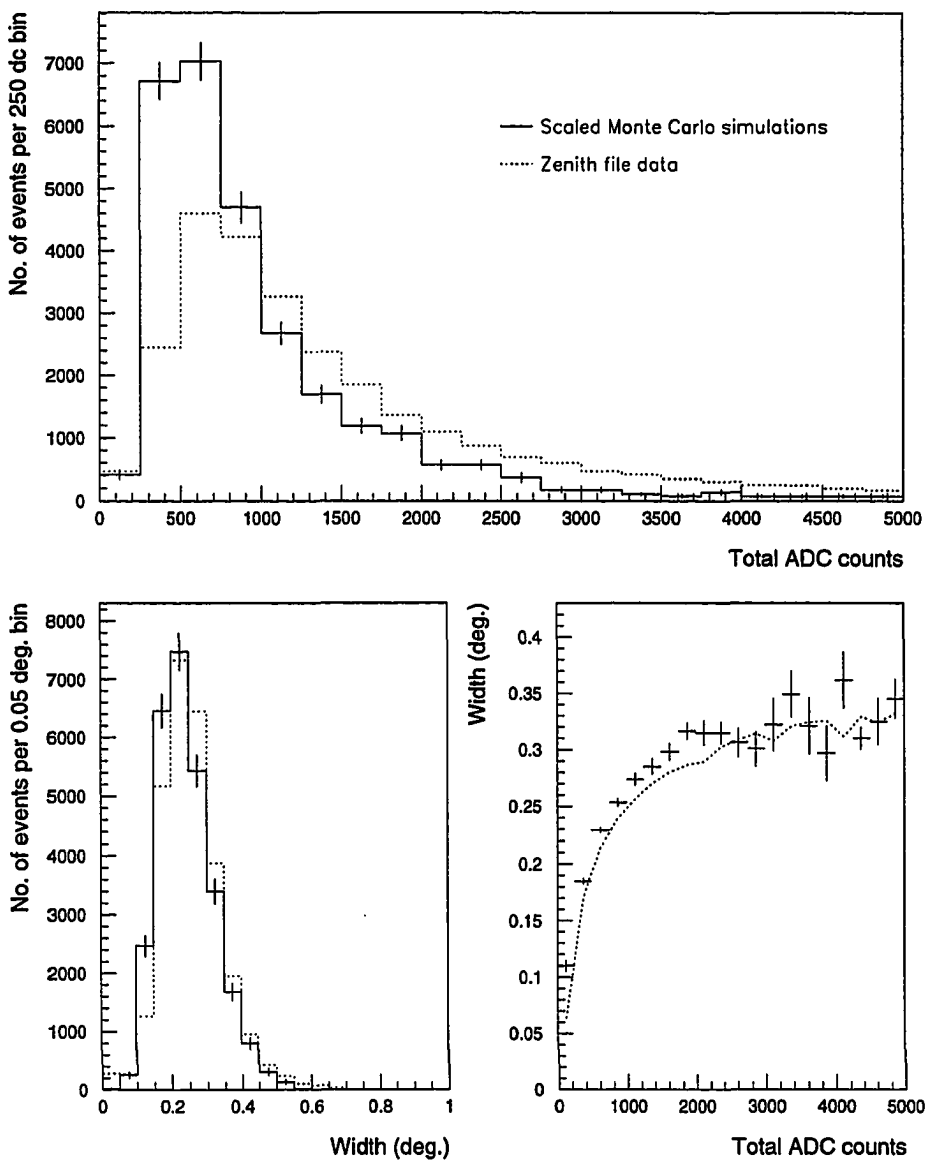

Figure 5.9: Comparison of Hillas parameter distributions.

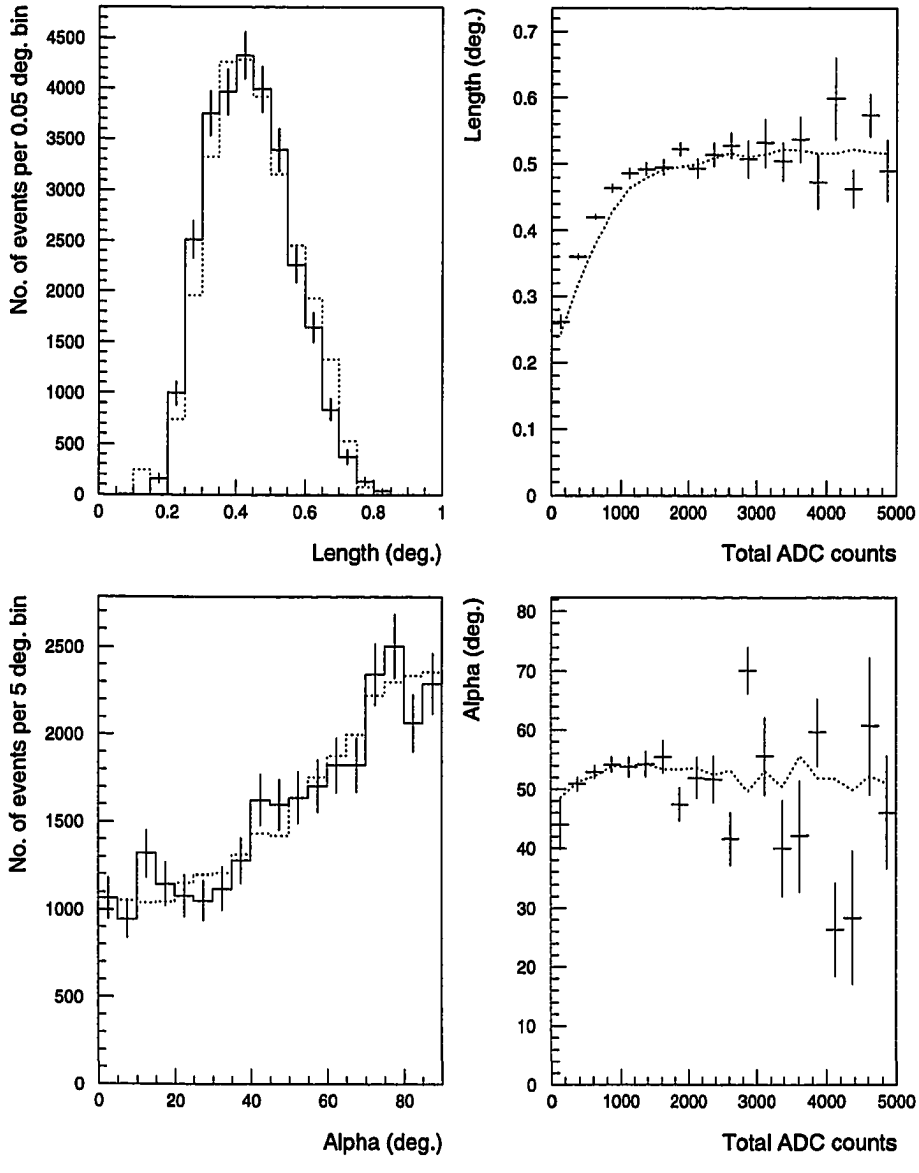

Figure 5.9 (Continued)

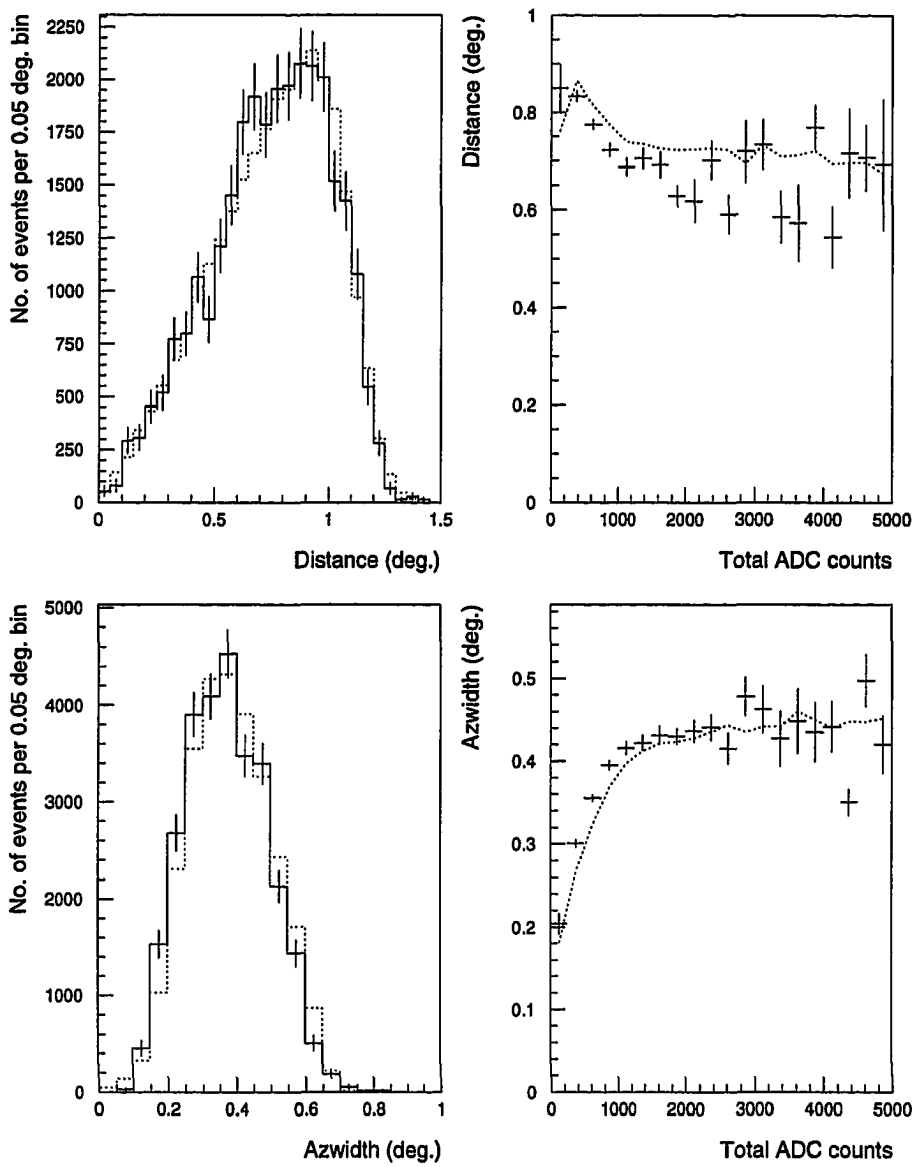

Figure 5.9 (Continued)

CHAPTER 6. DATA ANALYSIS

6.1 Overview

Results of applying extended supercuts to the Crab nebula data are presented here. It covers several observational periods, which are described below. For each such period, we use only a subset of the data, that has been checked for good weather and proper operation of the detector. Also, only data from the Whipple 10-meter telescope has been used, though it should be possible to develop extended supercuts for the new 11-meter telescope too.

The advantage of having a Monte Carlo derived set of cuts, such as extended supercuts is that it is not specific to the detector setup for a particular epoch; though it can be optimized to take advantage of a systematic change in the telescope properties (see 4.5.3). In this analysis, extended supercuts was first applied to the 1988-89 Crab database. It was then re-optimized for subsequent observing seasons where there was an appreciable change in the mirror reflectivity. It should be stressed however, that unless there is a major change in the detector, say, for example, a change in the configuration of the PMT array, the initial set of extended supercuts can still be applied successfully to data from a later epoch. The derived spectrum is compared with independent measurements of the Crab Nebula spectrum, and to theoretical fits to the same.

6.2 The Crab nebula

The canonical database in the building of both standard supercuts, and extended supercuts has been the Crab 1988-89 database. This is a large database where the detector has been operating in an optimal configuration (e.g., with freshly coated mirrors). The data from this period has been intensively examined by several re-

searchers, and the final database is restricted to a well-conditioned subset (see, for example, Lang [69, pg. 109] for further discussion of the tests performed on the data). Hence, this database is examined in detail. For each observing season, Appendix A gives the details of the runs analyzed. Here are the distinct observing seasons, each of which is treated separately:

1. *1988-89:* This database consists of 51 pairs of ON-OFF runs (see 3.3.5), with a total ON-source observation time of 1400 minutes[1], taken between Nov. 1988 and Jan. 1989. Two-thirds of the mirrors on the reflector were freshly recoated just prior to these observations.

2. *1989-90:* This consists of 48 ON-OFF pairs taken between Sep. 1989 and Feb. 1990. Unfortunately for spectrum determination purposes, the detector during this period also utilized an independent trigger, that pre-empted the normal 2/91 Cherenkov trigger. The independent trigger was based on the light collected by four 1.5 m mirrors, mounted on the arms of the telescope. Each mirror was viewed by a single, wide-angle PMT (see Lang [69, pg. 85] for details on this). I demonstrate that the events with the independent trigger are sufficiently different from the normal events that this database is not suitable for spectrum determination.

3. *1990:* This has 17 pairs of runs, with a total ON-source time of 411 minutes, taken between Jan. 1990 and Aug. 1990.

4. *1990-91:* This includes 39 pairs of runs, taken between Oct. 90 and January 1991. The total on-source observation time is 1072 minutes.

5. *1991-92:* The 10-meter detector was being upgraded and new hardware, such as light cones, was being tested during this period. Hence the instrument was not stable enough for spectrum determination during this period. Hence, we have had to discard a lot of the data and there are only 18 pairs with a total ON-source time of 491 minutes from this season.

[1]The usual 1988-89 database consists of 65 pairs of runs. Of these, the last 14 pairs were deemed unsuitable as they have a 3/91, rather than a 2/91 trigger.

6.2.1 1988-89 season

This database consists of 51 pairs of ON-OFF runs (see 3.3.5), with a total ON-source observation time of 1433 minutes[2], taken between Nov. 1988 and Jan. 1989. Two-thirds of the mirrors on the reflector were freshly recoated just prior to these observations. The input parameters for the Monte Carlo simulations were derived as described in sec. 3.4.1.

6.2.1.1 Significance of the detection Table 6.1 shows the significance of the detection of the $\sim$ TeV gamma ray flux from the Crab nebula, using extended supercuts. As the detector was operated in the standard ON-OFF mode, the significance of the detection is given by:

$$\sigma = \frac{N_{on} - N_{off}}{\sqrt{N_{on} + N_{off}}} \tag{6.1}$$

where, N_{on} is the number of events selected in the ON region, and N_{off} is the number of events selected in the OFF region. It should be noted that this represents only the significance for rejection of the null hypothesis, i.e., the significance that the observed excess does *not* arise from a chance fluctuation in the background. The proof that the excess is indeed from gamma ray showers rests on the fact that the selection criteria are derived *a priori* from Monte Carlo simulations of gamma ray showers.

The excess, and the significance is shown separately for each of the parameters that make up the set of extended supercuts. The column labelled "Shape" refers to the results from applying the shape parameters, width, and length in addition to the distance cut. The column labelled "Orient." shows the effect of applying the orientation parameter, alpha as well as the distance cut. Each of these subsets of the extended supercuts should separately select gamma ray images at a high level of significance. Finally, the column labelled "Both" shows the results of the full set of extended supercuts.

[2]The usual 1988-89 database consists of 65 pairs of runs, with a total ON-source observation time of 1723 min. Of these, the last 14 pairs were deemed unsuitable as they have a 3/91, rather than 2/91 trigger.

Table 6.1: 1988-89: Detection significance, using extended supercuts.

	Raw	Width	Length	Distance	Alpha	Shape	Orient.	Both
ON	413 281	115 775	57 137	327 768	52 874	28 597	38 605	6 760
OFF	407 152	111 078	53 154	322 573	48 965	25 155	34 898	3 996
Exc.	6 129	4 697	3 983	5 195	3 909	3 442	3 707	2 764
Sigma	6.8	9.9	12.0	6.4	12.2	14.8	13.7	26.7

Table 6.2: 1988-89: Detection significance, using standard supercuts.

	Raw	Width	Length	Distance	Alpha	Shape	Orient.	Both
ON	413 281	35 234	61 298	297 828	52 027	13 836	35 463	4 043
OFF	407 152	31 953	57 575	293 306	48 167	11 203	31 876	1 685
Exc.	6 129	3 281	3 723	4 522	3 860	2 633	3 587	2 358
Sigma	6.8	12.7	10.8	5.9	12.2	16.7	13.8	31.6

Table 6.2 shows the excesses and the signficances for the set of standard supercuts, with the columns having the same meaning.

As can be seen by comparing the two tables, the significance of the detection using extended supercuts is almost as good as with standard supercuts. The advantage of extended supercuts is that it is an *a priori* set of cuts, and has been shown not to be biased towards low energy showers. It is indeed better at retaining gamma ray like showers as can be seen from the fact that there is a 20 % larger excess with extended supercuts, even though standard supercuts is optimized to this database.

6.2.1.2 Spectrum of the VHE emission In this section, I present the results of the measurement of the spectrum from the 1988-89 Crab nebula database for four different cases, (a) distance independent energy estimate, with and without

Table 6.3: 1988-89 Crab flux, using distance independent estimate, and without energy resolution

Energy (TeV)	ON	OFF	σ	Actual flux	Fitted flux	Error	χ^2/bin
0.40–0.60	1158	661	11.7	1.68×10^{-6}	1.59×10^{-6}	1.437×10^{-7}	0.4
0.60–0.90	1106	626	11.5	5.08×10^{-7}	5.51×10^{-7}	4.404×10^{-8}	0.9
0.90–1.30	832	485	9.6	2.06×10^{-7}	2.03×10^{-7}	2.159×10^{-8}	0.1
1.30–1.90	625	385	7.6	8.04×10^{-8}	7.62×10^{-8}	1.065×10^{-8}	0.1
1.90–2.90	456	308	5.4	2.60×10^{-8}	2.65×10^{-8}	4.847×10^{-9}	0.0
2.90–4.60	289	163	5.9	1.17×10^{-8}	8.26×10^{-9}	1.970×10^{-9}	3.0
4.60–7.60	140	115	1.6	1.23×10^{-9}	2.32×10^{-9}	7.839×10^{-10}	2.0
7.60–13.60	75	57	1.6	4.36×10^{-10}	5.48×10^{-10}	2.781×10^{-10}	0.1

for four different cases, (a) distance independent energy estimate, with and without the application of the energy resolution functions, and (b) mixed energy estimate, with and without the application of the energy resolution functions. This allows us to check that all these methods give consistent answers.

1. *Distance independent estimate* Here, the energy estimate, that is based only on the total ADC counts is used. This is given by Eq. (4.23). In the first step, only the collection area of the detector is used, while in the second step the energy resolution functions discussed in sec. 4.7.4 are also applied.

   (a) *Collection area only:* Table 6.3 below is a list of the estimated energy bins, the ON-source counts, the OFF-source counts, the significance of the excess, the actual differential flux at mid-bin, the fitted differential flux at mid-bin, the statistical error in the actual differential flux, and the contribution to χ^2_{fit} from each bin. Note that the fitted flux is obtained by using a collection area averaged over the estimated energy bin. The bin widths in the estimated energy are approximately equal to the standard deviation of the energy resolution function. All flux values are quoted in $m^{-2}\ s^{-1}\ TeV^{-1}$. The overall value of χ^2 for 6 degrees of freedom, is 6.6, giving an acceptable fit. The best-fit spectrum, with 1-σ statistical errors,

Table 6.4: 1988-89 Crab flux, using distance independent estimate, and applying energy resolution.

Energy (TeV)	ON	OFF	σ	Actual flux	Fitted flux	Error	χ^2/bin
0.40–0.60	1158	661	11.7	2.40×10^{-6}	2.24×10^{-6}	2.062×10^{-7}	0.6
0.60–0.90	1106	626	11.5	6.15×10^{-7}	6.88×10^{-7}	5.328×10^{-8}	1.9
0.90–1.30	832	485	9.6	2.36×10^{-7}	2.26×10^{-7}	2.467×10^{-8}	0.2
1.30–1.90	625	385	7.6	8.27×10^{-8}	7.59×10^{-8}	1.094×10^{-8}	0.4
1.90–2.90	456	308	5.4	2.31×10^{-8}	2.33×10^{-8}	4.323×10^{-9}	0.0
2.90–4.60	289	163	5.9	8.79×10^{-9}	6.37×10^{-9}	1.484×10^{-9}	2.7
4.60–7.60	140	115	1.6	7.83×10^{-10}	1.54×10^{-9}	5.004×10^{-10}	2.3
7.60–13.60	75	57	1.6	2.37×10^{-10}	3.09×10^{-10}	1.511×10^{-10}	0.2

is given by:

$$\frac{dN}{dE} = (2.60 \pm 0.12) \times 10^{-7} \left(\frac{E}{1\,\text{TeV}}\right)^{-2.61\pm0.07} \quad \frac{\#}{\text{m}^2\ \text{s sr TeV}} \tag{6.2}$$

The fit is shown in Fig. 6.1(a).

(b) *Resolution function applied:* Table 6.4 below is the table of fluxes, when the energy resolution functions appropriate for the distance-independent energy estimate are applied to the data, in addition to the collection area of the detector. All flux values are quoted in $m^{-2}s^{-1}TeV^{-1}$. Again, note that the fitted flux averages both the area and the energy spectrum over the width of the bin. The overall value of χ^2 for 6 degrees of freedom, is 8.3. The best-fit spectrum, with 1-σ statistical errors, is given by:

$$\frac{dN}{dE} = (2.98 \pm 0.15) \times 10^{-7} \left(\frac{E}{1\,\text{TeV}}\right)^{-2.91\pm0.11} \quad \frac{\#}{\text{m}^2\ \text{s sr TeV}} \tag{6.3}$$

The spectral index becomes steeper when the energy resolution function is applied. The fit is shown in Fig. 6.1(b).

2. *Distance dependent estimate:* Here, the mixed energy estimate is used, as given by Eq. (4.33). In the first step, only the collection area of the detector is used, while in the second step the energy resolution functions discussed in sec. 4.7.4 are also applied.

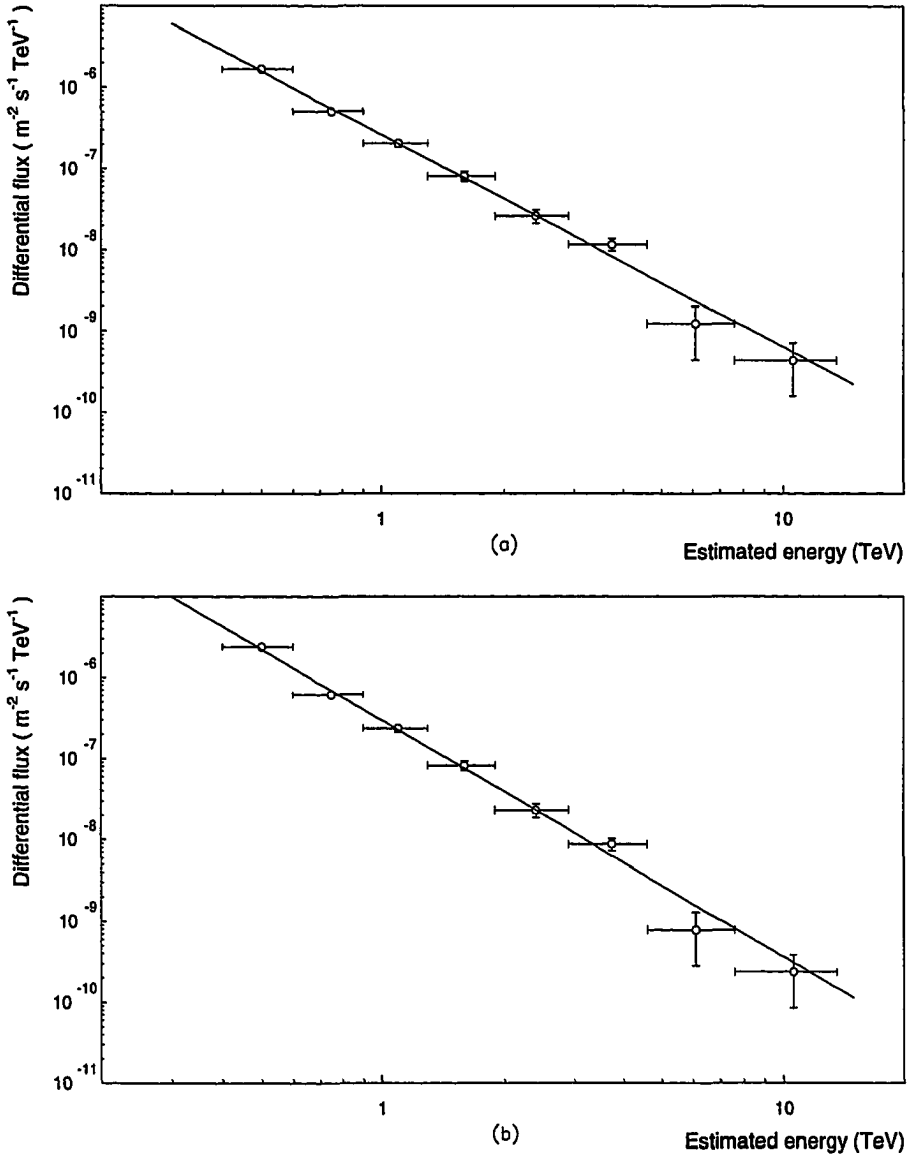

Figure 6.1: Fitted spectrum for the 1988-89 season, using the distance-independent energy estimate. (a) no energy resolution, and (b) energy resolution applied.

(a) *Collection area only:* Table 6.5 below gives the fluxes obtained by applying the collection area of the detector, but not using the energy resolution functions. The bin widths in the estimated energy are kept the same as for the distance-independent case. All flux values are quoted in $m^{-2}s^{-1}TeV^{-1}$.

Table 6.5: 1988-89 Crab flux, using distance dependent estimate, and without energy resolution

Energy (TeV)	ON	OFF	σ	Actual flux	Fitted flux	Error	χ^2/bin
0.40–0.60	1158	666	11.5	1.66×10^{-6}	1.57×10^{-6}	1.439×10^{-7}	0.3
0.60–0.90	1320	722	13.2	6.29×10^{-7}	5.26×10^{-7}	4.756×10^{-8}	4.7
0.90–1.30	452	257	7.3	1.15×10^{-7}	1.87×10^{-7}	1.574×10^{-8}	20.8
1.30–1.90	549	312	8.1	7.89×10^{-8}	6.80×10^{-8}	9.764×10^{-9}	1.2
1.90–2.90	538	321	7.4	3.77×10^{-8}	2.28×10^{-8}	5.095×10^{-9}	8.6
2.90–4.60	377	264	4.5	1.04×10^{-8}	6.82×10^{-9}	2.323×10^{-9}	2.3
4.60–7.60	185	161	1.3	1.16×10^{-9}	1.83×10^{-9}	9.021×10^{-10}	0.6
7.60–13.60	102	91	0.8	2.62×10^{-10}	4.13×10^{-10}	3.308×10^{-10}	0.2

The overall value of χ^2 for 6 degrees of freedom, is 38.8 which is a poor fit. The best-fit spectrum, with 1-σ statistical errors, is given by:

$$\frac{dN}{dE} = (2.42 \pm 0.12) \times 10^{-7} \left(\frac{E}{1\,\mathrm{TeV}}\right)^{-2.70\pm0.10} \quad \frac{\#}{\mathrm{m^2\ s\ sr\ TeV}} \qquad (6.4)$$

The fit is shown in Fig. 6.2(a).

(b) *Resolution function applied:* Table 6.6 below is the table of fluxes, when the energy resolution functions appropriate for the distance-dependent energy estimate are applied to the data, in addition to the collection area of the detector. All flux values are quoted in $m^{-2}s^{-1}TeV^{-1}$. Again, note that the fitted flux averages both the area and the energy spectrum over the width of the bin. The overall value of χ^2 for 6 degrees of freedom, is 49.7, which again is not an acceptable fit. . The best-fit spectrum, with 1-σ statistical errors, is given by:

$$\frac{dN}{dE} = (2.56 \pm 0.16) \times 10^{-7} \left(\frac{E}{1\,\mathrm{TeV}}\right)^{-3.04\pm0.18} \quad \frac{\#}{\mathrm{m^2\ s\ sr\ TeV}} \qquad (6.5)$$

Again, the spectral index steepens with the application of the energy resolution functions. The fit is shown in Fig. 6.2(b).

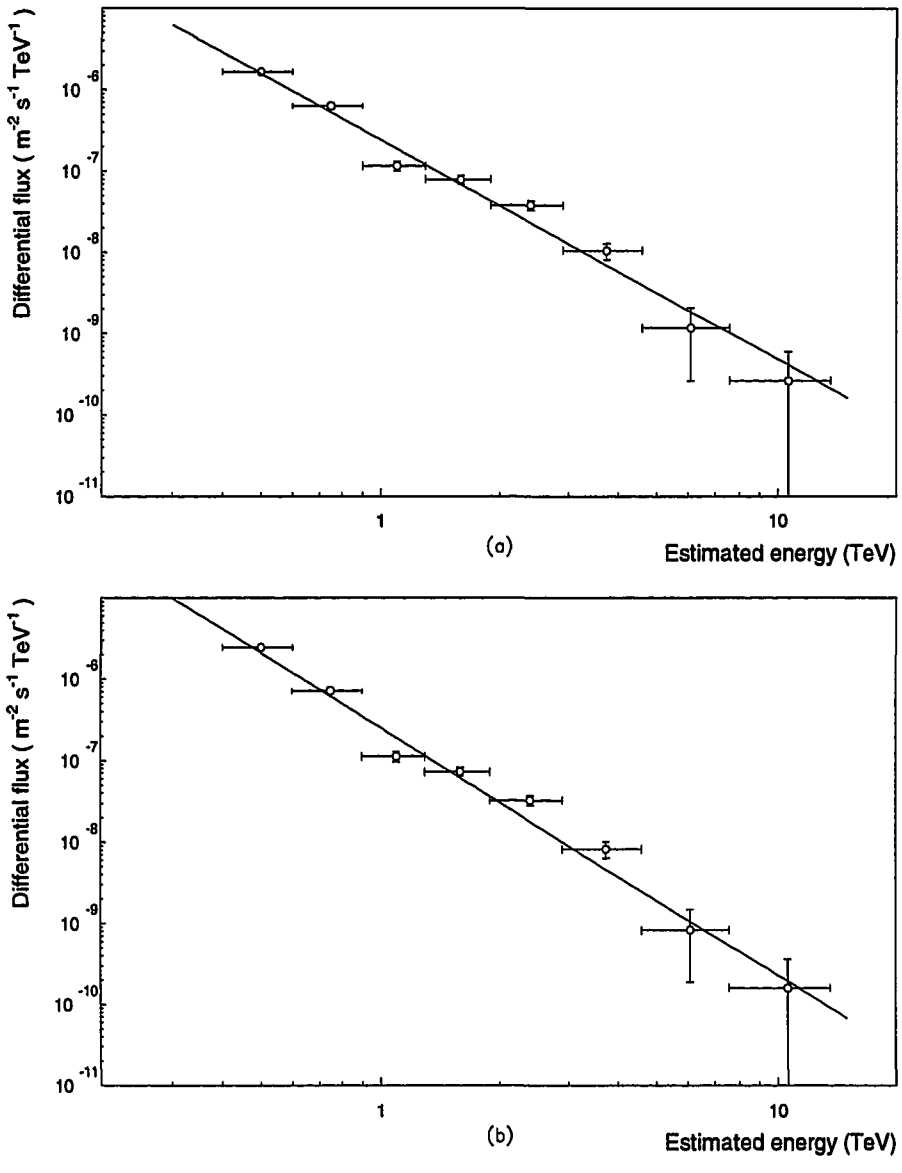

Figure 6.2: Fitted spectrum for the 1988-89 season, using the mixed energy estimate. (a) no energy resolution, and (b) energy resolution applied.

Table 6.6: 1988-89 Crab flux, using mixed energy estimate, and applying energy resolution.

Energy (TeV)	ON	OFF	σ	Actual flux	Fitted flux	Error	χ^2/bin
0.40–0.60	1158	666	11.5	2.45×10^{-6}	2.11×10^{-6}	2.131×10^{-7}	2.7
0.60–0.90	1320	722	13.2	7.16×10^{-7}	6.14×10^{-7}	5.410×10^{-8}	3.6
0.90–1.30	452	257	7.3	1.12×10^{-7}	1.92×10^{-7}	1.536×10^{-8}	26.5
1.30–1.90	549	312	8.1	7.31×10^{-8}	6.13×10^{-8}	9.050×10^{-9}	1.7
1.90–2.90	538	321	7.4	3.26×10^{-8}	1.79×10^{-8}	4.410×10^{-9}	11.2
2.90–4.60	377	264	4.5	8.28×10^{-9}	4.60×10^{-9}	1.855×10^{-9}	3.9
4.60–7.60	185	161	1.3	8.33×10^{-10}	1.05×10^{-9}	6.458×10^{-10}	0.1
7.60–13.60	102	91	0.8	1.60×10^{-10}	1.96×10^{-10}	2.024×10^{-10}	0.0

Thus it is clear that there are problems with the distance dependent energy estimate. Though the results agree with those for the distance-independent case, the fit to the data is rather poor. A closer look at the flux points reveals that the largest contribution to χ^2_{fit} comes from the bin close to the estimated energy, $\widetilde{E}_{switch}$, at which the mixed estimate changes to include a distance dependence (see sec. 4.7.3). I suspect that the errors in the flux are underestimated at that point, so that there is an unacceptably large contribution to χ^2_{fit} from this bin. For the rest of the results quoted in this work, I therefore consider only the distance independent energy estimate.

6.2.1.3 Restricted distance cut In sec. 4.7.2, we discussed the possible need to restrict the distance cut in order to avoid the truncation of shower images by the edge of the camera. It is also expected that this restricted distance cut will improve the energy resolution. This section considers the effect of applying such a restricted distance cut to the Crab 1988-89 data. Here, I use an energy estimate based only on the total ADC counts.

First, we need to find an acceptable range in distance. Fig. 6.3 shows the distributions for the distance parameter for the Crab 1988-89 ON-source region, OFF-source region, and the excess. The chosen restricted region for distance is shown by the dashed lines in Fig. 6.3(b). The restricted range is 0.65 < distance < 1.0, as compared to the usual range for extended supercuts which is 0.5 < distance < 1.2.

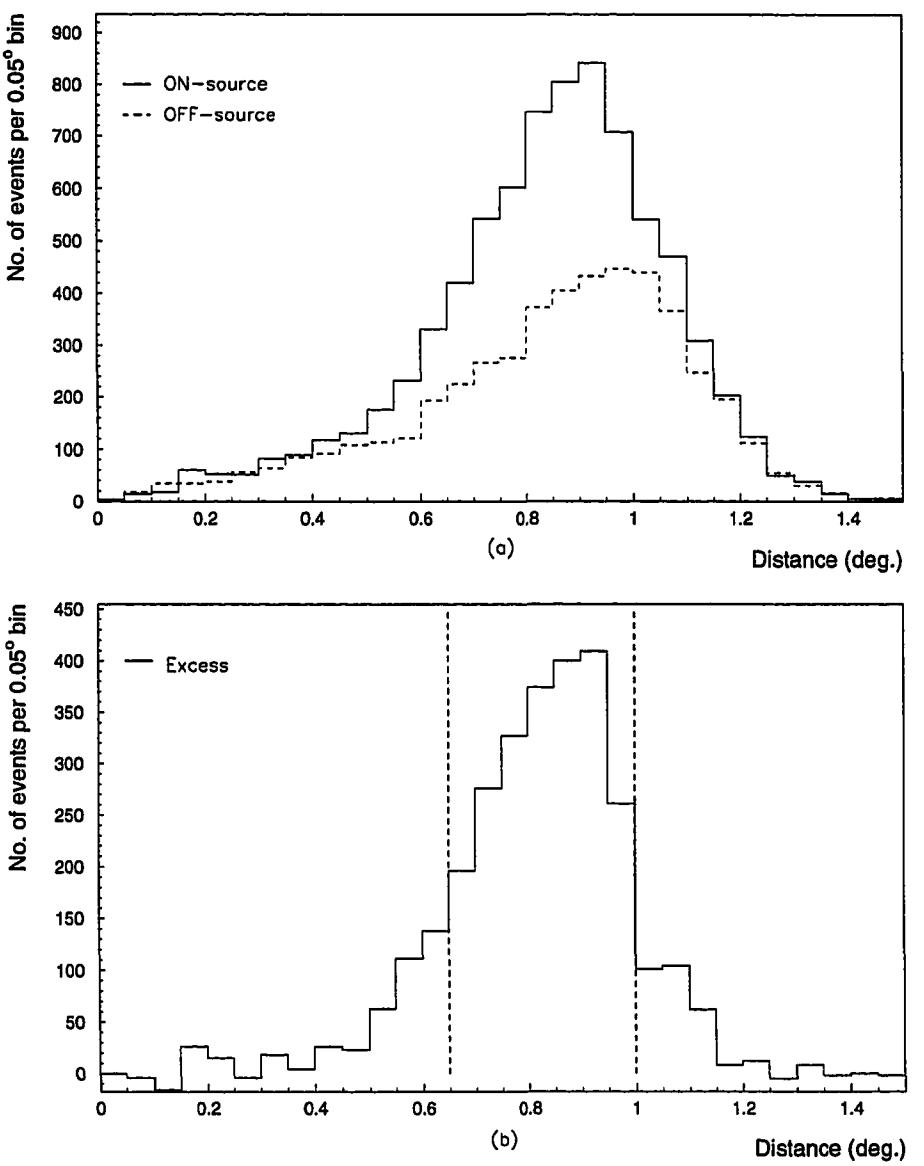

Figure 6.3: Crab 1988-89 distance distributions. (a) ON, and OFF distributions, and (b) distribution for the excess.

After choosing the restricted distance range, the entire spectrum determination procedure has to be repeated for this distance range. The steps in doing this, are:

1. Collection area: The parameterized collection area for the detector, found as described in sec. 4.6, is given by:

$$A(E) = 6.14 \times 10^3 \arctan\left(17.6 \times E^{4.37}\right) \ln(96.8 \times E) \exp(-E/14.6) \quad (6.6)$$

This is compared to the usual parameterized area for extended supercuts, as given by Eq. (4.16), in Fig. 6.4. As can be seen, the collection area is consider-

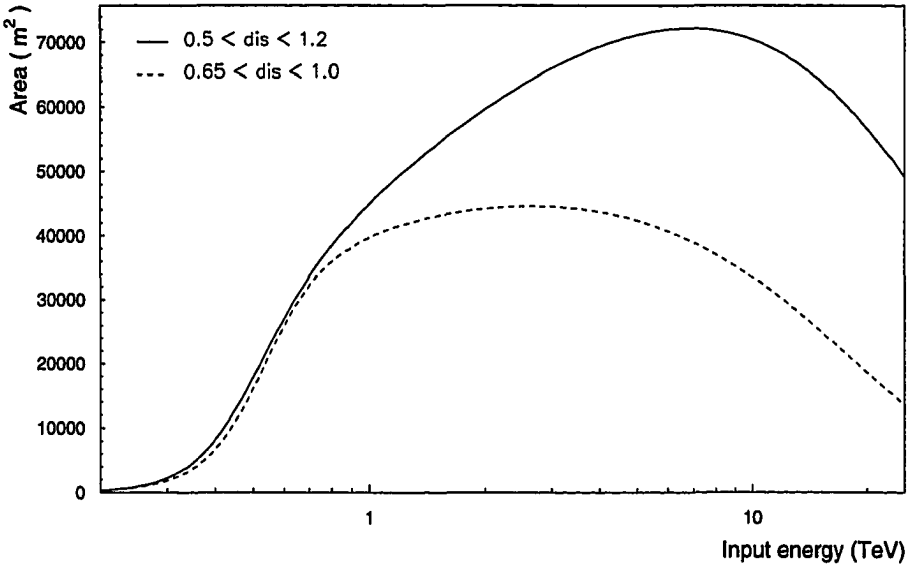

Figure 6.4: Comparison of parameterized areas, with and without a restricted distance cut.

ably reduced by the restricted distance cut, especially at high energies.

2. Energy estimate: This is derived, for the distance-independent energy estimate, as described in sec. 4.7.1. The fit for n_{dc} in terms of the energy, E and the energy estimation function derived by inverting this fit, are given by:

$$n_{dc} = 5.23 \times 10^3 \arctan\left[0.0368\ (E + 0.990)^{1.89}\right] \quad (6.7)$$

$$\tilde{E}(n_{dc}) = -0.0849 + 7.48\,[\tan(0.114\,n_{dc})]^{0.877} \qquad (6.8)$$

3. Energy resolution functions: Energy resolution functions are derived for the distance-independent estimate as described in sec. 4.7.4. As usual, these are described by truncated Breit-Wigner distributions, with mean equal to the real energy and a characteristic width derived from the fit to the observed widths. The fit to the simulated Breit-Wigner widths is given by:

$$\Gamma = -0.002 + 0.25E \qquad \text{Distance-independent case.} \qquad (6.9)$$

Fig. 6.5(a) compares the fits in n_{dc}, with and without a restricted distance cut. Fig. 6.5(b) compares the fit to the resolution functions in each case. For showers at a fixed energy, restricting the distance cut gives, in general, a larger value for the total ADC counts, as a larger portion of the shower image is contained in the camera. This effect should be particularly noticeable at higher energies, where the showers tend to be large and are only partially in the field of view. Fig. 6.5(a) agrees with this expectation.

Also, from Fig. 6.5(b), it can be seen that restricting the distance cut does decrease the variance in the energy estimation.

4. Spectrum estimation: Table 6.7 below gives the estimated flux values for the restricted distance cut. Only the collection area of the detector has been applied. All quoted fluxes are in $m^{-2}s^{-1}TeV^{-1}$. The best-fit spectrum for the restricted distance cut, applying only the collection area, is given by:

$$\frac{dN}{dE} = (2.42 \pm 0.12) \times 10^{-7} \left(\frac{E}{1\,\text{TeV}}\right)^{-2.55\pm0.08} \quad \frac{\#}{\text{m}^2\ \text{s sr TeV}} \qquad (6.10)$$

The fit gives an acceptable χ^2 of 11.3 for 6 degrees of freedom. When the effect of the finite energy resolution is included in addition to the collection area, the best-fit spectrum is given by:

$$\frac{dN}{dE} = (2.72 \pm 0.14) \times 10^{-7} \left(\frac{E}{1\,\text{TeV}}\right)^{-2.93\pm0.12} \quad \frac{\#}{\text{m}^2\ \text{s sr TeV}} \qquad (6.11)$$

with χ^2 equal to 6.2 for 6 degrees of freedom. The flux table is shown in Table 6.8.

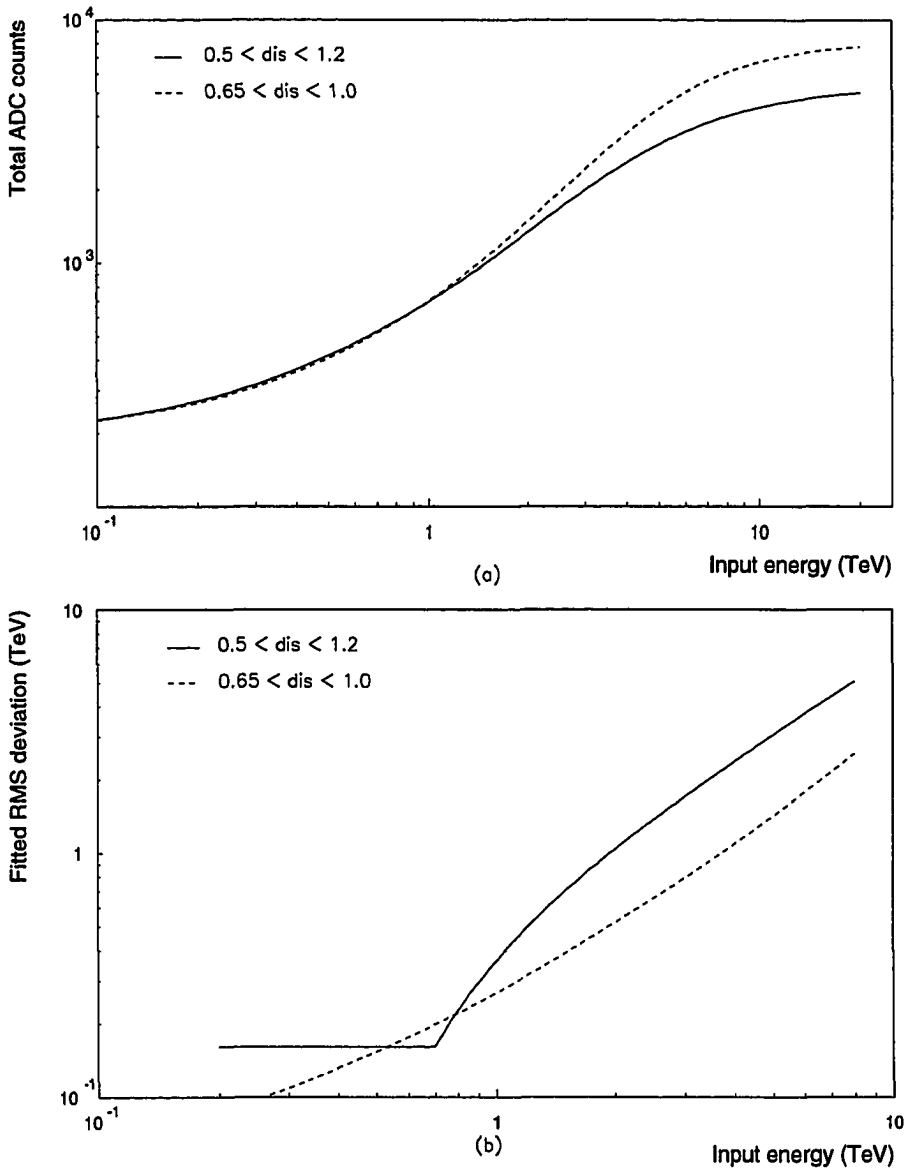

Figure 6.5: Crab 1988-89: (a) Comparison of fits of the total ADC counts, and (b) Comparison of fits to resolution function widths.

Table 6.7: 1988-89 Crab flux, for a restricted distance cut, using distance independent estimate, and without energy resolution.

Energy (TeV)	ON	OFF	σ	Actual flux	Fitted flux	Error	χ^2/bin
0.40–0.60	794	407	11.2	1.45×10^{-6}	1.42×10^{-6}	1.300×10^{-7}	0.1
0.60–0.90	809	398	11.8	4.59×10^{-7}	5.04×10^{-7}	3.879×10^{-8}	1.4
0.90–1.30	610	315	9.7	2.02×10^{-7}	1.90×10^{-7}	2.080×10^{-8}	0.3
1.30–1.90	452	261	7.2	8.10×10^{-8}	7.30×10^{-8}	1.132×10^{-8}	0.5
1.90–2.90	338	182	6.8	3.80×10^{-8}	2.60×10^{-8}	5.558×10^{-9}	4.7
2.90–4.60	170	116	3.2	7.70×10^{-9}	8.32×10^{-9}	2.413×10^{-9}	0.1
4.60–7.60	72	60	1.0	1.03×10^{-9}	2.41×10^{-9}	9.823×10^{-10}	2.0
7.60–13.60	25	24	0.1	5.03×10^{-11}	5.88×10^{-10}	3.519×10^{-10}	2.3

Table 6.8: 1988-89 Crab flux, for a restricted distance cut, using distance independent estimate, and including energy resolution.

Energy (TeV)	ON	OFF	σ	Actual flux	Fitted flux	Error	χ^2/bin
0.40–0.60	794	407	11.2	2.05×10^{-6}	1.42×10^{-6}	1.841×10^{-7}	12.0
0.60–0.90	809	398	11.8	6.21×10^{-7}	5.04×10^{-7}	5.251×10^{-8}	5.0
0.90–1.30	610	315	9.7	2.21×10^{-7}	1.90×10^{-7}	2.275×10^{-8}	1.8
1.30–1.90	452	261	7.2	7.69×10^{-8}	7.30×10^{-8}	1.076×10^{-8}	0.1
1.90–2.90	338	182	6.8	3.32×10^{-8}	2.60×10^{-8}	4.856×10^{-9}	2.2
2.90–4.60	170	116	3.2	6.44×10^{-9}	8.32×10^{-9}	2.015×10^{-9}	0.9
4.60–7.60	72	60	1.0	8.29×10^{-10}	2.41×10^{-9}	7.942×10^{-10}	3.9
7.60–13.60	25	24	0.1	3.79×10^{-11}	5.88×10^{-10}	2.651×10^{-10}	4.3

Thus, the estimated spectrum for the restricted distance cut of $0.65 <$ distance < 1.0 agrees, within statistical errors, to the spectrum measured for the usual set of extended supercuts which has a distance cut of $0.5 <$ distance < 1.2. Hence, for the other observing seasons, I use a distance cut of $0.5 <$ distance < 1.2. I will return to the restricted distance cut when estimating the systematic errors (see sec. 6.2.1.4), in order to see if it gives lower systematics.

6.2.1.4 Estimation of systematic errors The estimation of systematic errors is a tricky proposition. There are a vast number of input parameters to the simulations that have to be either experimentally measured or estimated from the

data. The overall reflectivity is derived from factors including atmospheric absorption, mirror reflectivity, PMT quantum efficiency, photoelectron to ADC counts conversion factor etc., which are poorly known. The amount of noise in the PMT channels affects the fluctuations in the total number of ADC counts, and thus worsens the energy resolution. Some of the noise contributions such as the night-sky and the non-Poissonian signal noise can be measured fairly well. However, I have made no attempt to model the noise arising from stars in the field of view of the camera[3]. Other systematic might arise from incomplete Monte Carlo statistics. Though we have simulated a large number of gamma ray showers, the energy resolution functions, for example, are still poorly determined.

A proper treatment of the systematic errors, obtained by varying each of the input parameters would be a tedious and lengthy task. Hence, I have chosen to lump all of these into the uncertainty in the overall reflectivity, which is probably the largest source of systematic error in the spectrum determination. Thus, I take a 25 % change on both sides of the best value for the overall reflectivity, and redo the spectrum analysis for the new reflectivity values. The best-fit spectrum then defines the systematic errors in the original estimate. This value of 25 % change in the reflectivity is an overestimate, as we can tell a change of this magnitude by matching the simulated by matching the background trigger rates from the proton simulations (see sec. 5.1.5.2, especially, Fig. 5.8). However, this overestimate also covers other sources of systematic error., besides the overall reflectivity.

Only the energy estimate independent of distance is considered, and the systematic errors for the usual set of extended supercuts are described below:

1. Collection area only: The systematic error in the spectral index is estimated to be 0.17, and the systematic error in the flux constant is found to be 1.4×10^{-7}.

2. Energy resolution applied: The systematic error in the spectral index is estimated to be 0.21, and the systematic error in the flux constant is found to be 1.4×10^{-7}.

[3]This is not a problem for the Crab, as the ON-source and OFF-source regions have almost identical average sky brightness. However, it needs to be addressed for a general method of spectrum determination.

The systematic errors for the restricted distance cut, 0.65 < distance < 1.0, are given below:

1. Collection area only: The systematic error in the spectral index is estimated to be 0.26, and the systematic error in the flux constant is found to be 7×10^{-8}.

2. Energy resolution applied: The systematic error in the spectral index is estimated to be 0.20, and the systematic error in the flux constant is found to be 8×10^{-8}.

6.2.2 1989-90 season

The data taken between Sep. 1989 and Feb. 1990 is unsuitable for spectral analysis, due to the inclusion of an independent Cherenkov trigger that was given preference over the normal Cherenkov trigger. The independent trigger events were tagged as a code 9 in the data stream, while the normal Cherenkov trigger was a given a code 8.

Here, I examine the rates of each type of event from the background data taken from zenith files. A code 8 event trigger in the hardware is approximately equivalent to at least two out of the inner 91 tubes exceeding a preset voltage threshold that nominally corresponds to an integrated number of 50 ADC counts in each of the two tubes. Thus, it might be naively assumed that this trigger condition can be emulated in software to convert the hardware code 9 events into software code 8 events, and the software code 8 events can be treated on par with the hardware code 8 events. However, as I shall demonstrate by examining the distribution of ADC counts in the second highest tube, the two types of events have quite different properties. While it is not unreasonable to treat both types of events on par in looking for a simple DC excess, it is dangerous to carry over this assumption into spectral analysis work.

I use nine zenith files from the fall of 1989, which have both code 8 and code 9 events, comprising a total observation time of 8078.0 s; and seven zenith files from Nov. to Dec. 1988, that have only code 8 events and a total observation time of 6282.3 s. Fig. 6.6 compares the event rates from the two sets of zenith files, with both code 8 and code 9 events included in the set for 1989. Fig. 6.6(a) shows the event rates with no software trigger, while in Fig. 6.6(b) a software trigger condition of 50 ADC counts in at least two out of the inner 91 tubes has been applied. It appears as if the

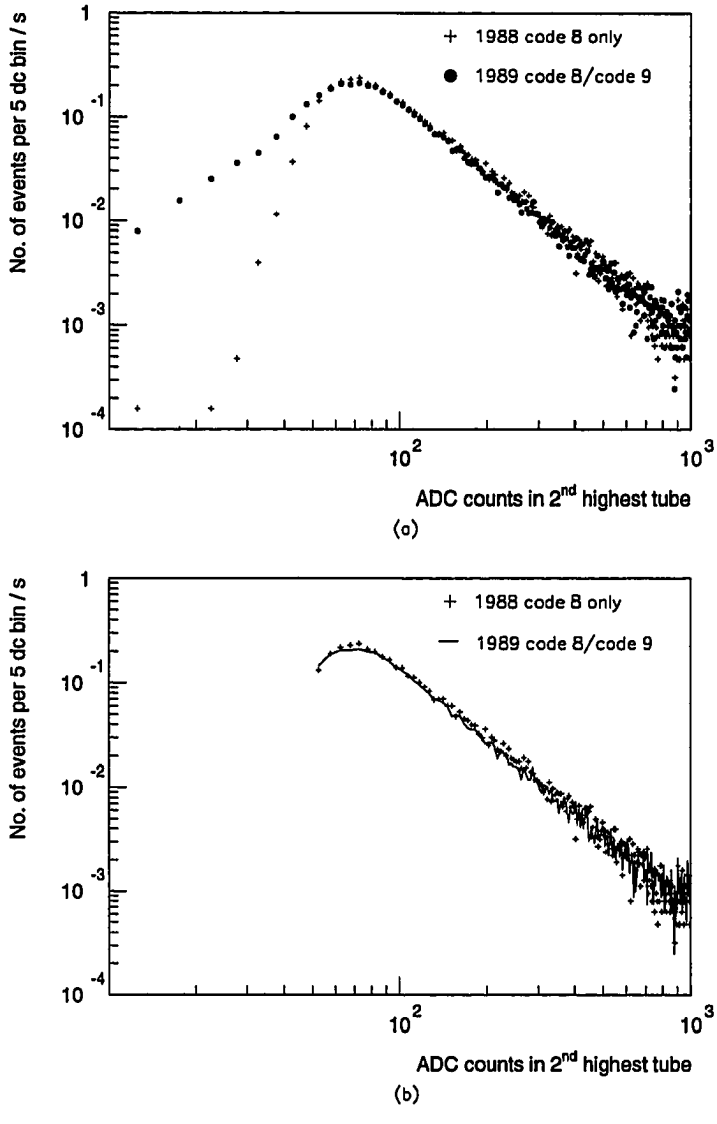

Figure 6.6: Comparison of event rates between 1988 and 1989 zenith files. (a) No software trigger. (b) 50 ADC counts in 2/91 software trigger.

differences apparent without a software trigger have been successfully eliminated by its application. However, a closer look reveals other differences. Fig. 6.2.2 compares the event rates in the 1989 set of zenith files, separately for the code 8 and code 9 events, after the use of a 2/91 software trigger. It can be seen that the spectra for the

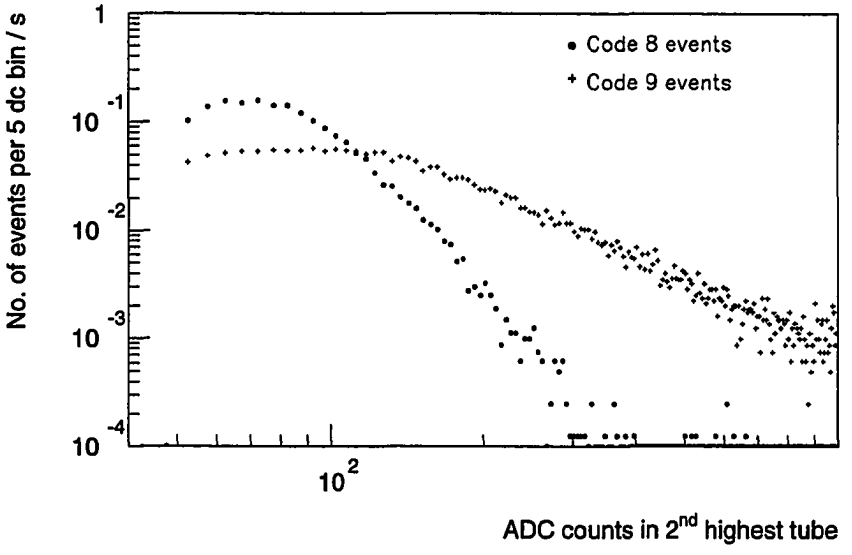

two types of events are markedly different, with the hardware code 8 events falling off rapidly with energy. Thus, this data is not suitable for the purposes of spectrum extraction.

The fact that the overall event rate (both code 8 and code 9 events) is similar to the case where there are only code 8 events implies that for a DC excess analysis, it is probably safe to treat code 9 events on par with code 8 events after the application of a software trigger condition. The difference between the software code 8 events and the hardware code 8 events probably arises from the 25 ns integration time in the ADCs.

6.2.3 1990 season

This has 17 pairs of runs, with a total ON-source time of 411 minutes, taken between Jan. 1990 and Aug. 1990. First, I give details of the input parameters used in the simulations for this season, and then I quote the results of applying these to the data.

6.2.3.1 Input parameters The standard deviations in the sky pedestals for the 1990 database are measured to be 3.62 ADC counts for the 2.9 cm inner tubes, and 3.34 ADC counts for the 4.3 cm outer tubes. The non-Poissonian factor or the signal noise is estimated to be 1.5 for the 2.9 cm tubes, and 1.6 for the 4.3 cm tubes; same as for the 1988-89 database. The discriminator trigger function is parameterized as:

$$D(x) = \begin{cases} 0, & \text{if } x < 21.8; \\ \frac{2}{\pi} \arctan\left[7.0 \times 10^{-7} \left(x - 21.8\right)^{3.73}\right], & \text{otherwise.} \end{cases} \tag{6.12}$$

Other input parameters for the simulations relevant to the 1990 database may be obtained by scaling from the 1988-89 values as described in sec. 3.4.3.2. The overall reflectivity (mirrors plus PMTs) is estimated to be 53 % of the 1988-89 reflectivity, and the photoelectron to ADC count conversion factor is estimated as 1.41 d.c./p.e.

6.2.3.2 Measured spectrum This section presents the results of using extended supercuts to measure the Crab spectrum for the 1990 observing season. I only quote results for the usual distance cut (0.5 < distance < 1.2), and a distance independent energy estimate based only on the total ADC counts.

1. *Extended supercuts:* The set of loose extended supercuts for the 1990 season is given by:

$$\begin{aligned} [-0.005 + 0.024 \ln(n_{dc})] - 0.058 < (\text{width}) &< [-0.005 + 0.024 \ln(n_{dc})] + 0.036 \\ [0.131 + 0.018 \ln(n_{dc})] - 0.086 < (\text{length}) &< [0.131 + 0.018 \ln(n_{dc})] + 0.046 \\ (\text{alpha}) &< [13.07 - 0.90 \ln(n_{dc})] + 10.0 \\ 0.50 < (\text{distance}) &< 1.2 \end{aligned}$$

2. *Collection area:* The collection area for the 1990 season is parameterized as:

$$A(E) = 1.46 \times 10^4 \arctan\left(17.5 \times E^{3.83}\right) \ln(8.19 \times E) \exp(-E/27.4) \quad (6.13)$$

3. *Energy estimate:* The energy estimate is obtained by the usual procedure of fitting the total ADC counts to the known Monte Carlo input energy, and then inverting the fit to get an energy estimation function. The fit, and the energy estimate are given by:

$$n_{dc} = 3.43 \times 10^3 \arctan\left[0.0889\ (E + 0.733)^{1.45}\right] \quad (6.14)$$

$$\tilde{E} = -0.701 + 5.30\ \left[\tan\left(2.92 \times 10^{-4}\, n_{dc}\right)\right]^{0.689} \quad (6.15)$$

4. *Energy resolution functions:* These have the usual Breit-Wigner form, with a characteristic width derived from the fit to the observed widths from the simulations. This fit is given by:

$$\Gamma = \begin{cases} 0.18, & \text{if } E < 0.89; \\ -0.40 + 0.66E, & \text{otherwise.} \end{cases} \quad (6.16)$$

5. Spectrum estimation: The flux values for extended supercuts, using the collection area of the detector only are given in Table. 6.9. The overall value of χ^2 for 5 degrees of freedom, is 1.8, The best-fit spectrum, with 1-σ statistical errors, is given by:

$$\frac{dN}{dE} = (2.40 \pm 0.29) \times 10^{-7} \left(\frac{E}{1\,\text{TeV}}\right)^{-2.73 \pm 0.21} \quad \frac{\#}{\text{m}^2\ \text{s sr TeV}} \quad (6.17)$$

Table 6.9: 1990 Crab flux, using distance independent estimate, and without energy resolution

Energy (TeV)	ON	OFF	σ	Actual flux	Fitted flux	Error	χ^2/bin
0.60–0.90	242	141	5.2	4.94×10^{-7}	5.26×10^{-7}	9.565×10^{-8}	0.1
0.90–1.30	201	112	5.0	2.09×10^{-7}	1.85×10^{-7}	4.147×10^{-8}	0.3
1.30–1.90	136	87	3.3	6.20×10^{-8}	6.65×10^{-8}	1.890×10^{-8}	0.1
1.90–2.90	106	70	2.7	2.34×10^{-8}	2.20×10^{-8}	8.632×10^{-9}	0.0
2.90–4.60	66	45	2.0	7.13×10^{-9}	6.50×10^{-9}	3.577×10^{-9}	0.1
4.60–7.60	39	27	1.5	2.13×10^{-9}	1.72×10^{-9}	1.440×10^{-9}	0.0
7.60–13.60	22	25	-0.4	-2.56×10^{-10}	3.81×10^{-10}	5.856×10^{-10}	1.2

Table 6.10: 1990 Crab flux, using distance independent estimate, and including energy resolution

Energy (TeV)	ON	OFF	σ	Actual flux	Fitted flux	Error	χ^2/bin
0.60–0.90	242	141	5.2	6.26×10^{-7}	6.74×10^{-7}	1.212×10^{-7}	0.2
0.90–1.30	201	112	5.0	2.34×10^{-7}	2.11×10^{-7}	4.652×10^{-8}	0.4
1.30–1.90	136	87	3.3	6.64×10^{-8}	6.79×10^{-8}	2.023×10^{-8}	0.4
1.90–2.90	106	70	2.7	2.18×10^{-8}	1.99×10^{-8}	8.033×10^{-9}	0.5
2.90–4.60	66	45	2.0	5.51×10^{-9}	5.14×10^{-9}	2.766×10^{-9}	0.5
4.60–7.60	39	27	1.5	1.36×10^{-9}	1.18×10^{-9}	9.204×10^{-10}	0.5
7.60–13.60	22	25	-0.4	-1.36×10^{-10}	2.21×10^{-10}	3.106×10^{-10}	1.8

The flux values for extended supercuts, using the energy resolution functions, in addition to the detector area are given in Table. 6.10. The overall value of χ^2 for 5 degrees of freedom, is 1.8, The best-fit spectrum, with 1-σ statistical errors, is given by:

$$\frac{dN}{dE} = (2.82 \pm 0.33) \times 10^{-7} \left(\frac{E}{1\,\mathrm{TeV}}\right)^{-3.03\pm0.29} \quad \frac{\#}{\mathrm{m^2\ s\ sr\ TeV}} \tag{6.18}$$

6.2.4 1990-91 season

This includes 39 pairs of runs, taken between Oct. 90 and January 1991. The total on-source observation time is 1072 minutes.

6.2.4.1 Input parameters The standard deviations in the sky pedestals for the 1990-91 database are measured to be 3.68 ADC counts for the 2.9 cm inner tubes, and 3.47 ADC counts for the 4.3 cm outer tubes. The non-Poissonian factor or the signal noise is estimated to be 1.5 for the 2.9 cm tubes, and 1.6 for the 4.3 cm tubes; same as for the 1988-89 database. The discriminator trigger function is parameterized as:

$$D(x) = \begin{cases} 0, & \text{if } x < 22.3; \\ \frac{2}{\pi} \arctan\left[2.2 \times 10^{-8} \left(x - 22.2\right)^{4.65}\right], & \text{otherwise.} \end{cases} \tag{6.19}$$

Other input parameters for the simulations relevant to the 1990-91 database may be obtained by scaling from the 1988-89 values in a manner similar to that

described in sec. 3.4.3. For this purpose, I use seven zenith files from 1988-89 with a total observation time of 6282.3 s and fifteen zenith files from 1990-91 with a total observation time of 12391.5 s, and vary the threshold cutoff from 90 ADC counts to 500 ADC counts. The results are summarized in Table 6.11 below. From the values

Table 6.11: Comparison of background rates: 1988-89 and 1990-91.

Threshold	1988 rate	1990-91 rate	F_{91}/F_{88}	$g_{91}r_{91}/g_{88}r_{88}$
90	2.44	1.82	0.75	0.80
100	2.14	1.58	0.74	0.80
200	0.81	0.57	0.70	0.77
300	0.42	0.30	0.71	0.78
400	0.25	0.18	0.72	0.78
500	0.16	0.12	0.75	0.81

in the table, we take the ratio of the telescope throughputs to be given by:

$$\frac{g_{91}\, r_{91}}{g_{88}\, r_{88}} = 0.79 \tag{6.20}$$

From Eq. 3.42, we also have the following relation between the photoelectron to ADC counts conversion factor, g, and the overall reflectivity, r:

$$\frac{g_{91}\sqrt{r_{91}}}{g_{88}\sqrt{r_{88}}} = \frac{\sigma_{91}}{\sigma_{88}} = 1.2 \tag{6.21}$$

Thus, the overall reflectivity (mirrors plus PMTs) is estimated to be 43 % of the 1988-89 reflectivity, and the photoelectron to ADC count conversion factor is estimated as 1.55 d.c./p.e.

6.2.4.2 Measured spectrum This section presents the results of using extended supercuts to measure the Crab spectrum for the 1990-91 observing season. I only quote results for the usual distance cut ($0.5 <$ distance < 1.2), and a distance independent energy estimate based only on the total ADC counts.

1. *Extended supercuts:* The set of loose extended supercuts for the 1990-91 season is given by:

$$[-0.007 + 0.024 \ln(n_{dc})] - 0.062 < (\text{width}) \;<\; [-0.007 + 0.024 \ln(n_{dc})] + 0.034$$

$$
\begin{aligned}
[0.126 + 0.018 \ln(n_{dc})] - 0.084 < (\text{length}) &< [0.126 + 0.018 \ln(n_{dc})] + 0.046 \\
(\text{alpha}) &< [12.76 - 0.90 \ln(n_{dc})] + 9.4 \\
0.50 < (\text{distance}) &< 1.2
\end{aligned}
$$

2. *Collection area:* The collection area for the 1990-91 season is parameterized as:

$$A(E) = 1.43 \times 10^4 \arctan\left(6.87 \times E^{4.22}\right) \ln(5.92 \times E) \exp(-E/33.7) \quad (6.22)$$

3. *Energy estimate:* The energy estimate is obtained by the usual procedure of fitting the total ADC counts to the known Monte Carlo input energy, and then inverting the fit to get an energy estimation function. The fit, and the energy estimate are given by:

$$n_{dc} = 3.35 \times 10^3 \arctan\left[0.0661\ (E + 0.943)^{1.52}\right] \quad (6.23)$$

$$\tilde{E} = -0.943 + 5.96\ \left[\tan\left(2.98 \times 10^{-4}\, n_{dc}\right)\right]^{0.657} \quad (6.24)$$

4. *Energy resolution functions:* These have the usual Breit-Wigner form, with a characteristic width derived from the fit to the observed widths from the simulations. This fit is given by:

$$\Gamma = \begin{cases} 0.23, & \text{if } E < 0.81; \\ -0.045 + 0.29E - 0.059E^2, & \text{otherwise.} \end{cases} \quad (6.25)$$

5. Spectrum estimation: The flux values for extended supercuts, using the collection area of the detector only are given in Table. 6.12. The overall value of χ^2 for 5 degrees of freedom, is 6.6, The best-fit spectrum, with 1-σ statistical errors, is given by:

$$\frac{dN}{dE} = (2.06 \pm 0.18) \times 10^{-7} \left(\frac{E}{1\,\text{TeV}}\right)^{-2.59 \pm 0.13} \quad \frac{\#}{\text{m}^2\ \text{s sr TeV}} \quad (6.26)$$

The flux values for extended supercuts, using the energy resolution functions, in addition to the detector area are given in Table. 6.13. The overall value of χ^2 for 5 degrees of freedom, is 4.9, The best-fit spectrum, with 1-σ statistical errors, is given by:

$$\frac{dN}{dE} = (2.68 \pm 0.23) \times 10^{-7} \left(\frac{E}{1\,\text{TeV}}\right)^{-2.95 \pm 0.19} \quad \frac{\#}{\text{m}^2\ \text{s sr TeV}} \quad (6.27)$$

Table 6.12: 1990-91 Crab flux, using distance independent estimate, and without energy resolution

Energy (TeV)	ON	OFF	σ	Actual flux	Fitted flux	Error	χ^2/bin
0.60–0.90	428	264	6.2	3.82×10^{-7}	4.34×10^{-7}	6.127×10^{-8}	0.7
0.90–1.30	380	219	6.6	1.61×10^{-7}	1.61×10^{-7}	2.445×10^{-8}	0.7
1.30–1.90	354	200	6.5	8.09×10^{-8}	6.10×10^{-8}	1.236×10^{-8}	3.3
1.90–2.90	247	148	5.0	2.63×10^{-8}	2.13×10^{-8}	5.286×10^{-9}	4.2
2.90–4.60	157	117	2.4	5.48×10^{-9}	6.72×10^{-9}	2.266×10^{-9}	4.5
4.60–7.60	66	55	1.0	7.75×10^{-10}	1.90×10^{-9}	7.752×10^{-10}	6.6
7.60–13.60	46	33	1.5	4.34×10^{-10}	4.55×10^{-10}	2.969×10^{-10}	6.6

Table 6.13: 1990-91 Crab flux, using distance independent estimate, and including energy resolution

Energy (TeV)	ON	OFF	σ	Actual flux	Fitted flux	Error	χ^2/bin
0.60–0.90	428	264	6.2	5.63×10^{-7}	6.26×10^{-7}	9.023×10^{-8}	0.5
0.90–1.30	380	219	6.6	1.96×10^{-7}	2.02×10^{-7}	2.977×10^{-8}	0.5
1.30–1.90	354	200	6.5	8.46×10^{-8}	6.70×10^{-8}	1.293×10^{-8}	2.4
1.90–2.90	247	148	5.0	2.41×10^{-8}	2.02×10^{-8}	4.828×10^{-9}	3.0
2.90–4.60	157	117	2.4	4.47×10^{-9}	5.43×10^{-9}	1.849×10^{-9}	3.3
4.60–7.60	66	55	1.0	5.70×10^{-10}	1.29×10^{-9}	5.695×10^{-10}	4.9
7.60–13.60	46	33	1.5	2.77×10^{-10}	2.53×10^{-10}	1.893×10^{-10}	4.9

6.2.5 1991-92

This includes 18 pairs of runs with a total on-source observation time of 491 minutes.

6.2.5.1 Input parameters The instrumentation of the 10-meter telescope was in a state of flux over this observing season, and the data acquisition system was not fully stable. Hence we have had to discard a large portion of the data, and have only 18 usable run pairs.

The standard deviations in the sky pedestals for the 1991-92 database are measured to be 3.79 ADC counts for the 2.9 cm inner tubes, and 3.20 ADC counts for the 4.3 cm outer tubes. The non-Poissonian factor or the signal noise is estimated

to be 1.5 for the 2.9 cm tubes, and 1.6 for the 4.3 cm tubes; same as for the 1988-89 database. The discriminator trigger function is parameterized as:

$$D(x) = \begin{cases} 0, & \text{if } x < 24.8; \\ \frac{2}{\pi} \arctan\left[6.5 \times 10^{-4} (x - 24.8)^{2.65}\right], & \text{otherwise.} \end{cases} \tag{6.28}$$

Other input parameters for the simulations relevant to the 1991-92 database may be obtained by scaling from the 1988-89 values in a manner similar to that described in sec. 3.4.3. For this purpose, I use seven zenith files from 1988-89 with a total observation time of 6282.3 s and four zenith files from 1991-92, and vary the threshold cutoff from 90 ADC counts to 500 ADC counts. The results are summarized in Table 6.14 below. From the values in the table, we take the ratio of the telescope

Table 6.14: Comparison of background rates: 1988-89 and 1991-92.

Threshold	1988 rate	1991-92 rate	F_{92}/F_{88}	$g_{92}r_{92}/g_{88}r_{88}$
90	2.44	1.63	0.67	0.74
100	2.14	1.44	0.67	0.74
200	0.81	0.56	0.69	0.76
300	0.42	0.29	0.69	0.76
400	0.25	0.17	0.68	0.75
500	0.16	0.10	0.63	0.70

throughputs to be given by:

$$\frac{g_{92}\, r_{92}}{g_{88}\, r_{88}} = 0.75 \tag{6.29}$$

From Eq. 3.42, we also have the following relation between the photoelectron to ADC counts conversion factor, g, and the overall reflectivity, r:

$$\frac{g_{92}\sqrt{r_{92}}}{g_{88}\sqrt{r_{88}}} = \frac{\sigma_{92}}{\sigma_{88}} = 1.2 \tag{6.30}$$

Thus, the overall reflectivity (mirrors plus PMTs) is estimated to be 39 % of the 1988-89 reflectivity, and the photoelectron to ADC count conversion factor is estimated as 1.63 d. c./p. e.

6.2.5.2 Measured spectrum This section presents the results of using extended supercuts to measure the Crab spectrum for the 1991-92 observing season. I

only quote results for the usual distance cut ($0.5 <$ distance < 1.2), and a distance independent energy estimate based only on the total ADC counts.

1. *Extended supercuts:* The set of loose extended supercuts for the 1991-92 season is given by:

$$\begin{aligned} [-0.018 + 0.025 \ln(n_{dc})] - 0.066 < (\text{width}) &< [-0.018 + 0.025 \ln(n_{dc})] + 0.034 \\ [0.125 + 0.018 \ln(n_{dc})] - 0.086 < (\text{length}) &< [0.125 + 0.018 \ln(n_{dc})] + 0.044 \\ (\text{alpha}) &< [11.92 - 0.79 \ln(n_{dc})] + 9.0 \\ 0.50 < (\text{distance}) &< 1.2 \end{aligned}$$

2. *Collection area:* The collection area for the 1991-92 season is parameterized as:

$$A(E) = 1.27 \times 10^4 \arctan\left(5.00 \times E^{4.20}\right) \ln(7.41 \times E) \exp(-E/40.6) \quad (6.31)$$

3. *Energy estimate:* The energy estimate is obtained by the usual procedure of fitting the total ADC counts to the known Monte Carlo input energy, and then inverting the fit to get an energy estimation function. The fit, and the energy estimate are given by:

$$n_{dc} = 3.16 \times 10^3 \arctan\left[0.0343\ (E + 1.52)^{1.82}\right] \quad (6.32)$$

$$\tilde{E} = -1.52 + 6.34\ \left[\tan\left(3.17 \times 10^{-4}\, n_{dc}\right)\right]^{0.548} \quad (6.33)$$

4. *Energy resolution functions:* These have the usual Breit-Wigner form, with a characteristic width derived from the fit to the observed widths from the simulations. This fit is given by:

$$\Gamma = \begin{cases} 0.26, & \text{if } E < 0.93; \\ -0.22 + 0.49E + 0.022E^2, & \text{otherwise.} \end{cases} \quad (6.34)$$

5. Spectrum estimation: The flux values for extended supercuts, using the collection area of the detector only are given in Table. 6.15. The overall value of χ^2 for 5 degrees of freedom, is 3.2, The best-fit spectrum, with 1-σ statistical errors, is given by:

$$\frac{dN}{dE} = (1.92 \pm 0.28) \times 10^{-7} \left(\frac{E}{1\,\text{TeV}}\right)^{-2.70 \pm 0.26} \quad \frac{\#}{\text{m}^2\ \text{s sr TeV}} \quad (6.35)$$

Table 6.15: 1991-92 Crab flux, using distance independent estimate, and without energy resolution

Energy (TeV)	ON	OFF	σ	Actual flux	Fitted flux	Error	χ^2/bin
0.60–0.90	172	99	4.4	4.13×10^{-7}	4.18×10^{-7}	9.312×10^{-8}	0.0
0.90–1.30	172	117	3.2	1.23×10^{-7}	1.48×10^{-7}	3.794×10^{-8}	0.5
1.30–1.90	170	108	3.7	7.20×10^{-8}	5.40×10^{-8}	1.937×10^{-8}	0.8
1.90–2.90	144	99	2.9	2.66×10^{-8}	1.81×10^{-8}	9.210×10^{-9}	0.9
2.90–4.60	90	76	1.1	4.27×10^{-9}	5.41×10^{-9}	3.930×10^{-9}	0.1
4.60–7.60	54	50	0.4	6.26×10^{-10}	1.46×10^{-9}	1.596×10^{-9}	0.2
7.60–13.60	22	23	-0.1	-7.30×10^{-11}	3.27×10^{-10}	4.899×10^{-10}	0.7

The flux values for extended supercuts, using the energy resolution functions, in addition to the detector area are given in Table. 6.16. The overall value of χ^2 for 5 degrees of freedom, is 2.9, The best-fit spectrum, with 1-σ statistical errors, is given by:

$$\frac{dN}{dE} = (2.52 \pm 0.36) \times 10^{-7} \left(\frac{E}{1\,\mathrm{TeV}}\right)^{-3.17 \pm 0.36} \quad \frac{\#}{\mathrm{m^2\ s\ sr\ TeV}} \tag{6.36}$$

Table 6.16: 1991-92 Crab flux, using distance independent estimate, and including energy resolution

Energy (TeV)	ON	OFF	σ	Actual flux	Fitted flux	Error	χ^2/bin
0.60–0.90	172	99	4.4	6.30×10^{-7}	6.27×10^{-7}	1.421×10^{-7}	0.0
0.90–1.30	172	117	3.2	1.49×10^{-7}	1.86×10^{-7}	4.609×10^{-8}	0.7
1.30–1.90	170	108	3.7	7.34×10^{-8}	5.68×10^{-8}	1.974×10^{-8}	1.4
1.90–2.90	144	99	2.9	2.26×10^{-8}	1.57×10^{-8}	7.831×10^{-9}	2.1
2.90–4.60	90	76	1.1	3.03×10^{-9}	3.82×10^{-9}	2.784×10^{-9}	2.2
4.60–7.60	54	50	0.4	3.78×10^{-10}	8.16×10^{-10}	9.645×10^{-10}	2.4
7.60–13.60	22	23	-0.1	-3.76×10^{-11}	1.42×10^{-10}	2.521×10^{-10}	2.9

CHAPTER 7. CONCLUDING REMARKS

7.1 Summary of results

1. *Monte Carlo input parameters:* I have taken pains to track down all of the important parameters that are used in the Monte Carlo simulations. Rather than take previously accepted values on faith, I have personally repeated the calculations, where possible. I have also tried to tie in with other determinations of various quantities, such as the photoelectron to ADC counts conversion factor.

2. *The set of extended supercuts:* By considering the 1988-89 Crab database, I have demonstrated that the loose extended supercuts perform almost as well as standard supercuts in source detection, while retaining a significantly larger number of gamma-ray-like showers. Recall that standard supercuts was optimized to this database, while extended supercuts are derived from simulations. Thus, this gain in retaining gamma rays while maintaining high significance can be expected to be even greater for other observing seasons.

   From the simulations, I have shown that the efficiency of extended supercuts in retaining gamma rays is almost independent of the energy of the primary gamma ray, at least out to an energy of $\sim$ 10 TeV, while the efficiency of standard supercuts falls off with energy. This fact might be useful in detecting a hypothetical source with an unusually hard spectrum.

3. *Energy estimation, and resolution:* I have used an energy estimate based only on the total number of ADC counts. The resolution of this estimate has been investigated using the simulations, and I have come up with a prescription for deconvolving the energy resolution from the observed spectrum. This, however, is probably the weakest point in the method of spectrum estimation as the

energy resolution functions are poorly determined and heavily dependent on the parameters used in the simulations.

I have also tried an energy estimate that has an additional distance dependence at higher estimated energies. Though this distance dependence seemed to help in reducing the variance of the estimated energy in the simulations, it was found to be unstable when applied to the data. This form of the energy estimate should be investigated further.

4. *Restricted distance cut:* I have tried restricting the distance cut to the range of 0.65 to 1.0, with the aim of improving the energy resolution. Though this helped in reducing the variance in the energy estimate, it results in a loss of collection area at higher energies. As the results obtained for the 1988-89 database were not significantly different for the restricted distance cut, I have chosen not to use it.

5. *Measured spectrum:* The final measured value of the spectrum of the flux from the Crab Nebula as observed for the 1988-89 season, using a distance-independent energy estimate, and applying only the collection area of the detector is given by:

$$\frac{dN}{dE} = (2.60 \pm 0.12 \pm 1.4) \times 10^{-7} \left(\frac{E}{1\,\mathrm{TeV}}\right)^{-2.61\pm0.07\pm0.17} \quad \frac{\#}{\mathrm{m^2\ s\ sr\ TeV}} \tag{7.1}$$

The two quoted errors for the flux constant and the spectral index, are, respectively, the statistical error, and the estimated systematic error. The systematic error derives predominantly from the uncertainty in the calibration of the of the observed ADC counts to the Cherenkov photons in the shower.

Upon application of the energy resolution functions appropriate for the distance-independent energy estimate, the measured spectrum is given by:

$$\frac{dN}{dE} = (2.98 \pm 0.15 \pm 1.4) \times 10^{-7} \left(\frac{E}{1\,\mathrm{TeV}}\right)^{-2.91\pm0.11\pm0.21} \quad \frac{\#}{\mathrm{m^2\ s\ sr\ TeV}} \tag{7.2}$$

These fits are shown in Fig. 7.1. The points with errorbars represent the estimated flux from the data, the solid line shows the best-fit spectrum, and the

dashed error box gives the 1-σ errors (both statistical and systematic) on the spectrum. Fig. 7.1(a) shows the fit when only the detector area is applied, and Fig. 7.1(b) shows the effect of applying the energy resolution functions in addition to this. Note that the two values for the flux agree to within statistical errors.

The fitted spectra for the other seasons also agree with the 1988-89 spectrum. The total integral flux is in fair agreement with an earlier measurement of the Crab Nebula spectrum by the Whipple Observatory (see Vacanti et al. [112]), though I estimate a steeper spectral index. The disagreement in the index is within the estimated systematic errors. The integral flux is also in agreement with measurements made by independent groups (see references in sec. 2.2). This agreement should not be over-interpreted, as the spectrum from an air Cherenkov telescope is poorly determined, and there are certainly large systematic differences between different detectors, in estimating the absolute energy.

6. *Final caveat:* I stress again that there are large errors in the determined spectrum, and it is meaningless to talk about small differences in the spectral index. The integral flux should, however, be a more meaningful number and has implications for detectors operating at higher energies.

   Also, all these results are very much dependent on the Monte Carlo simulations, and in particular, the inputs to the simulation programs. We have spent the past year and a half in trying to resolve intra-collaboration differences in the measured Crab spectrum. In the process, we feel that we have made a lot of progress in understanding the behaviour of the detector. There are still small differences between these results and those obtained by Michael Hillas and Matthew West at the University of Leeds. They have used a completely different set of simulation programs, and different selection criteria to calculate the spectrum. They measure approximately the same integral flux, but a slightly flatter spectrum. We are trying to pin down the last remaining differences between the two simulation programs, and expect to come to an agreement in the near future.

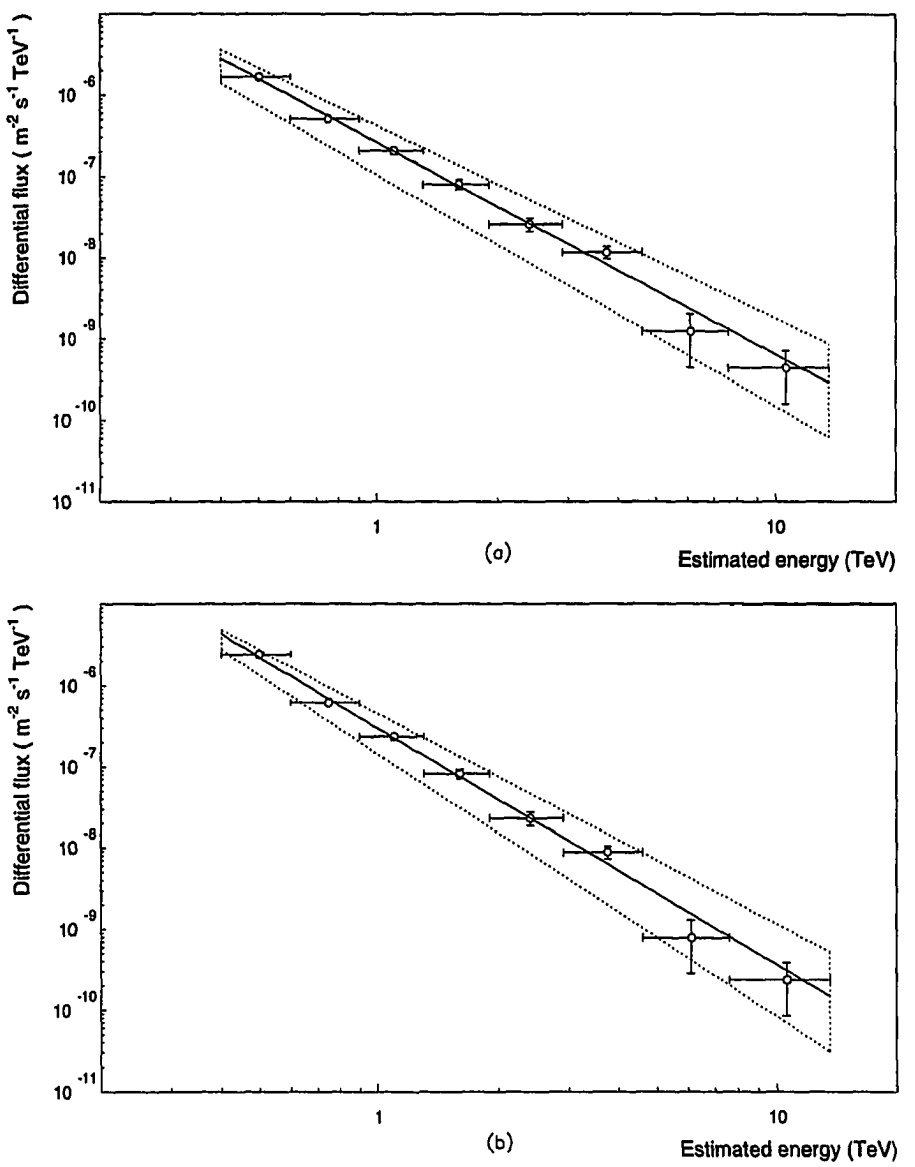

Figure 7.1: Fitted spectra to the Crab 1988-89 database, showing both statistical and systematic errors. (a) Without energy resolution, and (b) with energy resolution.

7.2 Future directions

The chief uncertainty in the spectrum estimation is the overall efficiency of the detector in converting Cherenkov photons to recorded ADC counts. In order to get a better handle on this, a twofold effort is required. On one hand, the knowledge of the various detector parameters that go into determining this conversion can be improved without a major upgrade of the detector hardware. In this line, the Whipple Observatory has started routine measurements of quantities like mirror reflectivity, PMT quantum efficiency. etc. The use of muon rings and arcs, produced by the Cherenkov light from relativistic muons that get close to the detector, holds out the promise of allowing for the accurate calibration of the reflectivity of the detector as a whole, and even of individual mirror facets and the efficiency of individual PMT's. This calibration of the detector is likely to become routine and even get merged into the data acquisition software, so that it would be possible to do online, real-time monitoring of the detector. Simultaneously, the improvement of the Monte Carlo programs, and the simulation of large numbers of background cosmic ray showers can help us understand the detector better, and provide an independent calibration from the known spectrum of the cosmic rays. A better treatment of the systematic errors, treating each contribution in detail is also obviously needed.

The other aspect of improving the spectrum measurement is the upgrade of the detector. A larger field of view for the focal plane detector will ensure that more of the shower light is sampled and allow retention of high energy gamma ray showers. Ultimately, it might be possible to record individual PMT pulse profiles, rather than having to integrate the pulses[1]. Improved tracking and pointing accuracy are also desirable. With an array of detectors, multiple views of a single shower can be taken from different angles, helping in the energy resolution.

Finally, the spectrum estimation method needs to be applied to other sources also. The obvious candidate is Markarian 421, whose spectrum has very interesting scientific implications.

[1]This is technically feasible now, but is prohibitively expensive for a large number of channels.

BIBLIOGRAPHY

[1] C. W. Allen. Astrophysical Quantities, 2nd ed. (Athlone Press, Univ. of London 1963).

[2] F. A. Aharonian. (private communication to de Jager et al.) 1994.

[3] C. W. Akerlof, J. DiMarco, H. Levy, D. Meyer, P. Radusewicz, R. Tschirhart, and Z. Yama. "Detection of very high energy gamma-rays from the Crab Nebula," Proc. of the GRO Science workshop (NASA/GSFC), ed. W. N. Johnson, (Naval Research Lab. Washington DC), 4-49 (1989).

[4] D. E. Alexandreas, et al. Proc. 23rd Int. Cosmic Ray Conf. (Calgary), **1**, 353 (1993).

[5] M. Amenomori, et al. Proc. 23rd Int. Cosmic Ray Conf. (Calgary), **1**, 342 (1993).

[6] W. I. Axford. Proc. 17th Int. Cosmic Ray Conf. (Paris), (1971).

[7] D. L. Bertsch, C. Fichtel, R. Hartman, S. Hunter, D. Thompson, B. Dingus, J. Esposito, R. Mukherjee, P. Sreekumar, C. von Montigny, J. Fierro, G. Kanbach, H. Mayer-Hasselwander, D. Kniffen, E. Schneid, and J. Mattox. "Recent results from the EGRET High Energy Gamma-Ray Telescope," Bull. Am. Astron. Soc., **186**, #05.08 (1995).

[8] H. J. Bhabha, and W. Heitler. "The passage of fast electrons and the theory of cosmic ray showers," Proc. R. Soc. London, Series A, **159**, 432 (1936).

[9] H. J. Bhabha, and S. K. Chakrabarty, Proc. Indian Acad. Sci., **15A**, 464 (1942).

[10] H. J. Bhabha, and S. K. Chakrabarty, "The cascade theory with collision loss," Proc. R. Soc. London, Series A, **181**, 267 (Sep. 1942–July 1943).

[11] H. J. Bhabha, and S. K. Chakrabarty, "Further calculations on the cascade theory," Phys. Rev., **74**, 1352 (1948).

[12] S. D. Biller. "Determination of the Discriminator Threshold Function." (Whipple Collaboration internal report) 1995.

[13] S. D. Biller. (private communication) 1995.

[14] S. D. Biller, C. W. Akerlof, J. Buckley, M. F. Cawley, D. J. Fegan, J. A. Gaidos, A. M. Hillas, A. D. Kerrick, R. C. Lamb, D. A. Lewis, D. I. Meyer, G. Mohanty, H. J. Rose, A. C. Rovero, M. S. Schubnell, G. Sembroski, T. C. Weekes and C. Wilson. "Calibration techniques for air-Cherenkov telescopes," Proc. 24th Int. Cosmic Ray Conf. (Rome), **3**, 412 (1995).

[15] S. D. Biller, C. W. Akerlof, J. Buckley, M. Chantell, D. J. Fegan, S. Fennell, J. A. Gaidos, A. M. Hillas, A. D. Kerrick, R. C. Lamb, D. A. Lewis, D. I. Meyer, G. Mohanty, K. S. O'Flaherty, M. Punch, P. T. Reynolds, H. J. Rose, A. C. Rovero, M. S. Schubnell, G. Sembroski, T. C. Weekes and C. Wilson. "An upper limit to the IR background from observations of TeV gamma-Rays," Proc. 24th Int. Cosmic Ray Conf. (Rome), **2**, 507 (1995).

[16] J. G. Bolton, and G. J. Stanley. "The position and probable identification of the source of galactic radio-frequency radiation Taurus-A," Aust. J. Sci. Res., Series A, **2**, 139 (1949).

[17] A. Borione, et al. Proc. 23rd Int. Cosmic Ray Conf. (Calgary), **1**, 286 (1993).

[18] A. L. Broadfoot, and K. R. Kendall. "The airglow spectrum, 3,100–10,000 A," J. Geophys. Res., **73**, 426 (1968).

[19] J. Buckley, J. Dwyer, D. Müller, and S. Swordy. "A new measurement of the light cosmic-ray nuclei at high energies," Astrophys. J., **429**, 736-747 (1994).

[20] J. F. Carlson, and J. R. Oppenheimer. "On multiplicative showers," Phys. Rev., **51**, 220 (1937).

[21] M. F. Cawley. "Noise reduction optimisation and new imaging algorithms," (Whipple Collaboration internal report) 1989.

[22] M. F. Cawley, D. J. Fegan, K. Harris, A. M. Hillas, P. W. Kwok, R. C. Lamb, M. J. Lang, D. A. Lewis, D. Macomb, P. T. Reynolds, D. J. Schmid, G. Vacanti, and T. C. Weekes. "A high resolution imaging detector for TeV gamma ray astronomy," Exp. Astron. , **1**, 173-193 (1990).

[23] M. Chantell. Ph. D. thesis, Univ. of Arizona, (1995).

[24] P. A. Cherenkov. "Visible radiation produced by electrons moving in a medium with velocities exceeding that of light," Phys. Rev., Letters to the editor, **52**, 378 (1937).

[25] D. H. Clark, and F. R. Stephenson. The historical supernovae, 1st ed. (Pergamon Press, New York, 1977).

[26] J. Clear. Ph. D. thesis, National Univ. of Ireland, (1984).

[27] J. W. Cronin, K. G. Gibbs, and T. C. Weekes. "The search for discrete astrophysical sources of energetic gamma radiation," Annu. Rev. Nucl. Part. Sci. **43**, 883-925 (1993).

[28] J. M. Davies and E. M. Cotton. J. Solar energy, science, and engineering, **1**, No. 2 and 3, 16-22 (1957).

[29] O. C. de Jager, H. I. Nel, A. K. Harding, P. Sreekumar, D. J. Thompson, P. F. Michelson, and P. L. Nolan. "Gamma Ray Observations of the Crab Nebula: a study of the Synchro-Compton Spectrum," (preprint). To be published in the Astrophysical Journal, 1995.

[30] B. L. Dingus, D. E. Alexandreas, R. C. Allen, R. L. Burman, and K. B. Butterfield. "Ultrahigh-energy pulsed emission from Hercules X-1 with anomalous air-shower muon production," Phys. Rev. Letters, **61**, 1906 (1988).

[31] A. Djannati-Atai. Ph. D. thesis, Univ. of P. et M. Curie (Paris) (1994).

[32] J. Engel, T K. Gaisser, P. Lipari, and T. Stanev. "Nucleus-nucleus collisions and interpretation of cosmic-ray cascades," Phys. Rev. D, **46**, Number 11, 5013 (1992).

[33] I. M. Felix. "On mice, rabbits and things that go eek," Annals of Irresistible Animals, **100**, 1 (1995)

[34] E. Fermi. Nuclear Physics, Rev. 1st ed. (Univ. of Chicago Press, 1950).

[35] D. J. Fegan, D. McLaughlin, J. Clear, M. F. Cawley, and N. A. Porter. "Fast large aperture camera and data acquisition system with applications in astrophysics, particle physics and nuclear medicine," Nucl. Instrum. Methods, **211**, 179 (1983).

[36] C. E. Fichtel, D. L. Bertsch, J. Chiang, B. L. Dingus, J. A. Esposito, J. M. Fierro, R. C. Hartman, S. D. Hunter, G. Kanbach, and D. A. Kniffen.

"The first energetic gamma-ray experiment telescope (EGRET) catalog," Astrophys. J. Suppl. Ser., **94, no. 2**, 551-581 (1994).

[37] G. J. Fishman. "The bursting, pulsing and transient high energy sky as Seen by the BATSE Experiment on the Compton Observatory," Bull. Am. Astron. Soc., **186**, #18.01 (1995).

[38] A. G. Frodesen, O. Skjeggestad, and H. Tøfte. Probability and Statistics in Particle Physics, (Universitetsforlaget, Bergen, Norway, 1979), chap. 4.1. Also available from Columbia Univ. Press, New York, 1979.

[39] W. F. Fry. Proc. NATO Advanced Workshop on VHE Gamma-Ray Astronomy, (Publ. Reidel, Boston; Dordrecht, Norwell) Distributed in the U. S. A. by Kluwer Academic, 1987.

[40] T. K. Gaisser, and T. Stanev. "Nucleus-nucleus collisions and interpretation of cosmic-ray cascades above 100 TeV," Phys. Rev. D, **25**, Number 9, 2341 (1982).

[41] T. K. Gaisser. Cosmic Rays and Particle Physics, 1st ed. (Cambridge Univ. Press, Cambridge, 1990)

[42] I. A. Getting. "A proposed detector for high energy electrons and mesons," Phys. Rev., Letters to the editor, **71**, 123 (1947).

[43] N. Gehrels, E. Chipman, and D. Kniffen. "The Compton Gamma Ray Observatory," Astrophys. J. Suppl. Ser., **92, no. 2**, 351-362 (1994).

[44] V. L. Ginzburg, and S. I. Syrovatskii. The origin of cosmic rays, (Pergamon Press, Oxford, 1964).

[45] P. Goret, T. Palfrey, A. Tabary, G. Vacanti, and R. Bazer-Bachi. "Observations of TeV gamma rays from the Crab nebula," Astron. Astrophys. **270**, 401 (1993).

[46] K. Greisen. "The extensive air showers," Progress in Cosmic Ray Physics. (North Holland Publishing Co., Amsterdam) **Vol. III**, 3 (1956).

[47] K. Greisen. "Cosmic ray showers," Annu. Rev. Nucl. Sci. (Annual Reviews, Inc., California) **Vol. 10**, 63 (1960).

[48] F. Halzen. "High-energy physics," Proc. 21st Int. Cosmic Ray Conf. (Adelaide), **12**, 101 (1990).

[49] "Photomultiplier tubes," Hamamatsu Corporation, New Jersey, (Feb. 1985).

[50] R. Hanbury-Brown. Philips Tech. Review, **27**, 141 (1966).

[51] R. Hanbury-Brown. Mon. Not. R. Astron. Soc. , **146**, 399 (1969).

[52] S. Hayakawa. Cosmic ray physics, Monographs and texts in physics and astronomy Vol. XXII (Wiley-InterScience, John Wiley & Sons, New York, 1969).

[53] W. Heitler. The quantum theory of radiation, 2nd ed. (Oxford Univ. Press, Oxford, 1949).

[54] W. Heisenberg. "The cascade theory," Cosmic Radiation. ed. W.Heisenberg. (Dover Publ., New York), 11 (1946).

[55] A. M. Hillas. "Differences between gamma-Ray and hadronic showers," Invited talk at Heidelberg Workshop on TeV Astrophysics, Oct. 1994. To be published in Space Science Reviews, 1995.

[56] A. M. Hillas. Cosmic rays, 1st ed. (Pergamon Press, Oxford, 1972).

[57] J. D. Jackson. Classical electrodynamics, 2nd ed. (John Wiley & Sons, New York, 1975).

[58] L. Janossy. "Rate of n-fold accidental coincidences," Nature, Letters to the editor, **153**, 165 (1944).

[59] J. V. Jelley. "Detection of μ-mesons and other fast charged particles in cosmic radiation, by the Čerenkov effect in distilled water," Proc. Phys. Soc. London, Sect. A, **64**, 82 (1951).

[60] J. V. Jelley. Cerenkov radiation, and its applications, (Pergamon Press, New York, 1958).

[61] Y. Jiang, P. Fleury, D. A. Lewis, G. Mohanty, E. Pare, A. C. Rovero, M. Urban, G. Vacanti and T. C. Weekes, "Absolute calibration of an atmospheric Cherenkov telescope using muon ring images," Proc. 23rd Int. Cosmic Ray Conf. (Calgary), **4**, 662 (1993).

[62] A. S. Jursa. (ed.). Handbook of Geophysics and Space Environments, 4th ed. (Hanscom Air Force Base, available from NTIS, 1985).

[63] A. D. Kerrick, C. W. Akerlof, S. D. Biller, J. H. Buckley, M. F. Cawley, M. Chantell, V. Connaughton, D. J. Fegan, S. Fennell, J. A. Gaidos. "Outburst of TeV photons from Markarian 421," Astrophys. J. Lett. **438, no. 2,** L59-L62 (1995).

[64] M. P. Kertzman and G. H. Sembroski. "Computer simulation methods for investigating the detection characteristics of TeV air Cherenkov telescopes," Nucl. Instrum. Methods A, **343**, 629-643 (1994)

[65] T. Kifune, T. Tanimori, S. Ogio, T. Tamura, H. Fujii, M. Fujimoto, T. Hara, N. Hayashida, S. Kabe, F. Kakimoto, Y. Matsubara, Y. Mizumoto, Y. Muraki, T. Suda, M. Teshima, T. Tsukagoshi, Y. Watase, T. Yoshikoshi, P. G. Edwards, J. R. Patterson, M. D. Roberts, G. Rowell, and G. J. Thornton. "Very High Energy gamma rays from PSR 1706-44," Astrophys. J. Lett. **438**, L91-L94 (1995).

[66] F. Krennrich, et al. Proc. 23rd Int. Cosmic Ray Conf. (Calgary), **1**, 251 (1993).

[67] P. W. Kwok. "Very High Energy gamma rays from the Crab Nebula and pulsar," Ph. D. thesis, Univ. of Arizona, (1989).

[68] R. C. Lamb, and T. C. Weekes. "Very high energy gamma-ray binary stars," Science, **238**, 1528 (1987).

[69] M. J. Lang. "The Observation of VHE gamma-rays from the Crab Nebula using the atmospheric Cherenkov imaging technique," Ph. D. thesis, University College, Dublin, (1991).

[70] D. A. Lewis. "Notes on optical properties of the 10m reflector," (Whipple collaboration internal report) 1987.

[71] D. A. Lewis, M. F. Cawley, D. J. Fegan, A. M. Hillas, P. W. Kwok, R. C. Lamb, P. T. Reynolds, N. A. Porter, and T. C. Weekes. Proc. 20th Int. Cosmic Ray Conf. (Moscow), **2**, 360 (1987).

[72] D. A. Lewis. "Optical characteristics of the Whipple Observatory TeV gamma-ray imaging telescope," Exp. Astron. , **1**, 213-226 (1990).

[73] D. A. Lewis, R. C. Lamb, M. J. Lang, D. Macomb, G. Mohanty, T. C. Weekes and T. Whitaker. "Energy spectrum determination with the atmospheric Cherenkov imaging technique," Proc. 22nd Int. Cosmic Ray Conf. (Dublin), **1**, 508 (1991).

[74] T. Li and Y. Ma. "Analysis Methods for results in gamma-ray astronomy," Astrophys. J. **272**, 317-324 (1983).

[75] M. S. Longair. High Energy Astrophysics. Vol. 1. Particles, photons and their detection, 2nd ed. (Cambridge Univ. Press, Cambridge, 1992).

[76] L. Lyons. Statistics for nuclear and particle physicists, 1st ed. (Cambridge Univ. Press, Cambridge, 1989), chap. 1.4.

[77] D. J. Macomb, C. W. Akerlof, H. D. Aller, M. F. Aller, D. L. Bertsch, F. Bruhweiler, J. Buckley, D. A. Carter-Lewis, M. F. Cawley, K. -P.Cheng, C. Dermer, D. J. Fegan, J. Gaidos, W. K. Gear, C. R. Hall, R. C. Hartman, A. M. Hillas, M. Kafatos, A. D. Kerrick, D. A. Kniffen, Y. Kondo, H. Kubo, R. C. Lamb, F. Makino, K. Makishima, A. Marscher, a.; J. McEnery, I. M. McHardy, D. I. Meyer, E. M. Moore, E. Ramos, E. I. Robson, H. J. Rose, M. S. Schubnell, G. Sembroski, J. A. Stevens, T. Takahashi, M. Tashiro, T. C. Weekes, C. Wilson, and J. Zweerink. "Multiwavelength observations of Markarian 421 during a TeV/X-Ray flare," Astrophys. J. Lett. **449**, L99 (1995).

[78] P. Massey, C. Gronwall, and C. A. Pilachowski. "The spectrum of the Kitt Peak night sky," Publ. Astron. Soc. Pac., **102**, 1046-1051 (Sept. 1990).

[79] M. Merck, et al. Proc. 23rd Int. Cosmic Ray Conf. (Calgary), **1**, 290 (1993).

[80] W. C. Miller. Astron. Soc. Pac. , Leaflet No. 314 (1955).

[81] S. Mitton. The Crab Nebula, 1st ed. (Faber and Faber, London, 1979).

[82] G. Mohanty. "Noise, mirror reflectivity, pe-to-dc conversion, and other things that go bump in the night." (Whipple collaboration internal report) 1995.

[83] D. Müller, S. P. Swordy, P. Meyer, J. L'Heureux, and J. M. Grunsfeld. "Energy spectra and composition of primary cosmic rays," Astrophys. J., **374**, 356-365 (1991).

[84] Y. Pal and B. Peters. "Meson Production at High Energies and the Propagation of Cosmic Rays through the Atmosphere," Mat. Fys. Medd. Dan. Vid. Selsk. **33**, no. 15 (1964).

[85] A. V. Plyasheshnikov and A. C. Konopelko. "The Determination of the VHE Cosmic Gamma-Radiation Energy Spectrum Parameters on the Base of Gamma-Ray Telescope Experimental Data," Proc. Intl. Workshop on VHE Gamma-Ray Astronomy, pg. 115 (1989)

[86] A. V. Plyasheshnikov and A. C. Konopelko. "The Energy Estimation of VHE Gamma-Quanta by the Gamma-Ray Telescope with the Multi-Channel Receiver of the Cherenkov light," Proc. Intl. Workshop on VHE Gamma-Ray Astronomy, pg. 120 (1989)

[87] M. Punch. (private communication) 1990.

[88] M. Punch, C. W. Akerlof, M. F. Cawley, D. J. Fegan, R. C. Lamb, M. A. Lawrence, M. J. Lang, D. A. Lewis, D. I. Meyer, K. S. O'Flaherty, P. T. Reynolds

and M. S. Schubnell. "Supercuts: an improved method of selecting gamma-rays," Proc. 22nd Int. Cosmic Ray Conf. (Dublin), **1**, 464 (1991).

[89] M. Punch, C. W. Akerlof, M. F. Cawley, D. J. Fegan, R. C. Lamb, M. A. Lawrence, M. J. Lang, D. A. Lewis, D. I. Meyer, K. S. O'Flaherty, P. T. Reynolds and M. S. Schubnell. "Supercuts: an improved method of selecting gamma-rays," Proc. Atmospheric Cherenkov Imaging Workshop, Whipple Observatory, (1992).

[90] M. Punch, C. W. Akerlof, M. F. Cawley, M. Chantell, D. J. Fegan, S. Fennell, J. A. Gaidos, J. Hagan, A. M. Hillas, Y. Jiang, A. D. Kerrick, R. C. Lamb, M. A. Lawrence, D. A. Lewis, D. I. Meyer, G. Mohanty, K. S. O'Flaherty, P. T. Reynolds, A. C. Rovero, M. S. Schubnell, G. Sembroski, T. C. Weekes, T. Whitaker, and C. Wilson, "Detection of TeV photons from the active galaxy Markarian 421," Nature, **358**, 477 (1992).

[91] J. Quinn, C. W. Akerlof, S. Biller, J. Buckley, D. A. Carter-Lewis, M. F. Cawley, M. Catanese, V. Connaughton, D. J. Fegan, J. P. Finley, J. Gaidos, A. M. Hillas, R. C. Lamb, F. Krennrich, R. Lessard, J. E. McEnery, D. I. Meyer, G. Mohanty, A. J. Rodgers, H. J. Rose, G. Sembroski, M. S. Schubnell, T. C. Weekes, C. Wilson, and J. Zweerink. "Detection of gamma rays with E ¿ 300 GeV from Markarian 501," To be published in the Astrophysical Journal 1995.

[92] RCA photomultiplier manual, (RCA Corporation, Harrison, New Jersey, 1970).

[93] P. T. Reynolds. Ph. D. thesis, National Univ. of Ireland, (1989).

[94] R. R. Robbins. Proc. Am. Astron. Soc. (Albuquerque), (1990).

[95] H. J. Rose, D. Bird, J. Buckley, M. F. Cawley, M. Chantell, K. Harris, R. Lessard, M. S. Schubnell, G. Sembroski, C. Wilson, "A data acquisition system for TeV stereo imaging telescopes," Proc. 24th Int. Cosmic Ray Conf. (Rome), **3**, 766 (1995).

[96] B. Rossi, and K. Greisen. "Cosmic-ray theory," Rev. Mod. Phys. **13**, 240 (1941).

[97] B. Rossi. High-Energy particles, 1st ed. (Prentice-Hall, New York, 1952).

[98] M. J. Ryan, J. F. Ormes, and V. K. Balasubramanyan. "Cosmic-ray proton and helium spectra above 50 GeV," Phys. Rev. Lett., **28**, No. 15, 985-988 (1972). Note that the quoted differential flux is in error. See also *ERRATA,* Phys. Rev. Lett., **28**, No. 22, 1497 (1972).

[99] M. Samorski and W. Stamm. "Muon densities of extended air showers induced by 10^{15}–2×10^{16} eV gamma-rays," Proc. 18th Int. Cosmic Ray Conf. (Bangalore), **11**, 244 (1983)

[100] M. S. Schubnell, C. W. Akerlof, M. F. Cawley, M. Chantell, D. J. Fegan, S. Fennell, S. Freeman, D. Frishman, J. A. Gaidos, J. Hagan., K. Harris, A. M. Hillas, A. D. Kerrick, R. C. Lamb, M. A. Lawrence, D. A. Lewis, D. I. Meyer, G. Mohanty, K. S. O'Flaherty, M. Punch, P. T. Reynolds, A. C. Rovero, G. Sembroski, C. Weaverdyck, T. C. Weekes, T. Whitaker and C. Wilson. "Granite–a stereoscopic imaging Cherenkov telescope system," Proc. Compton Observatory Symp., St. Louis, AIP Conf. Proc., **280**, 1171 (1992).

[101] W. T. Scott. "The Theory of small-angle multiple scattering of fast charged particles," Rev. Mod. Phys. **35**, 231 (1963).

[102] G. Sembroski. "Modeling the 10m Trigger Successes, Failures and Lessons Learned," (Whipple collaboration internal report) 1995.

[103] R. Serber. "Transition effects of cosmic rays in the atmosphere," Phys. Rev. **54**, 317 (1938).

[104] I. Shklovsky. Supernovae, 1st ed. (John Wiley & Sons Ltd., London, 1968). Translated from the original manuscript by Literaturprojekt, Austria.

[105] I. Shklovsky. Five billion vodka bottles to the moon, 1st ed. (W. W. Norton & Company, New York, 1991). Translated and adapted by M. F. Zirn, and H.Zirn.

[106] J. A. Simpson. "Elemental and isotopic composition of the galactic cosmic rays," Annu. Rev. Nucl. Part. Sci. , **33**, 323-381 (1983)

[107] H. S. Snyder. "Transition effects of cosmic rays in the atmosphere," Phys. Rev. **53**, 960 (1938).

[108] T. Takahashi et al., IAU Circ. 5993 (1995).

[109] T. Tanimori, T. Tsukagoshi, T. Kifune, P. G. Edwards, M. Fujimoto, T. Hara, N. Hayashida, Y. Matsubara, Y. Mizumoto, Y. Muraki, S. Ogio, J. R. Patterson, M. D. Roberts, G. Rowell, T. Suda, T. Tamura, M. Teshima, G. J. Thornton, Y. Watase and T. Yoshikoshi. "Observation of 7 TeV gamma rays from the Crab using the large zenith angle air Čerenkov imaging Technique," Astrophys. J. Lett. **429**, L61-L64 (1994).

[110] D. J. Thompson, D. L. Bertsch, B. L. Dingus, J. A. Esposito, A. Etienne, C. E. Fichtel, D. P. Friedlander, R. C. Hartman, S. D. Hunter, D. J. Kendig,

J. R. Mattox, L. M. McDonald, C. von Montigny, R. Mukherjee, P. V. Ramanmurthy, P. Sreekumar, J. M. Fierro, Y. C. Lin, P. F. Michelson, P. L. Nolan, S. K. Shriver, T. D. Willis, G. Kanbach, H. A. Mayer-Hasselwander, M. Merck, H. -D. Radecke, D. A. Kniffen, and E. J. Schneid. "The second EGRET catalog of high-energy gamma-ray sources," Astrophys. J. Suppl. Ser., **101**, 259 (1995).

[111] United States Committee on Extension to the Standard Atmosphere. U. S. Standard Atmosphere, 1976. (Supt. of Docs. , U. S. Govt. Print. Off. , 1976)

[112] G. Vacanti, M. F. Cawley, E. Colombo, D. J. Fegan, A. M. Hillas, P. W. Kwok, M. J. Lang, R. C. Lamb, D. A. Lewis, D. J. Macomb, K. S. O'Flaherty, P. T. Reynolds, and T. C. Weekes. "Gamma-ray observations of the Crab Nebula at TeV energies," Astrophys. J., **377**, 467 (1991).

[113] S. L. Valley (ed.). Handbook of Geophysics and Space Environments, (Air Force Cambridge Research Laboratories, McGraw-Hill), chap. 7

[114] R. Weast (ed.). Handbook of Chemistry and Physics, 65th ed. (CRC Press, Florida, 1984-85), pg. F-150 to F-152

[115] T. C. Weekes, G. G. Fazio, H. F. Helmken, E. O'Mongain, and G. H. Rieke. "A search for discrete sources of cosmic gamma rays of energy 10^{11}–10^{12} eV," Astrophys J., **174**, 165 (1972).

[116] T. C. Weekes. "Very High Energy Gamma-Ray Astronomy," Physics Reports, **160**, No. 1 and 2, 1-121 (1988).

[117] T. C. Weekes, M. F. Cawley, D. J. Fegan, K. G. Gibbs, A. M. Hillas, P. W. Kwok, R. C. Lamb, D. A. Lewis, D. Macomb, N. A. Porter, P. T. Reynolds, and G. Vacanti. "Observations of TeV gamma rays from the Crab Nebula using the atmospheric Cerenkov imaging technique," Astrophys J., **342**, 379 (1989).

[118] T. C. Weekes. "The atmospheric Cherenkov technique in Very High Energy gamma-ray astronomy," Heidelberg Workshop on TeV Astrophysics, Oct. 1994.

[119] T. C. Weekes, C. W. Akerlof, M. Chantell, E. Colombo, M. F. Cawley, V. Connaughton, D. J. Fegan, S. Fennell, J. Gaidos, A. M. Hillas, A. D. Kerrick, P. W. Kwok, D. A. Lewis, R. C. Lamb, D. I. Meyer, G. Mohanty, J. Rose, A. Rovero, G. Sembroski, M. S. Schubnell, M. Punch, M. West, T. Whitaker, and C. Wilson. "Observations of the Crab Nebula at TeV energies," Proc. 2nd Compton Symp., (ed. C. E. Fichtel, N. Gehrels, and J. P. Norris), AIP Conf. Proc. **304**, 270 (1994).

[120] M. West. Ph. D. thesis, Univ. of Leeds, (1994).

APPENDIX A. CRAB DATABASES FOR ALL EPOCHS

This appendix gives details of the Crab nebula databases used in each observing season. For each epoch, the first section gives the values of various quantities such as mirror reflectivity, photoelectron to ADC counts conversion factor etc., that were derived from the data and used in the simulations. We start out with the values for the 1988-89 database, that were partly derived from the data, and partly estimated. Then, these values are used to extrapolate to the other observing seasons. (See Chap. 3.4 for a description of the derivation of the parameters for 1988-89, and the manner in which they are scaled to other epochs.)

The second section for each observing season is a table giving details of the actual data runs, including run numbers, duration and source elevation.

A.1 1988-89 database

A.1.1 Mirror reflectivity, and other factors

The derivation of the 1988-89 data parameters can be found in sec. 3.4.1. They are repeated here for convenient reference.

The average hardware trigger threshold is estimated to be 50 ADC counts in each of two of the inner 91 tubes. The mirror reflectivity is taken to be 85 % of the manufacturer's specification (Liberty mirror company coating spec. no. 1050), and the PMT quantum efficiency is taken from the Hamamatsu typical response curve for a R1398 UV glass tube [49, pg. 66]. (Also, see Fig. 3.16 and Fig. 3.17.) The photoelectron to ADC counts conversion factor is estimated to be 0.85 d.c./p.e., as per the values measured by Kwok [67, Appdx. A3.3] using a radioactive source attached to the PMT. The night-sky noise is estimated by measuring the standard deviations in the sky pedestals, and is found to be 3.14 ADC counts for the 2.9 cm

inner tubes, and 2.74 ADC counts for the 4.3 cm outer tubes.

A.1.2 Details of data runs

Table A.1 below, gives details of the data runs for the 1988-89 epoch.

Table A.1: 1988-89 Crab database

	Run I. D.		No. of events		Calendar	UT	duration	Elevation
	ON	OFF	ON	OFF	date	at start	sid. min.	(degrees)
1	cr0702	cr0703	8455	8342	881109	809	28	67.1–72.6
2	cr0704	cr0705	8706	8384	881109	913	28	78.4–80.3
3	cr0707	cr0708	8456	8562	881109	1108	28	68.5–62.6
4	cr0721	cr0720	8219	8642	881110	715	28	56.9–63.0
5	cr0781	cr0782	8497	8051	881113	653	28	54.6–60.4
6	cr0783	cr0784	8605	8590	881113	753	28	67.1–72.5
7	cr0785	cr0786	8740	8931	881113	853	28	77.8–80.3
8	cr0787	cr0788	8651	8730	881113	957	28	78.2–73.8
9	cr0789	cr0790	8638	8344	881113	1057	28	67.6–61.9
10	cr0802	cr0801	8256	8374	881114	722	28	61.6–67.2
11	cr0804	cr0803	8396	8573	881114	823	28	73.6–78.0
12	cr0807	cr0806	8851	8865	881114	949	28	78.7–74.5
13	cr0809	cr0808	8525	8566	881114	1049	28	68.4–62.7
14	cr0818	cr0819	8943	8436	881116	712	28	61.0–66.8
15	cr0820	cr0821	8889	8680	881116	812	28	73.0–77.6
16	cr0822	cr0823	8841	8826	881116	914	28	80.3–78.6
17	cr0824	cr0825	8816	8764	881116	1015	28	73.4–68.1
18	cr0826	cr0827	8652	8340	881116	1115	28	61.5–55.6
19	cr0834	cr0835	8605	8499	881117	807	28	72.8–77.5
20	cr0901	cr0902	8312	8241	881202	609	28	61.0–66.8

Table A.1 (Continued)

	Run I. D.		No. of events		Calendar	UT	duration	Elevation
	ON	OFF	ON	OFF	date	at start	sid. min.	(degrees)
21	cr0922	cr0923	8385	8358	881203	635	28	67.2–72.6
22	cr0924	cr0925	8600	8305	881203	735	28	77.9–80.3
23	cr0955	cr0956	8464	8568	881206	722	28	77.8–80.2
24	cr0957	cr0958	8639	8517	881206	824	28	78.5–74.2
25	cr0959	cr0960	6063	5914	881206	923	20	68.3–64.2
26	cr1121	cr1122	8156	8128	881231	348	28	55.4–61.2
27	cr1123	cr1124	8564	8558	881231	448	28	67.8–73.2
28	cr1138	cr1139	8185	7855	890101	411	27	61.0–66.6
29	cr1154	cr1155	8194	8323	890106	321	28	54.6–60.5
30	cr1156	cr1157	8644	8579	890106	421	28	67.1–72.6
31	cr1198	cr1199	4931	4744	890109	318	19	56.6–60.5
32	cr1201	cr1202	5045	5493	890109	420	17	69.3–72.8
33	cr1203	cr1204	8759	8570	890109	509	28	77.9–80.3
34	cr1226	cr1227	7572	7354	890110	335	28	61.0–66.7
35	cr1228	cr1229	7826	7609	890110	435	28	72.9–77.6
36	cr1233	cr1234	7507	7573	890110	639	27	73.3–68.0
37	cr1251	cr1250	7813	7856	890111	501	28	77.8–80.2
38	cr1253	cr1252	9663	9863	890111	611	35	77.3–71.2
39	cr1255	cr1254	9617	9697	890111	731	35	62.3–54.7
40	cr1273	cr1274	8035	7969	890112	557	28	78.6–74.5
41	cr1275	cr1276	7921	7832	890112	657	28	68.4–62.7
42	cr1346	cr1347	7396	7357	890204	259	28	73.3–77.8
43	cr1348	cr1349	7230	7207	890204	400	28	80.3–78.5
44	cr1350	cr1351	7447	7179	890204	500	28	73.5–68.1
45	cr1352	cr1353	7155	6846	890227	559	28	42.6–36.7
46	cr1417	cr1418	6224	5969	890227	306	23	77.3–73.6
47	cr1419	cr1420	7158	6979	890306	359	28	62.2–56.4
48	cr1477	cr1478	7378	7424	890306	301	28	73.6–68.3

Table A.1 (Continued)

	Run I. D.		No. of events		Calendar	UT	duration	Elevation
	ON	OFF	ON	OFF	date	at start	sid. min.	(degrees)
49	cr1479	cr1480	7093	6447	890307	401	27	61.0–55.3
50	cr1501	cr1500	9485	9634	890308	328	38	66.9–59.1
51	cr1522	cr1523	7059	7053	890308	252	28	73.9–68.6
52	cr1524	cr1525	6819	6762	890308	353	28	61.8–56.0

A.2 1989-90 database

A.2.1 Mirror reflectivity, and other factors

The 1989-90 data files on the crab were deemed unsuitable for spectrum analysis due to the presence of an independent trigger that had priority over the normal Cherenkov trigger (see sec. 6.2.2 for further discussion of the effects of this trigger). While it would have been possible to model the formation of the independent trigger, we have chosen to discard this data, as we have plenty of Crab data from other epochs.

A.2.2 Details of data runs

For the sake of completeness, the runs from this season are given in Table A.2 below, though they are not used in the spectrum analysis. The number of events in each run includes both code 8 and code 9 events.

Table A.2: 1989-90 Crab database

	Run I. D.		No. of events		Calendar	UT	duration	Elevation
	ON	OFF	ON	OFF	date	at start	sid. min.	(degrees)
1	cr2418	cr2419	8933	8622	890928	1026	27	61.2–66.7
2	cr2440	cr2441	6531	6510	890929	1106	21	70.1–74.0
3	cr2463	cr2464	5900	5955	890930	1115	21	72.5–76.1
4	cr2486	cr2487	7770	7668	891001	1100	27	70.6–75.3
5	cr2507	cr2508	7915	8009	891002	1016	28	62.3–68.2
6	cr2539	cr2540	7707	7320	891008	954	27	62.6–68.1
7	cr2541	cr2542	7547	7594	891008	1054	27	74.4–78.5
8	cr2598	cr2599	2907	2952	891024	834	13	59.1–61.8

Table A.2 (Continued)

	Run I. D.		No. of events		Calendar	UT	duration	Elevation
	ON	OFF	ON	OFF	date	at start	sid. min.	(degrees)
9	cr2765	cr2766	6469	6497	891103	933	27	77.7–80.2
10	cr2767	cr2768	6508	6575	891103	1034	27	78.6–74.5
11	cr2794	cr2793	6205	6453	891104	1024	27	79.2–75.4
12	cr2796	cr2795	6414	6092	891104	1124	27	69.5–64.0
13	cr2827	cr2828	6486	6140	891106	751	27	60.8–66.3
14	cr2829	cr2830	6727	6537	891106	852	27	73.0–77.4
15	cr2831	cr2832	2496	2393	891106	953	10	80.3–80.2
16	cr2833	cr2834	6562	6606	891106	1053	27	73.8–68.5
17	cr2847	cr2848	6539	6539	891107	848	27	72.9–77.4
18	cr2849	cr2850	6621	6578	891107	949	27	80.3–78.9
19	cr2851	cr2852	6668	6543	891107	1049	27	73.9–68.7
20	cr2853	cr2854	2959	3121	891107	1148	13	62.2–59.5
21	cr2862	cr2863	6668	6727	891108	844	28	72.9–77.6
22	cr2864	cr2865	6775	6711	891108	945	28	80.3–78.7
23	cr2866	cr2867	6829	6671	891108	1045	28	73.9–68.5
24	cr2868	cr2869	2951	2902	891108	1144	28	62.2–59.5
25	cr2899	cr2898	4682	4786	891122	705	20	64.3–68.4
26	cr2901	cr2900	6815	6687	891122	805	28	75.7–79.3
27	cr2903	cr2902	3148	3262	891122	850	28	80.3–80.0
28	cr3003	cr3002	6527	6620	891203	824	27	79.8–76.5
29	cr3006	cr3005	6335	6179	891203	1009	28	61.5–55.6
30	cr3019	cr3018	6753	6492	891204	734	28	78.1–80.3
31	cr3021	cr3020	4505	4613	891204	834	19	78.4–75.5
32	cr3023	cr3022	4004	3971	891204	936	17	67.5–63.9
33	cr3033	cr3032	6423	6578	891205	658	28	73.0–77.6
34	cr3035	cr3034	6422	6428	891205	759	28	80.3–78.7
35	cr3037	cr3036	6424	6496	891205	859	28	73.8–68.3
36	cr3052	cr3051	5447	5460	891206	803	27	80.2–78.4
37	cr3054	cr3053	6641	6647	891206	857	28	73.5–68.1
38	cr3056	cr3055	6065	2905	891206	957	35	61.4–59.0

Table A.2 (Continued)

	Run I. D.		No. of events		Calendar	UT	duration	Elevation
	ON	OFF	ON	OFF	date	at start	sid. min.	(degrees)
39	cr3302	cr3301	5993	6095	900125	532	35	75.0–69.8
40	cr3304	cr3303	5774	5870	900125	632	28	63.3–57.5
41	cr3312	cr3311	5878	5908	900126	417	28	79.5–80.1
42	cr3314	cr3313	5926	5915	900126	517	28	76.8–71.9
43	cr3316	cr3315	5766	5838	900126	618	28	65.4–59.6
44	cr3386	cr3385	3892	3751	900129	356	28	78.4–80.0
45	cr3391	cr3390	3879	4073	900129	446	28	79.2–76.9
46	cr3395	cr3394	3987	3806	900129	530	23	72.5–69.0
47	cr3397	cr3396	3786	3787	900129	610	28	64.6–60.9
48	cr3498	cr3497	5838	5899	900218	435	28	67.9–62.2

A.3 1990 database

A.3.1 Mirror reflectivity, and other factors

The derivation of the parameters for the 1990 Crab database is described in sec. 6.2.3.1. The average hardware trigger threshold is estimated to be 52 ADC counts in each of two of the inner 91 tubes. The overall reflectivity is taken to be 50 % of the 1988-89 overall reflectivity. The photoelectron to ADC counts conversion factor is estimated to be 1.44 d.c./p.e. The night-sky noise is estimated by measuring the standard deviations in the sky pedestals, and is found to be 3.62 ADC counts for the 2.9 cm inner tubes, and 3.34 ADC counts for the 4.3 cm outer tubes.

A.3.2 Details of data runs

Table A.3 below, gives details of the data runs for the 1990 Crab database.

Table A.3: 1990 Crab database

	Run I. D.		No. of events		Calendar	UT	duration	Elevation
	ON	OFF	ON	OFF	date	at start	sid. min.	(degrees)
1	cr3302	cr3301	5374	5517	900125	502	26	79.2–75.6
2	cr3304	cr3303	5377	5459	900125	602	27	69.4–64.0
3	cr3312	cr3311	5328	5365	900126	345	26	75.1–78.8
4	cr3314	cr3313	5326	5344	900126	447	26	80.0–77.4
5	cr3316	cr3315	5327	5269	900126	548	26	71.3–66.2
6	cr3386	cr3385	2323	2213	900129	336	11	75.5–77.2
7	cr3391	cr3390	3292	3535	900129	426	16	80.3–79.6
8	cr3395	cr3394	3462	3270	900129	510	16	76.0–73.2
9	cr3397	cr3396	3418	3295	900129	550	16	68.7–65.4
10	cr3498	cr3497	5216	5319	900218	405	26	73.6–68.7

Table A.3 (Continued)

	Run I. D.		No. of events		Calendar	UT	duration	Elevation
	ON	OFF	ON	OFF	date	at start	sid. min.	(degrees)
11	cr3500	cr3499	5389	5579	900218	505	28	61.7–55.6
12	cr3524	cr3525	5496	2988	900220	425	28	68.4–65.1
13	cr3954	cr3953	5287	5228	900223	313	27	78.6–74.6
14	cr3956	cr3955	5026	4918	900223	414	28	68.2–62.5
15	cr3986	cr3985	5128	5218	900224	337	28	74.4–69.2
16	cr4016	cr4015	5156	5208	900225	305	28	78.7–74.5
17	cr4018	cr4017	4944	4968	900225	405	28	68.4–62.7

A.4 1990-91 database

A.4.1 Mirror reflectivity, and other factors

The derivation of the parameters for the 1990 Crab database is described in sec. 6.2.4.1. The average hardware trigger threshold is estimated to be 57 ADC counts in each of two of the inner 91 tubes. The overall reflectivity is taken to be 38 % of the 1988-89 overall reflectivity. The photoelectron to ADC counts conversion factor is estimated to be 1.79 d.c./p.e. The night-sky noise is estimated by measuring the standard deviations in the sky pedestals, and is found to be 4.00 ADC counts for the 2.9 cm inner tubes, and 3.74 ADC counts for the 4.3 cm outer tubes.

A.4.2 Details of data runs

Table A.4 below, gives details of the data runs for the 1990-91 Crab.

Table A.4: 1990-91 Crab database

	Run I. D.		No. of events		Calendar	UT	duration	Elevation
	ON	OFF	ON	OFF	date	at start	sid. min.	(degrees)
1	cr5117	cr5116	4499	4735	901015	852	27	55.2–61.1
2	cr5148	cr5149	3503	3387	901016	900	21	57.7–62.1
3	cr5150	cr5151	3460	3417	901016	1000	21	70.0–74.0
4	cr5152	cr5153	4592	4338	901016	1101	27	79.6–80.1
5	cr5229	cr5230	5130	4965	901021	1007	28	74.9–79.0
6	cr5231	cr5232	4749	4672	901021	1107	27	80.2–77.6
7	cr5257	cr5258	4794	4603	901022	920	27	66.7–72.2
8	cr5259	cr5260	2247	2176	901022	1021	13	77.7–79.3
9	cr5261	cr5262	4797	4889	901022	1123	27	78.4–74.3
10	cr5283	cr5284	4717	4695	901023	859	27	63.3–68.8

Table A.4 (Continued)

	Run I. D.		No. of events		Calendar	UT	duration	Elevation
	ON	OFF	ON	OFF	date	at start	sid. min.	(degrees)
11	cr5285	cr5286	4830	4999	901023	959	27	74.9–78.8
12	cr5287	cr5288	4766	4787	901023	1102	27	80.0–77.1
13	cr5311	cr5312	4692	4676	901024	1039	27	80.2–79.5
14	cr5314	cr5315	2272	2280	901024	1143	27	74.2–71.8
15	cr5336	cr5335	1772	1788	901025	1033	10	80.1–80.3
16	cr5339	cr5338	2708	2618	901025	1135	27	74.9–72.2
17	cr5351	cr5352	4637	4742	901026	937	27	73.1–77.5
18	cr5353	cr5354	4609	4571	901026	1038	27	80.3–78.8
19	cr5355	cr5356	4760	3075	901026	1140	27	73.3–70.0
20	cr5389	cr5388	2419	2225	901028	1057	13	78.8–77.1
21	cr5397	cr5396	4722	4817	901029	924	28	72.9–77.5
22	cr5399	cr5398	4782	4924	901029	1025	28	80.3–78.8
23	cr5566	cr5567	5151	4811	901118	711	28	62.1–67.8
24	cr5570	cr5571	4984	5305	901118	840	28	78.4–80.3
25	cr5572	cr5573	3666	3614	901118	1000	20	75.0–71.4
26	cr5574	cr5575	4964	5081	901118	1120	28	59.2–53.1
27	cr5820	cr5821	5332	5446	901219	545	28	69.4–74.8
28	cr5825	cr5826	5082	5250	901219	754	27	75.6–70.7
29	cr5827	cr5828	5099	5058	901219	854	28	64.1–58.3
30	cr5850	cr5851	5237	5307	901220	706	28	80.3–78.1
31	cr5852	cr5853	3642	3498	901220	806	19	72.8–69.2
32	cr5854	cr5855	3156	2974	901220	906	17	60.8–57.2
33	cr5887	cr5888	4871	5002	910111	510	28	78.7–80.3
34	cr5889	cr5890	4966	4862	910111	611	28	77.6–73.0
35	cr5909	cr5910	4779	4715	910112	501	28	78.1–80.3

Table A.4 (Continued)

	Run I. D.		No. of events		Calendar	UT	duration	Elevation
36	cr6006	cr6007	4891	4665	910118	416	27	74.8–78.7
37	cr6008	cr6009	4906	4865	910118	523	28	79.8–76.4
38	cr6028	cr6029	4967	4829	910119	428	35	77.3–80.1
39	cr6030	cr6031	5054	5065	910119	530	35	78.8–74.7
40	cr6032	cr6033	4817	5126	910119	630	28	68.7–62.8
41	cr6034	cr6035	4544	4618	910119	731	28	56.0–50.0

A.5 1991-92 database

A.5.1 Mirror reflectivity, and other factors

The derivation of the parameters for the 1991-92 Crab database is described in sec. 6.2.5.1. The average hardware trigger threshold is estimated to be 45 ADC counts in each of two of the inner 91 tubes. The overall reflectivity is taken to be 40 % of the 1988-89 overall reflectivity. The photoelectron to ADC counts conversion factor is estimated to be 1.61 d.c./p.e. The night-sky noise is estimated by measuring the standard deviations in the sky pedestals, and is found to be 3.79 ADC counts for the 2.9 cm inner tubes, and 3.20 ADC counts for the 4.3 cm outer tubes.

A.5.2 Details of data runs

Table A.5 below, gives details of the data runs for the 1991-92 Crab database.

Table A.5: 1991-92 Crab database

	Run I. D.		No. of events		Calendar	UT	duration	Elevation
	ON	OFF	ON	OFF	date	at start	sid. min.	(degrees)
1	cr7710	cr7711	5119	4863	911203	644	28	68.5–68.4
2	cr7712	cr7713	4754	4569	911203	745	27	78.7–79.3
3	cr7717	cr7718	4909	4956	911203	938	28	68.3–67.0
4	cr7728	cr7729	4143	4118	911204	707	26	73.5–74.3
5	cr7791	cr7792	4974	4722	911214	855	28	68.2–67.0
6	cr7802	cr7803	4833	4960	911215	842	31	68.8–68.7
7	cr7804	cr7805	4687	4663	911215	943	28	57.5–56.5
8	cr7825	cr7826	3997	3914	911228	411	28	57.1–58.4
9	cr7827	cr7828	4102	4133	911228	513	28	69.9–71.1
10	cr7866	cr7867	4697	4168	920126	458	28	79.4–78.7

Table A.5 (Continued)

	Run I. D.		No. of events		Calendar	UT	duration	Elevation
	ON	OFF	ON	OFF	date	at start	sid. min.	(degrees)
11	cr7877	cr7878	5881	5621	920127	601	28	68.4–67.1
12	cr7879	cr7880	5398	5396	920127	700	28	56.2–56.2
13	cr7888	cr7889	6010	5909	920128	334	28	74.1–75.2
14	cr7890	cr7891	5732	5384	920128	434	28	80.3–80.1
15	cr7892	cr7893	5778	5699	920128	534	28	72.9–71.7
16	cr7957	cr7958	6028	5923	920131	550	28	67.3–66.3
17	cr8150	cr8151	5370	5378	920222	344	28	74.9–65.7
18	cr8152	cr8153	2638	2869	920222	446	15	62.6–58.9

APPENDIX B. THE HILLAS PARAMETERS

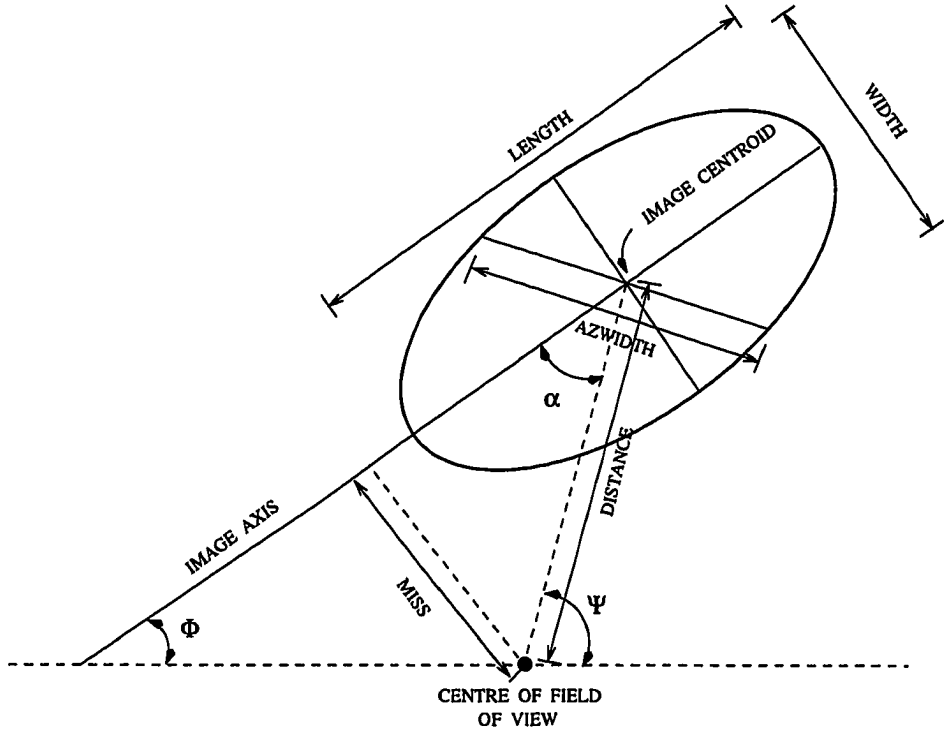

Figure B.1: Geometrical interpretation of Hillas parameters

Fig. B.1 above shows a typical elliptical image of the Cherenkov light in an air shower. Also, shown is the geometrical interpretation of the Hillas parameters, defined below. The centre of the field of view in the figure above is where the source location would be in the image plane, with the telescope pointed directly at a pointlike source. The parameters are also generally classified into "shape" parameters like width, and length, that define the size of the image, and into "orientation" parameters

like α, that defines the angle that the shower axis makes with the direction to the source location. Azwidth is an example of parameter that is a combination of both shape and orientation.

Here are the definitions of the moments, and the Hillas parameters, reproduced here courtesy of Punch [87]. The tube positions are given by the coordinates x, and y, measured in degrees. The number of counts in a tube, after gain renormalization, pedestal subtraction and image cleaning, is given by n. Each summation runs over all the tubes in the image. First, the various moments are defined as:

$$\begin{aligned}
\langle x \rangle &= \frac{\sum n_i x_i}{\sum n_i} \\
\langle y \rangle &= \frac{\sum n_i y_i}{\sum n_i} \\
\left\langle x^2 \right\rangle &= \frac{\sum n_i x_i^2}{\sum n_i} \\
\left\langle y^2 \right\rangle &= \frac{\sum n_i y_i^2}{\sum n_i} \\
\left\langle x^3 \right\rangle &= \frac{\sum n_i x_i^3}{\sum n_i} \\
\left\langle y^3 \right\rangle &= \frac{\sum n_i y_i^3}{\sum n_i} \\
\langle x\, y \rangle &= \frac{\sum n_i x_i y_i}{\sum n_i} \\
\left\langle x^2\, y \right\rangle &= \frac{\sum n_i x_i^2 y_i}{\sum n_i} \\
\left\langle x\, y^2 \right\rangle &= \frac{\sum n_i x_i y_i^2}{\sum n_i}
\end{aligned} \tag{B.1}$$

The spreads of the images in different directions, can then be defined in terms of the moments, as:

$$\begin{aligned}
\sigma_{x^2} &= \left\langle x^2 \right\rangle - \langle x \rangle^2 \\
\sigma_{y^2} &= \left\langle y^2 \right\rangle - \langle y \rangle^2 \\
\sigma_{xy} &= \langle x\, y \rangle - \langle x \rangle \langle y \rangle \\
\sigma_{x^3} &= \left\langle x^3 \right\rangle - 3 \langle x \rangle^2 \langle x \rangle + 2 \langle x \rangle^3 \\
\sigma_{y^3} &= \left\langle y^3 \right\rangle - 3 \langle y \rangle^2 \langle y \rangle + 2 \langle y \rangle^3
\end{aligned} \tag{B.2}$$

$$\sigma_{x^2y} = \left\langle x^2 y \right\rangle - \left\langle x^2 \right\rangle \langle y \rangle - 2 \langle x\, y \rangle \langle x \rangle + 2 \langle x \rangle^2 \langle y \rangle$$
$$\sigma_{xy^2} = \left\langle x\, y^2 \right\rangle - \langle x \rangle \left\langle y^2 \right\rangle - 2 \langle x\, y \rangle \langle y \rangle + 2 \langle x \rangle \langle y \rangle^2$$

Now, the various Hillas parameters can be defined in terms of the previously defined moments, and the image spreads, as:

$$\begin{aligned}
d &= \sigma_{y^2} - \sigma_{x^2} \\
s &= \sqrt{d^2 + 4 (\sigma_{xy})^2} \\
u &= 1 + \frac{d}{s} \\
v &= 2 - u \\
w &= \sqrt{(\langle y^2 \rangle - \langle x^2 \rangle)^2 + 4 \langle x\, y \rangle^2} \\
\tan\phi &= \frac{(d+s) \langle y \rangle + 2\sigma_{xy} \langle x \rangle}{2\sigma_{xy} \langle y \rangle - (d-s) \langle x \rangle} \\
\text{length} &= \sqrt{\frac{\sigma_{x^2} + \sigma_{y^2} + s}{2}} \\
\text{width} &= \sqrt{\frac{\sigma_{x^2} + \sigma_{y^2} - s}{2}} \\
\text{distance} &= \sqrt{\langle x^2 \rangle + \langle y^2 \rangle} \\
\text{miss} &= \sqrt{\frac{1}{2} \left(u \langle x \rangle^2 + v \langle y \rangle^2 \right) - \left(\frac{2\sigma_{xy} \langle x \rangle \langle y \rangle}{s} \right)} \\
\sin\alpha &= \frac{\text{miss}}{\text{distance}} \\
\text{azwidth} &= \sqrt{\frac{\langle x \rangle^2 \langle y^2 \rangle - 2 \langle x \rangle \langle y \rangle \langle x\, y \rangle + \langle x^2 \rangle \langle y \rangle^2}{(\text{ distance })^2}} \\
\text{akwidth} &= \sqrt{\frac{\langle x^2 \rangle + \langle y^2 \rangle - w}{2}} \\
\sigma'_{x^3} &= \sigma_{x^3} \cos^3\phi + 3\sigma_{x^2y} \cos^2\phi \sin\phi + 3\sigma_{xy^2} \cos\phi \sin^2\phi + \sigma_{y^3} \sin^3\phi \\
\text{asymmetry} &= \frac{\sqrt[3]{\sigma'_{x^3}}}{\text{length}}
\end{aligned} \tag{B.3}$$

The orientation parameter, α, is often spelt out as "alpha." The parameter, "akwidth," is the Akerlof azwidth. Of these parameters, only width, length, alpha, and distance are used in standard supercuts and in extended supercuts. The parameter,

azwidth, is also used in this work to select gamma rays in a search for the pulsed flux from the Crab, as it retains more gamma rays. "Asymmetry" is sometimes used to find an expected tail in the images of gamma ray showers.

APPENDIX C. COSMIC RAY FLUXES

This is meant to be a quick and dirty estimate of the cosmic ray fluxes in the region of interest for the comparisons (0.3 TeV to a few TeV), and is far from an exhaustive and complete compilation. The accuracy of the present numbers is good enough for the purposes of this work.

My fluxes are based mainly on three sources, Ryan et al [98], Müller et al [83], and Buckley et al [19]. Müller et al, and Buckley et al quote flux values that are reproduced in the tables below. I have converted their flux into what I call "proton equivalents," i.e., I assume that for the atmospheric cascades, a heavy cosmic ray nucleus with energy E can be treated as a collection of the individual nucleons, with the total energy distributed equally between them on the average. For example, if $(dN/dE)_{He}$ be the differential flux of helium nuclei (in [m^2 s sr (TeV/nucleon)]$^{-1}$), the flux in proton equivalents would be:

$$(dN/dE)_{prot.equiv.} = 4 \times (dN/dE)_{He} \tag{C.1}$$

Next, I make approximate fits to the cosmic ray spectra using the published differential spectrum and the values in the tables above. All fits are constrained to have a differential spectral index of -2.71, which is the index in the Monte Carlo simulations (all the measured spectra have indices close to this value, so this is not too bad an approximation).

1. *Ryan et al*

This paper gives a fitted spectrum rather than a table of flux values. The approximate fits are:

Protons (upto 2 TeV) :

Table C.1: Table of fluxes from Müller et al.

Element	Energy/nucleon (TeV/nucleon)	Differential flux $[m^2\ s\ sr\ (TeV/nucleon)]^{-1}$ Flux	Error	Proton equiv.	Error
C	0.0726	1.54×10^{-1}	2.0×10^{-2}	1.848	0.24
(Z = 6)	0.1026	6.26×10^{-2}	3.7×10^{-2}	0.751	0.44
(N = 12)	0.2068	1.04×10^{-2}	1.1×10^{-3}	0.124	0.013
	1.503	4.35×10^{-5}	1×10^{-5}	5.22×10^{-4}	1.2×10^{-4}
O	0.0726	1.88×10^{-1}	1.8×10^{-2}	3.008	0.288
(Z = 8)	0.1026	7.38×10^{-2}	1.0×10^{-2}	1.18	0.16
(N = 16)	0.2068	1.16×10^{-2}	1.2×10^{-3}	0.186	0.019
	1.503	5.9×10^{-5}	1.2×10^{-5}	9.4×10^{-4}	1.9×10^{-4}
Ne	0.050	9.3×10^{-2}	1.26×10^{-2}	1.86	0.252
(Z = 10)	0.0613	4.33×10^{-2}	7.0×10^{-3}	0.866	0.14
(N = 20)	0.0827	1.65×10^{-2}	3.4×10^{-3}	0.330	0.068
	0.1551	3.67×10^{-3}	3.7×10^{-3}	0.073	0.074
	1.028	1.50×10^{-5}	$^{+1.42\times10^{-5}}_{-8.1\times10^{-6}}$	3.00×10^{-4}	$^{+2.84\times10^{-4}}_{-1.62\times10^{-4}}$
Mg	0.050	1.07×10^{-1}	1.36×10^{-2}	2.57	0.326
(Z = 12)	0.0613	6.15×10^{-2}	7.9×10^{-3}	1.48	0.19
(N = 24)	0.0827	2.61×10^{-2}	3.7×10^{-3}	0.626	0.089
	0.1551	4.86×10^{-3}	4.1×10^{-4}	0.117	9.8×10^{-3}
	1.028	4.19×10^{-5}	$^{+2.0\times10^{-5}}_{-1.4\times10^{-5}}$	1.01×10^{-3}	$^{+4.8\times10^{-4}}_{-3.4\times10^{-4}}$
Si	0.050	9.46×10^{-2}	1.54×10^{-2}	2.65	0.431
(Z = 14)	0.0613	4.94×10^{-2}	9.3×10^{-3}	1.38	0.260
(N = 28)	0.0827	2.13×10^{-2}	3.9×10^{-3}	0.596	0.109
	0.157	3.72×10^{-3}	4.7×10^{-4}	0.104	0.013
	1.028	5.6×10^{-6}	$^{+1.26\times10^{-5}}_{-4.6\times10^{-6}}$	1.6×10^{-4}	$^{+3.52\times10^{-4}}_{-1.3\times10^{-4}}$
				(×56)	
Fe *like*	0.0526	6.23×10^{-2}	1.11×10^{-2}	3.49	0.622
($25 < Z < 27$)	0.0592	4.43×10^{-2}	6.7×10^{-3}	2.48	0.38
($55 < N < 60$)	0.0686	3.29×10^{-2}	5.7×10^{-3}	1.84	0.32
	0.0816	1.88×10^{-2}	3.0×10^{-3}	1.05	0.17
	0.1154	7.5×10^{-3}	1.0×10^{-3}	0.42	0.056

Table C.1 (Continued)

Element	Energy/nucleon (TeV/nucleon)	Differential flux $[m^2\ s\ sr\ (TeV/nucleon)]^{-1}$ Flux	Error	Proton equiv.	Error
Fe *like*	0.2220	1.5×10^{-3}	2.8×10^{-4}	0.084	0.016
(cont.)	0.6490	9.24×10^{-5}	$^{+4.12\times10^{-5}}_{-3.02\times10^{-5}}$	5.17×10^{-3}	$^{+2.31\times10^{-3}}_{-1.69\times10^{-3}}$
	1.563	9.23×10^{-6}	$^{+8.77\times10^{-6}}_{-5.01\times10^{-6}}$	5.17×10^{-4}	$^{+4.91\times10^{-4}}_{-2.81\times10^{-4}}$

$$\frac{dN}{dE} = 0.117 \left(\frac{E}{1\,\text{TeV}}\right)^{-2.71} \quad \frac{\#}{\text{m}^2\ \text{s sr TeV}} \tag{C.2}$$

Helium (upto $\sim$ 500 GeV, in proton equivalents) :

$$\frac{dN}{dE} = 1.76 \times 10^{-2} \left(\frac{E}{1\,\text{TeV/nucleon}}\right)^{-2.71} \quad \frac{\#}{\text{m}^2\ \text{s sr (TeV/nucleon)}} \tag{C.3}$$

2. *Müller et al*

These fits are approximately derived from the flux values in Table C.1.

Carbon (upto $\sim$ 1.5 TeV, in proton equivalents) :

$$\frac{dN}{dE} = 1.6 \times 10^{-3} \left(\frac{E}{1\,\text{TeV/nucleon}}\right)^{-2.71} \quad \frac{\#}{\text{m}^2\ \text{s sr (TeV/nucleon)}} \tag{C.4}$$

Oxygen (upto $\sim$ 1.5 TeV, in proton equivalents) :

$$\frac{dN}{dE} = 2.6 \times 10^{-3} \left(\frac{E}{1\,\text{TeV/nucleon}}\right)^{-2.71} \quad \frac{\#}{\text{m}^2\ \text{s sr (TeV/nucleon)}} \tag{C.5}$$

Neon (upto $\sim$ 1 TeV, in proton equivalents) :

$$\frac{dN}{dE} = 4.2 \times 10^{-4} \left(\frac{E}{1\,\text{TeV/nucleon}}\right)^{-2.71} \quad \frac{\#}{\text{m}^2\ \text{s sr (TeV/nucleon)}} \tag{C.6}$$

Magnesium (upto $\sim$ 1 TeV, in proton equivalents) :

Table C.2: Table of fluxes from Buckley et al.

Element	Energy/nucleon (TeV/nucleon)	Differential flux $[m^2\ s\ sr\ (TeV/nucleon)]^{-1}$ Flux	Error	Proton equiv.	Error
Helium	0.0480	2.36×10^1	2.8	9.44×10^1	1.12×10^1
	0.0597	1.32×10^1	1.4	5.28×10^1	5.6
	0.0790	6.02	0.64	2.408×10^1	2.56
	0.1252	1.80	0.21	7.20	0.84
	0.3144	0.168	0.0026	0.672	0.0104
Carbon	0.0481	9.4×10^{-1}	$^{+2.6\times10^{-1}}_{-2.1\times10^{-1}}$	1.128×10^1	$^{+3.12}_{-2.52}$
	0.0714	2.6×10^{-1}	$^{+1.1\times10^{-1}}_{-0.8\times10^{-1}}$	3.12	$^{+1.32}_{-0.96}$
	0.1389	5.5×10^{-2}	$^{+1.9\times10^{-2}}_{-1.5\times10^{-2}}$	0.66	$^{+0.228}_{-0.18}$
Oxygen	0.0481	5.9×10^{-1}	$^{+2.3\times10^{-1}}_{-1.8\times10^{-1}}$	9.44	$^{+3.68}_{-2.88}$
	0.0714	3.3×10^{-1}	$^{+1.2\times10^{-1}}_{-0.9\times10^{-1}}$	5.28	$^{+1.92}_{-1.44}$
	0.1389	5.5×10^{-2}	$^{+2.0\times10^{-2}}_{-1.5\times10^{-2}}$	0.832	$^{+0.32}_{-0.24}$

$$\frac{dN}{dE} = 7.5 \times 10^{-4} \left(\frac{E}{1\,\text{TeV/nucleon}}\right)^{-2.71} \quad \frac{\#}{\text{m}^2\ \text{s sr (TeV/nucleon)}} \tag{C.7}$$

Silicon (upto $\sim$ 1 TeV, in proton equivalents) :

$$\frac{dN}{dE} = 7 \times 10^{-4} \left(\frac{E}{1\,\text{TeV/nucleon}}\right)^{-2.71} \quad \frac{\#}{\text{m}^2\ \text{s sr (TeV/nucleon)}} \tag{C.8}$$

Iron-like (upto $\sim$ 1.6 TeV, in proton equivalents) :

$$\frac{dN}{dE} = 1.2 \times 10^{-3} \left(\frac{E}{1\,\text{TeV/nucleon}}\right)^{-2.71} \quad \frac{\#}{\text{m}^2\ \text{s sr (TeV/nucleon)}} \tag{C.9}$$

2. *Buckley et al*

These fits are approximately derived from the flux values in Table C.2.

Helium (upto $\sim$ 300 GeV, in proton equivalents) :

$$\frac{dN}{dE} = 2.5 \times 10^{-2} \left(\frac{E}{1\,\mathrm{TeV/nucleon}} \right)^{-2.71} \quad \frac{\#}{\mathrm{m^2\ s\ sr\ (TeV/nucleon)}} \quad \text{(C.10)}$$

Carbon (upto $\sim$ 140 GeV, in proton equivalents) :

$$\frac{dN}{dE} = 2.7 \times 10^{-3} \left(\frac{E}{1\,\mathrm{TeV/nucleon}} \right)^{-2.71} \quad \frac{\#}{\mathrm{m^2\ s\ sr\ (TeV/nucleon)}} \quad \text{(C.11)}$$

Oxygen (upto $\sim$ 140 GeV, in proton equivalents) :

$$\frac{dN}{dE} = 2.8 \times 10^{-3} \left(\frac{E}{1\,\mathrm{TeV/nucleon}} \right)^{-2.71} \quad \frac{\#}{\mathrm{m^2\ s\ sr\ (TeV/nucleon)}} \quad \text{(C.12)}$$

Putting all of this together, the approximate fit to the differential flux of all cosmic ray particles in this energy regime is:

All particles, in proton equivalents) :

$$\frac{dN}{dE} = 0.144 \left(\frac{E}{1\,\mathrm{TeV/nucleon}} \right)^{-2.71} \quad \frac{\#}{\mathrm{m^2\ s\ sr\ (TeV/nucleon)}} \quad \text{(C.13)}$$